

**PROfile**

# Geophysics in geothermal exploration

**A review**

**Jean-Luc Mari and Geoffroy Paixach**

**edp sciences**





# **Geophysics in Geothermal Exploration**

**A review**



# Geophysics in Geothermal Exploration

A review

Jean-Luc Mari  
and  
Geoffroy Paixach



edp sciences

DOI: 10.1051/978-2-7598-3752-6  
ISBN(ebook): 978-2-7598-3752-6

This book is published under Open Access Creative Commons License CC-BY-NC-ND (<https://creativecommons.org/licenses/by-nc-nd/4.0/en/>) allowing non-commercial use, distribution, reproduction of the text, via any medium, provided the source is cited.

© EDP Sciences, 2025



<b>Chapter 2 • Surface geophysical methods</b>	51
<i>J.-L. Mari and G. Paixach</i>	
2.1 Physical properties of rocks and pore space properties	55
2.1.1 Porosity	57
2.1.2 Permeability	58
2.2 Geophysical methods	61
2.2.1 Gravity method	63
2.2.2 Magnetic method	68
2.2.3 Electrical and EM methods	69
2.2.4 Seismic methods	80
Conclusion	107
References	108
<b>Chapter 3 • Borehole geophysical methods</b>	115
<i>J.L. Mari</i>	
3.1 Conventional logging methods	116
3.2 Hydrogeological methods	120
3.3 Full waveform acoustic methods	123
3.4 Borehole seismic method	129
Conclusion	140
References	141
<b>Chapter 4 • Towards a revisited geothermal conceptual model in the Upper Rhine Graben</b>	145
<i>A. Genter, C. Baujard, C. Glaas and V. Maurer</i>	
4.1 Geothermal development in the Upper Rhine Graben	146
4.2 Evolution of the geothermal concept during the SsF adventure	148
4.3 Pre-exploration phase	153
4.4 Optimizing borehole design according to the geological knowledge of the reservoir	159
Conclusion and perspectives	160
Acknowledgments	161
References	161

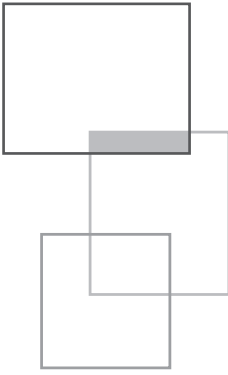
<b>Chapter 5 • DEEP ERT/IP for geothermal exploration and de-risking</b>	165
<i>A. Rosselli, C. Truffert, F. Barsuglia, F. Fischanger, A. Coletti, G. Morelli and S. Del Ghianda</i>	
5.1 Context	165
5.2 Why electrical resistivity tomography is useful?	166
5.3 Deep electrical resistivity tomography for geothermal exploration – an Italian example	166
5.3.1 Unconventional ERT data acquisition	167
5.3.2 Acquisition methodology	169
5.3.3 Acquisition layout	170
5.3.4 Current transmissions	172
5.3.5 Quality control	173
5.3.6 Processing of resistivity and chargeability measurements	175
5.3.7 Results	177
Conclusion	180
<b>Chapter 6 • The use of passive seismic methods for Geothermal exploration and monitoring</b>	181
<i>T. Kremer, J. M. Ars, T. Gaubert-Bastide, K. Khazraj and C. Voisin</i>	
Introduction	181
6.1 Methods	185
6.1.1 Seismological analysis	185
6.1.2 Ambient noise seismic interferometry (ANSI)	189
6.1.3 Tomography	190
6.1.4 Monitoring	191
6.2 Passive seismic methods for geothermal exploration	193
6.2.1 Seismological analysis	194
6.2.2 Ambient noise seismic interferometry (ANSI)	204
6.2.3 Integration into the geothermal exploration workflow	206
6.3 Geothermal monitoring	208
6.3.1 Seismological analysis monitoring	208
6.3.2 Ambient noise seismic interferometry monitoring	210
Concluding remarks	214
References	216

<b>Chapter 7 • Seismic inversion and characterization applied to geothermal energy</b>	223
<i>R. Baillet, T. Chrest, T. Defreminville and E. Masse</i>	
Introduction	223
7.1 Technical background	224
7.1.1 Seismic gathers and partial stacking	224
7.1.2 The subsurface as an isotropic elastic medium	225
7.1.3 Convolution and resolution	226
7.2 Seismic inversion	228
7.2.1 About seismic conditioning	228
7.2.2 Wavelet extraction and optimization	228
7.2.3 Construction of a low-frequency model	229
7.2.4 Performing a seismic inversion	230
7.3 Introduction to seismic characterization	232
7.3.1 Exploring well response through a petro-elastic model building	232
7.3.2 Seismic attributes related to faults and fractures	234
7.3.3 Characterization empowered by machine learning	235
7.4 Example: identification of lithology, good porosity and fractured areas through a seismic inversion study	237
Conclusions and perspectives	239
References	239

<b>Chapter 8 • Seismic anisotropy applied to geothermal prospection</b>	241
<i>R. Baillet, N. Desgoutte, V.Thomas and J. Caudroit</i>	
Introduction	241
8.1 Technical background	242
8.1.1 The HTI and VTI models for anisotropy models	242
8.1.2 Azimuthal stacking and required processing	243
8.2 Velocity versus Azimuth (VVAz): a shift detection methodology	244
8.3 Amplitude versus Azimuth (AVAz): an inversion methodology	245
8.4 Ellipse fitting on properties to estimate the anisotropy	245
8.5 From anisotropy to fracture attributes	247
8.6 Case study: Fracture characterization through azimuthal inversions to prospect the geothermal potential of Geneva basin	248
8.6.1 Processing, conditioning, shift detection	248
8.6.2 Model-based inversions	250
8.6.3 Results and way forward	251
Conclusions and perspectives	254
References	254

<b>Chapter 9 • Defining high enthalpy geothermal drilling target with multi-physics integrated exploration program. Mayotte's Petite-Terre Island case study</b>	257
<i>A. Stopin, C. Dezayes and T. Farlotti</i>	
Introduction	257
9.1 Integration of magnetotelluric data	260
9.2 Electric profile integration	264
9.3 Gravimetric data integration	267
9.4 Final model	268
9.5 Choice of the drilling target	271
References	272
<b>Chapter 10 • Feasibility of monitoring cold fronts of geothermal doublets using 4D active electromagnetic techniques – a field trial in the Dogger play in the Paris Basin</b>	275
<i>F. Dubois, A. Stopin, F. Bretaudeau and P. Wawrzyniak</i>	
Introduction	276
10.1 Context	277
10.2 Acquisition	278
10.3 Receiver conception	281
10.4 Survey	282
10.5 Data processing	284
10.6 Detectability of the cold front	287
Conclusions	288
References	290
<b>Synthesis</b>	291
<i>G. Paixach and J.L. Mari</i>	
A range of geothermal systems	291
A range of geophysical techniques	292
Geophysics for geothermal systems	293
From resource exploration to drilling project de-risking and asset monitoring	295
<b>Conclusion</b>	297
<i>J.L. Mari and G. Paixach</i>	





# Prefaces

---

An invitation in March 2024 to the scientific days of the “AGAP-Qualité” from Jean-Luc Mari and its president Michel Hayet made it possible to initiate interesting conversations between the applied geophysics community and the French administration on subsurface exploration.

This book entirely dedicated to geophysical investigation applied to the characterization of geothermal resources is, I hope, a first step in the dissemination of knowledge and know-how for everyone, from practitioners to a broad public.

We are all convinced that geothermal energy represents a promising renewable energy source, capable of meeting energy needs while reducing our carbon footprint.

I sincerely thank all the authors of the technical chapters constituting this book with a special mention to Geoffroy Paixach and Jean-Luc Mari who, in their free time, made it possible to develop this work.

Dear reader, I hope that, like me, you will have the pleasure of discovering this book and keeping it within reach.

Jean-Claude Lecomte

Geoscience expert  
Bureau des ressources énergétiques du sous-sol  
Direction Générale de l’Energie et du Climat  
Ministère de la transition écologique, de l’énergie,  
du climat et de la prévention des risques

It is with great pride and enthusiasm that I present this preface to the latest issue of *Cahiers de l'AGAP*. While the term “Cahiers” may evoke the idea of a lighter compilation, I believe, and I hope readers will agree, that the exceptional quality and depth of the contributions in this volume will serve as a valuable resource for professionals in the geothermal industry, supporting their future projects.

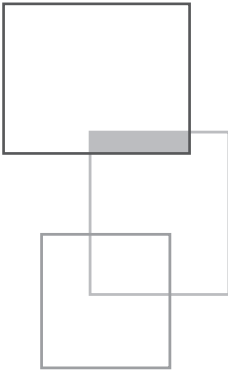
State-of-the-art geophysics has become essential to accelerate the exploration and development of new geothermal projects.

Geophysical methods, long established in fields such as petroleum exploration, mining, hydrogeology, and civil engineering, are now proving increasingly indispensable in the context of geothermal energy development.

Geothermal energy is becoming increasingly important in today's energy transition and is poised to play a growing role in the national, european, and global energy mix.

On behalf of AGAP-Qualité, I extend my sincere gratitude to all the authors for their remarkable contributions, as well as to the coordinators, Jean-Luc Mari and Geoffroy Paixach, for their involvement in bringing this work to fruition.

Michel Hayet  
Chairman of AGAP  
AGAP-Qualité  
Association for Quality in Applied Geophysics



# Foreword

J.-L. Mari and G. Paixach

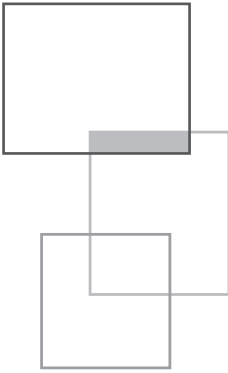
---

The book entitled “**Geophysics in Geothermal exploration: a review**” provides a practical guide on how to apply geophysical methods in geothermal exploration, illustrated with real-world field examples. These methods support resource exploration, the de-risking of drilling projects, and the ongoing monitoring of geothermal assets.

The book begins with an introduction to geothermal energy systems. It then delves into geophysical methods, presenting the current state of knowledge and illustrating how electrical-electromagnetic and active-passive seismic methods can be combined into a Multiphysics approach for geothermal exploration.

The book is published under Open-Source Creative Commons License CC-BY-NC-ND allowing non-commercial use, distribution, reproduction of the text, via any medium, provided the source is cited.





# The authors

---

## **Jean-Luc MARI**



A graduate of the *Institut Physique du Globe Strasbourg* and the IFP School (petroleum geosciences, major in geophysics in 1978), Jean-Luc Mari was employed by IFP *Energies Nouvelles* in 1979 as a research engineer in the Geophysics Department. Here he worked on several research projects, such as high-resolution seismic surveying, reservoir monitoring, and the development of borehole tools, in collaboration with industrial partners GdF-Suez, CGG, Total and ELF Aquitaine. In 1984, he was awarded a PhD in Astronomy and Celestial Mechanics by the Université Pierre et Marie Curie.

In 1986, he was seconded to ELF Aquitaine where he worked on reservoir geophysics. He joined IFPEN in 1987 and was seconded to the Reservoir Department, where he studied, in particular, the benefits of using geophysical methods in horizontal wells. In 1994 he was appointed to the IFP School as a professor and obtained the accreditation to supervise earth science research (HDR). He was an expert in geophysics for IFP *Energies Nouvelles*.

Jean-Luc, member of the EAGE, was an associate editor for *Near Surface Geophysics*. Currently retired from IFP *Energies Nouvelles*, Jean-Luc is an independent researcher and consultant in geophysics. He is a member of the board and of the accreditation committee for the Association for Quality in Applied Geophysics (AGAP - *Association pour la Qualité en Géophysique Appliquée*).

An author and co-author of patents and numerous scientific articles, Jean-Luc Mari has also contributed to educational scientific books and has been involved in the design and development of tutorials and e-books. In 2010, he received a Knighthood from the *Ordre des Palmes Académiques*.

## **Geoffroy PAIXACH**



Geoffroy is a geophysicist with a degree from the IFP School, Paris. He began his career with an Oil and Gas operator at the Geoscience Research Center in London, focusing on seismic processing amplitude preservation. Over the years, Geoffroy has held various positions in reservoir characterization for Beicip-Franlab, a subsidiary of IFPEN. Geoffroy worked in the Marine CSEM industry and the seismic multi-client industry, developing offshore seismic acquisition programs in multiple countries. He co-founded and managed a startup specializing in real-time simulation for basin modeling in Houston.

In 2025, he became the Chief Executive Officer of CFG Geothermal, a geothermal resource consulting and engineering services firm.

## **Jean-Michel ARS**



Graduated from École Normale Supérieure d'Electricité et de Mécanique in 2012 and from Université Paul Sabatier in 2013. Jean-Michel Ars obtained a PhD from Université Bretagne Occidentale in 2018 in the field of geophysics, focusing on multi-physics joint inversion applied to geothermal exploration. He was a post-doc for 3 years before becoming a geophysics researcher at Geolinks since 2022. He works primarily in the field of inverse methods for geophysical imaging but also studies seismic ambient noise as subsurface characterization and monitoring tools.

## **Romain BAILLET**



Romain Baillet is a Geophysicist with an Engineer Degree (MSc) from the “École et Observatoire des Sciences de la Terre” school in Strasbourg, France. He joined Beicip-Franlab in 2012 as a specialist in seismic inversion and characterization. Till then, he has been involved in many integrated or specialized studies for all energies, including geothermal activities. As an expert and project leader, he currently participates in the innovation of the methodologies proposed by Beicip-Franlab by designing and carrying out workflows including seismic data, to lower the risks in both prospection and production phases. As

a product manager of the geophysical software InterWell, he improves and optimizes the workflows of seismic inversion, seismic characterization or time-depth conversion. either in terms of technology (e.g. Machine Learning) or customer needs (Performance, data type/transfer...).

## **Clément BAUJARD**



Dr Clément Baujard is an experienced reservoir engineer with a strong background in flow, thermal exchanges and mechanical processes in fractured reservoir. He was graduated as a geoscience engineer in 2002 and obtained a PhD in quantitative hydrogeology in 2005 from Paris School of Mines. From 2006, he worked as a geothermal reservoir engineer in Switzerland and then joined geothermal industry at *Électricité de Strasbourg Géothermie* (ÉSG), a small company offering engineering services in deep geothermal energy in 2013. At ÉS-Géothermie, he is currently leading the subsurface engineering department.

He contributed to many European research projects in relation with geothermal energy and he was in charge of several industrial projects in the Upper Rhine Graben dealing with deep geothermal energy and geothermal lithium. He is author or co-author of many international scientific publications

## **Frédéric BUGAREL**



Graduating from Pierre et Marie Curie University (Paris VI) with a master's degree in hydrogeology in 2004, Frédéric Bugarel developed his skills in drilling project engineering by working successively in the international oil industry, in the monitoring and safety of former French mining sites and in geothermal energy. Since 2023, he has held the position of Project Director at CFG Geothermal, a subsidiary of BRGM and BEICIP-FRANLAB, an engineering firm specializing in deep geothermal energy.

## **Chrystel DEZAYES**



Chrystel Dezayes is a researcher at the French Geological Survey (BRGM) in the Geothermal Energy Department. Since her PhD in 1995, she is working about fracture network characterisation at the Soultz-sous-Forêts EGS site and elsewhere in the world. She joined BRGM in 2002 in the geothermal team as researcher. She continues her work about fractured deep geothermal reservoir and develop exploration methods for sedimentary basin context. She is also project leader for high temperature geothermal exploration in oversea islands and scientific coordinator for the geothermal energy and energy storage

at BRGM. She has authored and co-authored about 40 articles in scientific journals and numerous others in international conferences.

## **Frédéric DUBOIS**



Graduating from the *École et Observatoire des Sciences de la Terre de Strasbourg* in 2016, Frédéric Dubois is working at the BRGM (*Bureau de recherches géologiques et minières*) since 2020 as geophysicist specialized in electromagnetism. His expertise spans over the broad spectrum from magnetotelluric to intermediate frequency domain and through land and airborne controlled source electromagnetism.

## **Thomas GAUBERT-BASTIDE**



Thomas Gaubert-Bastide, graduated from Université Grenoble Alpes in 2017, obtained a PhD in geophysics from both Université de Pau et des Pays de l'Adour and Université Grenoble Alpes in 2023, focusing on water-table monitoring through seismic interferometry. Since early 2023, he has been working as a geophysicist researcher at Geolinks. His main research is centered on the characterization and monitoring of subsurface physical processes using seismic noise analysis at various scales.

## Albert GENTER



Graduating from University of Orléans with a PhD in Geology in 1989, Albert Genter carried out research on the Soultz-sous-Forêts pioneered geothermal project. After his PhD, he was employed by *BRGM*, working on Enhanced Geothermal System (EGS). At *BRGM*, he was successively a junior geologist, R&D project manager, then geo-energy unit manager and finally deputy manager of the geothermal division.

In 2007, he joined the *Heat Mining industrial Group* as the scientific manager of the EGS Soultz site. He was responsible for a geoscientific program for monitoring this geothermal plant producing electricity. From 2014 to now, he joined geothermal industry at *Électricité de Strasbourg Géothermie* (ÉSG) as deputy general manager. He was, for example, the main coordinator of the European Horizon 2020 MEET project from 2018 to 2022. Since 2025, he is retired but still involved in geothermal energy as an independent consultant.

Albert was elected at the board directors of the International Geothermal Association (IGA) from 2013 to 2020. He was also elected at the board of directors of the French Geothermal Association (AFPG) from 2022 to 2024. He is author or co-authors of about 70 international scientific publications. He has also contributed to educational purposes by providing academic lectures in universities (Mainz, Neuchâtel, Paris, Orléans, Strasbourg) and in High Schools (Mines Nancy, École de Géologie de Nancy, IFP School). During his career, he was examiner or supervisor of about 30 students (PhD, master) and 2 accreditations to supervise earth sciences research.

He got two best presentation awards at the geothermal US conference GRC in 2009 and 2014. He got also an award from the WING (Women in Geothermal) association.

## Carole GLAAS



Dr Carole Glaas is a junior geologist with an expertise in fractured reservoirs from the Upper Rhine Graben (URG). She was graduated in 2021 with a PhD from French Universities of Strasbourg and Poitiers. She did her PhD in relation with *Électricité de Strasbourg Géothermie* (ÉSG). She focussed on the crystalline part of geothermal wells drilled in fractured reservoirs located in the URG. During her PhD, she investigated hydrothermal alteration minerals like clay minerals as well as the fractured reservoirs from a structural point of view. At ÉSG, she was in charge of geological studies and well log interpretation

for a geothermal well drilled South of Strasbourg and contributed to the well testing operations. Recruited at ÉSG in 2021, as a junior geologist, she contributed to many national and EU research projects dealing with deep geothermal energy and geothermal lithium. She is author or co-author of many international scientific publications

### ***Kaoutar KHAZRAJ***



Kaoutar Khazraj graduated with an engineering diploma from the École Nationale Supérieure d'Électricité et de Mécanique in Nancy in 2015, specializing in hydrodynamic reservoir engineering. She also obtained research master's degree in Petroleum Geosciences and Reservoir Engineering from Université de Lorraine in 2015. In 2024, she completed her PhD in geophysics at CY Cergy Paris Université. Her doctoral research focused on developing an innovative hybrid full-waveform inversion method for borehole seismic data to improve inversion results for under-determined seismic problems. Since

June 2024, she has been a geophysical researcher at Geolinks, specializing in inverse methods and the development of numerical algorithms for geophysical imaging.

### ***Thomas KREMER***



Thomas Kremer received a PhD degree received in 2015 from Institut de Physique du Globe de Paris. He is now a 13-year-old experienced research geophysicist specialized in geophysical monitoring applications with. His research work initiated with the use of electromagnetics methods for the monitoring of CCUS projects. He also developed innovative methods for the monitoring and characterization of hydrogeological systems.

Since 2020, he has been managing the R&D department at Geolinks services, an innovative company that promotes the development of passive seismic methods for multiple subsurface monitoring applications, such as hydrogeological characterization, geotechnical risk assessment, geothermal exploration, and CCUS and UGS projects monitoring.

## Éric LASNE



Geologist with a PhD in hydrogeology, Éric Lasne has held project management and management positions at Compagnie Française de Géothermie since 1992. As such, he has extensive knowledge of the challenges of the subsurface in terms of all the applications and uses of geothermal resources. On the technical side, Éric Lasne has worked on several low-energy geothermal projects in France (Dogger in the Paris Basin, Aquitaine Basin, Alsace, Centre Region, etc.) and for electricity generation in the French overseas territories (Guadeloupe, Martinique, La Réunion) and abroad (Azores – Portugal, Dominica, Indonesia, China, Russia, etc.). Involved in the development of CFG's activities, he is also active in professional organizations dedicated to the promotion and development of geothermal energy. A representative of one of the founding members of AFPG, Éric Lasne is also a member of the geothermal energy committee of the French Renewable Energy Union (SER).

## Vincent MAURER



Dr Vincent Maurer is a senior geophysicist specialized in seismology with skills in design and installation of seismic networks for monitoring induced micro-seismicity. He was graduated in 2009 with a PhD on geophysics at ETH-Zürich in Switzerland. From 2010 to now, he worked for geothermal industry at *Électricité de Strasbourg Géothermie* (ÉSG) as a geophysicist and is responsible for the seismic monitoring of the Soultz-sous-Forêts and the Rittershoffen geothermal plants. In parallel, he is involved in many geophysical surveys for geothermal exploration in Alsace: 2D/3D seismic acquisition, 3D MT/CSEM survey, aeromagnetic and gravity campaigns, and passive seismology. He also contributed to the interpretation of the geophysical acquisition to design well trajectories. At ÉSG, he is currently involved in several industrial geothermal projects in Northern Alsace. He contributed to national R&D projects and EU research projects dealing with geothermal energy. He is author or co-author of many international scientific publications.

## **Alberto ROSSELLI**



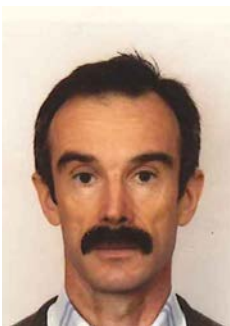
PhD in geophysics from the University of Lausanne, Switzerland. In 2001 he started a postdoc at the Laboratoire de Géophysique of the École Polytechnique de Montréal (Québec). In 2010 Alberto Roselli was employed by PGS as a seismic navigator. In 2012 he started to work as offshore and onshore client representative for Total EP and ENI. He has been employed as Party Chief by Geo2X. In 2021 he co-founded GEG Experts and he's currently General Director of the company.

## **Alexandre STOPIN**



Alexandre Stopin is an experienced geophysicist currently working at BRGM (Bureau de Recherches Géologiques et Minières). His expertise spans geophysical exploration, geothermal resource assessment, and geological CO<sub>2</sub> storage. He has contributed to several European projects and is responsible for the geophysical acquisition and processing of the Geoscan project. Earlier in his career, he worked at Shell Global Solutions International BV, where he led a team specialized in advanced seismic methods, including Elastic Full Waveform Inversion (FWI), to tackle complex subsurface imaging challenges. Beyond his research contributions, Alexandre actively shares his findings through scientific publications and international conferences, promoting sustainable energy solutions and innovative geophysical techniques.

## **Hervé TRINEAU**



Hervé Traineau is a senior geologist and geothermal expert. He got a PhD in Petrology-Volcanology at the University of Paris 11 in 1982. He began his career in 1981 as a geologist at the BRGM. Assigned to the Geothermal Department, he participated in numerous geothermal exploration campaigns in the West Indies (Haiti, Santo Domingo, Martinique, Guadeloupe, Dominica). From 1983 to 1997, he was assigned to the Institut Mixte de Recherches Géothermiques and then to the BRGM Research Department, where he participated in various applied research programs and exploration

campaigns in the fields of high-enthalpy geothermal energy. He also participated in the European geothermal research program “Roches Chaudes Sèches” in Soultz-Sous-Forêts (Alsace).

In 1998, Hervé Traineau joined CFG (Compagnie Française de Géothermie) where he was particularly involved in development projects for power generation in the volcanic islands of the Caribbean (Guadeloupe, Martinique, Dominica). Between 2000 and 2015, he actively participated in the development of the field and then in the O&M activities of the Bouillante geothermal power plant (belonging to Géothermie Bouillante). At the same time, he carried out expertise and due diligences on various high-temperature geothermal fields in the Caribbean and around the world (Chile, Indonesia, Italy, Nevada...). Between 2017 and 2020, he worked as a well site geologist during the drilling of two deep geothermal wells (>5 km) in the Rhine Graben.

## ***Catherine TRUFFERT***



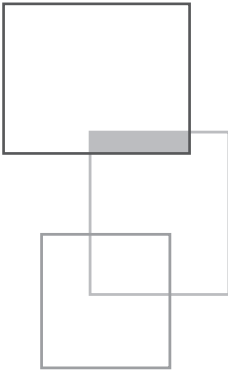
Holding a PhD in Geophysics issued by Marie Curie University France, she worked for more than twenty years in the French Geological Survey, BRGM. Catherine has served IRIS Instruments as the CEO since March 2017, managing day-to-day operations and working in research and innovation with electrical engineers and geophysicists. In 2024, Catherine received the insignia of Chevalier de la Légion d’Honneur.

## ***Christophe VOISIN***



Graduating for the École Normale Supérieure de Lyon in 1996, Christophe Voisin received a Ph.D. in the fields of geophysics and applied mathematics focused on earthquake physics at Université Grenoble Alpes in 2000. He has been a CNRS researcher since 2002 located at the Institut des Sciences de la Terre (ISTerre). Among different topics, he developed the field of environmental seismology (using ambient seismic noise). In 2018, he developed a new patented approach to seismic noise correlations aiming at capturing the intrinsic attenuation linked to the presence of fluids. Christophe Voisin has been the scientific advisor for Geolinks since 2021.





# Introduction

J.L. Mari and G. Paixach

---

## The Role of Geophysics in Geothermal Energy

Geothermal energy represents one of the most promising paths to a more sustainable energy future. It offers a reliable, renewable source of heat and power while significantly contributing to global decarbonization efforts. However, harnessing geothermal energy is anything but straightforward. Geological uncertainties, high exploration and drilling costs, and regulatory hurdles create significant risks that can limit project development. This is where geophysics becomes indispensable, acting as the “eyes and ears” of engineers in the subsurface world.

This book explores the critical role of geophysics throughout the lifecycle of geothermal projects – from initial exploration and feasibility studies to reservoir management and long-term monitoring. By employing advanced geophysical techniques, project developers can reduce uncertainties, identify optimal drilling locations, and minimize costly mistakes. The objective of geophysicists is to transform measurements of the subsurface into actionable insights, enabling engineers to unlock the Earth’s geothermal potential with greater confidence and precision.

We invite the geophysical community to take on the challenge of innovating and collaborating to advance geothermal energy. Developing new technologies, refining multi-physics approaches, and monitoring are essential steps toward mitigating risks and optimizing resource extraction. Yet, progress in geophysics alone is not enough. The responsibility for advancing geothermal energy must be shared.

Project developers, institutional stakeholders, and policymakers also have a critical role to play in enabling the success of geothermal projects. Investment in the acquisition and interpretation of geophysical data is vital for de-risking exploration and maximizing project efficiency. Without sufficient geophysical data, engineers and decision-makers are effectively navigating in the dark, increasing the likelihood of costly errors and missed opportunities. By prioritizing geophysical studies and integrating their findings into project planning, stakeholders can significantly enhance the success rate of geothermal developments.

## Glossary of Geothermal Energy

### Definition and Sources

Geothermal energy leverages the Earth's internal heat, originating from radioactive decay and residual heat from planetary formation. This heat transfers through conduction, convection, and radiation, creating a geothermal gradient where temperature increases with depth. Variations in the geothermal gradient arise due to subsurface geological differences.

### Harnessing Geothermal Energy

Despite geothermal heat at the surface being minimal ( $0.06 \text{ W/m}^2$ ), subsurface temperatures stabilize below 10–20 meters, enabling surface applications like geothermal heat pumps. Deeper geothermal energy is tapped for direct heating ( $50 \text{ }^\circ\text{C}$  and above) or power generation ( $150 \text{ }^\circ\text{C}$  and above), with temperature-dependent applications ranging from district heating to electricity production.

### Applications and Impact

Geothermal systems provide sustainable, year-round heat, contributing to electricity generation and industrial processes with minimal emissions. As heating accounts for 50% of global energy consumption, geothermal energy supports decarbonization efforts and reduces greenhouse gases. Installed capacity has grown globally, reaching over 16 GW for power and expanding direct-use heating applications.

### Technological Advancements and Challenges

Advances in geophysics and drilling have expanded geothermal capabilities, but challenges like regulatory barriers, high drilling costs, and geological risks hinder growth. Enhanced Geothermal Systems (EGS) and closed-loop systems offer solutions in regions lacking natural hydrothermal resources, unlocking untapped geothermal potential.

### Geothermal Systems

Geothermal resources manifest naturally (e.g., hot springs, geysers) or via engineered systems:

- **Direct Use:** Low-temperature fluids ( $30\text{--}80 \text{ }^\circ\text{C}$ ) for heating and agriculture.
- **Electricity Generation:** High-temperature reservoirs ( $150 \text{ }^\circ\text{C}$  and above).

- **Heat Pumps:** Stable subsurface temperatures (10–16 °C) for efficient building heating and cooling.

### Geothermal Resources

- **Conventional Hydrothermal Systems:** These systems involve naturally occurring hot water or steam reservoirs. They are typically used in volcanic or high-geothermal-gradient areas and are well-suited for electricity generation.
- **Non-Conventional Systems (Enhanced Geothermal Systems and Closed Loop).** In regions lacking natural hydrothermal reservoirs, EGS can artificially create or enhance pathways in hot dry rock/low permeability rocks for water to circulate, picking up heat for use at the surface. Closed-loop systems involve circulating a working fluid through pipes underground without any interaction with natural groundwater, making them potentially viable and after a complete economic assessment in a broad range of geological environments.

### Hydrothermal Play

Conventional hydrothermal systems exploration requires four key elements: a heat source (e.g., magmatic activity or geothermal gradients), a porous and permeable reservoir for fluid storage, a circulating fluid to transfer heat, and a caprock to trap fluids. Geophysical methods can contribute to the assessment of these components.

### Derisking subsurface elements

- **Identifying subsurface structures:** For instance, faults, fractures, and geological boundaries between different geological formations are important to characterize.
- **Mapping temperature distribution:** Mapping the temperature distribution underground and monitoring its variation over time allows engineers to target regions with sufficient heat for effective geothermal energy production.
- **Characterizing reservoirs:** It is important to have insights into rock types and properties away from the wellbore to estimate the size, depth, porosity, permeability and productive thickness of the geothermal reservoir.
- **Characterizing geothermal fluids:** Identifying fluid pathways, assessing fluid properties, tracking thermal and cold fronts in the reservoir are important to address success.
- **Fault activity assessment:** Avoiding active faults minimizes the risk of induced seismicity and other drilling complications, enhancing operational safety.
- **Real-time well steering:** Need reassurance on optimal drilling trajectories by guiding wells toward the targeted zones.

## Geothermal Energy in France

Here's a summary of the geothermal energy landscape in France from the 2023 report from the AFPG (2023), including upcoming projects, current operations, and both deep and shallow geothermal energy contributions:

- Upcoming Projects:
  - 22 geothermal research permits granted for mainland France,
  - 7 research permits were issued for geothermal exploration in French overseas territories.
- Heat Production:
  - 79 deep geothermal operations are currently active in France,
  - 1 million people benefit from geothermal heating in the country,
  - deep geothermal operations generate 2.05 TWh of heat energy annually.
- Geothermal lithium extraction: several projects in Upper Rhine Graben are underway.
- Power Generation: Two geothermal power plants are operational:
  - Bouillante, Guadeloupe: 15.5 MW capacity,
  - Soultz-sous-Forêts, Alsace: 1.7 MW capacity.
- Shallow Geothermal Energy:
  - over 205, 300 shallow geothermal installations provide heating and cooling,
  - shallow geothermal systems contribute 4.58 TWh of heating and cooling energy annually from near-surface resources.

This range of geothermal initiatives highlights France's commitment to leveraging both deep and shallow geothermal energy for sustainable heating, cooling, and power generation.

## Book content

After an introduction on geothermal energy and an overview of the different geothermal systems (chapter 1), the book focuses on geophysical methods. Chapters 2 and 3 give the current state of knowledge respectively in surface methods (gravity, magnetic, electrical – EM and seismic methods) and borehole methods (conventional logging, hydrogeological measurements, full waveform acoustics, VSP). Fundamentals of each method are described in basic words and illustrated with field examples, notably geothermal examples. The reader is invited to refer to the selected papers or books listed in the references for detailed information on each method.

Chapter 4 describes the integrated approach that led to the establishment of the geothermal model in the Upper Rhine Graben. It shows how the occurrence of fractured reservoirs characterized by natural brine circulations with fractured zones

obliged developers to adapt geophysical exploration methods, geophysical well logging strategies as well as technical well design for reaching geothermal targets.

Chapters 5 to 10 illustrate the use of geophysical methods for geothermal exploration and monitoring, with the following topics:

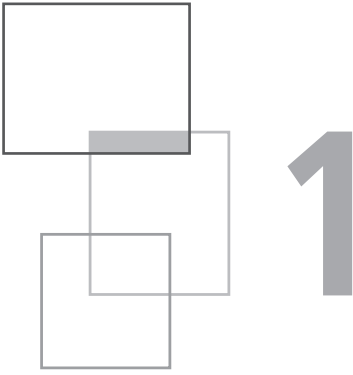
- ERT-IP for geothermal exploration and de-risking,
- The use of passive seismic methods for geothermal exploration and monitoring,
- Seismic inversion and characterization applied to geothermal energy,
- Seismic anisotropy applied to geothermal prospection,
- Feasibility of monitoring cold fronts of geothermal doublets using 4D active electromagnetic techniques – a field trial in the Dogger play in the Paris Basin,
- Defining high enthalpy geothermal drilling target with multi-physics integrated exploration program. Mayotte's Petite-Terre Island case study.

This book serves as both a guide and a call to action. It highlights the value of geophysical methods in building a sustainable energy future and emphasizes the need for collaboration across disciplines and sectors. Geophysics is not just a tool; it is the bridge between the subsurface's hidden secrets and the engineers striving to harness them. Together, by investing in and advancing geophysical science, we can overcome the challenges of geothermal energy and unlock its full potential.

## Reference

AFPG (2023) *La géothermie en France, Étude de filière 2023*, 6<sup>e</sup> édition.





# Overview of the different geothermal systems: role of geophysics in exploration and production

G. Paixach, H. Traineau, F. Bugarel,  
E. Lasne and C. Mailhol

---

## 1.1 What is geothermal energy?

Geothermal energy is all about tapping into and utilizing the Earth's internal heat, which comes from two primary sources: the decay of radioactive elements and the residual heat left over from the planet's formation billions of years ago. Heat is a form of energy associated with the movement of particles within matter. Heat can be transferred in three ways: conduction, convection, and radiation. Heat

naturally flows from areas of higher temperature to areas of lower temperature. These processes create a transfer of heat from the Earth's hot interior to its cooler surface where we live, resulting in what's known as a geothermal gradient, which is a measure of how temperature increases with depth (Figure 1.1). In general, the deeper we go into the Earth's crust, the hotter it gets. On average, temperatures rise by roughly 25–30 °C for every kilometer below the surface, but this geothermal gradient varies significantly depending on location due to the underlying geology.

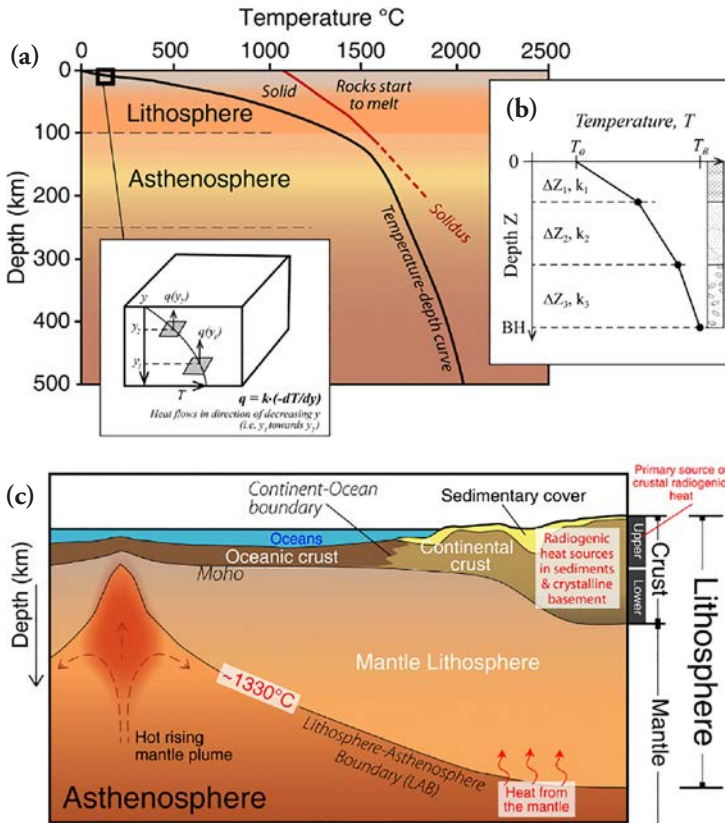


Figure 1.1 From Kolawole and Evenick (2021). (a) Typical averaged (and simplified) temperature profile of the Earth, showing the variation of temperature with depth (modified after McKenzie and Bickle, 1988; Boehler, 1996). Inset in panel (a) shows a zoom-in of the non-zero curvature of slope of temperature( $T$ )-depth( $y$ ) profile, in which the local slope is defined by Fourier's law, and for a constant thermal conductivity ( $k$ ), heat flow ( $q$ ) is a function of depth,  $y$ ,  $q = q(y)$  (modified after Turcotte and Schubert, 2002). (b) Schematic representation of variation in geothermal gradient with depth ( $Z$ ) as a function of  $k$  in sedimentary sequences (after Chapman et al., 1984). (c) Cartoon showing the crustal and lithospheric structures of the Earth with the primary sources of geogenic heat (after Evenick, 2019).

Variation in measured heat flow at the surface of the Earth (Figure 1.2) highlights significant lateral differences across regions, suggesting a strong influence of subsurface characteristics. Indeed, the subsurface is far from being homogenous. This heat is stored in rocks and reservoirs of water deep underground. Different rock types, fractures, water presence, and other geological features, particularly related to tectonic plate activity, play a role in how heat is stored and transferred underground.

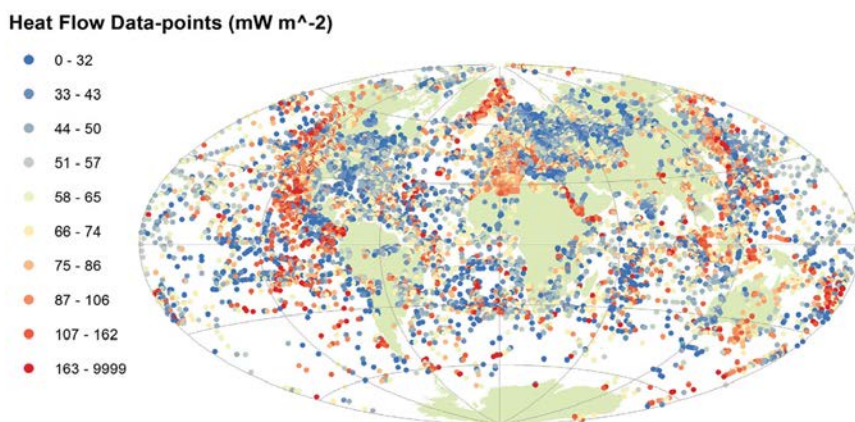


Figure 1.2 From Davies (2013). Map of heat flow measurement points.

Geothermal energy is all about harnessing the natural heat generated beneath the Earth's surface. However, harvesting geothermal heat directly from the Earth's surface is challenging because on average, the natural geothermal heat flux reaching the Earth's surface is only about 0.06 watts per square meter, which is a tiny amount compared to solar power, which delivers around 200 watts per square meter on a sunny day.

While the Earth's surface temperature is highly influenced by atmospheric conditions, fluctuating with daily and seasonal changes, this effect diminishes rapidly just a few meters below the ground. After descending around 10 to 20 meters, the Earth's temperature becomes nearly constant throughout the year, insulated from surface weather variations. This stable temperature zone is primarily influenced by the geothermal gradient. This stable subsurface temperature zone is crucial for surface geothermal applications, as it provides a reliable, year-round source of heat for geothermal heat pumps.

To access deep geothermal energy for more energy-intensive applications like direct heating or power generation, we must drill deeper into the Earth's crust, where temperatures are significantly higher. For direct heating applications, temperatures typically need to reach between 50 °C and above. At these depths, geothermal fluids can be used directly for district heating, greenhouse heating, aquaculture, and industrial processes. For electricity generation, however, much higher temperatures,

generally above 150 °C, are required to produce steam or vaporize a working fluid that drives turbines.

The diagram displayed in Figure 1.3 highlights how different temperature levels of geothermal fluids are suited for various direct-use applications. It showcases the versatility of geothermal energy, illustrating how it can be utilized for both power generation and numerous direct heat applications, depending on the resource temperature. At the high end of the temperature spectrum, above 150 °C, geothermal fluids are typically used for electricity generation through dry steam, flash steam, or binary cycle power plants. Moving down in temperature, between 100 °C and 150 °C, geothermal fluids can be used in processes like drying, industrial heating, and chemical extraction. At lower temperatures, around 50 to 100 °C, geothermal fluids are ideal for district heating, aquaculture, greenhouse heating, and various agricultural applications. Finally, even low-temperature geothermal fluids, between 20 and 50 °C, have applications in bathing, balneology, and heat pump systems for residential heating and cooling.

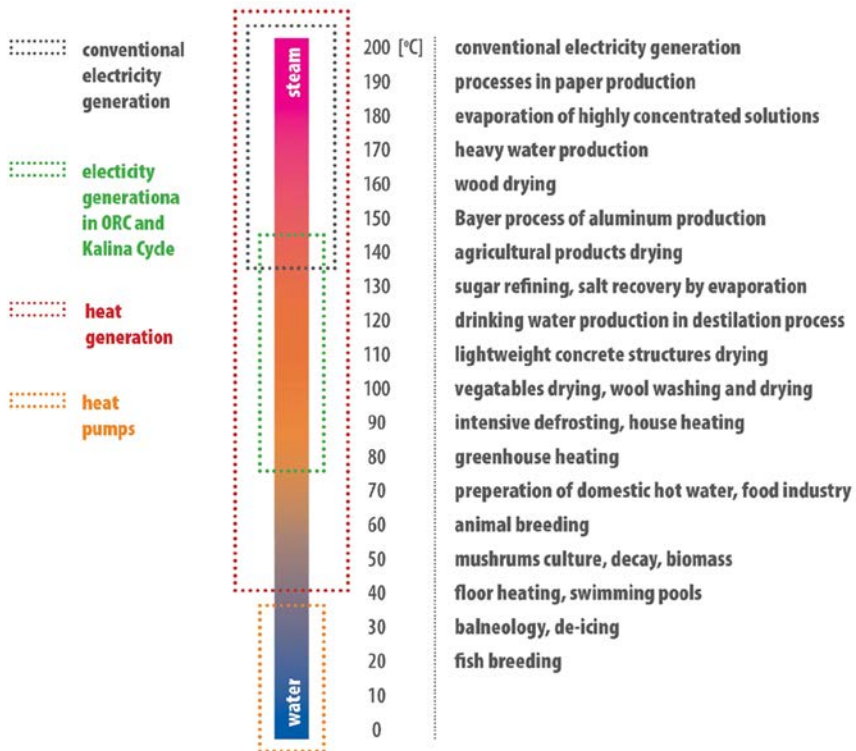


Figure 1.3 Modified Lindal diagram about possible usage of geothermal fluids (from Kaczmarczyk et al., 2020; based on Gudmundsson et al., 1985; Operacz and Chowaniec, 2018).

Heating has always been essential to human societies, forming the backbone of daily life and industrial activities. Today, heating and cooling account for a substantial portion of global energy consumption worldwide. According to the International Energy Agency (IEA), heating alone, used for residential, commercial, and industrial purposes, accounts for about 50% of final energy consumption globally (Figure 1.4). In colder climates, space heating for homes and buildings is a major energy expense, especially during winter, and accounts for nearly 40% of energy demand in the building sector. Meanwhile, the need for cooling is rapidly increasing, especially in warmer regions, where air conditioning and refrigeration demand has soared over the last few decades. Given the immense need for heating and cooling, geothermal energy presents a powerful, sustainable alternative, as it can provide constant, low-emission heat for both buildings and industry, helping to meet this demand while reducing greenhouse gas emissions.

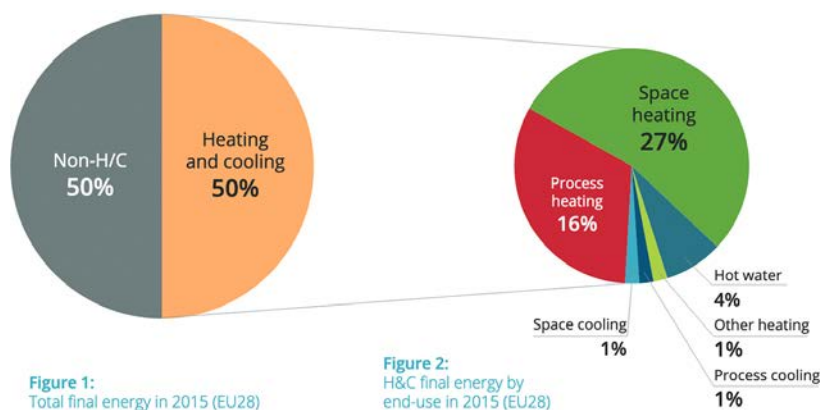
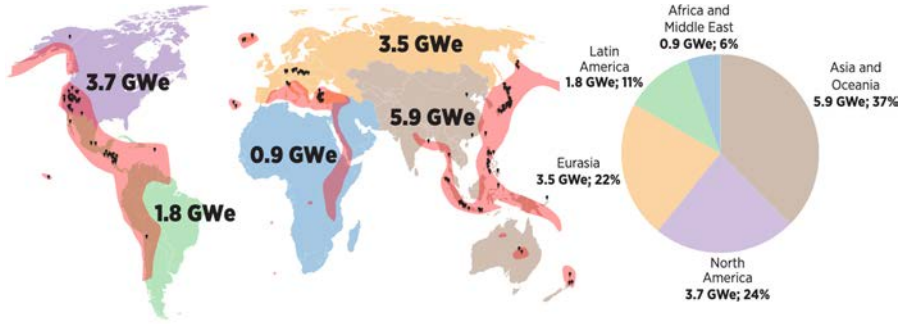


Figure 1.4 Heat Roadmap Europe (2019), Heating and Cooling facts and figures.

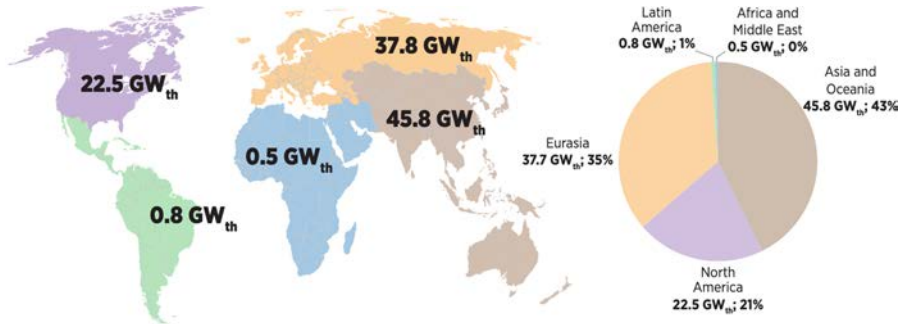
By tapping into this steady, abundant heat source, geothermal systems can produce electricity, provide direct heating, and power industrial processes with minimal environmental impact. Geothermal energy offers a unique advantage in the push to decarbonize societies because it provides a constant, reliable power supply independent of weather conditions.

The installed capacity for geothermal heat and power generation has seen a steady increase, with global geothermal power capacity exceeding 16 gigawatts in recent years (Figure 1.5) and direct-use heating capacity growing even faster (Figure 1.6), especially for district heating, greenhouses, and aquaculture. As of the latest trends, geothermal heating is expanding quickly in regions with abundant low-to-medium temperature resources, while geothermal power plants continue to rise in areas with high-temperature resources. In recent years, advancements in geophysics, hydrogeology, and drilling technology, and have expanded the potential of geothermal energy.



Source: IRENA, 2022a; ThinkGeoEnergy, 2022 (b); Hutterer, 2021.

Figure 1.5 From IRENA and IGA (2023). Estimated installed geothermal electricity capacity, by region, 2021.



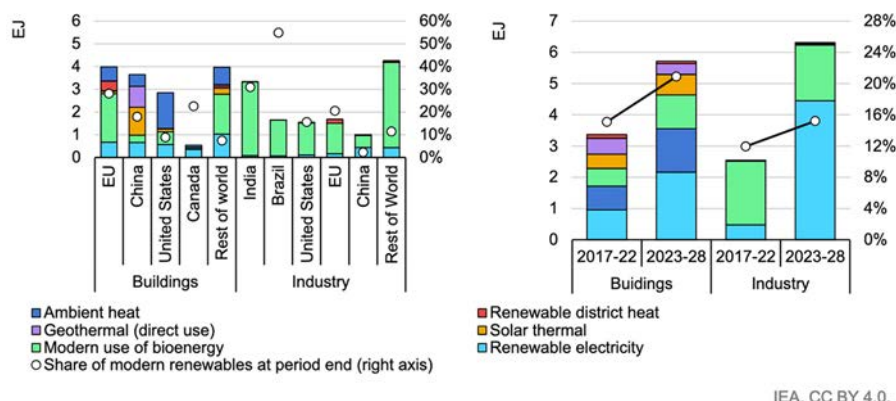
Adapted from: Lund and Toth (2021).

Figure 1.6 IRENA and IGA (2023). Estimated geothermal heating and cooling installed capacity, by region, 2020.

In the renewable energy sector, there is competition between technologies like solar, wind, biomass, and geothermal for investment, policy support, and market share. Solar and wind energy have surged in deployment due to their rapid advancements, decreasing costs, and modular nature, making them accessible and scalable across a wide range of locations (Figure 1.7). In contrast, geothermal energy faces distinct challenges that can slow its expansion despite its potential for stable, baseload power or direct heat usage. One of the significant hurdles is the regulatory landscape: accessing deep geothermal resources requires extensive permits and regulatory compliance due to their subsurface nature.

Another challenge for geothermal energy deployment is the inherent risk and complexity of drilling deep into the Earth to access high-temperature resources. Deep drilling is costly and carries geological risks, including the lack of targeted

geothermal fluids or the possibility of triggering seismic activity. Current drilling technologies also have limitations, as they can only reach certain depths before technical constraints and costs become prohibitive. This restriction means that vast geothermal potential, notably for power generation remains untapped. Addressing these challenges requires continued advancements in drilling technologies, risk mitigation strategies, investment, and regulatory support, all of which would help make geothermal a more prominent player in the global renewable energy mix.



Notes: EU=European Union. Ambient heat from heat pumps used in the industry sector is not accounted for due to limited data availability  
 Sources: IEA (2023), [World Energy Outlook 2023](#); IEA (2023), [Global Energy and Climate Model](#).

Figure 1.7 Renewable energy consumption and shares of heat demand in selected regions, 2022 (left), and global increases in renewable energy consumption, 2017-2028 (right). Source: World Energy Outlook 2023 (IEA Report, 2023).

## 1.2 What are the main geothermal systems?

In nature, geothermal activity is well known through phenomena like geysers, hot springs, and fumaroles, where the Earth’s internal heat escapes to the surface. These features form in geologically active areas, such as near tectonic plate boundaries or volcanic zones, where heat is channeled through fractures in the Earth’s crust, bringing hot water or steam to the surface. Historically, these natural hot water sources have been harnessed by people for bathing, cooking, and warming homes, using the naturally occurring thermal energy produced deep within the Earth.

The first deliberate attempt to generate power from geothermal energy was made in 1904 in Larderello, Italy, where the French engineer François Jacques de Larderel used steam from a geothermal well to generate electricity. Since then, geothermal technology has evolved significantly, with modern techniques now

allowing us to drill deep into the Earth and access high-temperature geothermal reservoirs. Today, geothermal power plants can produce electricity by tapping into hot water, two-phase or steam reservoirs, while enhanced geothermal systems (EGS) create artificial reservoirs by injecting water into low permeability rocks to generate hot geothermal fluids. Additionally, ground-source heat pumps make it possible to use stable temperatures just below the Earth's surface for efficient heating and cooling in residential and commercial buildings.

These advancements allow us to make use of geothermal energy far beyond natural manifestations, making it a sustainable and reliable source of heat and power. However, it's essential to recognize that geothermal energy is not a one-size-fits-all resource. We can classify geothermal systems based on the intended usage, the fluid or geological context involved, and even the energy production design.

### **Classifying by Usage**

- **Direct Use of Hot Water:** This is one of the oldest and most straightforward uses of geothermal energy, in which naturally heated water (30–80 °C) from geothermal springs or wells is used for heating buildings, agricultural greenhouses, aquaculture ponds, and industrial processes.
- **Electricity Generation:** Higher temperatures, typically above 150 °C, are required to produce electricity. In these systems, steam from geothermal reservoirs drives turbines connected to generators. These are commonly used in areas with high geothermal activity, like volcanic regions.
- **Geothermal Heat Pumps (GHPs):** GHPs leverage stable ground temperatures (10–16 °C) found a few meters below the surface to provide efficient heating and cooling for buildings. This technology is widely applicable and doesn't require high temperatures.

### **Classifying by Geological Settings**

- **Shallow Geothermal Systems:** This involves tapping into the moderate temperatures found at shallow depths, typically up to a few hundred meters, to power geothermal heat pumps.
- **Sedimentary Basin Systems:** In regions with porous/fractured/karstified sedimentary layers, geothermal reservoirs of hot water can be found at moderate depths, often used for direct heating or low-temperature electricity production.
- **Volcanic Systems:** High-temperature geothermal reservoirs in volcanic regions are ideal for electricity generation. Countries like Indonesia and New Zealand are renowned for tapping volcanic geothermal resources for power.
- **Rift and Fault Zones:** In areas where tectonic plates pull apart or fracture, crust is thinner and heat flow is higher than usual promoting geothermal reservoir development in conjunction with volcanic activity.
- **Fractured Granite and Crystalline Rock:** Some geothermal resources are found in fractured hard rock, where engineered geothermal systems (EGS) create or enhance pathways for water to circulate and absorb heat.

1. Overview of the different geothermal systems: role of geophysics



Figure 1.8 Diagrams showing the processes for shallow and deep geothermal systems source<sup>1</sup>.

1. <https://www.bgs.ac.uk/geology-projects/geothermal-energy/geothermal-technologies/>

Play type	Region	The Americas Eastern Pacific	Asia Pacific	Europe Atlantic Africa
<b>Convection-dominated plays</b>				
<b>Magmatic play type</b>				
<i>Geologic controls:</i> Intrusion of different age, hydrothermal <i>Geologic setting:</i> active to extinct volcanic fields (convergent, divergent, transform faults, hot spots, plumes)		46	57	36
<b>Extensional domain type</b>				
<i>Geologic controls:</i> active faults, amagmatic, high porosity, high permeability strata <i>Geologic settings:</i> active rifts, metamorphic core complexes, back-arc basins, segmented strike-slip faults		21	4	11
<b>Conduction-dominated plays</b>				
<i>Geologic controls:</i> Faults, fractures, lithofacies, diagenesis <i>Geologic settings:</i> sedimentary basins, basement provinces, orogenic belts		0	2	10

Figure 1.9 Geothermal systems (187) developed worldwide, grouped by play types and regions. Sources: IGA and IFC (2014); systems drawn from www.thinkgeoenergy.com; www.geotis.de; Zheng and Dong (2008).

### Conventional and Non-Conventional Geothermal Resources

- Conventional Hydrothermal Systems. These systems involve naturally occurring hot water or steam reservoirs. They are typically used in volcanic or high-geothermal-gradient areas and are well-suited for electricity generation.
- Non-Conventional Systems (Enhanced Geothermal Systems and Closed Loop). In regions lacking natural hydrothermal reservoirs, EGS can artificially create or enhance pathways in hot dry rock/low permeability rocks for water to circulate, picking up heat for use at the surface. Closed-loop systems involve circulating a working fluid through pipes underground without any interaction with natural groundwater, making them potentially viable and after a complete economic assessment in a broad range of geological environments.

Here’s a summary of the geothermal energy landscape in France from the 2023 report from the AFIG (2023), including upcoming projects, current operations, and both deep and shallow geothermal energy contributions:

- Upcoming Projects:
  - 22 geothermal research permits granted for mainland France,
  - 7 research permits were issued for geothermal exploration in French overseas territories.
- Heat Production:
  - 79 deep geothermal operations are currently active in France,
  - 1 million people benefit from geothermal heating in the country,
  - Deep geothermal operations generate 2.05 TWh of heat energy annually.

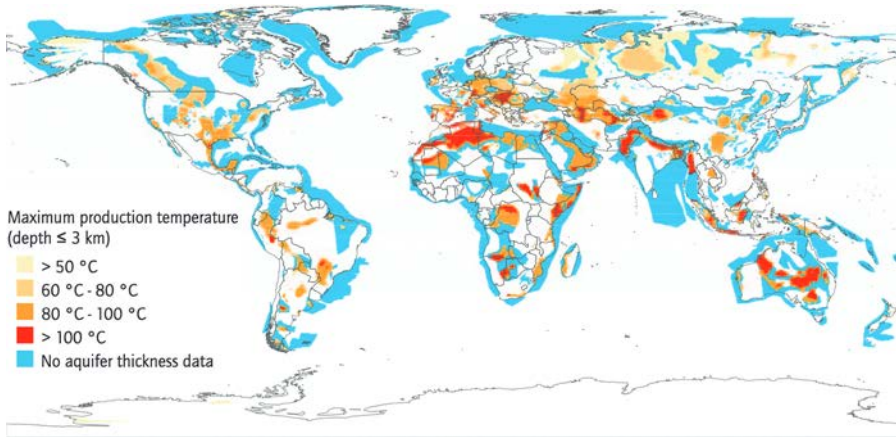


Figure 1.10 World map of estimated deep aquifer systems from IEA Report (2011). Source: TNO.

- Geothermal lithium extraction: several projects in Upper Rhine Graben are underway.
- Power Generation, two geothermal power plants are operational:
  - Bouillante, Guadeloupe: 15.5 MW capacity,
  - Soultz-sous-Forêts, Alsace: 1.7 MW capacity.
- Shallow Geothermal Energy:
  - Over 205, 300 shallow geothermal installations provide heating and cooling,
  - Shallow geothermal systems contribute 4.58 TWh of heating and cooling energy annually from near-surface resources.

This range of geothermal initiatives highlights France's commitment to leveraging both deep and shallow geothermal energy for sustainable heating, cooling, and power generation.

Geothermal district heating in the Paris Basin, France, is one of Europe's most successful examples of sustainable heating from geothermal resources (Negrel and Lasne, 2021). The Paris area sits atop an extensive low-temperature geothermal reservoir within the Dogger aquifer, a sedimentary horizon rich in warm groundwater. Found at depths between 1500 and 2000 meters, this aquifer has temperatures ranging from 55 to 85 °C, making it ideal for direct heating applications. Since the 1970s, Paris and its surrounding suburbs have developed a network of geothermal district heating systems that utilize this geothermal resource to provide heat for residential buildings, schools, hospitals, and other public facilities. In geothermal district heating systems, a well doublet is typically drilled to optimize the extraction and reinjection of geothermal fluids from a deep aquifer reservoir.

This doublet consists of one production well and one reinjection well, Figures 1.11 and 1.12. The production well taps into the geothermal reservoir to bring hot water to

the surface, which is then circulated through a primary network. This hot geothermal fluid is directed to a heat exchanger, where its heat is transferred to a secondary network used to distribute warmth to buildings across the district. After the heat has been extracted, the now-cooled geothermal fluid is directed into the reinjection well, where it is returned to the underground reservoir. This reinjection process is critical for maintaining the pressure balance within the geothermal reservoir, ensuring that the resource remains stable and sustainable over the long term.

A list of the good practice guidelines on deep geothermal drilling and exploitation from experience in the Paris Basin (Dogger and Albian aquifers) is regularly published (Hamm et al., 2022).

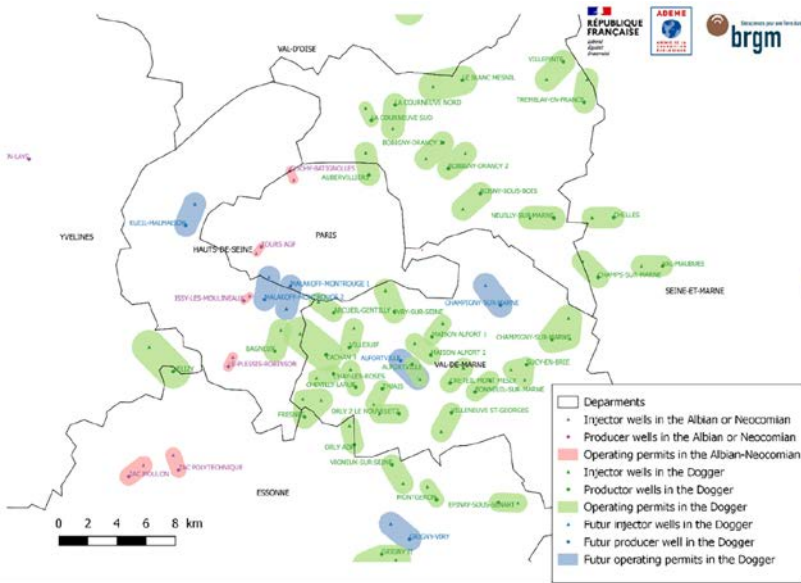


Figure 1.11 Localization of the geothermal doublets tapping the Albian or Neocomian sands (pink) or the Dogger Limestones (green and blue) in Paris area (Hamm et al., 2022).

In the Alsace region, geothermal energy in fractured granite and crystalline rock represents a promising frontier for accessing geothermal resources. The dense granite or crystalline rock basement of the Upper Rhine Graben sometime lacks adequate permeability. To overcome this, water is injected into the rock to create or expand existing fractures (Enhanced geothermal systems or EGS). The high thermal conductivity of granite and crystalline rock makes them efficient at transferring heat, allowing them to reach elevated temperatures that are suitable for both direct heating and electricity generation. France’s Soultz-sous-Forêts project, for example, has demonstrated the feasibility of EGS in fractured granite, highlighting the potential of these formations to supply substantial geothermal energy.



Figure 1.12 *Drilling pad for a geothermal doublet near Paris (source: CFG).*

The Bouillante geothermal plant in Guadeloupe is one of the Caribbean's most significant geothermal power projects, providing renewable energy to the island. Located on the western coast of Basse-Terre, this power plant taps into a high-temperature hydrothermal system associated with volcanic activity. Geothermal fluid is extracted from production wells at depths of 500 to 1000 meters, where temperatures can reach 250 °C. The steam and brine are then used to generate electricity through turbines, producing approximately 15.5 MW of gross power.

### 1.3 The role of geophysics

Geophysics is becoming increasingly important not only in the exploration of geothermal resources but also in their exploitation and monitoring (Paixach, 2024). By measuring variations in the subsurface's physical properties, geophysical surveys can provide valuable insights into geological features, helping to identify critical characteristics of geothermal systems before the costly process of drilling. Ultimately, geophysical surveys aim to optimize the success of exploration and minimize risks. Generally, no single geophysical method can characterize all the elements of a geothermal play. Each technique has unique strengths and limitations, responding to specific subsurface properties and functioning at different scales, depths, and spatial resolutions. Therefore, selecting the most cost-effective geophysical methods for a given geothermal prospect requires a customized approach, Figure 1.13. Often, this includes conducting onsite feasibility studies to verify that the selected methods are effective in the particular geological conditions.

### THE CHOICE OF GEOPHYSICAL METHODS

Methods		Selection Criteria	Acquisition & Processing	Modeling & Multi-Disciplinary Integration
<b>Seismic</b>	Mechanical waves (speed)	Vertical and lateral resolution		Faults & Fractures
<b>Electric</b>	Electric field (Resistivity)	Depth penetration		Fluids
<b>Magnetic</b>	Magnetic field (susceptibility)	Noise level		Porosity & Permeability
<b>Gravimetry</b>	Gravitational field (Density)	Operational and environmental constraints		Structure
<b>Electromagnetic</b>	Electromagnetic field (Resistivity)	Type of geology		Heterogeneities...
		Budget .....		



Figure 1.13 *Geophysical methods.*

The concept of hydrothermal play is central to understand and explore geothermal resources. A geothermal play refers to a naturally occurring geological system with conditions favorable for the accumulation, heating and circulation of fluids. Heat is stored in the reservoir host rocks. Water is the vector to transfer energy to the surface. Successful geothermal exploration relies on a detailed understanding of these plays, as they dictate where, how, and to what extent geothermal energy can be effectively extracted. Hydrothermal plays, like other geological plays (such as petroleum systems), are complex systems that depend on a specific set of geological conditions. Four main elements define a hydrothermal play:

- **Heat Source:** The heat source in a hydrothermal play can be due to natural geothermal gradients (the Earth’s internal heat flow), magmatic intrusions, or tectonic activity. In volcanic regions, for example, magma intrusion degassing and cooling represent the prime heat source for geothermal developments.
- **Reservoir:** The reservoir is the underground porous and/or fractured formation where the hot geothermal fluid is stored. The host rock can be of sedimentary, magmatic, volcanic or metamorphic origin. The quality of a geothermal reservoir depends on the rock’s porosity, permeability and productive thickness, which determine how much fluid it can store and how easily fluids can flow.
- **Fluid (Hydrothermal System):** Geothermal energy depends on the presence of fluids that absorb heat from the reservoir rock and can be brought to the surface. In hydrothermal plays, the water is meteoric water or seawater that has infiltrated into the Earth’s crust, circulated, chemically reacted with host rock and been heated. Fluid is essential to transport heat from the reservoir to the surface, either naturally or through engineered systems.
- **Caprock or Seal:** A caprock is an impermeable layer that helps trap geothermal fluids within the reservoir, preventing them from migrating to the surface or into

other rock layers. Without an effective caprock, the hydrothermal fluids could escape, reducing the potential of the play.

Geothermal exploration begins with identifying regions that meet the basic geological conditions for a hydrothermal play. Then, specific techniques, including geological, geochemical and geophysical surveys (the 3G), Figure 1.14, are employed to gather data about subsurface structures, fluid presence, and temperature.

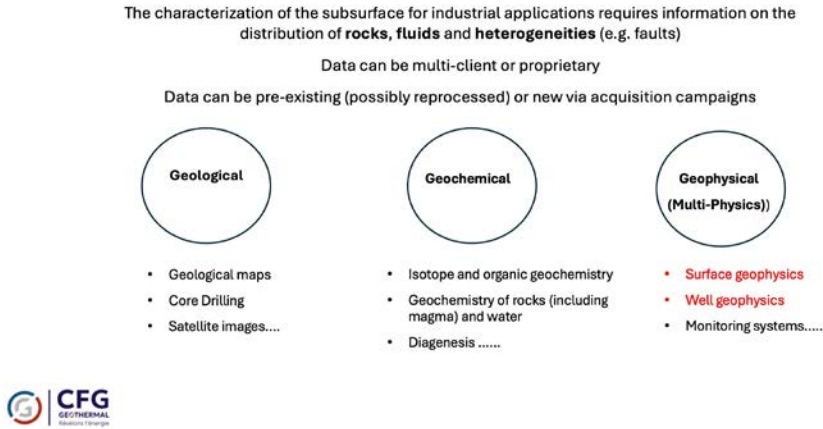


Figure 1.14 *Type of data required in geothermal exploration.*

Geophysical methods provide essential insights that can significantly assist engineers in optimizing and managing geothermal projects. During exploration, scientists and engineers focus on understanding how the different elements of the hydrothermal play interact. For instance, determining the temperature distribution in the reservoir, mapping potential fault lines and fractures that could act as fluid pathways, and locating caprock layers are all crucial to evaluating a play’s feasibility. In practice, hydrothermal plays require a combination of geological, geophysical, hydrological, and thermal studies to build a model of the system that can guide drilling campaigns and optimize resource extraction.

One of the main challenges in geothermal exploration is that no single geophysical, geochemical or geological method can directly identify and assess a hydrothermal play. Instead, a combination of techniques, often termed a “multi-physics” approach, is used to obtain a comprehensive view of the subsurface conditions.

This is precisely where one of the greatest challenges facing geophysicists lies: in the transformation of geophysical models (resistivity, velocity, density, susceptibility, permittivity, etc.) into reservoir models (faults, rock types, cavities, aquifers, hydrocarbons, minerals, etc.). This transformation lacks uniqueness and requires contextualizing the geophysical model with an initial subsurface model and integrating boundaries and constraints derived from other data types.

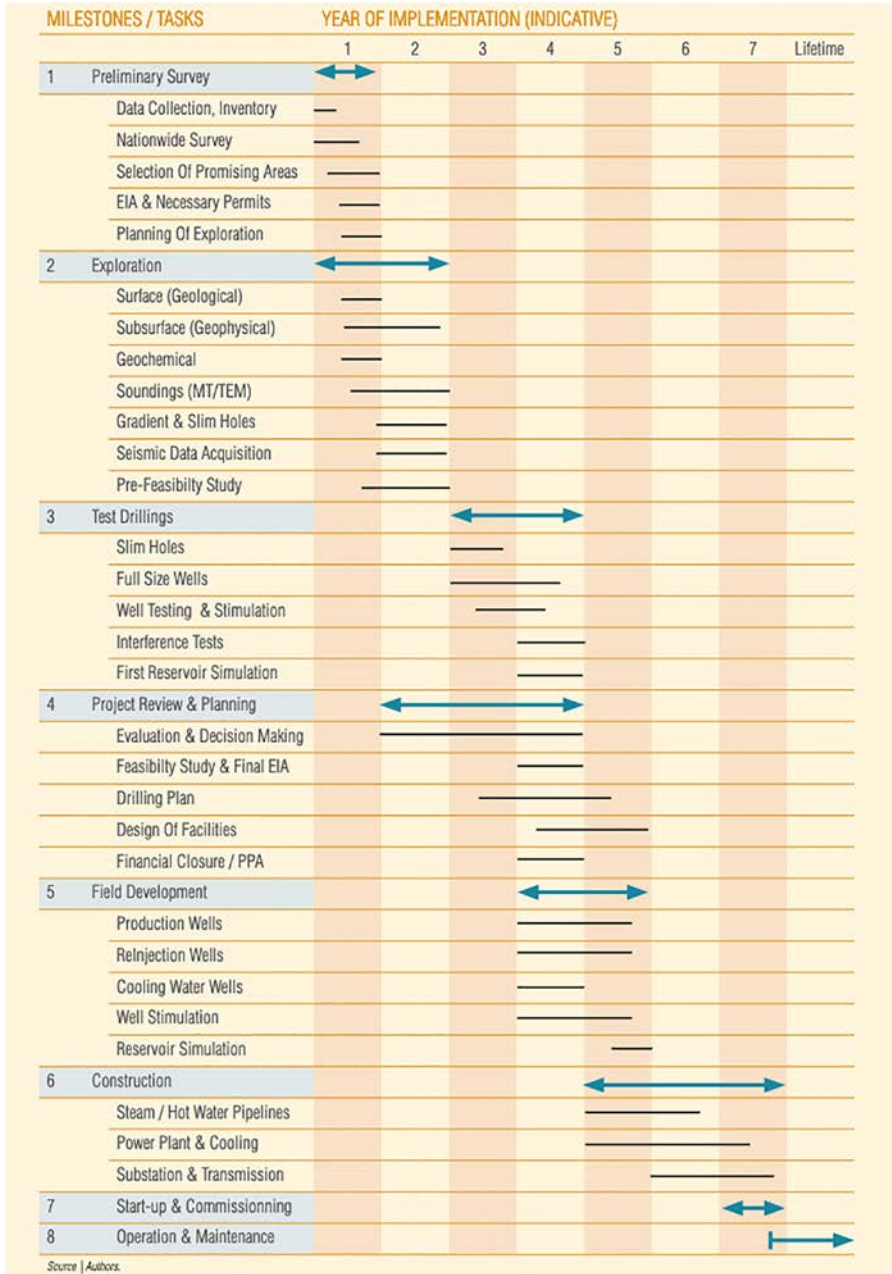


Figure 1.15 Example of geothermal project development phases for a Power Plant. Source: ESMAP (2012).

Furthermore, the geophysicist must communicate not only the results but also how various geophysical methods operate, the limitations of their usage, and the inherent measurement uncertainties and resolution limits. Clear and comprehensive communication of geophysical work results is paramount, especially for organizations seeking assurance in the design and planning of their projects. The value of geophysicists lies not only in obtaining the optimal geophysical model but also in their ability to integrate it effectively into the geological or geotechnical context. This process requires deep expertise to overcome challenges related to the interpretation of geophysical models and the communication of results and related uncertainties to engineers and project stakeholders. For industries, such as geothermal energy, where geophysical studies play an important role, the ability to articulate how the methods work, their applicability limits, and the uncertainties surrounding the results become critical.

**Often engineers have few questions and geophysicists many answers**

Questions.....	Answers .....	Clarifications.....
Is there a geothermal resource?	IP - TDIP - CR      DC - ERT    PS	Seismic reflection, Seismic refraction, Ground-penetrating radar (GPR) Electrical resistivity tomography (ERT), Magnetotellurics (MT) Gravity surveying, Induced polarization (IP)
How deep is the geothermal resource?	MT    CSEM    FWI      RTM    MTEM	Ground-based LiDAR (Light Detection and Ranging) Differential Interferometric Synthetic Aperture Radar (DInSAR) Radio-magnetotellurics (RMT), Controlled-Source Electromagnetic (CSEM)
Is there a reservoir ?	GPR      MASW      AVO - AVA	Vertical seismic profiling (VSP), Crosshole seismic tomography Time-lapse seismic monitoring (4D seismic) Microseismic monitoring, Time-domain electromagnetic (TEM) surveys
What is the permeability of the reservoir ?	4D AHM      OBEM - OBMP      VLF      TTI	Frequency-domain electromagnetic (FEM) surveys Controlled-source audio-frequency magnetotellurics (CSAMT) Full waveform inversion (FWI) for seismic imaging Ground-based interferometric synthetic aperture radar (GB-InSAR)
What is the temperature of the geothermal resource?	MC      OBN      FDEM      VTI      OBC	Near-surface geophysical methods (e.g., MASW, GPR, ERT) Generalized Radon Transform (GRT) depth migration Reverse Time Migration (RTM) Transient Electromagnetic or Time-Domain EM (TEM) Frequency-Domain EM Induction (FDEM)
	TEM      SEM      GRT DM      DAS	Very-low-frequency (VLF) Methods Induced Polarization, Time-domain IP & Complex Resistivity (IP,TDIP,CR) DC Resistivity) ; The seismo-electromagnetic method (SEM), Ocean-bottom electromagnetic (OBEM), Ocean-bottom multiphysics (OBMP), Passive seismic interferometry, Distributed acoustic sensing (DAS)
		CSAMT      VSP

Figure 1.16 Selected list of geophysical techniques available to contribute to geothermal exploration and exploitation.

By providing insights into the subsurface’s physical properties, geophysical methods help better understand, assess, and monitor geothermal resources. The goal is to enable engineers to optimize production, mitigate risks, and ensure the sustainability of the reservoir. Here is a selected list of the key information that geophysicists can contribute.

- Identifying Subsurface Structures:  
It is important to assess the subsurface structure for geothermal energy production. For instance, faults, fractures, and geological boundaries between different geological formations are important to characterize. By understanding the geometry and distribution of these structures, engineers can identify areas where geothermal reservoirs are likely located.

- **Temperature Distribution:**  
One of the primary goals of geothermal exploration is identifying areas with high heat flow. Mapping the temperature distribution underground and monitoring its variation over time allows engineers to target regions with sufficient heat for effective geothermal energy production.
- **Characterizing Rock Types and Reservoir Properties:**  
It is important to have insights into rock types and properties away from the wellbore to estimate the size, depth, porosity, permeability and productive thickness of the geothermal reservoir.
- **Geothermal fluids:**
  - **Identifying Fluid Pathways:** Locate pathways within the reservoir that allow geothermal fluids (hot water or steam) to circulate,
  - **Assessing Fluid Properties:** Estimate fluid properties such as salinity, temperature, and pressure, which are critical for predicting how fluids will behave during extraction and reinjection,
  - **Tracking thermal and cold fronts in the reservoir.** This monitoring allows engineers to observe changes in temperature and fluid pathways over time, providing critical feedback on how injected fluids interact with the reservoir. With this information, engineers can adapt injection strategies to optimize heat extraction while preserving the resource.
- **Others Monitoring:**
  - Fault activity Assessment:** By identifying active fault zones, geophysics helps engineers assess potential hazards, which is crucial for designing safe drilling paths. Avoiding active faults minimizes the risk of induced seismicity and other drilling complications, enhancing operational safety.
  - Real-Time Well Steering During Drilling:** Geophysical data provides guidance for steering wells during drilling. This information enables engineers to keep the well trajectory in contact with the hottest, most permeable zones while avoiding undesirable features like low-permeability zones or faults, maximizing heat extraction efficiency.

In geothermal exploration, geophysics provides a non-invasive and cost-effective way to gather critical information about the subsurface, reducing the risk associated with drilling. It helps in identifying potential geothermal sites, mapping underground structures, estimating heat flow, characterizing reservoirs, and monitoring the long-term sustainability of geothermal systems. By combining different geophysical methods, scientists can develop a more comprehensive understanding of the geothermal potential of an area.

In geothermal exploration, a single method rarely provides all the information needed to understand the resource. Instead, multi-physics approaches combine several geophysical techniques, allowing experts to construct a more reliable picture of the subsurface. By integrating data from seismic, magnetotelluric, gravity, and

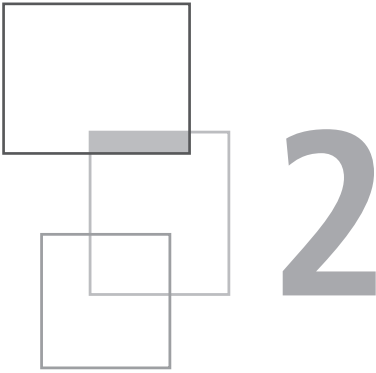
geochemical surveys, geophysicists can develop models of geothermal systems that help guide drilling decisions and reduce financial risk.

Geothermal energy offers a unique and promising solution to meet society's heating, cooling, and power needs. By understanding different geothermal systems and employing advanced geophysical techniques, we can harness this sustainable energy more effectively. Geophysics provides the tools to explore and define these hidden geothermal resources, giving us the insight to tap into the Earth's heat with precision and efficiency, ensuring that geothermal energy continues to play an essential role in a sustainable energy future.

## References

- AFPG (2023) *La géothermie en France, Étude de filière 2023, 6<sup>e</sup> édition.*
- Boehler R. (1996) Melting temperature of the Earth's mantle and core: Earth's thermal structure, *Annu. Rev. Earth Planet. Sci.* 24(1), 15-40.
- Chapman D.S., Keho T.H., Bauer M.S., Picard M.D. (1984) Heat flow in the Uinta Basin determined from bottom hole temperature (BHT) data, *Geophysics* 49(4), 453-466.
- Davies J.H. (2013) Global map of solid Earth surface heat flow, *Geochem. Geophys. Geosyst.* 14(10), 4608-4622, <https://doi.org/10.1002/ggge.20271>.
- ESMAP (2012) The World bank Group. Technical Report 002/12. Geothermal Handbook: Planning and financing power generation. [https://www.geothermal-advancement.com/\\_files/ugd/d41d81\\_0c0a624014b6497da56162e7122b49fe.pdf](https://www.geothermal-advancement.com/_files/ugd/d41d81_0c0a624014b6497da56162e7122b49fe.pdf).
- Evenick J.C. (2019) *Introduction to well logs and subsurface maps*, Tulsa, PennWell, p. 314.
- Gudmundsson J., Freeston D., Lienau P. (1985) The lindal diagram, *GRC Trans.* 9, 15-17.
- Hamm V., Maurel C., Bugarel F., Hervé J.-Y. (2022) Good practice guidelines on deep geothermal drilling and exploitation from experience in the Paris Basin (Dogger and Albian aquifers), European Geothermal Congress (EGC) 2022, Oct 2022, Berlin, Germany. fihal-03703216. Good practice guidelines on deep geothermal drilling and exploitation from experience in the Paris Basin (Dogger and Albian aquifers).
- Heat Roadmap Europe (2019) Heating and Cooling, facts and figures, The transformation towards a low-carbon Heating & Cooling sector, available at: [https://heatroadmap.eu/wp-content/uploads/2019/03/Brochure\\_Heating-and-Cooling\\_web.pdf](https://heatroadmap.eu/wp-content/uploads/2019/03/Brochure_Heating-and-Cooling_web.pdf).

- IEA Report (2011) Technology Roadmap Geothermal Heat and Power. [https://www.geothermal-advancement.com/\\_files/ugd/d41d81\\_91a9a77c3e0d4277bec0a0e06b6d3092.pdf](https://www.geothermal-advancement.com/_files/ugd/d41d81_91a9a77c3e0d4277bec0a0e06b6d3092.pdf).
- IEA Report (2023) Renewables 2023 Analysis and Forecast to 2028, <https://www.iea.org/reports/renewables-2023/heat>
- IGA and IFC (2014) Best Practices Guide for Geothermal Exploration, <https://documents1.worldbank.org/curated/en/190071480069890732/pdf/110532-Geothermal-Exploration-Best-Practices-2nd-Edition-FINAL.pdf>.
- IRENA and IGA (2023) Global geothermal market and technology assessment, International Renewable Energy Agency, Abu Dhabi; International Geothermal Association, The Hague, [https://www.irena.org/-/media/Files/IRENA/Agency/Publication/2023/Feb/IRENA\\_Global\\_geothermal\\_market\\_technology\\_assessment\\_2023.pdf](https://www.irena.org/-/media/Files/IRENA/Agency/Publication/2023/Feb/IRENA_Global_geothermal_market_technology_assessment_2023.pdf).
- Kaczmarczyk M., Tomaszewska B., Operacz A. (2020) Sustainable Utilization of Low Enthalpy Geothermal Resources to Electricity Generation through a Cascade System, *Energies* 13(10), 2495, <https://doi.org/10.3390/en13102495>.
- Kolawole F., Evenick J.C. (2023) Global distribution of geothermal gradients in sedimentary basins, *Geoscience Frontiers* 14(6), 101685, <https://doi.org/10.1016/j.gsf.2023.101685>.
- Mckenzie D.A.N., Bickle M.J. (1988) The volume and composition of melt generated by extension of the lithosphere, *J. Petrol.* 29(3), 625-679.
- Negrel G., Lasne É. (2021) Les exploitations géothermales au Dogger, *Géologue* 211, ISSN 0016.7916, co-édité par AVENIA et Société Géologique de France.
- Operacz A., Chowanec J. (2018) Prospective of geothermal water use in the Podhale Basin according to geothermal step distribution, *Geol. Geophys. Environ.* 44, 379-389.
- Paixach G. (2024) Evolution of Geophysical Techniques over the Last Twenty Years: Commercialization, Societal Impact, and Research and Development Perspectives Journées Scientifiques AGAP Qualité 2024, Poitiers, France, Edited by F. Asfirane, J.-L. Mari, E3S Web of Conferences, Volume 504, id.00001, <https://doi.org/10.1051/e3sconf/202450400001>
- Turcotte D.L., Schubert G. (2002) *Geodynamics*, Cambridge University Press, New York, NY.
- Zheng K., Dong Y. (2008) The possible role of geothermal energy to the Chinese energy development. Proceedings, 8th Asian Geothermal Symposium, Dec 9-10, 2008, Vietnam Institute of Geosciences and Mineral Resources, Hanoi, Vietnam.



# Surface geophysical methods

J.-L. Mari and G. Paixach

---

Historically, geophysical methods have played a pivotal role in the exploration of oil, gas, and minerals, serving as the backbone of resource discovery for decades. However, the landscape of geophysical applications is evolving to meet the demands of emerging domains holding significant economic, technological, social, and environmental importance. One such domain is geothermal energy, which is becoming a potential candidate in the global push toward heat and electricity decarbonization.

The shift towards geothermal energy requires a deeper understanding of the subsurface, not only in sedimentary basins but also in areas characterized by igneous formations. Effective site investigation for geothermal projects needs characterization of the subsurface through different geophysical methods.

There are various geophysical methods, each based on distinct theoretical principles, that provide valuable data about subsurface materials. By acquiring and analyzing this data through specific geophysical surveys, we can better understand the subsurface properties and characteristics, offering important insights for exploring and managing subsurface resources and developing geotechnical engineering.

Geophysical methods encompass various techniques, each designed to characterize specific properties of geological formations and rocks. Among the most widely used methods are seismic, magnetic, electrical, electromagnetic, and gravity surveys.

Each method provides unique and complementary information about the subsurface, highlighting the importance of using multiple geophysical techniques in geothermal exploration. Integrating results from these diverse geophysical methods is crucial for creating a comprehensive image of the subsurface, which is essential for successful geothermal exploration, production, and monitoring.

By combining seismic data with electrical resistivity, for example, geoscientists can correlate structural information with fluid content, improving the accuracy of reservoir models. Similarly, integrating magnetic and gravity data can enhance the understanding of the geological context, such as the presence of igneous intrusions or fault systems, which are critical for assessing geothermal potential. This multidisciplinary approach not only enhances the precision of subsurface imaging but also reduces the uncertainty in locating and exploiting geothermal resources, ultimately contributing to more efficient and sustainable geothermal energy production.

Surface geophysical methods are usually non-invasive techniques used to investigate the properties of subsurface materials from the Earth's surface. Surface geophysical methods are relatively cost-effective and efficient, covering large areas quickly without drilling. They provide broad, low to medium-resolution data making them ideal for exploration and mapping.

However processing and interpreting surface geophysical survey data usually requires prior knowledge of the subsurface geological structure, typically obtained from preliminary reconnaissance geological field studies, borehole data, and rock physics modeling.

- Reconnaissance geological field studies involve visual inspections and preliminary assessments of geological formations, using either on-foot surveys or satellite imagery. Detailed mapping and rock sampling are subsequently conducted to gain a more precise understanding of the surface geology, typically onshore.
- Borehole data are collected by placing sensors inside drilled wells to measure subsurface properties at specific depths. This method provides high-resolution, localized information on properties like lithology, porosity, and fluid content. Borehole data acquisition is generally expensive due to the need for drilling, logging equipment, and operational time to drill and instrument the borehole.
- Rock physics modeling is fundamental to interpreting and processing the results of geophysical surveys because it bridges the gap between raw geophysical data and the underlying geological realities. It provides the essential framework for understanding how different rock types, with their unique mineral compositions, porosities, and fluid contents, respond to various geophysical methods such as seismic, electrical, and magnetic surveys.

The best strategy for selecting and combining different geophysical methods hinges on balancing the four key factors that govern their effectiveness:

- penetration depth,
- vertical and lateral resolutions,
- signal-to-noise ratio,
- and contrast in physical properties.

First, penetration depth is crucial for determining how deeply a method can probe the subsurface. Methods like seismic surveys offer deep penetration in general, making them ideal for exploring deeper geothermal reservoirs, while methods like electrical resistivity are best suited for shallower investigations. Therefore, selecting a method with appropriate penetration depth ensures that the target depth of interest is adequately covered. The concept of penetration depth in geophysical methods is controlled by several factors, which vary depending on the specific technique used. These factors include the type of energy source (such as seismic waves, electrical currents, or electromagnetic fields), the frequency or wavelength of the signal, the physical properties of the subsurface materials, and environmental conditions. A key factor controlling penetration depth is the frequency or wavelength of the signal. In general, lower-frequency signals penetrate deeper into the Earth, but with lower resolution, while higher-frequency signals provide more detailed images but with shallower penetration. The composition and physical properties of the subsurface materials also play a significant role in determining penetration depth. The strength or intensity of the energy source also affects how deep a geophysical signal can penetrate. In seismic methods, for example, a stronger source (such as a large explosion) will generate seismic waves capable of traveling deeper into the subsurface compared to a weaker source (like a small hammer strike).

Second, vertical and lateral resolutions are essential for accurately imaging subsurface features. The vertical and lateral resolutions of geophysical methods – the ability to distinguish between subsurface features at different depths (vertical resolution) and across horizontal distances (lateral resolution) – are influenced by several key factors. High-resolution methods, such as ground-penetrating radar (GPR) or high-frequency seismic surveys, are excellent for detailed imaging of shallow subsurface structures, whereas lower-resolution methods might be more suitable for broader, regional surveys. Combining methods with complementary resolutions helps build a detailed and comprehensive subsurface model. These include the frequency or wavelength of the signal, the spacing of data collection points (survey geometry), the physical properties of the subsurface, and the processing techniques used to refine the data. The wavelength of the signal used largely determines the vertical resolution of a geophysical method. In seismic surveys, for example, higher-frequency seismic waves can detect thin layers, whereas low-frequency waves may smooth over fine details but penetrate deeper. Lateral resolution is typically controlled by the density of data acquisition across the survey area. Closely spaced measurement points (e.g., seismic receiver stations, electrodes, or magnetometers) provide better lateral resolution, enabling the detection of smaller subsurface features. In contrast, widely spaced points result in a coarser lateral image, potentially missing finer details. In areas with complex geological structures or heterogeneous materials, lateral resolution can be reduced as the signal may be scattered or absorbed by irregularities in the subsurface. This is particularly relevant in seismic and electromagnetic methods, where subsurface heterogeneities can blur or obscure smaller features.

The signal-to-noise ratio is another critical factor. The concept of signal-to-noise ratio (SNR) is critical in geophysical methods as it measures the clarity and reliability of the data collected during a survey. In essence, SNR compares the strength of the desired

signal – representing the geophysical properties of the subsurface – to the background noise, which may originate from environmental, instrumental, or human-made sources. A high SNR indicates that the signal is clear and distinct from the noise, enabling a more accurate interpretation of subsurface features. A low SNR means the signal is masked by noise, making it difficult to extract useful information. Each geophysical method is affected by noise differently. For instance, seismic methods can be disrupted by surface vibrations from traffic or machinery, while electromagnetic methods are sensitive to electrical interference from power lines or other sources. Improving SNR is crucial for ensuring reliable geophysical survey results. Techniques like stacking, filtering, and signal processing are commonly used to enhance the signal and reduce noise across various methods. Seismic surveys, for example, often employ stacking, where multiple seismic traces are combined to amplify the signal and diminish random noise. In electrical and electromagnetic surveys, filtering techniques can be applied to isolate the frequencies of interest and suppress unwanted noise. The success of a geophysical method depends on achieving a balance between maximizing signal strength and minimizing noise, which varies depending on the survey environment and the specific method used.

In passive seismic methods, the concept of signal-to-noise ratio is redefined because what is traditionally considered “noise” becomes the primary source of useful data. Unlike active seismic surveys, which generate artificial seismic waves using controlled sources like explosions or vibrators, passive seismic techniques rely on naturally occurring or ambient seismic noise, such as microtremors, ocean waves, or human activities. This background noise, which would typically be seen as a nuisance in active seismic methods, is instead harnessed as the signal itself. Passive seismic methods, such as seismic interferometry or ambient noise tomography, process this ambient noise to extract valuable information about the Earth’s subsurface. The challenge in passive seismic surveys is not eliminating noise but rather distinguishing between different types of noise to identify the most useful signals. For example, seismic interferometry uses cross-correlation techniques to turn ambient noise into coherent seismic waves, which can then be interpreted similarly to traditional seismic data. This approach is particularly valuable in environments where active seismic surveys are not feasible, such as urban areas or environmentally sensitive regions. It offers a cost-effective, non-invasive means of subsurface exploration, making it an important tool in geothermal energy exploration and monitoring.

Finally, the contrast in physical properties refers to how distinct the geological features are in terms of their physical characteristics. Geophysical methods are most effective when there is a significant contrast, such as differences in density or electrical conductivity, between target formations and surrounding materials. Therefore, choosing methods that can exploit these contrasts – like gravity surveys for density differences or electromagnetic methods for conductivity variations – optimizes the detection of specific subsurface features.

By carefully considering these factors, geoscientists can select and combine geophysical methods that complement each other, providing a more accurate and comprehensive understanding of the subsurface, which is crucial for effective geothermal exploration and other subsurface investigations.

Subsurface investigations inherently carry uncertainty, especially when working in complex or poorly understood geological environments. A feasibility study reduces this uncertainty by identifying the limitations and strengths of each method in the specific context of the site. This helps reduce the risk of failed surveys or inaccurate interpretations, which can lead to expensive rework or the failure of large-scale projects, such as geothermal energy exploration or construction planning. A feasibility study helps identify the most suitable methods based on the geological conditions of the site. For example, if there is little contrast in the seismic velocities of rock layers but a strong difference in electrical resistivity, electrical methods may be more effective than seismic methods. This preliminary evaluation ensures that only the most appropriate and effective methods are deployed in the main survey. Full-scale geophysical surveys can be costly, especially when multiple methods are involved. A feasibility study allows for testing the effectiveness of the methods on a smaller scale, reducing the risk of investing in techniques that may not produce useful results. Also, geophysicists can tailor their approach to mitigate potential problems, such as improving signal-to-noise ratios or adjusting survey geometry.

Before delving into the specifics of each geophysical method, it is essential to review the characteristics of rocks, including their mineral composition, porosity, and other physical properties. These characteristics significantly influence the outcomes of geophysical surveys. For instance, the mineral content of a rock determines its magnetic and electrical properties, while porosity affects its ability to store and transmit fluids, impacting seismic and resistivity measurements. Additionally, the overall rock properties, such as density and elasticity, play a crucial role in how seismic signals propagate.

A thorough review of these rock properties is necessary to accurately interpret geophysical data and effectively apply these methods in geothermal exploration and other subsurface investigations. Following a concise review of the physical and pore space properties of rocks, we provide an overview of surface geophysical methods and illustrate their application with selected field examples. Since different geophysical methods provide complementary information, integrating their results often provides the best subsurface model.

## 2.1 Physical properties of rocks and pore space properties

This discussion emphasizes the characterization of natural rocks, which are inherently heterogeneous and composed of diverse minerals with varying physical properties, shapes, sizes, and spatial arrangements. These complexities, along with boundary effects, interactions, and thermodynamic conditions, fundamentally influence the physical properties of rocks.

For a geophysicist, rock is composed of three elements: the matrix, the porosity, and the fluids.

The matrix is the solid part constituted of minerals, each of them characterized by their physical properties such as density, velocity, resistivity, susceptibility, etc.

Porosity refers to the amount of empty space within the rock, often described as the fraction of the rock's total volume that is occupied by voids, cracks, or pores. These pores can vary greatly in size, shape, and connectivity, and they significantly influence the rock's ability to store fluids. Porosity is expressed as a percentage, with higher values indicating more pore space. The arrangement and distribution of these pores within the matrix are crucial for determining other properties, such as permeability, which describes how easily fluids can move through the rock. Permeability seems to be the most important (and hard to determine) property for all reservoir problems. It controls whether the rock can deliver or transmit fluids or not.

The fluids are pore-filling materials: water, oil, gas, air, and pollutants, each of them having specific physical properties. These fluids, with their specific physical properties like viscosity and conductivity, play a major role in the rock's overall behavior.

The physical properties of these elements will condition the physical properties of the rock (Figure 2.1).

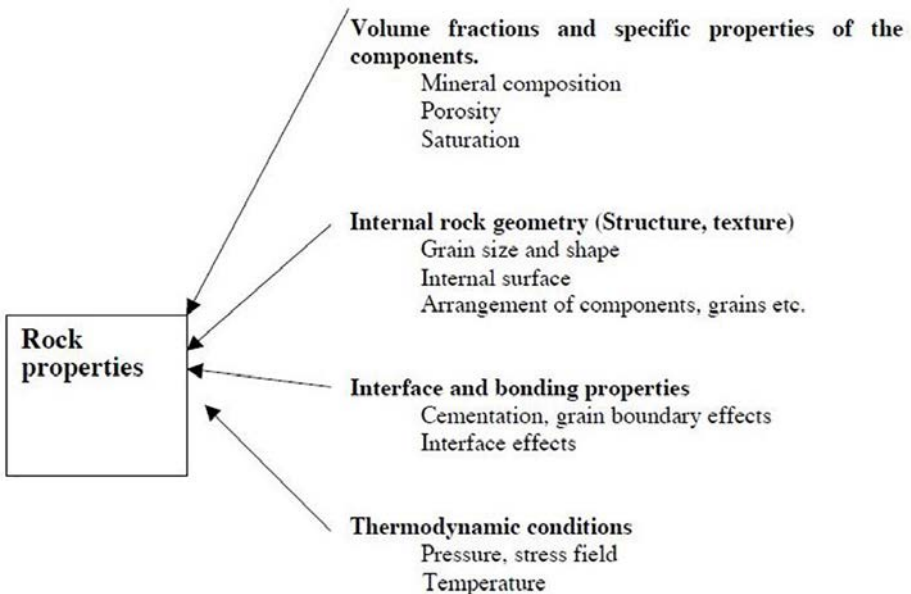


Figure 2.1 Physical properties of rocks (after D. Chapellier, IFP School course, personal communication).

**Rock physics modeling** is the process of quantitatively describing the relationship between the physical properties of rocks (such as porosity, mineral composition, and fluid saturation) and their geophysical properties (such as elastic wave velocities, and electrical conductivity). The ultimate objective is to interpret subsurface geology, reservoir characteristics, and fluid content from geophysical measurements.

Rock physics modeling can involve **theoretical models** based on physical laws combined with numerical simulations or **empirical relationships** derived from laboratory measurements or field data.

The estimation of physical parameters such as seismic velocities and attenuation or resistivity obtained by geophysical methods associated with experimental relationships established from laboratory experiments allows the estimate of porosity or permeability distributions in geological formations.

### 2.1.1 Porosity

Porosity  $\Phi$  is defined as the ratio of the volume of pore space to the total or bulk volume of the rock. Porosity is expressed as a decimal fraction or a percentage (%). Porosity is the result of various geological, physical, and chemical processes, and is generated during the genesis of the rock as “primary porosity”, and/or during the geological history of the rock as “secondary porosity” (tectonic processes (fractures), chemical processes, dissolution). Total porosity is the sum of the primary and the secondary porosity.

The main factors, which influence primary porosity, are:

- Grain and pore geometrical properties (arrangement and shape of the rock grains, grain size distribution),
- Diagenetic processes, amount of cement,
- Depth and pressure (which also influences secondary porosity)

Theoretically, porosity for given packing is independent of grain size. However, porosity shows a tendency to increase with the change from spherical or well-rounded grains to angular particles. Decrease of porosity primarily results from packing and cementation for sands and sandstone, and from compaction for clays and shale. This reflects a general tendency of decreasing porosity with increasing depth.

Effective porosity is the porosity that is available for free fluids; it excludes all non-connected porosity. Effective porosity could be much lower than the total porosity when the pores are not connected or when the pores are so small that fluids cannot circulate.

For a clean formation, if the matrix and fluid velocities are known, porosity can be computed from the acoustic  $V_p$  velocities by using the formula given by Wyllie et al. (1956) expressed in velocities. It is given by the following equation:

$$\Phi = \left( \frac{V_{ma} - V_p}{V_{ma} - V_f} \right) \frac{V_f}{V_p} \quad (2.1)$$

with  $V_{ma}$  the matrix velocity,  $V_f$  the fluid velocity.

Porosity can also be estimated by electrical measurement. Archie (1942) has shown empirically that for water-saturated permeable formations, the relation between the true formation resistivity,  $R_t$ , and the resistivity,  $R_w$ , of the water impregnating the formation is given by:

$$\frac{R_t}{R_w} = F = \Phi^{-m} \quad (2.2)$$

where  $F$  is the “resistivity formation factor”.  $\Phi$  is proportional to the formation porosity and  $m$  is a “cementation factor”, that is a formation characteristic. The  $F$  value derived from the resistivity measurement,  $R_t$ , is unaffected by the mineralogical constituents of the formation matrix. Although the “cementation factor” value may vary between 1.3 and 3 according to the formation lithology, an approximate value equal to 2 is generally adopted.

### 2.1.2 Permeability

Permeability describes the property of a porous rock regarding fluid flow through the pore space. It depends on the porosity, the pore space dimension, and geometry. In hydrogeology, the hydraulic permeability  $K_f$  has the dimension of a velocity (mostly given in cm/s) (Figure 2.2). In practice, the unit DARCY (d) is commonly used. 1 Darcy is the permeability of a material that permits a volume flow of 1 cm<sup>3</sup>/s through a section of 1 cm<sup>2</sup> under a pressure gradient of 1 atm/cm of a fluid with a viscosity of 1 centipoise. One millidarcy, 1 md = 10<sup>-6</sup>cm/s.

Permeability depends in a very complex way on the properties of the pore space. The dominant influences are:

- Porosity: Permeability increases with increasing porosity, but this is strongly influenced by the rock type.
- Pore size: Permeability increases with increasing grain size; this is the dominant parameter, especially for sedimentary rocks.
- Pore shape and specific surface: Pore space geometry determines permeability and the capillary forces; these forces control the retention of water in the angles and capillaries between the grains.
- Arrangement of pores
- Permeability decreases with compaction and cementation.

Morlier and Sarda (1971) have looked at ultra-sonic data (P-wave and S-wave velocities, frequencies, and attenuations) and petrophysical data (porosity, permeability, specific surface) of numerous core plugs of different rock types (sandstone, limestone, carbonate). Their laboratory experiments have led them to the following results:

- When there is only one saturating fluid, the attenuation is an increasing function of frequency  $f$  and of the reverse of the kinematic viscosity ( $\rho_f/\mu$  with  $\rho_f$ : fluid density,  $\mu$ : fluid viscosity (centipoise)).

- The attenuation  $\delta$  depends on the structure of the rock (i.e. pore geometry).
- The attenuation  $\delta$  can be expressed in terms of three structural parameters: porosity, permeability, and specific surface.

A law which fits their experimental results has been established:

$$\delta = \frac{CS}{\varphi} \left( \frac{2\pi k f \rho_f}{\mu} \right)^{1/3} \tag{2.3}$$

with:

$\delta$ : attenuation (dB/cm),  $f$ : frequency (Hz),  $\rho_f$ : fluid density,  $\mu$ : fluid viscosity (centipoise),  $\varphi$ : porosity,  $S$ : Specific surface ( $\text{cm}^2/\text{cm}^3$ ),  $C$ : calibration coefficient,  $k$ : permeability (mD,  $1 \text{ mD} = 10^{-15} \text{ m}^2$ ).

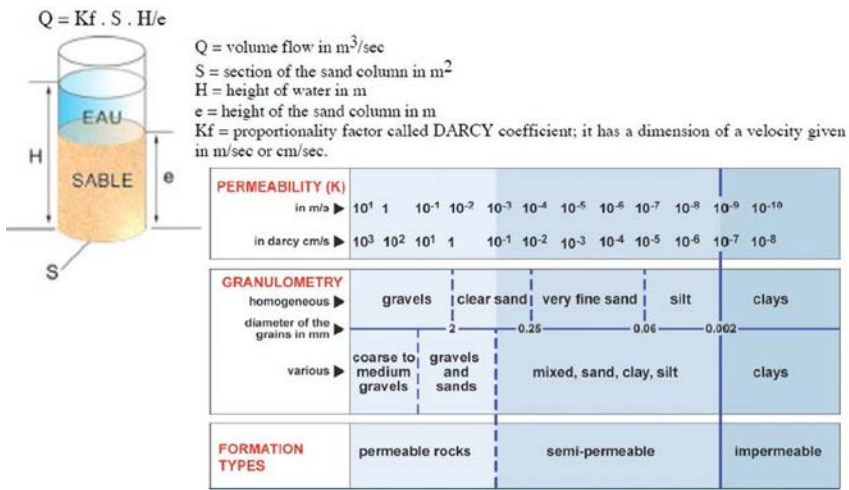


Figure 2.2 Permeability  $Kf$  versus granulometry and formation types. After Dominique Chapellier (2001a).

Figure 2.3 is an example of laboratory measurements on sandstone core plugs. The upper part of the figure shows the results obtained on cores with a constant specific surface, the lower part on cores with a variable specific surface, the specific surface being estimated based on the average pore radius measurement.

From equation (2.3), Mari et al. (2012) derived an indicator of permeability  $I_k$ -Seis, useable with seismic or acoustic data

$$I_k\text{-Seis} = \frac{(\varphi\delta / S)^3}{f} = \frac{(\varphi / SQ)^3}{f} \tag{2.4}$$

with

$f$ : P-wave frequency,  $Q$ : quality factor,  $\delta$ : attenuation,  $S$ : specific surface,  $\varphi$ : porosity.

It is necessary for computing the permeability from equations (2.3) or (2.4) to measure the attenuation of the formation and to calculate the effective specific surface of the formation.

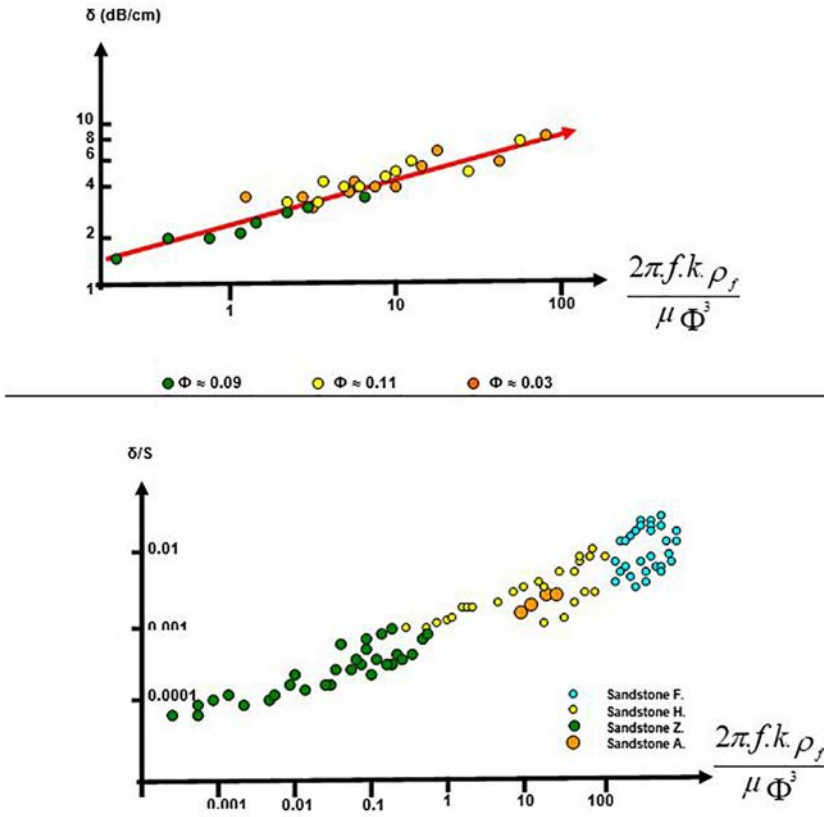


Figure 2.3 Relationship between attenuation and petrophysical parameters (after Morlier and Sarda, 1971). Top: laboratory measurements on cores with constant specific surface. Bottom: laboratory measurements on cores with variable specific surface

Theoretically, the effective specific surface  $S$  can be calculated from the porosity  $\phi$  and the Klinkenberg permeability  $k$  (given in  $m^2$  in equation (2.5) but typically reported in mD) using Kozeny’s equation (Kozeny, 1927)

$$k = C_k(\phi^3/S^2) \tag{2.5}$$

$$S_g = S/(1 - \phi) \tag{2.6}$$

with  $\phi$ : porosity,  $S$ : Specific surface,  $S_g$ : Specific surface with respect to grain volume,  $C_k$ : Kozeny’s factor

The Kozeny’s factor can be calculated from the porosity via a simple model of linear 3D interpenetrating tubes (Mortensen et al., 1998). The specific surface  $S_g$  with respect to the bulk volume is given in  $1/m$  in equations (2.5) and (2.6) but typically reported in  $m^2/cm^3$ . Fabricius et al. (2007) have found that the specific surface with

respect to grain volume ( $S_g$ ) apparently does not depend on porosity. To remove the porosity effect on  $V_p/V_s$  and mimic a reflected  $\phi$  vs.  $\log(S_g)$  trend, they propose to use the following relationship between porosity  $\phi$ ,  $V_p/V_s$  and  $S_g$ :

$$\log(S_g m) = a\phi + b(V_p/V_s) + c \tag{2.7}$$

where it should be observed that  $S_g$  is multiplied by  $m$  to make  $S_g$  dimensionless.

To establish equation (2.7), Fabricius et al. (2007) have looked at ultra-sonic data, porosity, and the permeability of 114 carbonate core plugs.

## 2.2 Geophysical methods

Geophysical methods are currently used to build 2D or 3D models of the sub-surface associated with variations of physical properties of rocks:

- Gravity method with density variations,
- Magnetic method with rock magnetization properties (magnetic susceptibility  $\kappa$  and remanence),
- Low frequency Electrical and EM methods with resistivity variations,
- High-frequency EM methods with permittivity variations (GPR),
- Seismic methods with velocity and density variations.

Figure 2.4 gives links between rocks and petrophysical parameters.

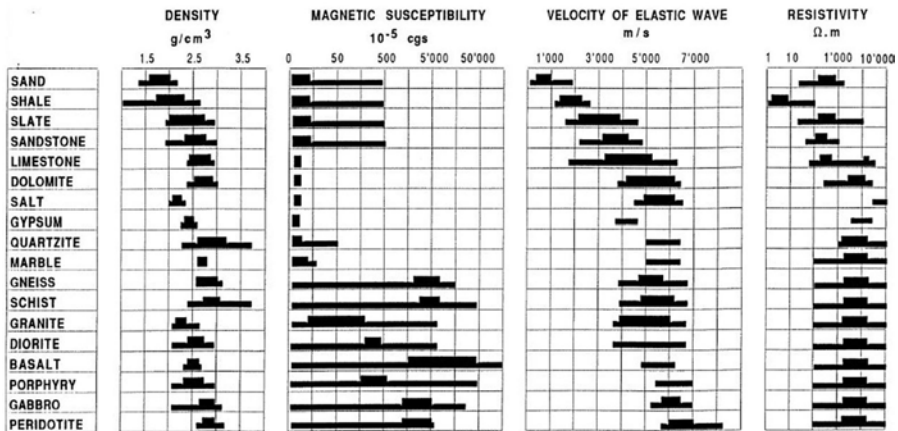


Figure 2.4 Rocks and petrophysical parameters (density, magnetic susceptibility, velocity of elastic P-wave, resistivity) (after D. Chapellier, IFP School course, personal communication).

The acquisition parameters must be selected to reach the depth of the target. The vertical and horizontal resolutions must be evaluated to know if the chosen method is well adapted to the sizes of the expected anomalies. Several methods can be combined as indicated in Figure 2.5, depending on the objective: Geological, Resources, Engineering.

<b>Problem</b>		<b>Example</b>	<b>Methods and remarks</b>
<b>Geological</b>	<b>Stratigraphical</b>	Sediments over Bedrock	Seismic refraction Resistivity  seismic reflection
	<b>Erosional</b>	Buried channel	Seismic refraction, gravity, electromagnetic and resistivity
		Buried Karstic surface	Electromagnetic and resistivity Radar Seismic reflection
	<b>Structural</b>	Faults and fractures zones	Resistivity and EM Seismic refraction and reflection Magnetic and gravity
<b>Resources</b>	<b>Hydrocarbons</b>	Location of reservoir	Seismic reflection Gravity and Magnetic Borehole geophysics
	<b>Water</b>	Location of aquifer	Resistivity, EM, seismic refraction and reflection Gravity and magnetic
	<b>Sand and gravel</b>	Gravel banks	Resistivity, EM Gravity and magnetic Marine: continuous seismic profiling
	<b>Clay</b>	Clay pockets	Resistivity and EM P.P.
<b>Engineering</b>	<b>Elasticity modulus, density and porosity</b>	Dynamic deformation modulus	Seismic surface waves Borehole seismic and density and porosity logs
	<b>Rock rippability</b>	Choice of excavation method	Seismic refraction
	<b>Corrosivity of soils</b>	Pipeline surveys	Resistivity

Figure 2.5 Geophysical methods versus objectives: Geological, Resources, Engineering (after D. Chapellier, IFP School course, personal communication).

## 2.2.1 Gravity method

Gravity method concerns the study of the gravity field. The variations in gravity over the earth's surface have become a powerful technique in the investigation of geological structures at various depths. The variations in gravity reflect the inhomogeneous distribution of the densities in the ground. The density of the rocks (Figure 2.6) depends mainly on the rock composition and its porosity.

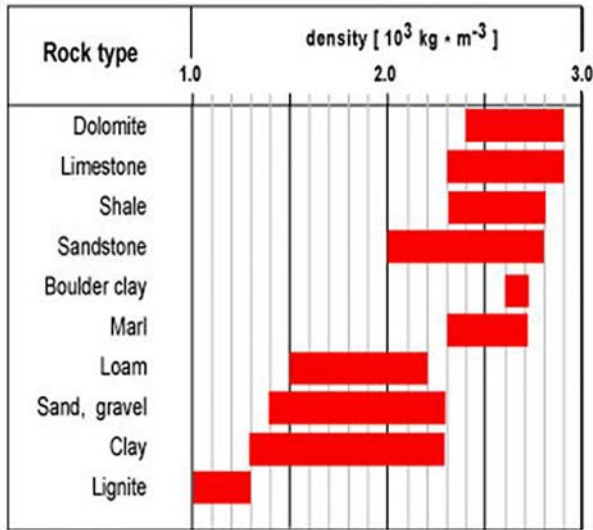


Figure 2.6 Density versus rock type. After D. Chapellier (2001a).

The purpose of a relative gravity survey is to directly map the structure of the subsurface. Gravity is the attractive force between two or more bodies of mass. The force, given by Newton's law, is proportional to the mass  $m$  of the object and decreases with distance  $R$ :

$$F = G M m / R^2 \quad (2.8)$$

$G = 6.674 \times 10^{-11} \text{ N} \cdot \text{m}^2 \cdot \text{kg}^{-2}$  is the universal gravitational constant,  $R = 6371 \text{ km}$  radius of the earth,  $M_{\text{earth}} = 5977 \times 10^{24} \text{ kg}$ .

The force exerted on a body at the earth's surface is due to the attraction of the earth. The gravitational acceleration  $g$  (referred as gravity) may be considered as the force exerted by the earth on a unit mass:  $g = F/m$ .

The SI unit for the gravity,  $g$ , is  $\text{m/s}^2$ . In geophysics this unit is referred to as the Gal (in honor of Galileo). One-tenth of a miligal is called a gravity unit (g.u.), which is used more commonly in exploration work.  $1 \text{ g.u.} = 0.1 \text{ mGal}$ .

The density contrast leads to a different gravitational force which is measured, and usually presented in mgal or  $10^{-3} \text{ cm/s}^2$ . To obtain information about the subsurface density from the gravity measurement, it is necessary to make several corrections to the measured value. The final corrected values of the gravity anomaly, is called Bouguer anomaly and is given by:

$$\Delta g = g_{\text{obs}} - g\phi + \Delta g_{\text{al}} - \Delta g_{\text{Boug}} + \text{TC} \quad (2.9)$$

where  $g_{\text{obs}}$  are gravity readings observed at each gravity station after corrections have been applied for instrument drift and earth tides.  $g\phi$  is the gravity at latitude  $\phi$ .  $\Delta g_{\text{al}} = 0.3086h$  is the Free air correction or elevation correction to consider the variation of elevation  $h$  between the measurement locations (a vertical decrease of gravity is associated with an increase of elevation).  $\Delta g_{\text{Boug}} = 0.042\rho h$  is the correction from the excess mass material between the station and sea level. (variation of elevation  $h$ , density  $\rho$ ). TC is the terrain correction that accounts for the presence of mass (for example hill) in the vicinity of the measurement station.

Bouguer anomalies are differences between actual gravity values and what would be expected from a uniform earth, which has the same latitude, elevation, and terrain. Gravity interpretation frequently begins with some procedure that separates the anomalies of interest from the smooth presumably deep regional effects. The regional effect could be obtained by a filtering process, such as upward continuation intended to emphasize or enhance the long wavelength components. The regional is subtracted from the observed gravity map or profile, and the resulting residual contains the component of the field which are caused by mass representing geological disturbances of interest.

Figure 2.7 is an example of Bouguer anomaly observed in Martinique (Girard, 2017). The studied area is located close to the site called “Anses d’Arlets”, south-West of Martinique (Figure 2.7a). Geology is mainly composed of andesitic to dacitic products with basaltic lavas (age ranges from 1.5 to 0.35 million years). The density variation in the ground affects the gravity recorded in surface, and after some corrections have been applied, a Bouguer anomaly map can be obtained. The average density which decorrelates the more the topographic effect (Nettleton, 1939) is close to 2, and was used to compute the map shown in Figure 2.7b. A high pass filter was applied (cut length 8 km). Black dots are gravimetric measurements.

The U.S. Navy has developed a system to measure gravity gradients. In 1994, this technology began to be used in exploration (Bell et al., 1997). Normal gravity field  $g_z$ , also noted  $G_z$ , is the vertical pull of gravity at a location and is made up of two signals: one from the local geology and the other from the best-fitting ellipsoid field (Fairhead, 2015). In airborne gravity, the airborne gravimeter measures the sum ( $g_z + a$ ) of the vertical acceleration “ $a$ ” and of the normal gravity field  $g_z$ . To recover the normal gravity field, the vertical acceleration must be canceled using additional information given by GPS measurements. The measurement of  $g_z$  at two elevations  $z + \Delta z/2$  and  $z - \Delta z/2$  leads to the cancelation of the kinematic acceleration by computing the first vertical derivative  $G_{zz}$  of the gravity field. Such an approach is known as Gravity-gradiometry, the measurements being done by gravity gradiometers.

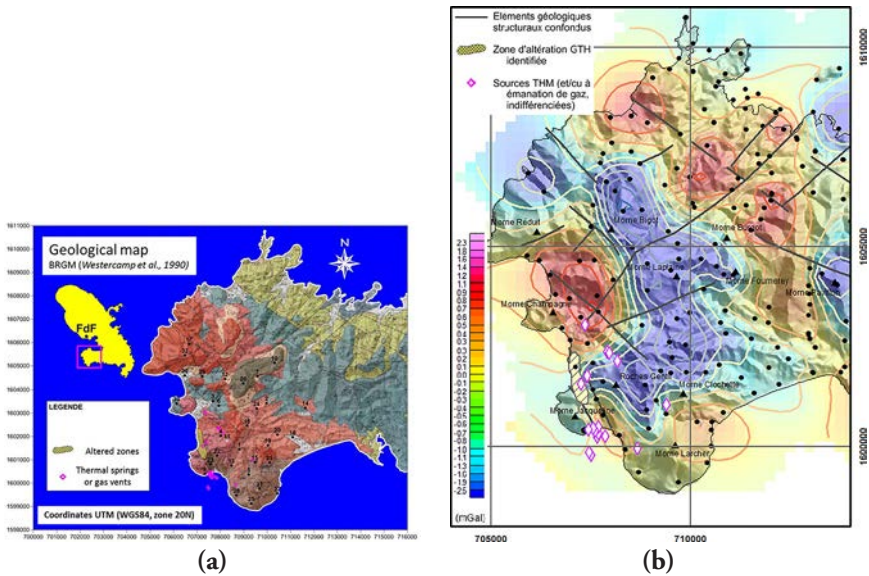
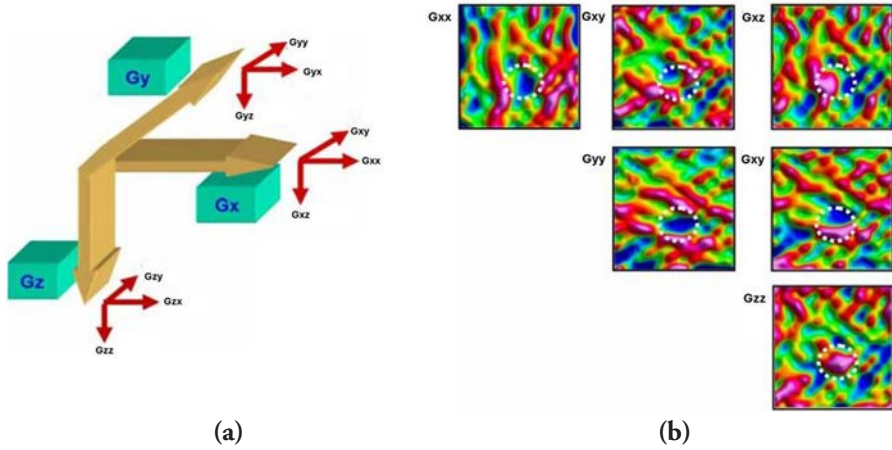


Figure 2.7 Gravity method. Bouguer anomaly observed in Martinique (after Girard, 2017). Location map (a), Bouguer anomaly map (b)

The gravitational field is composed of 3 vectors: the vertical vector component  $G_z$ , and two horizontal vector components  $G_x$  and  $G_y$ . The 3 vector components of gravity  $G_x$ ,  $G_y$  and  $G_z$  have vertical and horizontal gradients:  $G_{xx}$ ,  $G_{xy}$ ,  $G_{xz}$  for  $G_x$ ;  $G_{yx}$ ,  $G_{yy}$ ,  $G_{yz}$  for  $G_y$ ;  $G_{zx}$ ,  $G_{zy}$  and  $G_{zz}$  for  $G_z$ . The gradients are known as tensors. Because partial derivatives are independent of the order of differentiation, three of the tensors are identical to three other tensors ( $G_{xy} = G_{yx}$ ,  $G_{xz} = G_{zx}$ , and  $G_{yz} = G_{zy}$ ). Consequently, one only needs to measure five of the tensors to measure the Full Tensor Gradiometry (FTG) field (Figure 2.8a).

An  $11 \times 11$  km Air-FTG<sup>TM</sup> survey with 100 m in-line, spacing (orientation NS) was flown over the Vinton, Salt Dome area onshore Louisiana, USA, in 2002 (Murphy and Mumaw, 2004). All five independent Tensor components were recorded and are shown in Figure 2.8b.

$G_{zz}$  clearly maps the near-surface high-density caprock (outline shown in white). The other Tensor components reveal detailed information relating to the dominant geological structural control on the salt emplacement.  $G_{xx}$  and  $G_{yy}$  locate the NS and EW edges of the caprock feature and their negative sum yielding  $G_{zz}$  gives the expected positive  $G_{zz}$  anomaly. The variation in  $G_{zz}$ ,  $G_{xx}$  and  $G_{yy}$  anomaly intensity indicate that the caprock itself is not of uniform shape.  $G_{xz}$  and  $G_{yz}$  locate the central axes of the salt feature, and with  $G_{xx}$  and  $G_{yy}$  help identify the dominant structural pattern. The salt appears to have been emplaced at the intersection of two dominant trends, i.e. NWSE and NESW.  $G_{xy}$ , showing the characteristic “2 positive 2 negative” anomaly pattern, helps constrain the geometric extent of the salt caprock.



**Figure 2.8** Gravity Gradiometry method. (a) The full tensor gravitational field, (b) Tensor Display for the Vinton Dome Air-FTG™ survey. *Gzz* clearly images the cap rock on the salt dome (outline in white). The cap rock's response in each of the independent components is also circled (after Murphy and Mumaw, 2004).

Time-lapse microgravity is used to identify the mass deficit that occurs in reservoirs in petroleum and geothermal fields because of mass extraction carried out during exploitation. The study, conducted by Pasaribu et al. (2024), explores the application of the time-lapse microgravity method at the Awibengkok geothermal field in Indonesia since the commencement of production. This method utilizes gravimeter equipment with a precision of up to 0.001 miligal (mgal) to monitor mass changes resulting from fluid extraction. Gravity measurements since 1994 reveal a significant annual average decrease in gravity acceleration (−9.2 microgals per year), indicating ongoing mass depletion in the reservoir. The approach includes digital leveling for gravity data correction and subsidence risk assessment. Gravity data modeling employs inversion methods to visualize density changes beneath the surface, demonstrating notable density decreases in production areas and localized increases near injection wells, suggesting potential dynamics of fluid recharge. Gravity changes that occurred from 1998 to 2008 and 1998 to 2017 are depicted in Figure 2.9. Decreasing gravity acceleration from 1998 to 2010 was −230  $\mu$ gal and increased in 2017 to over −500  $\mu$ gal. The largest decrease in gravity acceleration occurs in the middle of proven area (blue to purple).

The gravity and gravity-gradiometry methods are particularly suitable for evaluating depth to basement and mapping basin 3D structures and basement features such as lineament, faults, etc.

For more information about the gravity method, we recommend reading the book written by Fairhead (2015).

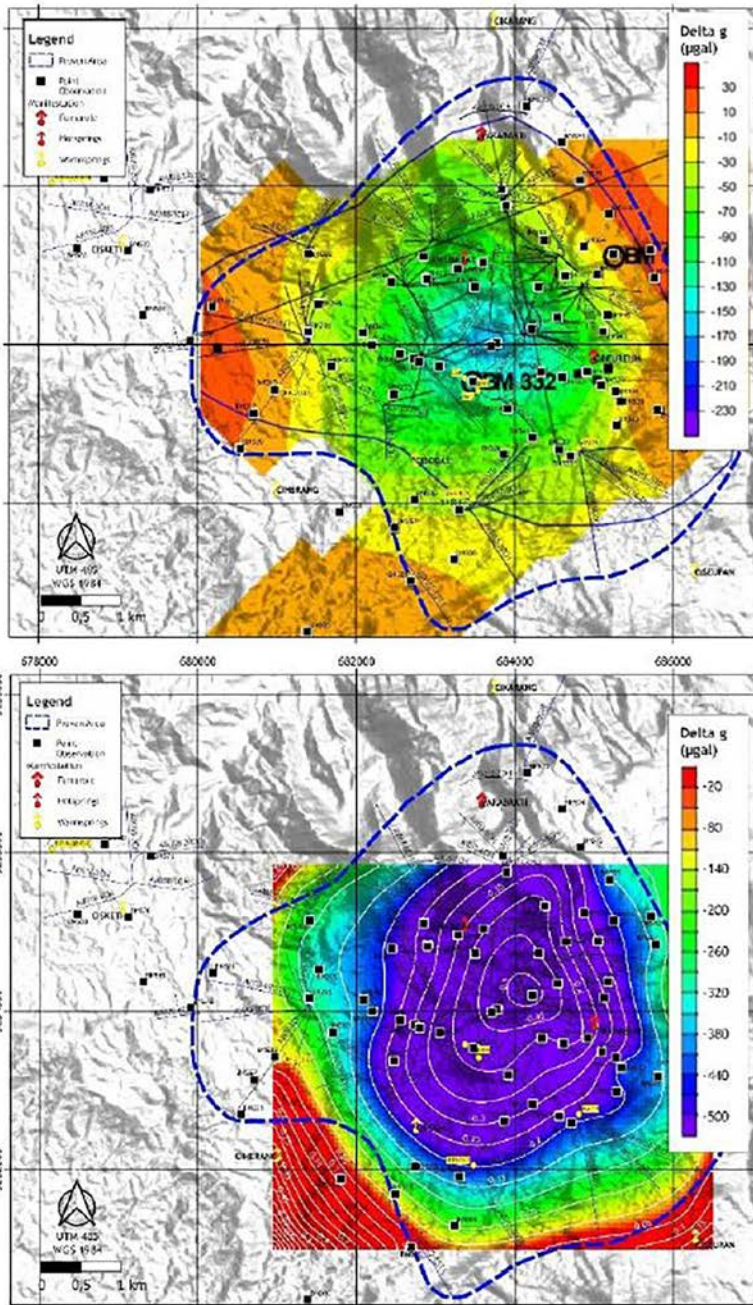


Figure 2.9 Geothermal fluid production impact on density (after Pasaribu et al., 2024). Gravity changes map (on  $\mu\text{gal}$ ) from 1998 to 2010 (top) and to 1998 to 2017 (bottom)

### 2.2.2 Magnetic method

Magnetic properties describe the behavior of any substance under the influence of a magnetic field. All minerals are affected in some way by a magnetizing field. The capacity of a mineral to acquire magnetism by induction is described by its magnetic susceptibility. The strength of the induced magnetization  $M$  (magnetic dipole moment per unit volume) is directly related to the strength of the applied magnetic field  $H$ :

$$M = \kappa H \tag{2.10}$$

with  $\kappa$  the magnetic susceptibility.

Rock types vary in magnetic susceptibility (Figure 2.10a). The most important fact in magnetic exploration for petroleum is that sedimentary rocks are nearly non-magnetic, that is; have very small susceptibility compared to basement rocks. The susceptibilities of non-sedimentary rock types are larger than those of sedimentary rocks by a factor of 10 to 1000 times. The magnetic fields measured in practice are flux densities. The unit is called Tesla T. For most geophysical purposes the tesla is too large as a unit and flux densities are more conveniently expressed in nanotesla ( $nT = 10^{-9} T$ ).

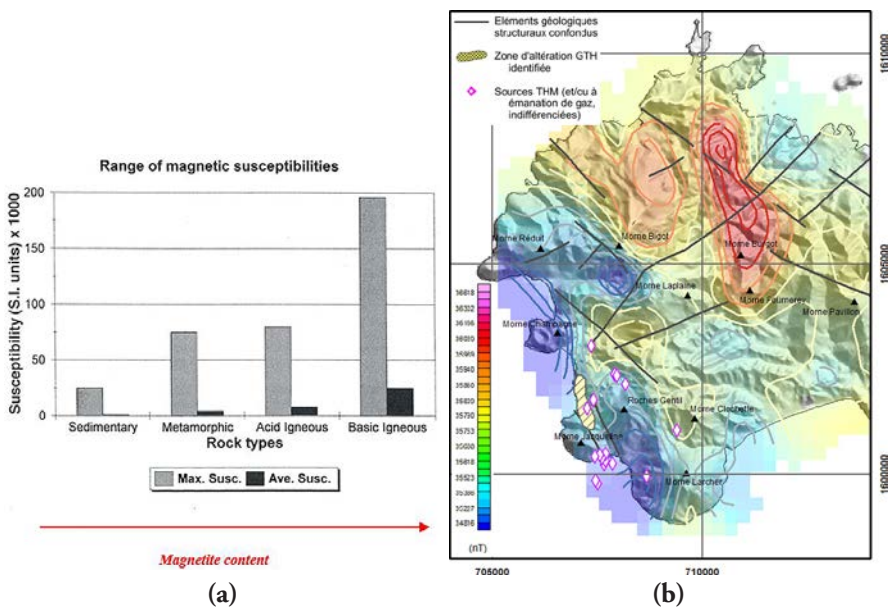


Figure 2.10 Magnetic method. a: Magnetic susceptibility versus rock type (after D. Chapellier, IFP School course, personal communication), b: Magnetic anomaly observed in Martinique (after Girard, 2017).

Magnetic exploration is primarily used in the first phases of geophysical work in the area. Magnetic surveying, performed with magnetometers (fluxgate magnetometer, proton-precession magnetometer...), is carried out on land, at sea, and in the air. For extensive areas, reconnaissance over both land and sea is conveniently done with an airborne magnetometer.

As in the case of gravity, the magnetic field anomaly is simply the observed minus the predicted value at the observation site. If  $T_{\text{obs}}$  is the measured total field (corrected for temporal variation (diurnal correction)) and  $T_{\text{R}}$  the reference field, given by the IGRF tables (International Geomagnetic Reference Field) at the site, the geomagnetic anomaly in the total field  $\Delta T$ , is given by  $\Delta T = T_{\text{obs}} - T_{\text{R}}$ . The advent of satellites dedicated to measuring the total field  $T$  or its vector components has remarkably augmented the global coverage and improved the data for analysis of the earth's field (the International Geomagnetic Reference Field is revised every five years). Observations of the  $\Delta T$  anomaly field (or its vertical or horizontal component) over the area of the survey reflect subsurface variations in the magnetization of rock formations. Specific procedures such as derivatives and filtering procedures are useful in separating anomalies. Upward and downward continuation are also used for the determination of regional and residual. A special procedure is to reduce the field to the pole. It consists in the transformation of the anomaly observed at the survey latitude where the field is inclined in an anomaly that would be observed at the magnetic north.

For most applications of magnetic surveying, the magnetic effect of the sedimentary rocks may be considered as approximately the same as if the sediments were not present and the magnetic disturbances recorded have their origin at or below the base of the sediments. This is the basis for use of magnetic measurements to map the basement surface. The magnetic method is particularly suitable for mapping basement features such as lineament, faults, shear zones, lithologic contact, etc., which may be hidden from direct view because overlying sedimentary cover.

Figure 2.10b shows the magnetic anomaly after pole reduction (Girard, 2017) observed in Martique in the area investigated by a gravimetric survey (Figure 2.7). The volcanic material of various ages highlights generally various responses in link with the varying geomagnetic field.

For more information about the magnetic method, we recommend reading the book written by Fairhead (2015).

### 2.2.3 *Electrical and EM methods*

On the historical side, Electrical methods dedicated to Geosciences began with the Schlumberger Brothers in the late 20's. In a century, technology started from a simple DC resistivity method and went up to complex Electromagnetism methods implying natural or controlled sources, from 1D to 4D models, from acquisition in boreholes to land, air and sea. EM is now used in, tectonic studies,

Oil & Gas and Mining Industry, Geothermal and Near surface studies (civil engineering, groundwater monitoring and environmental purposes).

First known success occurred with mineral exploration on highly conductive sulfide metal ores bodies.

A behavior of an EM field is controlled by 3 main parameters:

- Electrical conductivity/resistivity
- Dielectric permittivity
- Magnetic susceptibility

The Electrical conductivity or resistivity is the most important for DC and low frequency methods (i.e. below 1 kHz for MT, AMT, mCSEM, AEM) whereas the Electric permittivity is the most important for high frequency methods (i.e. above 1 MHz for GPR).

The chart (Figure 2.11) shows that materials which are part of E&P investigations are distributed over a massive range of orders of magnitudes regarding electric resistivity. Resistivity variations in sediments are controlled by variations of porosity, permeability, pore connectivity geometry and the fluids contained by the pores.

As standard approximations, the industry often takes 0.3  $\Omega\cdot m$  for seawater, 1.5 to 3  $\Omega\cdot m$  for sediments saturated with brine and up to 100  $\Omega\cdot m$  for hydrocarbon bearing reservoirs. Almost two orders of magnitude between sediments containing brine and those containing HC. On the other side, elastic waves could not even pretend to be 1 order of magnitude of difference.

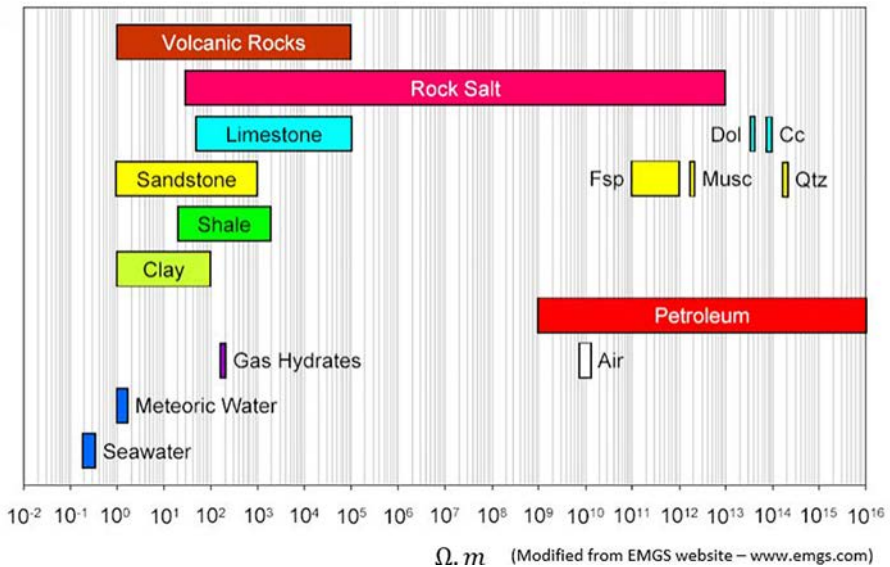


Figure 2.11 Electric resistivity versus rock type.

## Electrical methods

Electrical methods, in DC current, are based on the measurement from the surface of the apparent resistivities of the ground. Resistivity of geological formations can vary:

- from 1 to 10 ohm.m for clay and marl,
- from 10 to 100 ohm.m for sands and sandstone,
- from 100 to several thousands of ohm.m for limestone and the eruptive rocks,
- in practice DC currents are sent in formation using current electrodes A or B (Figure 2.12a).

The current sent by an electrode A(+) is collected by an electrode B(-), but according to the principle of superposition, the potential in a point M or N is the same one for a current I(+) independently sent by A or B. The measurement of the potential difference  $\Delta V$  created by the passage of the current I between two electrodes M and N allows to estimate the resistivity  $\rho$  of the formation (Figure 2.12b). If the formation is isotropic and homogeneous the measured resistivity is the true resistivity of the formation. If the ground is heterogeneous, the measured resistivity is an apparent resistivity, which is a function of the nature of the ground and the dimension of the array used. The array is conventionally a 4 electrodes array AMNB (Figures 2.12b and 2.12c), the depth of investigation of which being function of its characteristic length L (Figure 2.12c).

AMNB array, with constant distances between electrodes and a given characteristic length L, moved along profiles, is currently used to establish profiles or maps of resistivity, associated with a depth of about constant depth investigation. To investigate several depths, several profiles must be recorded with several characteristic lengths L (Figure 2.12d). Figure 2.12e shows an example of a resistivity map obtained with a characteristic length of 100 m.

A Schlumberger array with a constant distance between electrodes M and N and a variable increasing distance between electrodes A and B is used to obtain a distribution of resistivity versus depth. One of the limitations of the electrical soundings comes to the fact that they do not consider the horizontal variations of the resistivity of the ground.

Methods of electrical imagery 2D and 3D have been developed to obtain a model of the ground where the distribution of resistivities varies vertically and horizontally along the profile. 2D or 3D acquisitions generally use a great number of electrodes connected to multicore cables and placed along profiles. An acquisition device automatically selects the electrodes used for the injection of the current and for the measurement of the potential difference  $\Delta V$ . It also computes the distribution of apparent resistivities versus depth Z and distances X and Y, considering the different geometries of acquisition. In a next step, 2D or 3D iterative electrical tomographic inversion algorithms are used to obtain resistivity distribution in the 2D, or 3D space. The methodology, called electrical resistivity tomography ERT, requires an a priori distribution of resistivity used to initiate the inversion process. The process

works iteratively and stops when the updated distribution of resistivity allows to compute a set of apparent resistivities which fits, in a root mean square sense, the measured apparent resistivity distribution. Figure 2.13 shows an example of 2D electrical tomography, obtained on the rock glacier of Verbier in Switzerland. The example is a near surface example, with a depth investigation of 30 m.

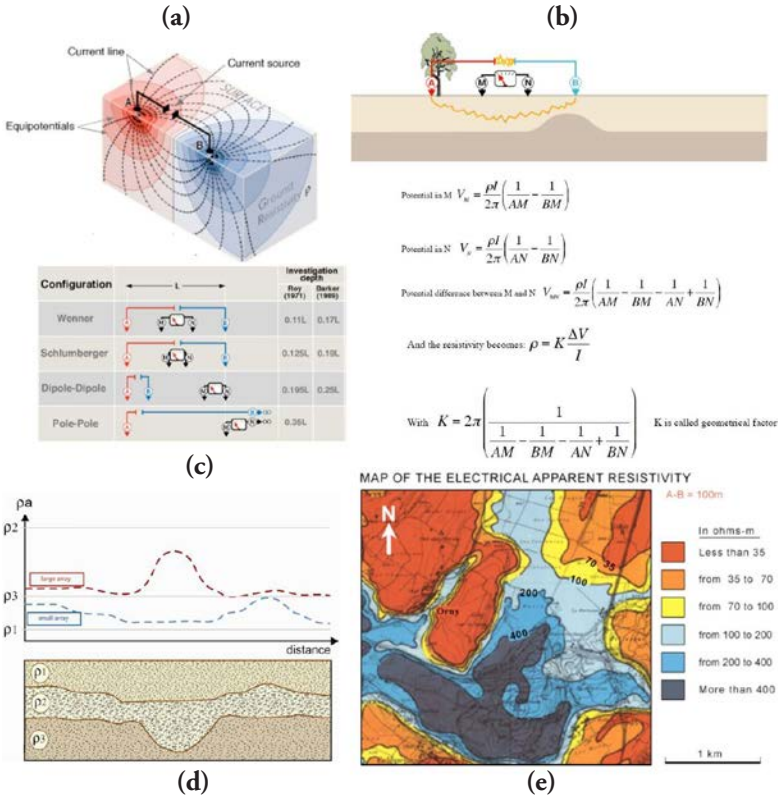
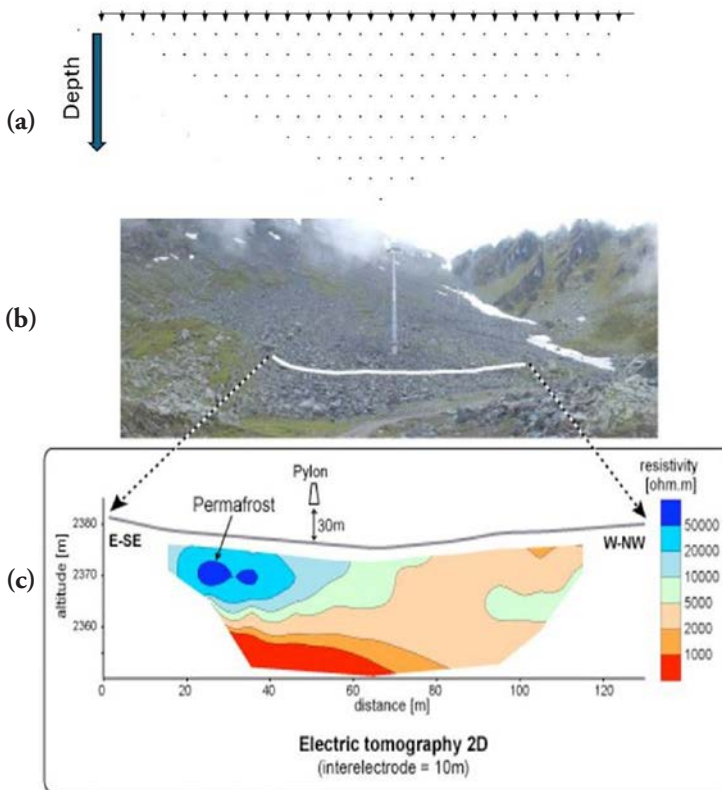


Figure 2.12 Electrical method. After D. Chapellier (2001b). (a) Equipotential and current flow lines for two sources of current. (b) Measurement of apparent resistivity. (c) Depth investigation of the electrical method versus the spread configuration. (d) Resistivity profiles. (e) Electrical apparent resistivity map. Document IGL.

For deep target, specific field apparatus has been developed (Carrier et al., 2019). It consists of a set of 2-channel independent receiving nodes called V-Fullwavers, one current measurement unit called I-Fullwaver, an induced polarization transmitter (VIP). Current is injected through the induced polarization transmitter. The transmitter enables to inject current up to 10 Amps, 5000 W and 3000 V, with a frequency of 0.5 Hz. The receiving nodes (V-Fullwavers) continuously record the electrical field and the injection electrodes can be moved inside and outside the receiving nodes with any type of electrode array configuration. For the field

example shown in Figure 2.14, the distance between 2 injection electrodes is 50 m, the distance between 2 receiving nodes is 100 m, the overall length of the profile is 4500 m. After electrical resistivity inversion, the resistivity section has a depth investigation of several hundred meters.

Electrical resistivity tomography (ERT) and Induced polarization (IP) surveys can provide resistivity, porosity, reaction temperature and cation exchange capacity (CEC) tomograms from surface measurements (Piolat et al., 2024). ERT/IP survey results for the Amashyuza geothermal prospect (Rwanda) are shown in Figure 2.15 (after Piolat et al., 2024). Electrical geophysical methods are of great value in this context, as they provide vital information on fluid flow networks, alteration intensity, hydrothermal temperatures, and geological identifications.



**Figure 2.13** Example of 2D electrical tomography, obtained on the rock glacier of Verbier in Switzerland. (a) line of electrodes (distance between two adjacent electrodes is 10 m) and theoretical location (indicated by dots) of apparent resistivity measurement depending on the array configuration, (b) view of the rock glacier of Verbier, c: resistivity section. After D. Chapellier (2001b, Document IGL).

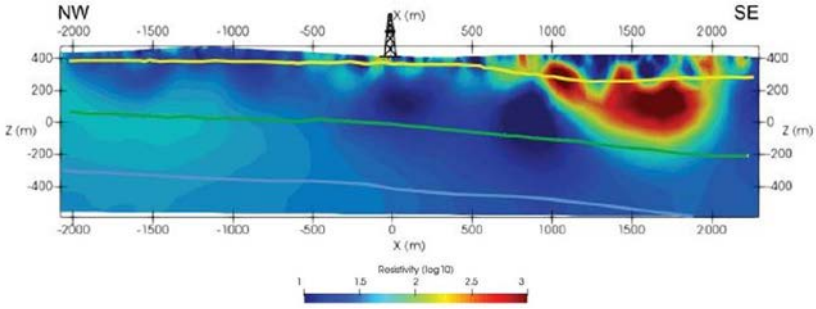


Figure 2.14 Example of deep electrical resistivity tomography. After Carrier et al. (2019).

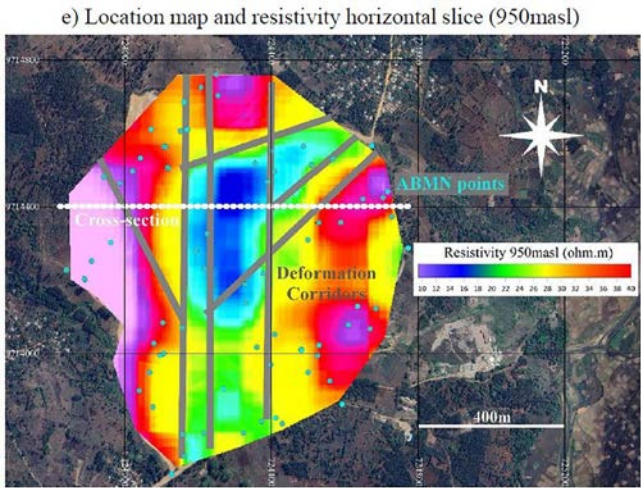
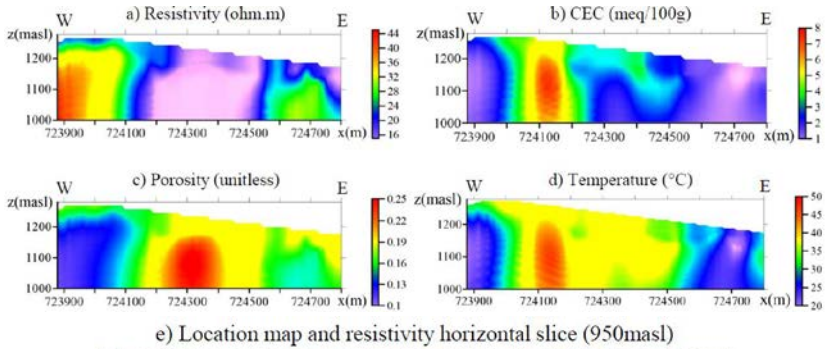


Figure 2.15 DEEP-ERT cross-section results of resistivity (a), CEC (b), porosity (c), reaction temperature (d), and resistivity plan section (e) for the Amashyuza geothermal prospect in Rwanda (after Piolat et al., 2024).

For more information, we recommend the reading of the part of the online course of geophysics (<http://www-ig.unil.ch/>), devoted to electrical methods.

## EM methods (AC)

Electromagnetism methods (EM) are based on the study of electromagnetic field generated either by natural or controlled sources.

With natural source (EM fields occurring naturally), the incident signal tends to behave like a plane wave at the air interface. The two components  $E_x$  and  $E_y$  of the electric field and the associated two components  $H_x$ ,  $H_y$  and potentially  $H_z$  components of the magnetic field are measured. The apparent resistivity already defined in the previous section (in ohm.m) of the subsurface structure is usually estimated:

$$\rho_{a,xy} = \frac{1}{2\pi f} \frac{|E_x|^2}{|H_y|^2} = \frac{1}{2\pi f} |Z|^2 \quad (2.10)$$

with  $Z$ , the impedance tensor,  $E_x$  and  $E_y$  the spectral horizontal components of the electric field expressed in V/m in the horizontal  $x$  and  $y$  directions,  $H_x$  and  $H_y$  the spectral horizontal components of the magnetic field expressed in A/m in the horizontal  $x$  and  $y$  directions,  $f$  the frequency in Hz. Inversion of apparent resistivity and phase of the impedance tensor, leads to earth resistivity model (2D and 3D).

With controlled sources, manmade electric dipoles, current loops, ..., the two components  $E_x$  and  $E_y$  of the electric field and the associated two components  $H_x$ ,  $H_y$  of the magnetic field are measured. In some borehole applications, both vertical components:  $E_z$  and  $H_z$  can also be measured. The link between data and earth resistivity cannot be simplified anymore to the apparent resistivity concept, because the incident signal is not a plane wave anymore.

Natural or manmade sources, 2D and 3D interpretation of EM data requires the derivations of the Maxwell's equations (numerical modelling and inversion).

At those frequencies, the EM signal is strongly attenuated through a diffusion process. Such attenuation is controlled by the so-called skin depth:

$$\delta \approx 503 \sqrt{\rho / f} \quad (2.11)$$

Skin depth is defined as the distance along which the electromagnetic field has reduced to  $e^{-1}$  (or 37 percent) of its original amplitude value at the surface or source location. Signal penetration is therefore function of frequency and earth resistivity for natural source and also offset (distance in between source and receiver) for manmade source.

Active audiomagnetotellurics (AAMT), transient electro-magnetic (TEM), time domain electromagnetic method (TDEM), controlled source electromagnetics (CSEM) and controlled source audiomagnetotellurics (CSAMT) methods fall in the category of active EM methods.

Figure 2.16 is an example of receiver and dipole source for marine CSEM acquisition, the dipole source being towed behind the vessel and receivers dropped down on the sea floor.

Magneto-telluric (MT) and audio-magneto-telluric (AMT) methods fall in the category of passive EM methods with natural source. The origin of the variations of earth's magnetic fields, called magnetic micro-pulsation, is the ionospheric and

magnetospheric currents caused by plasma (solar winds) emitted from the sun and interfering with the earth's magnetic field. The micro pulsations induce eddy currents in the ground, called telluric currents, and their density and distribution depend on the local conductive structure of the ground. The natural EM-field has a very wide spectrum, low frequencies, from 0.0001 to 10 Hz are used in investigations for depths of several tens to hundreds of kilometers (actual MT method), while higher frequencies mostly due to lightning around the world, from 10 to 1000 Hz are used for shallower targets (audio-magneto-telluric method – AMT). MT, in association with gravimetric (Figure 2.7) and magnetic (Figure 2.10b) surveys, has been successfully used for geothermal exploration in Martinique (Girard, 2017).

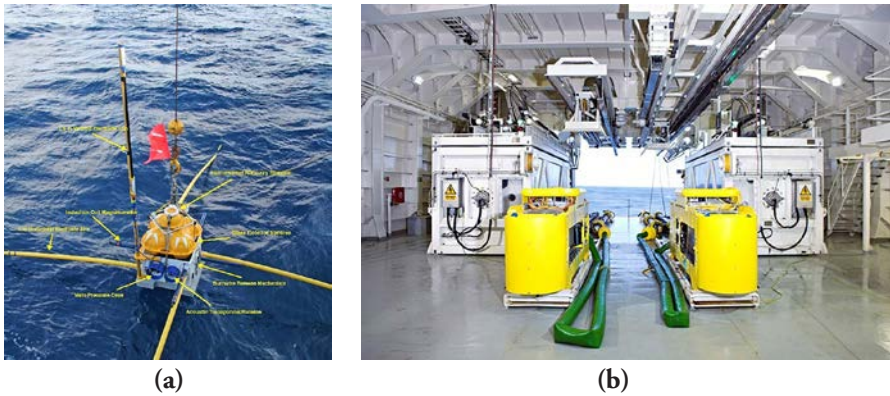


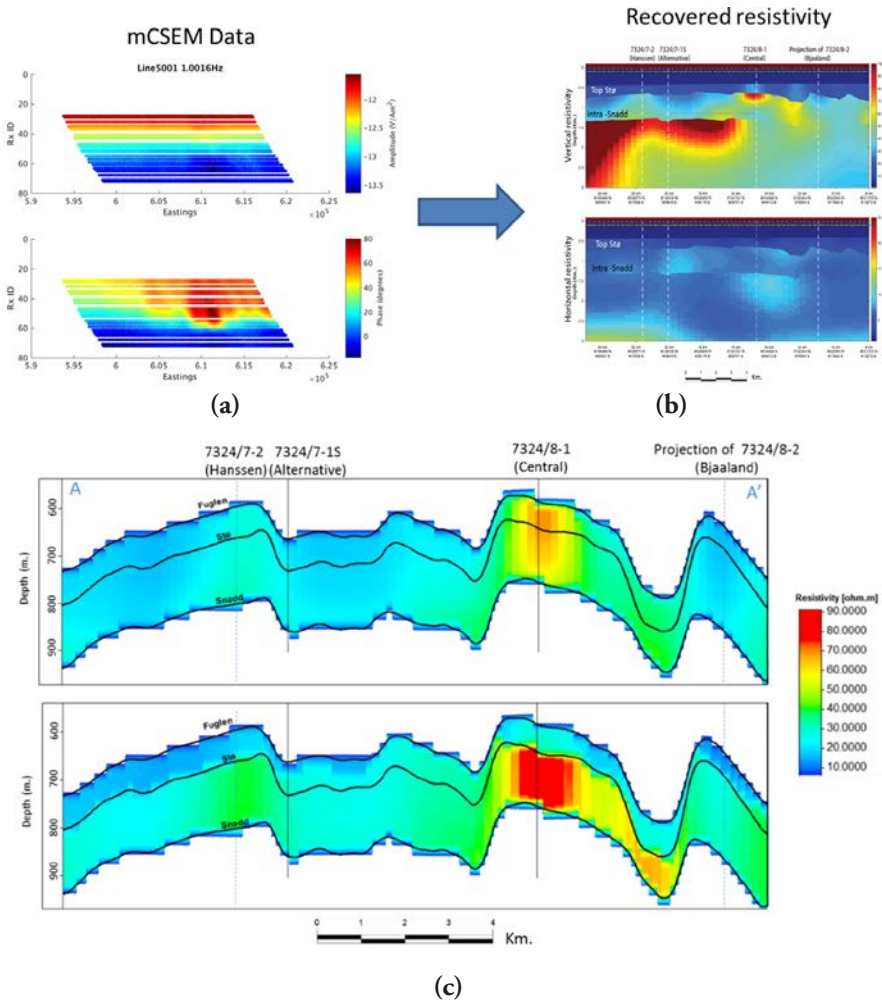
Figure 2.16 Receiver (a, courtesy of Cripps Institution of Oceanography) and dipole source (b, courtesy of EMGS) for marine CSEM acquisition.

Figure 2.17 is an example of mCSEM (marine CSEM) from the Hoop area of the Barents Sea. The area in question covers a significant oil discovery in the Hoop Fault Complex on the Bjarmeland Platform in the Barents Sea, Norway (Alvarez et al., 2017). A densely sampled dataset consisting of six lines of 2D seismic and towed streamer CSEM data were acquired concurrently in 2015 by PGS. The survey area lies in water depths of approximately 400 m. Two public domain wells in the area provide calibration for the integrated analysis. Some mCSEM data acquired along line 5001, in the form of source gathers at 1 Hz are shown. A significant response to the accumulation encountered at Wisting Central can be clearly seen in the CSEM data, particularly in the phase response (Figure 2.17a, lower panel around 611 km Easting). This is observed across a wide band of frequencies.

The mCSEM data for six frequencies (0.2 Hz, 0.8 Hz, 1 Hz, 1.4 Hz, 2.2 Hz, 2.6 Hz) were inverted using an Occam approach (Constable et al., 1987; Key, 2016) to derive anisotropic resistivity models. The inversion was performed in stages. Firstly, an unconstrained inversion was run to examine the resistivity structure obtained in the absence of any a priori information. However unconstrained inversions in general have poor resolution. Resolution can be improved by including structural

information from the seismic data. This also ensures consistency between seismic and CSEM derived results, which is important for subsequent integrated interpretation. In this way, vertical (Figure 2.17b, upper panel) and horizontal (Figure 2.17b, lower panel) resistivity were recovered. Good RMS residual was achieved insuring that such recovered resistivity model honored the data.

Vertical resistivity for the unconstrained and constrained inversions run are shown in the interval of interest: the top one (Figure 2.17c, top) corresponding to the unconstrained



**Figure 2.17** mCSEM example from the Hoop area of the Barents Sea. After Alvarez et al. (2017). (a) mCSEM data in the frequency domain (amplitude (top) and phase (bottom)), (b) recovered resistivity results by seismically constrained inversion (vertical resistivity (top) and horizontal resistivity (bottom)), (c) vertical resistivity for the unconstrained (top) and seismically constrained (bottom) inversions run shown in the interval of interest.

inversion, and the bottom image (Figure 2.17c, top) shows the results of the constrained inversion previously shown. Both models are equivalent mCSEM wise (same mCSEM data fit) as they have the same transverse resistance (integration of the resistivity with respect to depth). The constrained results are preferred given the a priori information available. A qualitative interpretation of the CSEM inversion results supports the outcome of the Alternative, Central and Bjaaland wells. A prominent resistivity anomaly is recovered at Central, in which there was a significant oil discovery, which agrees with the high resistivity values measured at the reservoir location. On the other hand, the Realgrunnen structures penetrated at Alternative and Bjaaland, two dry wells, are related to low resistivity values that support the petrophysical outcome. Such analysis of the CSEM data in isolation does not allow to go beyond the previous qualitative conclusion. Only a quantitative approach that integrates the resistivity measurements with the seismic analysis can lead to reservoir properties

Figure 2.18 is an MT example (Avram, 2017). Uzbekistan, along with Russia and other FSU countries have long histories deploying MT measurements on their oil and gas fields especially for those one that are poorly covered by seismic. In the example, Uzbekgeofizyka partnered with Phoenix Geophysics deployed a very large, dense MT survey over East Buzakhur. The results shown here concern the East Buzakhur – Karabay contact (Figure 2.18a).

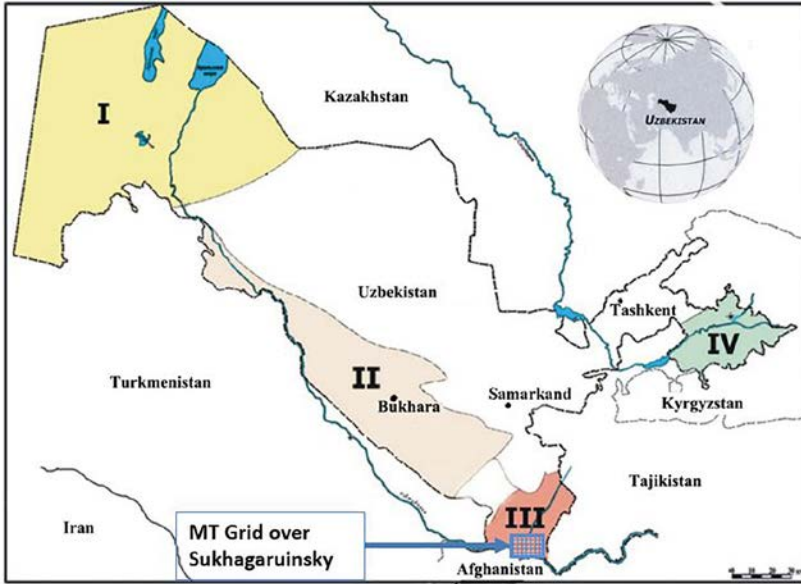
MT was tasked with the following:

1. bring additional information regarding the extent of the hydrocarbon system West of the main fault,
2. confirm and map the faults that control the East extent of the hydrocarbon system,
3. bring additional information that better characterize the source of these systems, their origin, and their relations from one basin to the next one, if any.

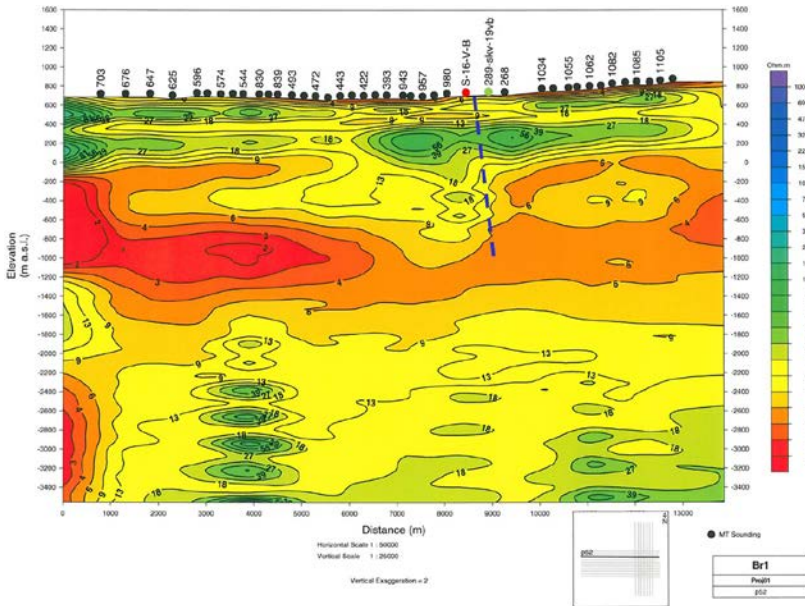
After data analysis and preprocessing, the MT resistivity pseudo sections are converted in resistivity by inversion (Figure 2.18b). The data analysis has put into evidence the following: MT responses have different behavior whether they are collected over the known deposit or away from it. The main structural N-S fault is visible and seems to control the Eastern trap of the reservoir.

mCSEM is best suited for deep waters acquisition layout. Shallow waters could lead to absence of sensitivity to resistive targets. Resolution of mCSEM is lower than for reflected amplitude seismic methods, but better than for potential fields methods. Transmitter frequencies must be chosen regarding target depth and host rock resistivity, keeping in mind skin depth concept. MT data could help to invert mCSEM data to image subsurface resistivities distribution. Combination of MT and gravity methods can be used in a Multiphysics approach to reduce the uncertainties and enhance resolution (Ceci et al., 2024a,b).

For more information, we recommend the reading of the e-book devoted to electromagnetic methods in geophysics (<http://books.ifpenouvelles.fr/ebooks/ifpen-electro/>).



(a)



(b)

Figure 2.18 MT example in Uzbekistan. After Avram (2017), courtesy of Phoenix Geophysics. (a) Major Mesozoic hydrocarbon bearing basins in Uzbekistan and location map of the MT survey, (b) MT resistivity pseudo sections converted in resistivity by inversion.

## 2.2.4 Seismic methods

Seismic prospecting consists of generating very low-amplitude artificial earthquakes at predetermined times and positions. The seismic disturbances generated by a seismic source are recorded by a seismic receiver spread. The acquisition geometry is defined by the distribution of the source spread and the receiver spread.

The following elements are needed to observe the propagation of seismic, acoustic, or elastic waves:

1. A source spread. The source is a device capable of producing a deformation in a medium. In land acquisition, it can be an explosive charge (dynamite), a weight dropper or a vibrator. In marine acquisition, it can be an air gun, a sparker, or a vibrator. Seismic energy radiated by the source is split between body waves (compressional P and shear S waves) and surface waves.

A P-wave has a particle motion parallel to the direction of propagation. A S-wave has a particle motion perpendicular to the direction of propagation. P and S waves propagate at  $V_P$  and  $V_S$  velocities respectively. When a P- or S- wave strikes an interface at some angle of incidence not equal to zero, four waves are generated: two transmitted (one P- and one S-wave) and two reflected (again one P- and one S-wave). The angular relationships between the propagation directions of each of these waves are given by Snell's law (Figure 2.19a). When P- or S-waves strike the interface at the critical angle  $i_c$ , head waves or refracted waves are generated. This only occurs when a wave perturbation passes from a medium with velocity  $V_i$  to another with velocity  $V_{i+1}$  which is greater than  $V_i$  and at the critical angle given by  $\sin(i_c) = V_i/V_{i+1}$ .

The critical angle  $i_c$  is the criterion for differentiating the various seismic methods associated to body wave propagation (Figure 2.19b):

- $i < i_c$ : the method is seismic reflection,
  - $i = i_c$ : the method is seismic refraction,
  - $i > i_c$ : the method is wide angle reflection. In wide angle reflection there is no transmitted energy, only reflected.
2. A physical medium defined by its geometric and mechanical characteristics. Here we consider the geological formations defined by the following mechanical properties:
    - propagation velocity of the compressional P-waves in the rock:  $V_P$  (expressed in m/s),
    - propagation velocity of the shear S-waves in the rock:  $V_S$  (expressed in m/s),
    - density  $\rho$  (expressed in  $\text{g/cm}^3$  or  $\text{kg/m}^3$ ),
    - quality factor  $Q$  which characterizes the ability of the rock to absorb seismic energy: a higher value indicates lower absorption of seismic energy. Sedimentary rocks have  $Q$  ranging from about 10 to several hundred.
  3. An elastic deformation of the medium after the initial shaking caused by the source. A deformation is considered elastic when the medium returns to its

original state after the causes of deformation have disappeared, i.e. when the medium has not been damaged by the wave passing through it.

4. A receiver spread. It is capable to record the deformations generated by the source after propagation in the geological medium:
  - either by variations in the displacement, velocity, or acceleration of particles (geophones, accelerometers),
  - or by pressure variations (hydrophones).

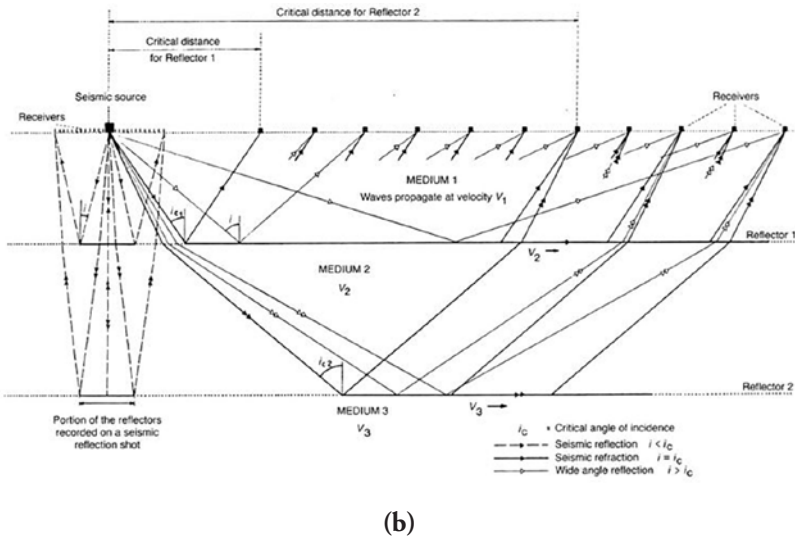
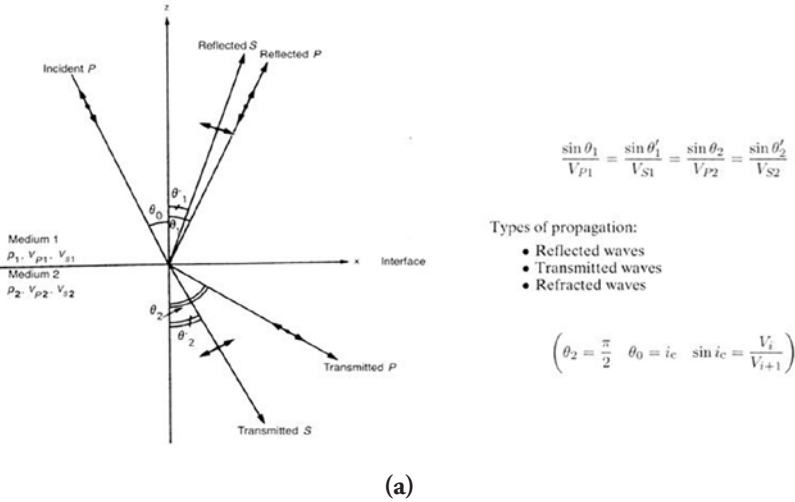


Figure 2.19 Seismic wave propagation. (a) Snell's law, after Lavergne (1986), (b) the various types of seismic surveying versus critical angle.

Figure 2.20 gives the range of values of propagation velocities,  $V_P$  and  $V_S$ , and densities of the principal rock types. It also gives the expressions of the main mechanical modules (Poisson's coefficient, Young's modulus).

Type of rock or medium	P-velocity $V_P$ (m/s)	S-velocity $V_S$ (m/s)	Density $\rho$ (g/cm <sup>3</sup> )
Weathered rocks	300 – 700	100 – 300	1.7 – 2.4
Dry sands	400 – 1200	100 – 500	1.5 – 1.7
Wet sands	1500 – 4000	400 – 1200	1.9 – 2.1
Clay	1100 – 2500	200 – 800	2.0 – 2.4
Marl/shale	2000 – 3000	750 – 1500	2.1 – 2.6
Sandstone	3000 – 4500	1200 – 2800	2.1 – 2.4
Limestone	3500 – 6000	2000 – 3300	2.4 – 2.7
Chalk	2300 – 2600	1100 – 1300	1.8 – 2.3
Salt	4500 – 5500	2500 – 3100	2.1 – 2.3
Anhydrite	4000 – 5500	2200 – 3100	2.9 – 3.0
Dolomite	3500 – 6500	1900 – 3600	2.5 – 2.9
Granite	4500 – 6000	2500 – 3300	2.5 – 2.7
Basalt	5000 – 6000	2800 – 3400	2.7 – 3.1
Coal	2200 – 2700	1000 – 1400	1.3 – 1.8
Water	1450 – 1500	–	1
Ice	3400 – 3800	1700 – 1900	0.9
Oil	1200 – 1250	–	0.6 – 0.9

First Lamé parameter	$\lambda = \rho (V_P^2 - 2V_S^2)$
Shear modulus (or second Lamé parameter)	$\mu = \rho V_S^2$
Poisson's coefficient	$\sigma = \frac{\gamma^2 - 2}{2(\gamma^2 - 1)}$ where $\gamma = \frac{V_P}{V_S}$
Young's modulus	$E = \rho V_P^2 \frac{(1 - 2\sigma)(1 + \sigma)}{1 - \sigma}$
Bulk modulus	$K = \rho \left( V_P^2 - \frac{4}{3} V_S^2 \right)$

Figure 2.20 Seismic velocities and densities, mechanical modules. After Lavergne (1986).

A seismic spread is composed of a source spread and a receiver spread. In 2D seismic survey, the sources and the receivers are located on the same line which defines a 2D seismic profile. In 3D seismic survey, the sources and the receivers are usually located on 2 orthogonal lines: a line of sources and the line of receivers. A seismic record is a set of seismic traces recorded at different receiver positions. The seismic trace represents the vibrations of the ground due to wave propagation generated by a seismic source. On a field record, the geophysicist can identify the different seismic waves (Figure 2.21). Figure 2.21 shows examples of 2D and 3D records.

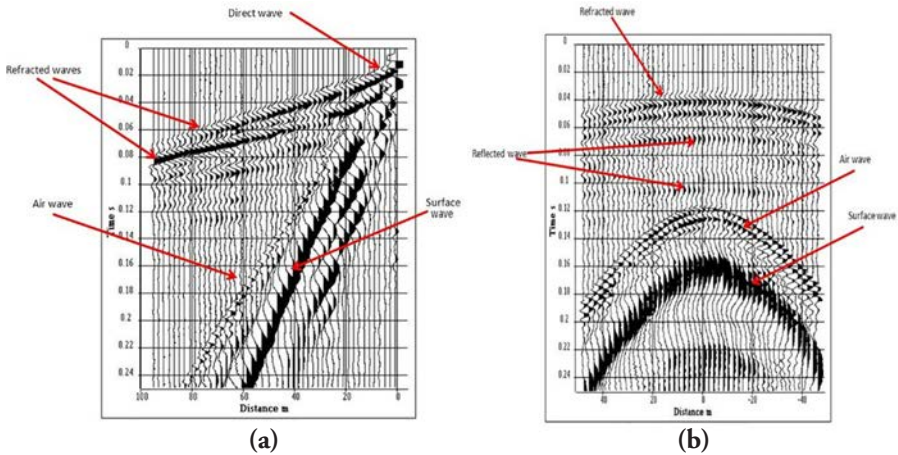


Figure 2.21 Examples of 2D (a) and 3D (b) seismic records. After Mari and Mendes (2019).

In addition to body waves (P- and S-waves) which propagate within the subsurface, a surface seismic source generates surface waves (Love and Rayleigh waves). These waves are used in civil engineering to determine the mechanical parameters (shear velocity and shear modulus) of the first tens of meter below the ground surface. The seismic method based on the analysis of surface waves is called MASW (Multiple Analysis of Surface Waves).

For more complete information on wave propagation, the reader is invited to consult other works such as Achenbach (1973), Lavergne (1986), Dobrin and Savit (1988), Quiblier (1997), Mari and Mendes (2019).

Today, seismic acquisitions are done with recording systems which can simultaneously record seismic vibrations on several hundreds of sensors. The distance between two adjacent sensors must be chosen small enough to have correctly sampled data and avoid any phenomenon of spatial aliasing. Consequently, the different types of waves are correctly recorded, and the same seismic record can be used whatever the seismic method.

## Refraction seismic method

Today, the refraction method is a quick reconnaissance-mapping tool for delineating near-surface velocity structures. It requires only the measurement of arrival times of first arrival waves (direct and refracted waves) to provide a geologic model while the reflection methods require a complete processing of the recorded wavefield. Picking of first arrivals is much easier than identifying and picking of other events.

Seismic refraction is currently used in civil engineering and hydrogeology for objective depths less than 300 m (Mari et al., 1997). The method is particularly suited for the following studies:

In civil engineering for:

- preliminary studies for construction sites,
- determination of the near surface structures,
- rock mechanics (rippability, Poisson ratio),
- search for cavities.

In hydrogeology for:

- highlighting channels carved in the bed rock,
- highlighting fractured areas in the bed rock,
- measurement of the water table depth.

Refraction-based velocity estimation of the subsurface can be conventionally done by using well-known methods, such as the Hagedoorn's Plus-Minus method (1959) or the generalized reciprocal method (GRM) proposed by Palmer (1986), which gives simple models of the subsurface defined by refractors with simple geometry and mainly constant velocity distribution. The GRM method, widely used in refraction prospecting requires direct and reverse shots. It assumes that first-arrivals are only originated by critical refraction and lateral continuous refractors with relatively simple velocity distributions. It assumes small lateral variation and it is used to define refractors with simple geometry and mainly constant velocity distribution.

Picked times of direct and reverse shot points (Figures 2.22a and 2.22b) give access to the  $t$  plus ( $t^+$ ) and  $t$  minus ( $t^-$ ) curves which allow the computation of the refractor velocity analysis function, and the generalized time-depth or delay time, respectively.

The refractor velocity analysis function  $t_V$ , at position G (Figure 2.22c), is defined by the equation:

$$t_V = \frac{1}{2} t_G^- = \frac{1}{2} (t_{AY} - t_{BX} + t_{AB}) \quad (2.12)$$

This function is computed for each pair of forward and reverse arrival times,  $t_{AY}$  and  $t_{BX}$ , and the reciprocal time,  $t_{AB}$ . The value of the function  $t_V$  is referenced to G which is midway between X and Y, and it is plotted as a function of the distance AG. Considering a multi-layer model, the  $t_V$  curve is approximately a linear function (Figure 2.22d), the slope  $1/V_n'$  of which gives an apparent velocity  $V_n'$  which approximates the velocity  $V_n$  of the refractor.

The generalized time-depth or Delay, at position G (Figure 2.22c), is defined by:

$$t_G = \frac{1}{2} t_G^+ = \frac{1}{2} (t_{AY} + t_{BX} - (t_{AB} + XY/V_n)) \quad (2.13)$$

The Plus-Minus method (a simplified version of the GRM method with  $XY = 0$ ) assumes that first-arrivals are only originated by critical refraction and laterally continuous refractors with relatively simple velocity distributions.

Figure 2.22 is an example of a refraction survey. The refraction line is rectilinear. In the acquisition of data, a 48-channel recorder was used. An explosive source (25 g) was detonated and a single geophone (10 Hz) per trace was deployed. Such a source makes it easy to identify and pick first arrivals. The distance between two adjacent geophones was 5 m. A direct shot and a reverse shot were recorded (Figures 2.22a and 2.22b). To obtain the velocity of the refractor (top of the reservoir) and its depth, the Plus– Minus method has been used. It requires recordings where geophones are aligned with shot points. The arrival times of the direct and refracted waves have been picked on the two in line shots. The picked times from the in-line shots (direct and reverse) have been used to compute the  $t$  plus and minus curves to obtain the velocity  $V_2$  of the refractor and the generalized time-depth curve. The  $t$  minus curve (Figure 2.22d) can be approximated by a straight line, the slope of which gives the velocity of the refractor which was found to be 3350 m/s. The slope of the direct wave gives the velocity  $V_1$  of the medium situated above the refractor. The medium situated above the refractor is defined as the weathering zone (Wz). Its velocity was found to be 850 m/s. The generalized time-depth, also called Delay time, shows the shape in time of the refractor (Figure 2.22d).

The University of Poitiers (France) has developed a Hydrogeological Experimental Site (HES, Figure 2.23a) for the sole purpose of providing facilities to perform long-term monitoring and experiments for a better understanding of fluid flow and transfers in fractured rocks (Bourbiaux et al., 2007).

Due to the limitations of the area, the length of the seismic line could not exceed 250 m in the in-line direction. In the crossline direction, the extension of the area does not exceed 300 m. As a result, 20 receiver lines have been implemented, with a 15 m distance between adjacent lines. Figure 2.23b shows the map locating the seismic lines. In the acquisition of data, a 48-channel recorder was used. An explosive source (25 g) was detonated and a single geophone (10 Hz) per trace was deployed. Such a source makes it easy to identify and pick first arrivals. A 5 m distance between two adjacent geophones was selected to avoid any spatial aliasing.

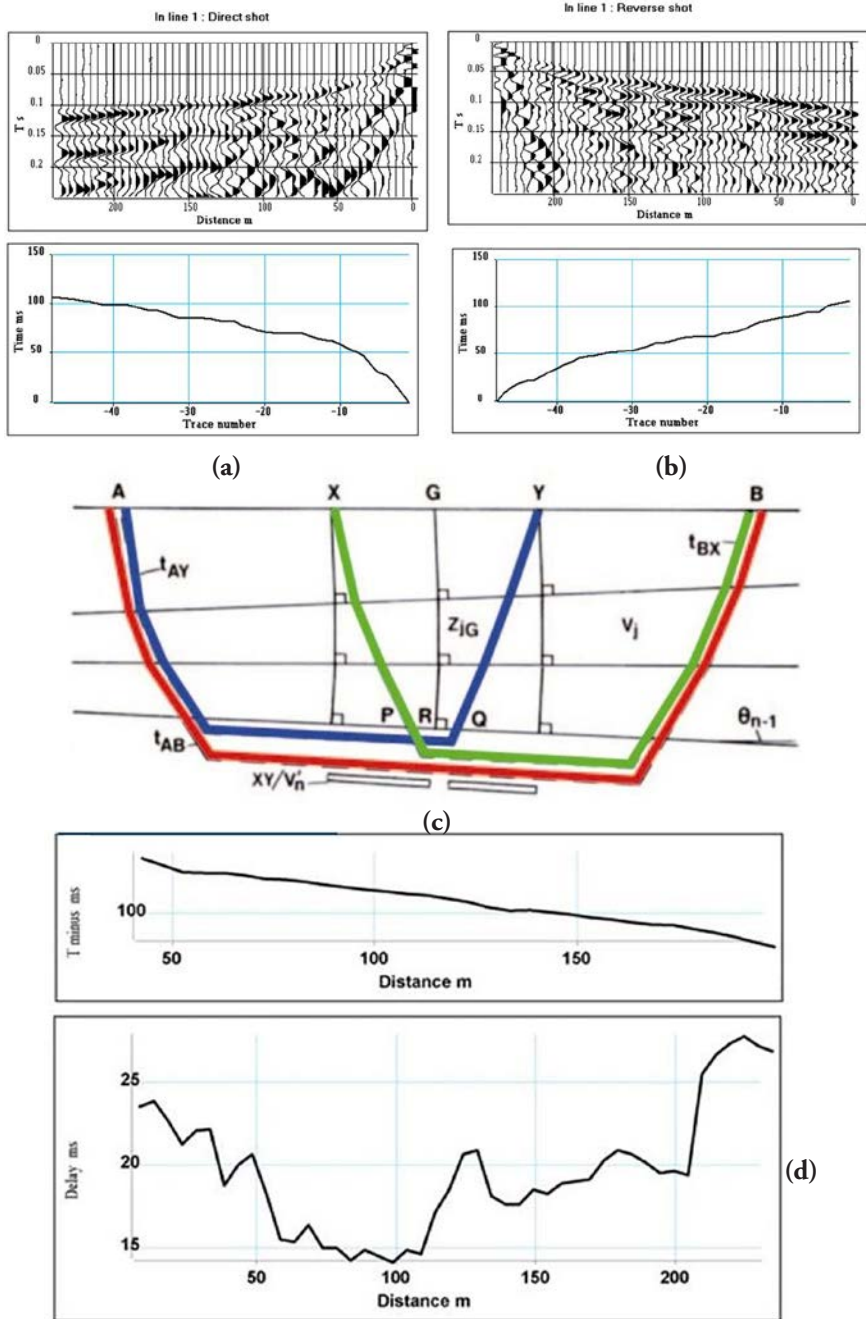
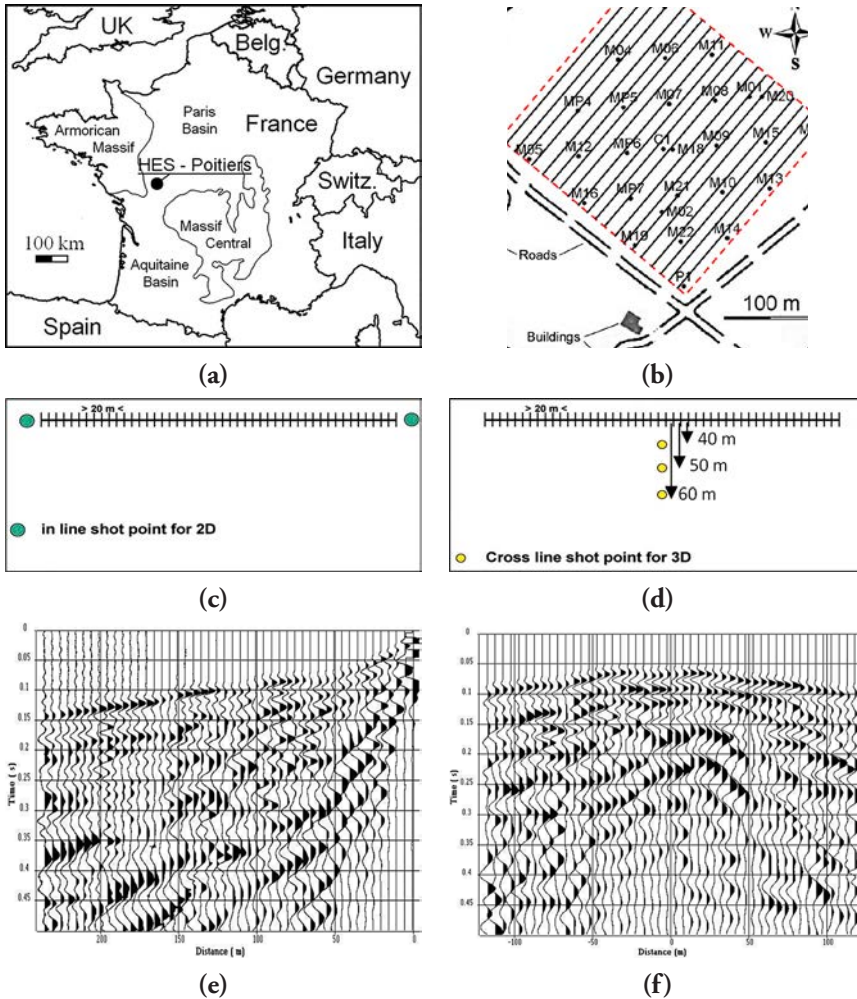


Figure 2.22 GRM method. (a) and (b) Direct and reverse shots with first arrival picked times, (c) refracted wave raypaths, (d)  $T$  minus and delay curves. After Mari and Mendes (2019).



**Figure 2.23** *Hydro-geological experimental site in Poitiers; (a) location map, (b) seismic line implementation. Seismic acquisition: (c) 2D in line acquisition geometry, (d) 3D cross line acquisition geometry, (e) example of in line shot gather, (f) example of cross line shot gather with 60 m of lateral offset. After Mari and Mendes (2019).*

A direct shot and a reverse shot were recorded per receiver line (Figure 2.23c). Three shot points in the crossline direction were fired at distances of 40, 50 and 60 m from the receiver line under consideration (Figure 2.23d). Figure 2.23e shows an example of an in line shot gather and Figure 2.23f a cross line shot gather with a lateral offset of 60 m. The picked times of the first seismic arrivals on all the shots (in line and cross lines shots), the  $W_z$  depth map and the velocity model obtained by the Plus–Minus method are input data for the inversion procedure, called tomography which is appropriate to obtain the velocity distribution in depth (Mendes, 2009; Mari and Mendes, 2012).

Figure 2.24 shows the velocity distribution at different depths (15 and 20 m), the 2500 m/s iso-velocity depth map, and a 3D block with vertical velocity sections located at a 0 m, 60 m, and 180 m distance in the crossline direction and velocity map located at 20 m in depth.

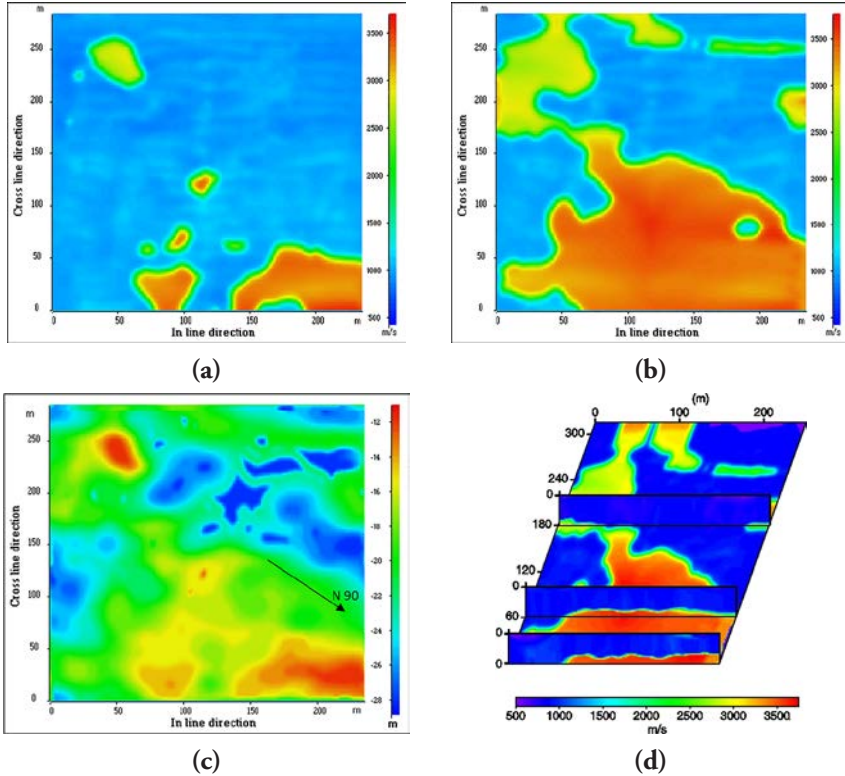


**Figure 2.24** Results of 3D tomography. (a) Velocity distribution at 15 m in depth, (b) velocity distribution at 20 m in depth, (c) 2500 m/s iso velocity depth map, (d) 3D block with vertical velocity sections located at a 0 m, 60 m, and 180 m distance in the crossline direction and velocity map located at 20 m in depth. After Mari and Mendes (2019).

### Reflection seismic method

Seismic reflection is the most widely used seismic technique which has the advantage of providing a picture of the subsurface in two or three dimensions (2D or 3D) in a regular grid (Figure 2.25).

3D data are now increasingly used for field development and production and not only as an exploration tool. Pre-planning of the 3D surveys became then

a fundamental step to ensure the 3D data quality will meet structural, stratigraphy and lithology requirements. Pre-planning includes the evaluation of both geophysical and non-geophysical parameters such as environment considerations, health and safety requirements, etc. Specific pre-planning tools (Cordson et al., 2000) were developed to estimate all characteristics of the future acquisition such as offset, fold and azimuth distributions, effects of surface obstacles, make up shots, etc. The pre-planning aims at defining the geological targets of the 3D with the associated geophysical parameters, design and costs.

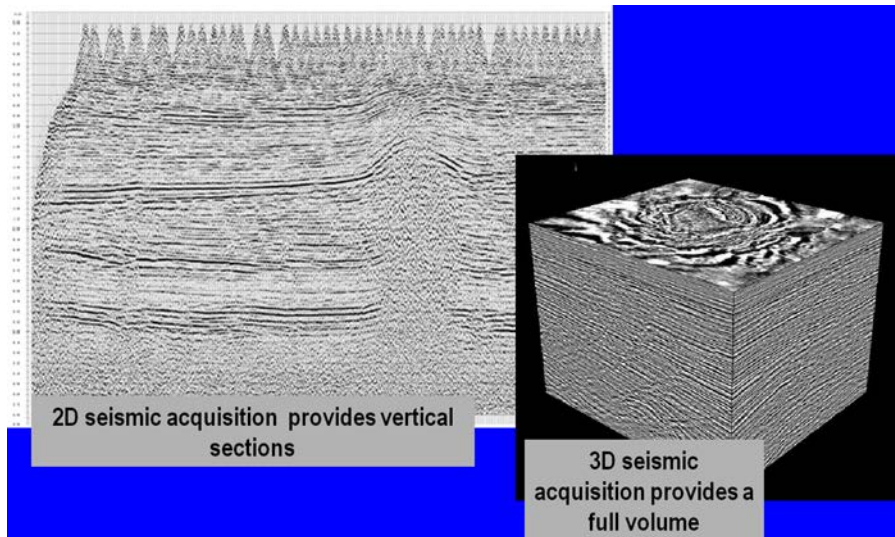


Figure 2.25 2D and 3D seismic imaging (after J. Meunier, 1998, 1999, IFP School course).

In 2D the image obtained after processing is a vertical seismic section. The horizontal axis of the section represents the geographical abscissas of subsurface points along the acquisition profile and the vertical axis represents the record time. The seismic events that appear on the records correspond to the arrivals of waves reflected at normal incidence on the seismic horizons. The seismic horizons correspond to discontinuities of acoustic impedance; their picks provide a structural image of the subsurface.

3D seismic acquisition provides a full volume consisting of a collection of sections parallel to each other. Surface seismic has vertical and horizontal resolutions measured in tens of meters with lateral investigation distances only limited by the size of the area investigated by the seismic surveys.

2D seismic acquisition is achieved with spreads which are either end-on also called off-end or split dip spread (Figure 2.26a). The individual shot element is defined by the source to the first receiver distance, the number of receivers and the distance between two adjacent receivers. A receiver can be a single sensor (geophone for

land acquisition) or an array of sensors. If the receiver is a single sensor, the interval between 2 receivers is of several meters, if it is an array, the interval is of several tens of meters. The maximum source-receiver offset to the far receiver is about the same as the maximum depth of the geological objective. The offset of the near receiver is chosen to minimize interference between ground roll (surface waves) and the reflection arrivals.

Acquisition is more complex for land 3D. Source and receiver lines are laid out to provide the most homogeneous coverage. The more conventional implementation is the cross-spread design with lines of sources perpendicular to lines of receivers (Figure 2.26b).

In 2D or 3D, the number of times a reflecting point in the sub surface is reached by different raypaths associated with different source-receiver pairs provide the fold of seismic coverage. Such a gathering, called Common Midpoint point (CMP), is theoretically valid for flat and horizontal geological models. In 2D, the distance between two CMP is equal to half the receiver interval. In 3D, the CMP is replaced by a cell or bin, the size of it being the product of half the source interval by half the receiver interval (Figure 2.26b). Traces contributing to the same CMP bin have irregularly distributed azimuths and offsets. Implementation is optimized to ensure the most regular azimuth and offset distribution possible. In the case of complex geological structures, the CMP is replaced by a common image gather.

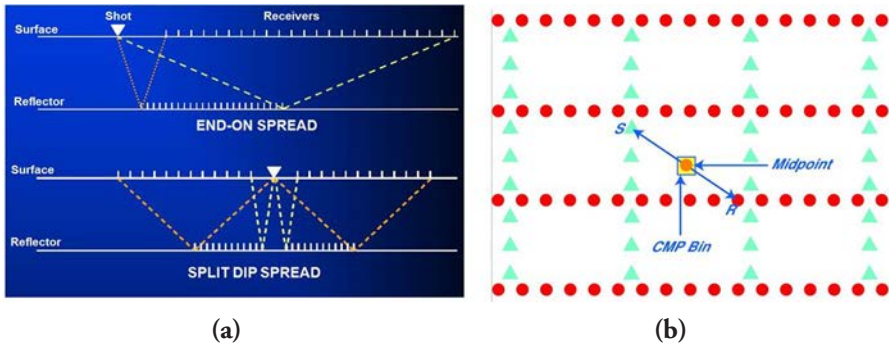


Figure 2.26 *Seismic spread; (a) in 2D, (b) 3D (lines of sources are indicated by green triangle, lines of receivers are indicated by red points). After Mari and Mendes (2019).*

The reader will find more information about acquisition and survey design in Galbraith (2000), Lansley (2000), Mayne (1962), Meunier and Gillot (2000), Meunier (2011), Monk and Yates (2000), Musser (2000), Vermeer and Hornman (2000), Chaouch and Mari (2006), about signal processing in Mari (2011), and about seismic processing in Yilmaz (1987), Robein (2003).

The classical approach to seismic processing can be summarized in two main steps.

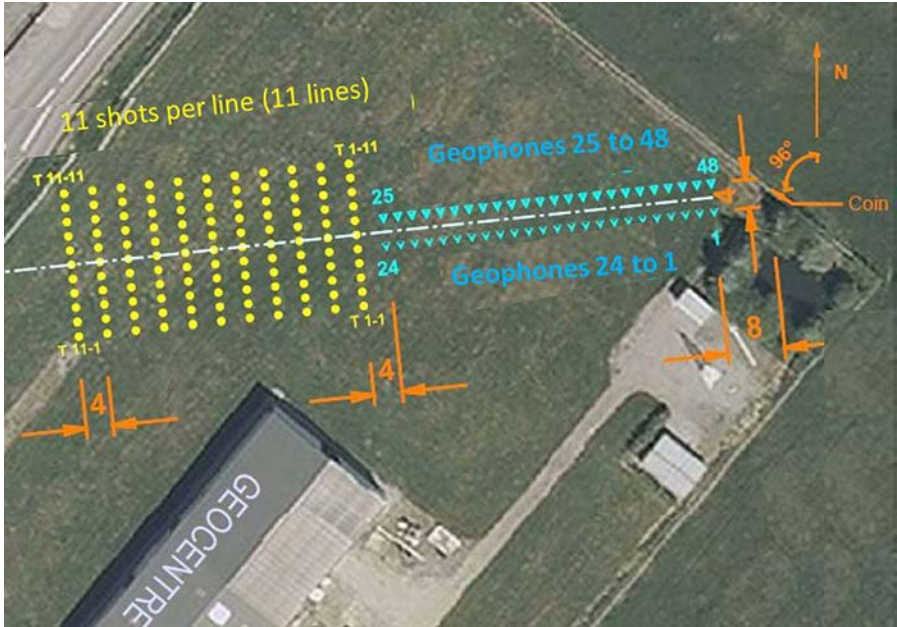
The first step includes pre-processing of the data and the application of static corrections. The purpose of pre-processing is to extract reflected waves from individual shots, by filtering out the waves which are not reflected waves: direct and refracted arrivals, surface waves, converted waves, and noise. The conventional wave separation methods are the F-K method and the SVD method (Singular Value Decomposition). Pre-processing is intended to compensate for amplitude losses related to propagation. Deconvolution operators are applied to improve resolution (as example spiking deconvolution), harmonize records by considering source efficiency variations and eventual disparities between receivers, and attenuate multiples (predictive deconvolution). Any deconvolution is sensitive to noise. Some specific processes, such as SVD decomposition, are used to enhance signal to noise ratio, by splitting the data in a noise space and a signal space. Static corrections, that are specific to land seismic, are intended to compensate for the effects of the weathered zone and topography. Records are then sorted in common mid-point gathers or common offset gathers.

The second processing step is the conversion of common mid-point gathers or common offset gathers into time or depth migrated seismic sections. This second step includes the determination of the velocity model, with the use of stacking velocity analyses, or tomography methods. The role of migration is to place events in their proper location and increase lateral resolution, by collapsing diffraction hyperbolas at their apex. Proper migration requires the definition of a coherent velocity field, which must be a field of actual geologic velocities in migrated positions. Determination of the velocity field is the most critical aspect of migration. The migration process can be done post or pre stack in time or depth. After migration, vertical and horizontal resolutions can be estimated by a quarter of the dominant wavelength of the seismic signal. An inversion process can be applied to post stack migrated sections to recover acoustic impedance distribution  $I_p$  ( $I_p = \rho V_p$  with  $\rho$  density and  $V_p$  P-wave velocity of the formation). An inversion process, which considers the amplitude variations versus offset of the reflected signal, can be applied to pre stack migrated sections to recover elastic impedance distributions  $I_p$  and  $I_s$  ( $I_p = \rho V_p$ ,  $I_s = \rho V_s$  with  $\rho$  density,  $V_p$  and  $V_s$  respectively P-wave and S-wave velocities of the formation).

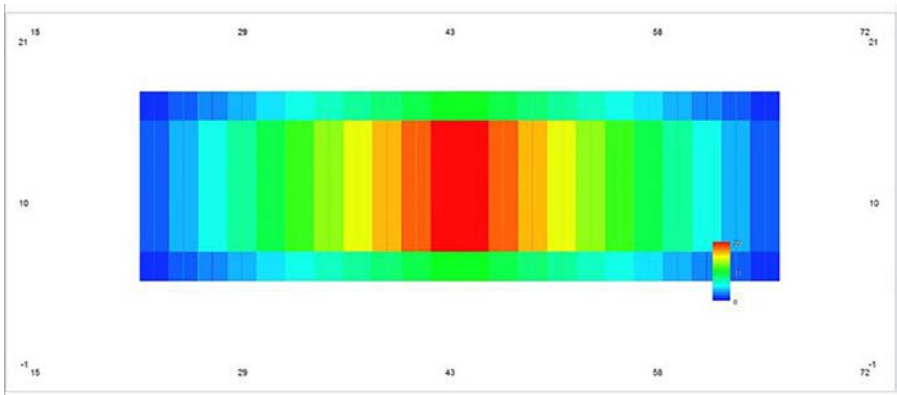
Figure 2.27 is an example of 3D seismic spread for near surface imaging.

The seismic spread is composed of a receiver spread and a source spread (Figure 2.27a). The receiver spread, displayed in green, is composed of 2 receiver lines. Receiver line direction is called the in-line direction. Distance between receiver lines is 4 m. There are 24 geophones per line. Distance between geophones is 2 m. The source spread, displayed in yellow, is composed of 11 source lines oriented perpendicularly to the receiver lines. 11 shots are fired per line. Distance between shots is 2 m. Distance between source lines is 4 m. The source lines and the receiver lines are oriented perpendicularly. The distance between receiver spread and source spread is 4 m. There is no overlap between the source and the receiver spread. Due to the geometry of acquisition, the geometry fold is symmetric. Figure 2.27b shows the fold variation. It varies from 0 to 22.

The processing has been done with the SPW software developed by Parallel Geoscience. The listening time is limited to 250 ms, the sampling time interval is 0.5 ms. Figure 2.28 is an example of shot point.



(a)



(b)

Figure 2.27 Near surface imaging. (a) 3D seismic spread, (b) fold variation. It varies from 0 to 22. In the display, the horizontal axis is the in-line direction. The vertical axis is the crossline direction. After Mari and Mendes (2019).

## Example of 3D shot point

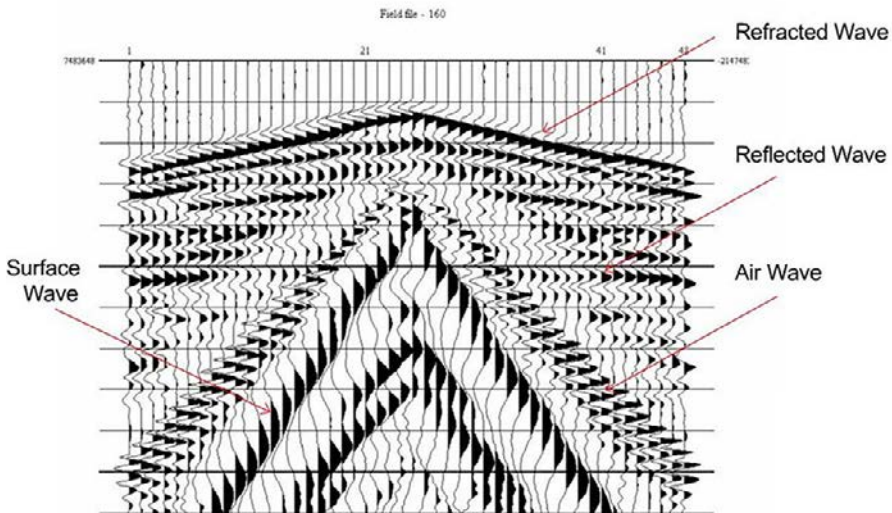
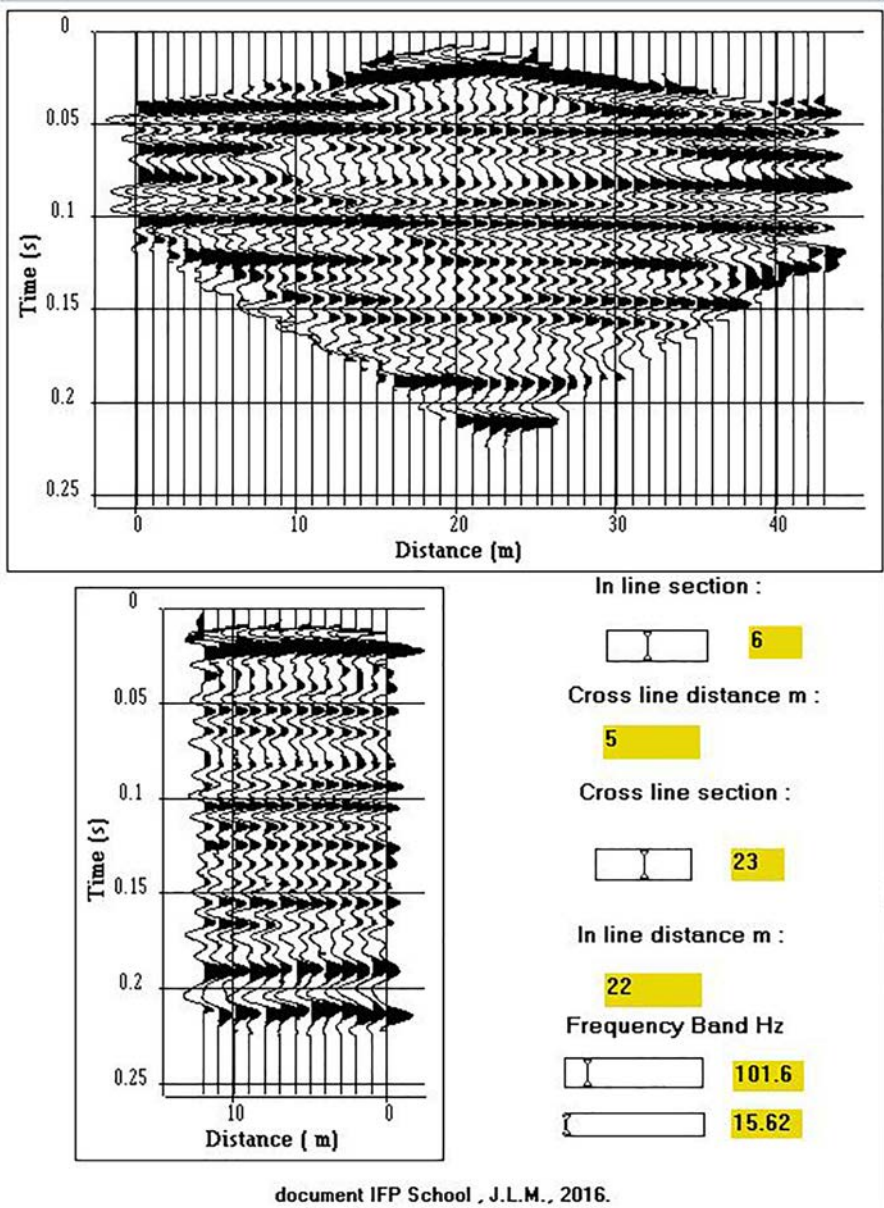


Figure 2.28 Example of a 3D shot point. You can see the refracted wave, the reflected wave, the air wave, and the surface wave. The air wave is aliased. After Mari and Mendes (2019).

The processing sequence of each shot includes amplitude recovery, deconvolution in the 15–150 Hz frequency bandwidth, tail mute, static corrections computed with the GRM method. The deconvolution is done to increase the resolution and attenuate the surface waves. A tail mute is used to kill the air waves and the surface waves. The static corrections are done to compensate the effects of the weathering zone. In the example, the 3D static corrections are very weak.

The data are sorted in Common Mid-Point gathers (CMP). Normal Move Out (NMO) corrections are done with a stacking velocity model obtained by velocity analysis. Surface consistent residual statics are computed to enhance the signal to noise ratio and preserve the high resolution of the data in the CMP stack procedure.

The 3D block is composed of 13 in-line sections 1 m apart. Each section is composed of 44 CMP points 1 m apart. Figure 2.29 shows an example of in-line and crossline seismic sections extracted from the 3D block. The two sections presented (section 6 in the in-line direction, and section 23 in the crossline direction) intersect in the middle of the 3D block. They have been filtered in the 15-100 Hz bandwidth, which provides an excellent signal-to-noise ratio.



document IFP School , J.L.M., 2016.

Figure 2.29 CMP stacked sections. The high-resolution 3D cube has revealed near surface seismic horizons between 50 and 200 ms. After Mari and Mendes (2019).

The safety of the Callovo-Oxfordian argillaceous rock (Cox) storage in the eastern Paris Basin is the major concern of the French National Radioactive Waste Management Agency (Andra). Extensive research on the clay sealing and healing properties as well as on the best way to characterize them on site have been conducted for over 20 years now. High resolution 3D seismic data have been acquired on a 30km<sup>2</sup> underground zone, known as a zone of interest for in-depth reconnaissance (ZIRA), in the vicinity of 3 exploration drillholes. Figure 2.30a shows a view of the geological model of the site and the location map of the 3D seismic survey. The seismic processing sequence is basically a pre stack time migration and an elastic inversion of the 3D block in time (Mari and Yven, 2019). Figures 2.30b to 2.30d shows the PSTM section, the  $I_p$  and  $I_s$  impedance sections obtained for the in-line IL405.

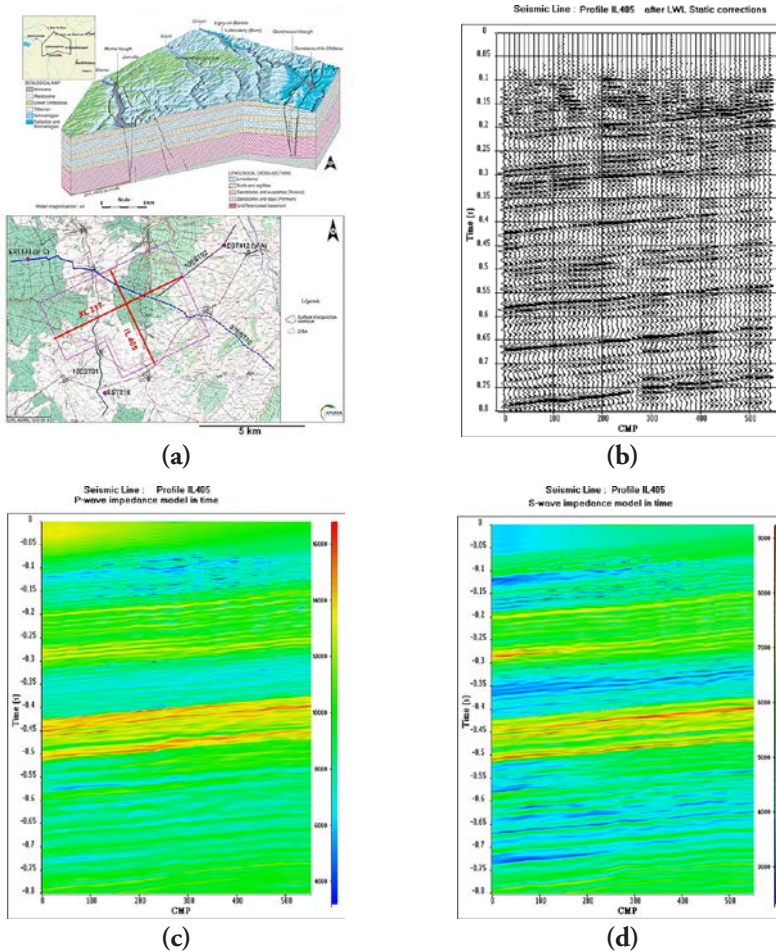


**Figure 2.30** 3D pre stack time migration and elastic inversion of the IL 405 profile. (a) Geological model and location map of the 3D survey, (b) PSTM sections, (c)  $I_p$  section, (d)  $I_s$  section. After Mari and Yven (2019), (Andra document).

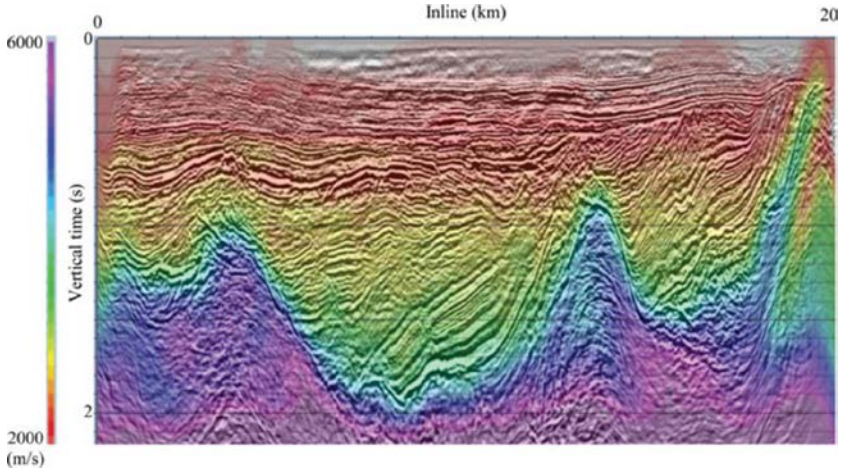


Figure 2.31 *Migrated section superimposed on the FWI velocity model, in a land example (Baeten et al., 2013).*

Full Waveform Inversion (FWI; Chauris, 2019) is a processing technique to derive quantitative images of the subsurface from seismic measurements. By quantitative, we mean for example P-wave velocity models expressed in m/s, and not only a structural image of the Earth as a classical stack section would provide. The principle is simple: the optimal model is the one for which the computed shot gathers are reproducing the observed shot data. More details on the formulation are provided in the literature (Louboutin et al., 2017, 2018). Beyond the apparent simplicity, the practical applicability of FWI is a difficult task. This is a non-linear process; the user should provide an initial model; the quality of the final inverted model depends on the reliability of the low frequency content of the observed data. A proper strategy should be established to iteratively determine the model (typically by successively introducing higher frequencies). One also needs to use the adequate wave equation to generate synthetic wave fields and associated shot gathers to mimic the physics of wave propagation. Finally, due to the limited data frequency band and limited data acquisition from the surface only, FWI does not necessarily lead to a unique solution. For example, if the user is interested in determining P-velocity and density models, there is an intrinsic trade-off between the two quantities, especially for short offset data. This is not specific to FWI: other imaging techniques suffer from the same effect, but this is visible in the FWI context as FWI is expected to provide quantitative results. Many FWI results have been published on real data in seismology, as well as at the exploration scales, at least in the marine case. The use of the technique on land with onshore data, however, has only been proven for a limited number of applications due to the presence of strongly energetic surface waves.

The example shown in Figure 2.31, in a land acquisition context (Inner Mongolia, China), is challenging due to the presence of highly energetic surface waves (Baeten et al., 2013; Brossier et al., 2009). Here, surface waves are filtered out in

a pre-processing step. The initial velocity is derived from travel time tomography and is mainly a 1D model (not represented here). Specific attention is paid to the preservation of energy in the dataset between 1.5 to 2 Hz: this is a crucial step in the FWI construction of the velocity model.

Acoustic FWI largely outperforms standard travel time tomography. More work is needed in future to consider higher frequencies and more complex physics.

The obtention of accurate velocity models is a key point for seismic imaging and for estimating mechanical and petrophysical properties of geological formations. Velocity models can be obtained by tomography, full waveform inversion or simultaneous joint inversion of seismic and non-seismic measurements (De Stefano et al., 2021). Simultaneous joint inversion of two sets of geophysical data (seismic and ERT) can lead to obtaining two consistent geophysical models (seismic velocity and resistivity) to characterize geological heterogeneities (Gallardo and Meju, 2004). Ceci et al. (2024a,b) shows an example of application of an integrated Multiphysics modelling workflow, including 3D MT, 2D seismic and 3D gravity data where the combined use of the data allows the reduction of the intrinsic uncertainty of each method and the obtention of a consistent seismic velocity field controlled by MT and gravity measurements.

Geothermal reservoirs can be explored and characterized using reflection seismic methods. The use of seismic methods remains a challenge for geothermal exploration due to a lack of reliable well and seismic data stemming from limited budgets and access restrictions when operating in urbanized areas.

Through the last few years, porosity and permeability in the Dogger and in the Triassic reservoirs of Paris basin have been a big challenge depending on their location, particularly under tertiary deposits. Nowadays, predicting the reservoir quality from seismic is one of current challenge to derisk the geothermal topics, west of Paris Basin, near to the “Sillon marneux” area. For decades, this subject has been a real challenge, as a dedicated 3D seismic survey was shot in the Villeperdue area in 90’s to study the capacity of seismic to highlight reservoir quality variations. The approach needs to strongly correlate well and seismic data. Because of the distance between wells with interesting information, the use of seismic needs to integrate several seismic lines. CDP Consulting developed through these past years several programs of regional lines combining old vintage lines to recognize an overall basin.

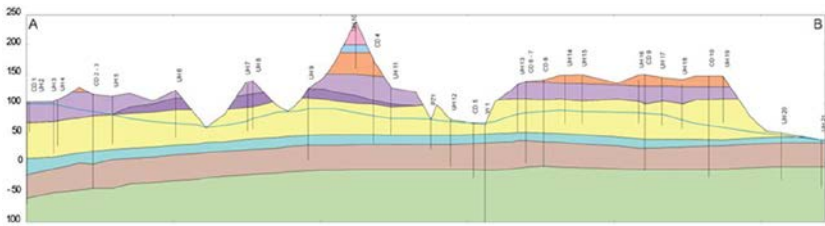
In this way, an innovative sequence must be developed to highlight the favourable reservoir areas, for many topics, particularly for geothermal derisking. This integrates an accurate 2D seismic sequence, possibility to provide seismic inversion on true amplitude PSTM.

To perform accurate reservoir study from seismic line, it is very important to avoid some key points:

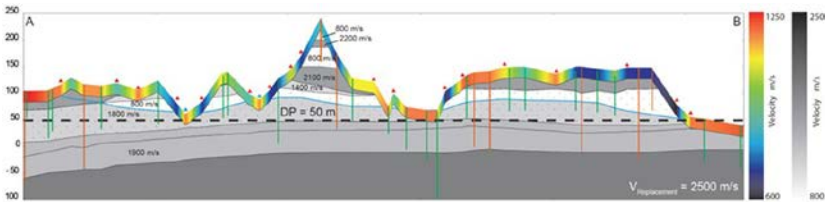
- avoid seismic artefact, particularly due to stack optimization (problem of statics and signal to noise ratio),
- avoid effects linked to the change of seismic parameters between lines from different seismic campaigns and introducing several difficulties in many steps of processing.

For seismic onshore data, and particularly in the centre part of Paris basin (mainly on Tertiary cover in the Ile de France), the quality of the seismic processing is particularly dependent on static corrections.

The Tertiary units have a thickness never exceeding 250 m. But the wide variability of seismic units (limestones, marls, evaporites, sands, clays) make the velocity variations very strong and dependant on the different aquifers. Many velocity inversions make totally forbidden the use of refraction statics to compute primary statics. Indeed, such use of refraction statics is totally unsuitable in this area and provides wrong structural shapes, cycle skips and loose of signal noise ratio. Such wrong artefact caused by refraction statics have induced in the past very strong artefacts and misunderstanding in reservoir characterization. They also lead in the past to drill a lot of wrong structures in time that have no reality in depth and cause the main failure of the oil and gas exploration in Paris Basin.



(a)



(b)

Figure 2.32 Example of geological modelling for static computation based on geological data (up holes). (a) Geological model, (b) geological velocity model (CDP Consulting document).

The only way to optimize the stack quality and get confidence in final seismic data needs to follow an accurate processing sequence. This needs to integrate a modelling of primary statics supported by a well constrained geological velocity model of the Tertiary units. CDP Consulting has developed a dedicated methodology for primary static computation based on Franck Hanot experience and widely discussed in many publications (Hanot, 1992; Hanot et al. 2012; Miquelis et al., 2016, 2019; Nosjean et al, 2017). Consequently, the pitfalls induced by static problem can be solved and need to be integrated in derisking of geothermal exploration (depth/temperature well design and reservoir characterization).

Figure 2.32 is an example of geological modelling for static computation based on geological data (up holes). The methodology is particularly efficient when the merge of seismic data with different parameters is strong, and when the quality of refraction is very poor as in Fontainebleau sands area or noisy locations in densely populated areas. A particular attention must be also to tackle the noise effect depending on the location and phenomena of signal absorption due to thick deposit of dry sands (west part of Paris basin). Figure 2.33 shows the effects of static corrections on a vintage line of a seismic campaign “Paris Ile de France” (1986). Figure 2.33a shows the line processed with conventional refraction static corrections (paragraph 2.4.1) and highlights the strong difficulty to stack below the Fontainebleau sands (central part of the figure). Figure 2.33b shows the same line processed with the CDP Consulting methodology for the primary statics. One can notice a good continuity of the seismic horizons below the Fontainebleau sands, sustaining a good reservoir quality approach.

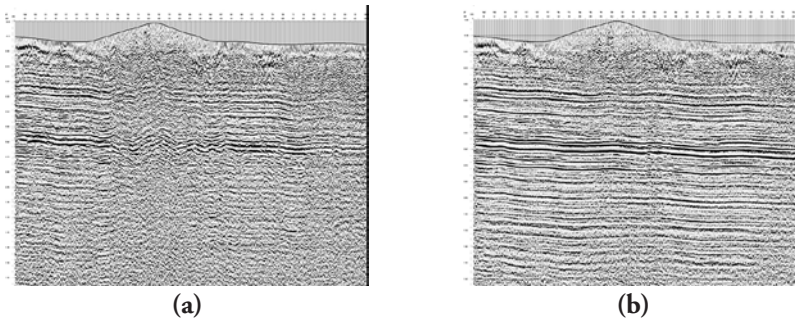


**Figure 2.33** *Effect of static corrections on the seismic stack (CDP Consulting document). (a) Conventional static method, (b) CDP Consulting method.*

In Paris Basin, static problems due to the chalk diagenesis, already described in 1961 by Millouet, is superposing to the static problems induced by tertiary deposits. In the same way than the tertiary deposits, the chalk effects could lead to strong artefacts of dogger reservoir imagery. The problems are particularly difficult to master because they are very often wider than the seismic line. The chalk problem needs to be accurately considered for geothermal exploration in sensitive place of Paris Basin, particularly under tertiary deposits (Hanot et al., 2012; Miquelis et al., 2016).

After having solved individual static problem and stack quality of individual line, producing regional line in true amplitude processing needs to follow a very detailed specific sequence including homogenous static modelling over the whole area, and a very specific approach in terms of geometry, noise removal, velocity picking and migration parameter. Once this very specific workflow is successful, extended regional lines could be used for the seismic reservoir quality quantification, notably for geothermal energy.

Figure 2.34 is an example of a regional line of more than 100 km in true amplitude PSTM processing composed of 12 vintage lines belonging to 8 seismic campaigns with different parameters (sweep, number of vibrators, distance between shots, distance between seismic traces, geophone filtering, etc.).

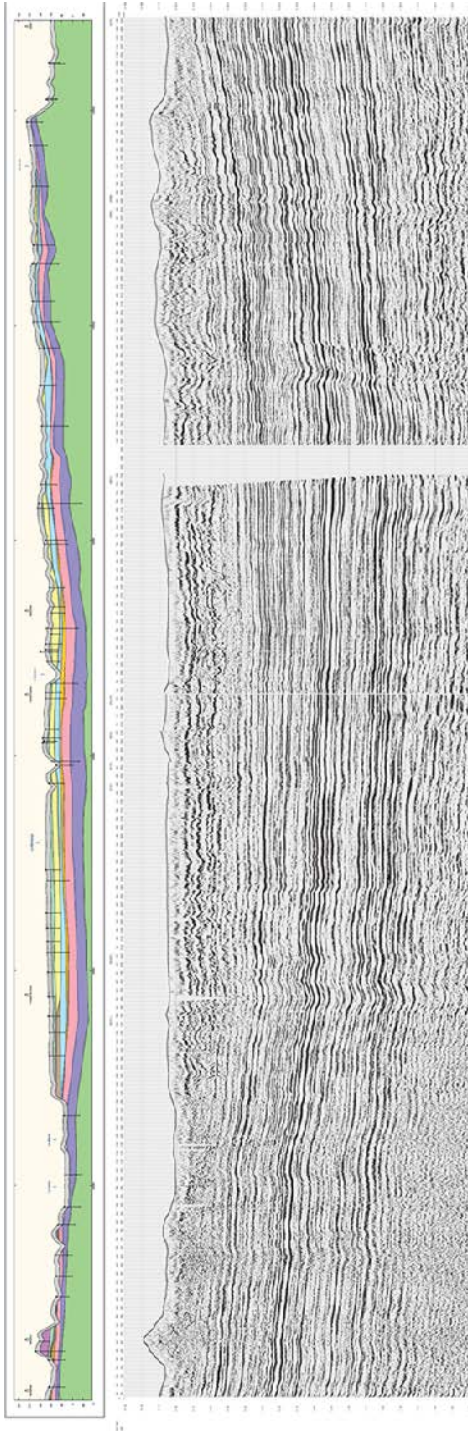


**Figure 2.34** Example of regional line (CDP Consulting document). The line is composed by the merge of 12 individual seismic line belonging to 8 different seismic campaigns and resulting in a homogenous Prestack time Migration stack section in true amplitude processing, and that could be then integrated in an advanced reservoir quantification approach allowed by the numerous wells crossing this line. The regional line is here superposed to the geological model of Tertiary deposits used for static corrections.

The recent development of advanced deep neural networks (DNNs) has opened the door to a new viable approach for directly estimating reservoir properties from seismic data (Formento et al., 2021). Although this kind of neural network requires a large amount of labelled data to be trained, only a limited amount of real well data is required as synthetic data can be used to augment the training set. Recently introduced theory-guided techniques based on rock physics models can help generate a large training set of pseudo-logs, representative of geologic variations, used to feed the DNN for a prediction of petrophysical properties of geological formations from full stack seismic profiles (Formento et al., 2021).

The methodology was successfully applied to improve the understanding of the potential for deep geothermal energy in the south of the Paris Basin (Souvannavong et al., 2024). The available seismic data are limited to 600 km of old 2D lines acquired between 1970 and 1990 and 10 old wells which had an available set of Caliper, Gamma Ray (GR), compressional sonic (DTP), density (RHOB), neutron (NPHI) and resistivity logs. The old seismic lines were reprocessed. More than 800 pseudo wells were generated to account for possible geological changes within the 3 reservoir units (Oxfordian, Dogger and Trias), allowing to have a large training set to feed the deep neural network, for a better prediction of total porosity (PHIT) and volume of clays (VCL) from full stack seismic. Figure 2.35a shows a seismic line passing through one of the wells with color-coded reservoir intervals (blue for Oxfordian, purple for Dogger and red for Trias). The estimated PHIT and VCL sections are shown in Figures 2.35b and 2.35c. Figure 2.35d shows the match between the recorded and synthetic seismic traces. On this figure, from left to right: the AI log is displayed in grey to show the acoustic contrast between layers. Then the comparison between the synthetic (black) and recorded seismic trace (red) shows a satisfactory match within the Oxfordian and Dogger intervals but a relatively poor one for the Trias where seismic signal-to-noise ratio (S/N) is lower. Figure 2.35e shows the match between the estimated attributes and the well logs. The predicted attributes (red traces) match well to the log data in general. In the Oxfordian interval, the predicted porosity correctly captures the layer with high porosity at the top of the reservoir (blue arrow on Figure 2.35e). This study illustrates how rock physics-guided deep neural networks were used as a practical alternative to derive accurate total porosity and volume of clay attributes for two carbonate reservoirs (Oxfordian and Dogger) and a clastic reservoir (Trias) directly from full-stack seismic and limited well data (Souvannavong et al., 2024).

Reinsch et al. (2017) demonstrated that temperature influences seismic velocities significantly. Du et al. (2024) have studied the Influence of temperature on the velocity-porosity relationship, with laboratory measurements on geothermal core samples. Laboratory measurements have shown that P-wave velocity continually decreases with increasing temperature. This trend in seismic velocity with temperatures is related to microfractures. Using the temperature-dependent Kuster-Toksöz equation (Kuster, 1974), it is suggested that the presence of fluid and microfractures can reduce the effective elastic properties of rocks (Du et al., 2024).

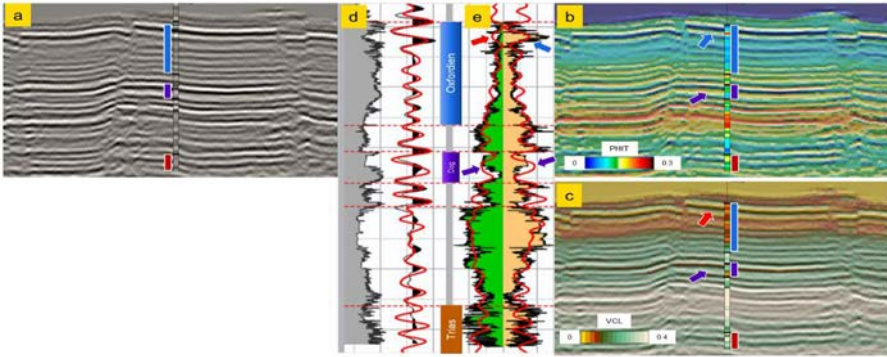


Figure 2.35 DNN results: (a) seismic section with well synthetic; (d) 1D QC at well location showing from left to right AI log (grey), well synthetic (black), seismic (red); (e) 1D QC at well location showing VCL log (green), PHIT log (orange) and corresponding inferred PHIT and VCL (red); (b) PHIT section and log; (c) VCL section and log (after Souvannavong et al., 2024).

By adopting the thermoacoustic wave equation, Yang et al. (2024) have proposed a full-waveform inversion method to directly invert temperature and velocity parameters using seismic data. The method has been checked on synthetic data sets. Figure 2.36 shows the exact or real velocity and temperature models, composed of 301 traces over 3 km (a trace every 10 m). Figure 2.37 shows the a priori or initial velocity and temperature models used as input data for the inversion process. Figure 2.38 shows the inversion results both for the complete models and for the trace 135, situated at the abscissa 1.35 km. The results are promising (comparison of inversion results with real models at trace 135). Further developments may enhance the method’s applicability and accuracy in geothermal reservoir assessment (Yang et al., 2024).

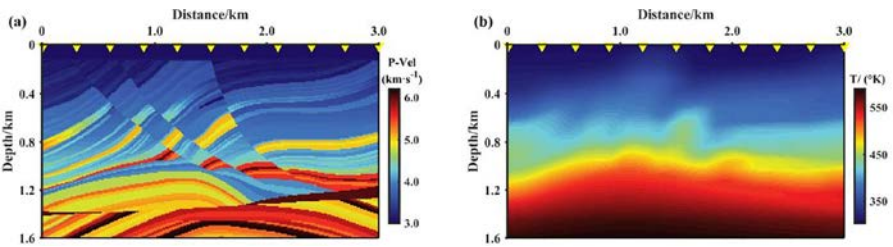


Figure 2.36 Velocity and temperature full waveform inversion (after Yang et al., 2024). Real models: velocity (a) and temperature (b).

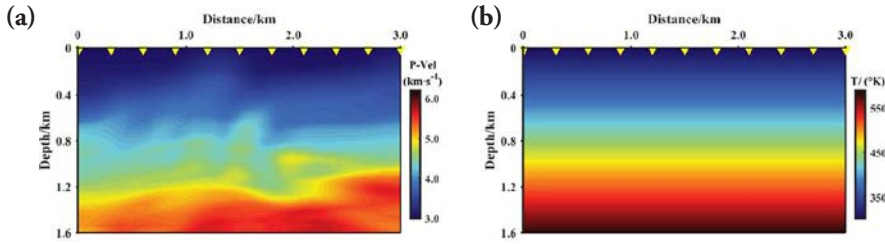


Figure 2.37 Velocity and temperature full waveform inversion (after Yang et al., 2024). Initial models: velocity (a) and temperature (b).

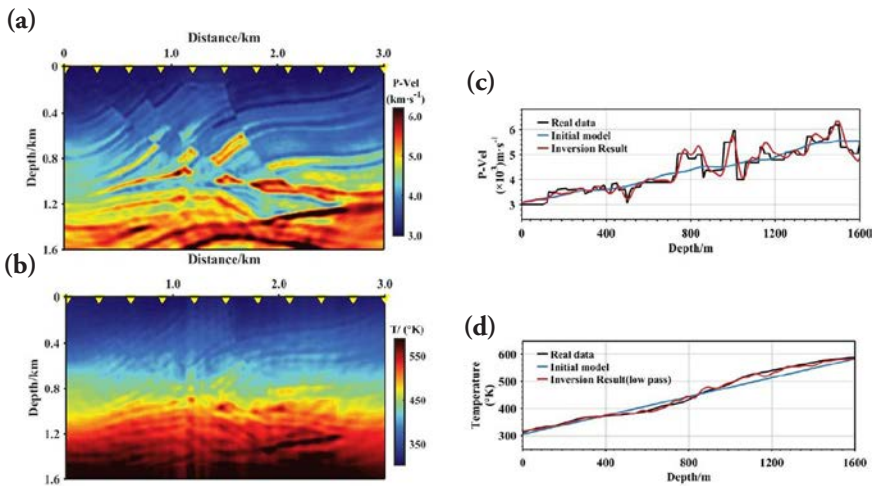


Figure 2.38 Velocity and temperature full waveform inversion (after Yang et al., 2024). Inversion results: velocity model (a) and temperature model (b), velocity at trace 135 (c) and temperature at trace 135 (d).

### Passive seismic method and MASW method

In addition to body waves (P- and S-waves) which propagate within the subsurface, a surface seismic source generates surface waves (Love and pseudo-Rayleigh waves). The seismic method based on the analysis of surface waves is called MASW (Multiple Analysis of Surface Waves). Surface waves, which are mainly sensitive to the shear modulus of the formation, propagate through the earth with their energy concentrated near to the surface. Their propagation velocity is frequency-dependent (dispersion). The degree of dispersion is a measure of seismic wave velocity as a function of depth and can be used to calculate the thickness of surface layers. Travelling only within a few seismic wavelengths from the surface of a solid, the lower the frequency of a surface wave, the deeper its penetration depth into the earth. Therefore, in the same medium, waves of different wavelengths affect different depths.

The processing classically applied to surface waves is based on spectral analysis and involves two steps. The first step is the construction of a dispersion curve (a plot of phase-velocity against frequency). The next step aims to obtain shear wave velocity (i.e. stiffness) profiles as a function of depth and horizontal position along the seismic survey line. The profiles are calculated using one of the two iterative purposes: matching the experimental dispersion curves to a theoretical curve derived from forward analytical modeling (usually 1D model) or an automatic least-squares approach.

A geophysical survey was carried out in Yellowstone National Park (USA), in the Obsidian Pool Thermal Area. The goal of the seismic survey carried out at this site was to study shallow hydrothermal systems, characterize fluid pathways and improve understanding of the depths at which steam separates from liquid water. The area is characterized by extensive CO<sub>2</sub> diffuse degassing and isolated thermal features with water temperatures between 21.9 and 84.0 °C. Seismic data were collected in July 2016 along a south-southwest–north-northeast transect, crossing a heat-flow anomaly between 50 and 120 m and a degassing feature between 86 and 96 m.

The equipment and parameters used in the seismic survey were:

- a 5.4 kg sledgehammer source swung onto a metal plate. The plate was hit five times at each position to increase the S/N,
- 10 Geometrics Geode seismographs, with 24-channels in each one,
- 4.5 Hz vertical component geophones spaced every 1 m, obtaining a 239 m long profile,
- 25 shot gathers recorded every 10 m,
- a sampling rate of 0.125 ms and a recording time of 0.75 s, to include the full surface wavefield.

In addition, a GPS survey and airborne LiDAR data collection were carried out to extract the topography.

The processing of the surface waves data was carried out using SWIP and readers can find supplementary information about this practical processing sequence in Pasquet and Bodet (2017).

After field data windowing for validation of the 1D model hypothesis, the seismic record from its original time–distance domain was transformed into the frequency–phase-velocity domain. This step results in a set of frequency–phase-velocity pairs specifying dispersion curves. The experimental dispersion curves were identified in the *f-k* domain and the location of maxima energy were picked. The dispersion curve is a diagram of phase velocity versus frequency and Figure 2.39 (Top) shows examples of single dispersion curves from shots located at 0 m, 10 m, 50 m, and 60 m. Through the utilization of multi-shot acquisition setups, the inversion of the sets of dispersion curves leads to Pseudo-2D section of average S-wave velocity model (Figure 2.39, bottom) The S-wave velocity model is characterized by velocities ranging between 50 and 600 m/s, with higher shallow velocity below the heat-flow anomaly observed between 50 and 120 m.

Passive seismic can be implemented for MASW. Passive seismic tomography or interferometry is a technique used to explore (image and monitor) the subsurface using ambient noise generated by natural or anthropogenic sources (Shapiro et al., 2005; Gouedard et al., 2008; Mordred et al., 2013).

Interferometry is based on calculating cross-correlations of the noise signal between pairs of seismic sensors. The noise is dominated by surface waves propagating in the shallow subsurface (Roux et al., 2011; Shapiro and Campillo, 2004). The calculation of cross-correlation between pair of sensors allows the extraction of the surface wave contained in the noise propagating between the sensors. As for MASW, dispersion curves of surface waves are computed and inverted to obtain distribution of S-wave velocity in the subsurface. In practice, several tens of sensors (vertical geophones) are deployed on the ground surface, the listening time can be of several hours or days, the analysis of the dispersion of surface waves is done in the low frequency domain (5–20 Hz).

Figure 2.40 shows an example of 3D shear velocity model obtained by passive seismic tomography, implemented for 3D imaging of the subsurface in a tunnel area (Saade et al., 2024). For the study, 199 surface sensors are used, covering the study area with a variable inter-sensor distance averaging about 20 m, and approximately 336 hours of measurements were recorded.

Passive seismic interferometry can be used for the monitoring of subsurface fluids – from shallow groundwater to native or storage gas reservoirs (Kremer et al., 2024)

Seismic interferometry has been used to investigate velocity variations, and subsequently strain sensitivities, related to a seismic swarm activity that occurred in 2013 along the Alto Tiberina low angle normal fault (Mikhael et al., 2024). Through an optimization procedure based on synthetic modeling to separate the non-tectonic from the tectonic induced velocity variations, a significant velocity variation in response to small strain perturbations has been unraveled. The deduced strain sensitivity value is comparable to values observed in volcanic settings suggesting the presence of pressurized fluids at depth (Mikhael, 2024). The same approach could be applied in similar contexts where fluids are involved including the monitoring of geothermal systems.

In the Eastern Vienna array, a seismic ambient noise survey was conducted for geothermal exploration (Esteve et al., 2024). A reservoir-scale 3-D shear velocity model of the central Vienna basin was obtained by passive seismic interferometry using recordings of ambient seismic noise. 100 seismic nodes were deployed for a duration of 6 weeks during the summer 2023. It has been shown that the location of the Markgrafneuseidl fault is highlighted by a strong velocity contrast in the 2D Love wave group-velocity maps at periods shorter than 3s. The 3D shear-wave velocity model shows a basin shape structure, which is interpreted to be the seismic signature of the Schwechat depression, the main target for geothermal exploration in Vienna (Esteve et al., 2024). Ambient Noise Tomography can support the growth of geothermal sector by providing reliable and affordable exploration methods. This can improve understanding of the subsurface and help reduce drilling uncertainty (Esteve et al., 2024).

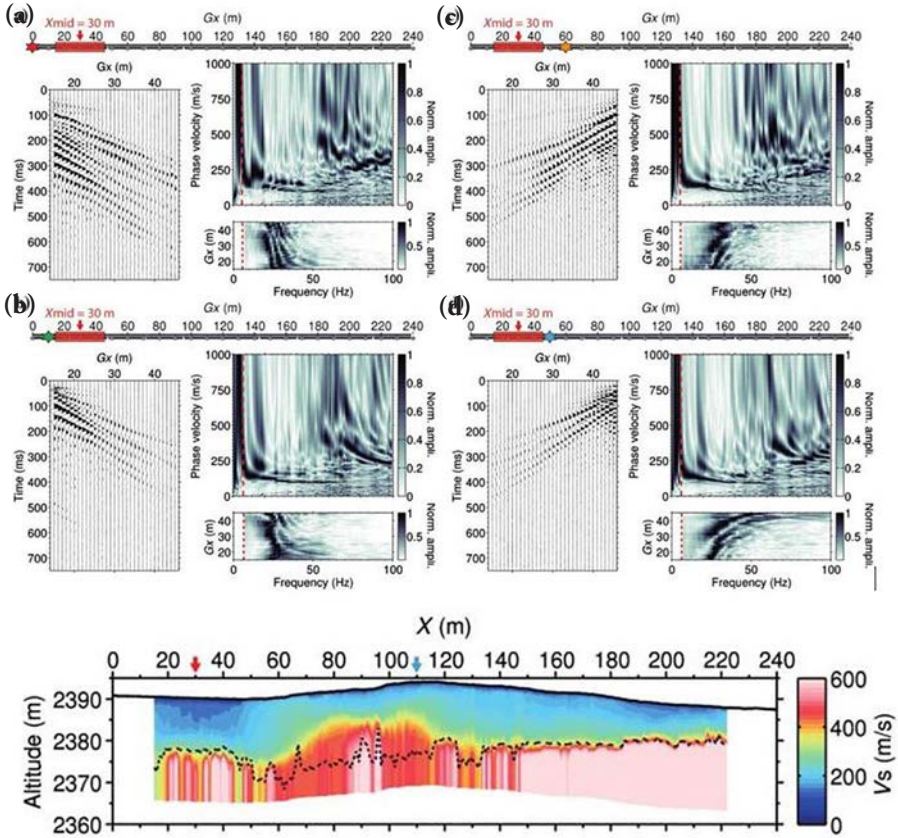


Figure 2.39 Example of MASW (after Pasquet and Bodet, 2017). Top: Extraction of single dispersion images for a 31-trace window centered at  $X_{mid} = 30$  m, using shots located at (a) 0 m, (b) 10 m, (c) 50 m, and (d) 60 m. On each inset, windowed shot gathers are on the left, corresponding spectrograms are at the bottom right, and computed dispersion images are at the top right. The dashed red lines on the spectrograms and dispersion images correspond to automatic low-cut frequencies defined from the spectrogram amplitude. Bottom: pseudo-2D section of average S-wave velocity model computed from accepted models at each  $X_{mid}$  position along the line. The dashed black line corresponds to the depth of investigation estimated with an S-wave velocity model standard deviation threshold of 150 m/s. The topography extracted from airborne LiDAR data is represented with a solid black line.

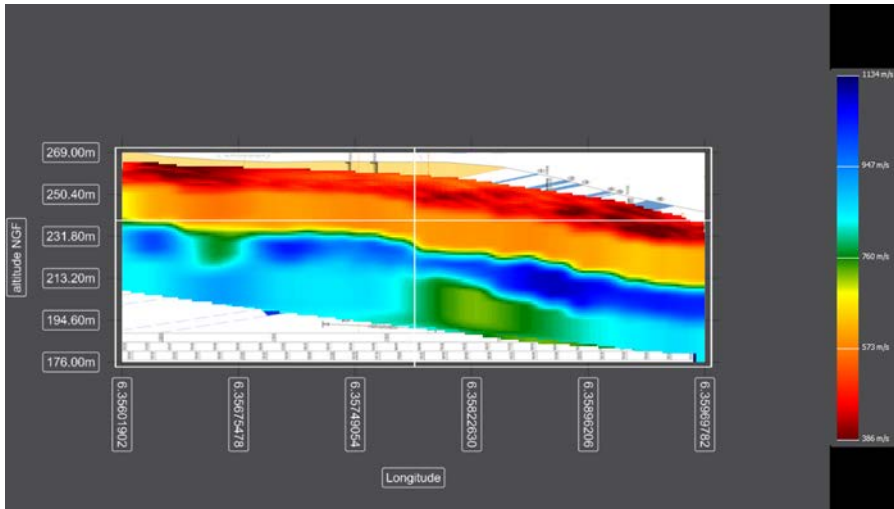


Figure 2.40 3D shear velocity model obtained with surface data (Saade et al., 2024).

## Conclusion

In conclusion, we have introduced the physical properties of rocks and pore spaces, followed by a review of geophysical methods and their field applications, notably for geothermal energy. These methods play a crucial role in building 2D or 3D subsurface models:

- gravity and gravity-gradiometry are sensitive to density variations,
- magnetic methods respond to rock magnetization properties, including magnetic susceptibility and remanence,
- electrical and electromagnetic (EM) methods capture resistivity variations,
- seismic methods are influenced by both velocity and density variations.

The selection of a geophysical method must be guided by the specific contrasts in petrophysical properties best suited to detecting the desired anomalies. Additionally, acquisition parameters need to be carefully chosen to target the appropriate depth, and both vertical and horizontal resolutions must be evaluated to ensure the method's suitability for identifying anomalies of a given size.

In many cases, combining multiple geophysical methods can improve the recovery of several physical rock properties simultaneously or enhance the capabilities of one method through the complementary strengths of another. For instance, the resolution of EM methods can be significantly enhanced through the integration of seismic methods (Alvarez et al., 2017).

Processing these data often involves simultaneous or joint inversion techniques, such as:

- refraction tomography combined with electrical resistivity tomography (ERT),
- acoustic impedance inversion paired with controlled-source EM (CSEM), magnetotelluric (MT), or deep ERT.

In near-surface studies, multiple methods can be used together to produce a more detailed geological model. For example, combining P-wave refraction tomography with MASW provides both P-wave and S-wave distributions, allowing for the computation of mechanical parameters such as Poisson's ratio (Pasquet and Bodet, 2017).

For deeper targets, seismic reflection methods, which provide both structural and petrophysical information about a reservoir, can be combined with CSEM to detect the presence of hydrocarbons (Alvarez et al., 2017). However, it is essential to calibrate surface geophysical results with borehole measurements, including well log and borehole seismic data.

Passive methods, being less invasive and cost-effective, are valuable tools. When combined, passive seismic, MT, and gradiometry can yield a shear velocity model, resistivity distribution with depth, and insights into bedrock location and fault structures. Passive techniques can also identify specific areas for more detailed active seismic surveys and extend coverage where conventional seismic methods are impractical.

Overall, the integration of multiple geophysical methods enhances subsurface imaging and offers more reliable insights, enabling more informed decision-making in geological exploration and reservoir characterization.

## References

*The writing of the chapter (text and relative figures) is mainly based on the following papers and books.*

Achenbach J.D. (1973) *Wave propagation in Elastic solid*, North Holland Publishing Company, 3<sup>rd</sup> Ed.

Alvarez P., Alvarez A., MacGregor L., Bolivar F., Keirstead R., Martin T. (2017) Reservoir properties prediction using controlled-source electromagnetic, pre-stack seismic, and well-log data: Case study in the Hoop Area, Barents Sea, Norway, *Interpretation* 5(2), 1-17, <https://doi.org/10.1190/INT-2016-0097.1>.

Archie G.E. (1942) The electrical resistivity log as an aid in determining some reservoir characteristics, *Petroleum Technology* 1, 55-67.

- Avram Y. (2017) MT for onshore oil discovery, from e-book devoted to electromagnetic methods in geophysics (<http://books.ifpenergiesnouvelles.fr/ebooks/ifpen-electro/>).
- Baeten G., De Maag J.W., Plessix R.-E., Klaassen R., Qureshi T., Kleemeyer M., Ten Kroode F., Rujie Z. (2013) The use of low frequencies in a full-waveform inversion and impedance inversion land seismic case study, *Geophysical Prospecting* 61(4), 701-711, <https://doi.org/10.1111/1365-2478.12010>.
- Bell R.E., Anderson R., Pratson L. (1997) Gravity gradiometry resurfaces, *The Leading Edge* 16, 55-59.
- Bourbiaux B., Callot J.P., Doligez B., Fleury M., Gaumet F., Guiton M., Lenormand R., Mari J.L., Pourpak H. (2007) Multi-Scale Characterization of a Heterogeneous Aquifer Through the Integration of Geological, Geophysical and Flow Data: A Case Study, *Oil and Gas Science and Technology, Rev. IFP* 62, 347-373.
- Brossier R., Operto S., Virieux J. (2009) Seismic imaging of complex on-shore structures by 2D elastic frequency-domain full-waveform inversion, *Geophysics* 74, WCC105–WCC118, <https://doi.org/10.1190/1.3215771>.
- Carrier A., Fischanger F., Gance J., Cocchiararo, Morelli G., Lupi M. (2019) Deep electrical resistivity tomography for the prospection of low – to medium – enthalpy geothermal resources, *Geophys. J. Int* 219, 2056-2072.
- Ceci F., Clementi M., De Luca L., Marin M., Wojdyla M., Sito Ł., McConvey P., Raine R., Clements S. (2024a) Multiphysics data acquisition and modelling in a highly urbanized area: a case study from Northern Ireland, 5<sup>th</sup> Global Energy Transition Conference & Exhibition, Rotterdam, Nederland.
- Ceci F., De Luca L., Sirtori A., Olaiz A., Garcia I., Torre J., Garcia A., Marro G., Ambrogio A. (2024b) Geothermal potential assessment via Multiphysics modelling: a case study from Gran Canaria, 5<sup>th</sup> Global Energy Transition Conference & Exhibition, Rotterdam, Nederland.
- Chaouch A., Mari J.L. (2006) 3-D land seismic surveys: Definition of Geophysical parameters, *Oil & Gas Science and Technology, Rev. IFP* 61(5), 611-630, <https://doi.org/10.2516/ogst:2006002>.
- Chapellier D. (2001a) Basic principles course, from On-line course of geophysics (<http://www-ig.unil.ch/>).
- Chapellier D. (2001b) Electrical methods, from On-line course of geophysics (<http://www-ig.unil.ch/>).
- Chauris H. (2019) “Full waveform inversion”, Chapter 5 in *Seismic imaging: a practical approach*, EDP Sciences, <https://www.edp-open.org/seismic-imaging-a-practical-approach>.

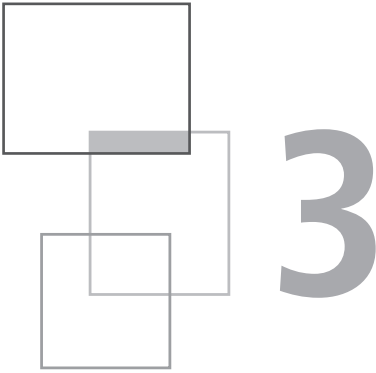
- Constable S., Parker R., Constable C. (1987) Occam's inversion: A practical algorithm for generating smooth models from electromagnetic sounding data, *Geophysics* 52, 289-300.
- Cordson A., Galbraith M., Peirce J. (2000) Planning land 3-D seismic surveys – SEG Series n° 9, Bob A. Hardage Ed.
- De Stefano M., Golfre' Andreasi F., Re S., Virgilio M., Snyder F.F. (2011) Multiple-domain, simultaneous joint inversion of geophysical data with application to subsalt imaging, *Geophysics* 76(3), R69-R80.
- Dobrin M.B., Savit C.H. (1988) *Introduction to Geophysical Prospecting*, 4<sup>th</sup> edition McGraw-Hill Book Co. 867 p.
- Du Q., Yasin Q., Sohail G.M., Majdanski M. (2024) A Study of the Influence of Temperature on the Velocity-Porosity Relationship in Geothermal Core Samples, 85<sup>th</sup> EAGE Annual Conference & Exhibition, Oslo, Norway.
- Esteve C., Lu Y., Bokelmann G., Gosselin J. (2024) Seismic ambient noise tomography for geothermal exploration: the Eastern Vienna Array, paper 1124, 85<sup>th</sup> EAGE Annual Conference & Exhibition, Oslo, Norway.
- Fabricius I.L., Baechle G., Eberli G.P., Weger R. (2007) Estimating permeability of carbonate rocks from porosity and Vp/Vs, *Geophysics* 72(5), 185-191, <https://doi.org/10.1190/1.2756081>.
- Fairhead J.D. (2015) *Advances in gravity and magnetic processing and interpretation*, EAGE publications, ISBN 978-94-6282-175-0.
- Faust L.Y. (1953) A velocity function including lithologic variation, *Geophysics* 18, 271-288.
- Formento J.L., Allo F., Coulon J.P., Reboul R., Capar L., Darnet M., Marc S., Issautier B., Stopin A. (2021) Unlocking geothermal reservoir seismic characterization with physics-guided deep neural networks, *2nd EAGE Conference on Global Energy Transition*, Extended Abstracts.
- Galbraith M. (2000) 3D seismic survey design: a solution, *First break* 18(5), 171-176.
- Gallardo L.A., Meju M.A. (2004) Joint two-dimensional DC resistivity and seismic travel time inversion with cross gradient constraints, *J. Geophysical Research Atmosphere* 109, B03311, <https://doi.org/10.1029/2003JB002716>.
- Girard J.F. (2017) MT for geothermal exploration, from e-book devoted to electromagnetic methods in geophysics, <http://books.ifpennergiesnouvelles.fr/ebooks/ifpen-electro/>.
- Gouedard P., et al. (2008) Cross-correlation of random fields: mathematical approach and applications, *Geophys. Prospect.*, 56(3), 375-393.
- Hagedoorn G.J. (1959) The Plus–Minus method of interpreting seismic refraction sections, *Geophysical Prospecting* 7, 158-182.

- Hanot F. (1992) Seismic applications of a Paris Basin shallow geology database, *First Break* 10(5), 175-188.
- Hanot F., Vicelli J., Miquelis F., Oliviero G. (2012) Diagenèse de la craie du bassin parisien. Hypothèse d'un biseau salé d'âge éocène. Couplage des données industrielles et géologiques, *Bulletin d'information Géologique du Bassin de Paris* 49(2), 6-24.
- Key K. (2016) A 2-D inversion code for controlled-source electromagnetic and magnetotelluric data, *Geophysical Journal International* 207, 571-588.
- Kozeny J. (1927) Über kapilläre Leitung des Wassers im Boden, *Sitzungsberichte der Wiener Akademie der Wissenschaften* 136, 271-306.
- Kremer T., Voisin C., Gaubert-Bastide T., Ars J.M., Mouquet P., Moinet F., Ferran J.C. (2024) The use of passive seismic interferometry for the monitoring of subsurface fluids – from shallow groundwater to native or storage gas reservoirs, Journées Scientifiques AGAP 2024, EDP Sciences, <https://doi.org/10.1051/e3sconf/202450402003>.
- Kuster G.T. (1974) Velocity and Attenuation of Seismic Waves in Two-Phase Media: Part I. Theoretical Formulations, *Geophysics* 39, 587.
- Lansley M. (2000) 3D seismic survey design: a solution, *First break* 18(5), 162-166.
- Lavergne M. (1986) *Seismic Methods*, Editions Technip, Paris.
- Louboutin M., Witte P., Lange M., Kukreja N., Luporini F., Gorman G., Herrmann F.J. (2017) Full-waveform inversion, Part 1: Forward modelling, *The Leading Edge* 36(12), 1033-1036, <https://doi.org/10.1190/tle36121033.1>.
- Louboutin M., Witte P., Lange M., Kukreja N., Luporini F., Gorman G., Herrmann F.J. (2018) Full-waveform inversion, Part 2: Adjoint modeling, *The Leading Edge* 37(1), 69–72, <https://doi.org/10.1190/tle37010069.1>.
- Mari J.L. (2011) *Signal processing for geologists and geophysicists*, IFP Energies Nouvelles ebook, <http://books.ifpenergiesnouvelles.fr/ebooks/signal-processing/>.
- Mari J.L., Guillemot D. (2012) Detection of porous and permeable formations: from laboratory measurements to seismic measurements, *Oil & Gas Science and Technology Rev. IFP Energies nouvelles* 64(4), 703-721, <https://doi.org/10.2516/ogst/2012009>.
- Mari J.L., Mendes M. (2012) High resolution 3D near surface imaging of fracture corridors and cavities by combining Plus-Minus method and refraction tomography, *Near Surface Geophysics* 10, <https://doi.org/10.3997/1873-0604.2011052>.
- Mari J.L., Mendes M. (2019) *Seismic imaging: a practical approach*, EDP Sciences, <https://www.edp-open.org/seismic-imaging-a-practical-approach>.

- Mari J.L., Vergniault C. (2018) *Well seismic surveying and acoustic logging*, EDP Sciences, <https://www.edp-open.org/well-seismic-surveying-and-acoustic-logging>.
- Mari J.L., Yven B. (2019), "Integrated seismic study", Chapter 7 in *Seismic imaging: a practical approach*, EDP Sciences, [https://www.edp-open.org/images/stories/books/contents/SeismicImaging/SeismicImaging\\_10.1051\\_978-2-7598-2351-2.c009.pdf](https://www.edp-open.org/images/stories/books/contents/SeismicImaging/SeismicImaging_10.1051_978-2-7598-2351-2.c009.pdf).
- Mari J.L., Glangeaud F., Coppens F. (1997) *Signal processing for geologists and geophysicists*, Technip Ed., Paris.
- Mari J.L., Peignard L., Andreis D., Girard J.F. (2017) *Electromagnetic methods in geophysics*, <http://books.ifpenergiesnouvelles.fr/ebooks/ifpen-electro/>.
- Mayne W.H. (1962) Common reflection point horizontal data stacking techniques, *Geophysics* 27, 927-938, <https://doi.org/10.1190/1.1439118>.
- Mendes M. (2009) A hybrid fast algorithm for first arrivals tomography, *Geophysical Prospecting* 57, 803-809, <https://doi.org/10.1111/j.1365-2478.2008.00755.x>.
- Meunier J. (1998) Land 3D acquisition geometry: what is the cost of ground roll?, 68<sup>th</sup> annual international meeting, SEG, expanded abstracts, 58-61.
- Meunier J. (1999) 3D geometry, velocity filtering and scattered noise, 69<sup>th</sup> annual international meeting, SEG, expanded abstracts, 1216-1219.
- Meunier J. (2011) *Seismic acquisition from Yesterday to Tomorrow*, distinguished instructor series, n° 14, SEG, ISBN 978-1-56080-281-5 (volume), ISBN 978-1-56080-086-06 (series).
- Meunier J., Gillot E. (2000) 3D seismic survey design: a solution, *First break* 18(5), 176-179.
- Mikhael N. (2024) Investigating seismic velocity changes for an in-depth monitoring of the crustal mechanical properties in the Apennines, Italy, PhD, University Grenoble Alpes.
- Mikhael N., Poli P., Garambois S. (2024) *Non-linear seismic velocity variations observed during a seismic swarm in the Alto Tiberina low angle normal fault from ambient noise correlation measurements*, *JGR Solid Earth*, <https://doi.org/10.1029/2023JB028232>.
- Millouet J. (1961) Problèmes posés à la sismique dans la région parisienne, *Geophysical prospecting* IX(1), 1-18.
- Miquelis F., Hanot F., Vicelli J., Kőrös M., Pöstyéni F. (2016) Geological modelling of static corrections for seismic processing, Example of Paris basin, France: New insight for onshore exploration, Petex.
- Miquelis F., Hanot F., Vicelli J., Picornell V. (2019) *Diagenèse de la Craie: application sismique*, RST Caen.

- Monk D., Yates M. (2000) 3D seismic survey design: a solution, *First break* 18(5), 180-183.
- Mordret A., Shapiro N.M., Singh S., Roux P., Barkved O.I. (2013) Helmholtz Tomography of ambient noise surface wave data to estimate Scholte wave phase velocity at Valhall Life of the Field, *Geophysics* 78(2), WA99-WA109. <https://doi.org/10.1190/geo2012-0303.1>.
- Morlier P., Sarda J.P. (1971) Atténuation des ondes élastiques dans les roches poreuses saturées, *Revue de l'Institut Français du Pétrole* 26(9), 731-755.
- Mortensen J., Engstrom F., Lind I. (1998) The relation among porosity, permeability, and specific surface of chalk from the Gorm field, Danish North Sea, *SPE Reservoir Evaluation & Engineering* 1, 245-251.
- Murphy C.A., Mumaw G.R. (2004) 3D Full Tensor Gradiometry: a high-resolution gravity measuring instrument resolving ambiguous geological interpretations, *ASEG Extended Abstracts* 1(1-4), <https://doi.org/10.1071/ASEG2004ab104>
- Musser J.A. (2000) 3D seismic survey design: a solution, *First break* 18(5), 166- 171.
- Nettleton L.L. (1939), Determination of density for the reduction of gravimeter observations, *Geophysics* 4, 176-183.
- Nosjean N., Hanot F., Gruffeille J.P., Miquelis F., 2017, Statics: from imaging to interpretation pitfalls and an efficient way to overcome them, *First Break* 35(1), 175-188.
- Palmer D. (1986) *Refraction seismic*, Geophysical Press, 13.
- Pasaribu A.H., Pratama A.B., Machrani M. (2024) Evaluating Geothermal Fluid Production Impact on Density Using Time-Lapse Microgravity in Awibengkok Field, 5<sup>th</sup> Global Energy Transition Conference & Exhibition, Rotterdam, Nederland.
- Pasquet S., Bodet L. (2017) SWIP: An integrated workflow for surface-wave dispersion inversion and profiling, *Geophysics* 82(6), WB47-WB61.
- Piolat L., Geraud Y., Revil A., Diraison M., Favier A., Cosme P., 2024, Quantifying geophysical electrical signatures in hydrothermal reservoirs, 5<sup>th</sup> Global Energy Transition Conference & Exhibition, Rotterdam. Nederland
- Quiblier J. (1997) *Propagation des ondes en géophysique et en géotechnique*, Modélisation par méthodes de Fourier, Editions Technip, Paris.
- Reinsch T., et al. (2017) Utilizing supercritical geothermal systems: a review of past ventures and ongoing research activities, *Geothermal Energy* 5(1), 16.
- Robein E. (2003) *Velocities, Time-Imaging and depth Imaging, in Reflection seismics*, Principles and Methods, EAGE Publications bv, ISBN 90-73781-28-0.
- Roux P., Roueff A., Wathelet M. (2011) The San Andreas Fault revisited through seismic-noise and surface-wave tomography, *Geophys. Res. Lett.* 38, L13319.

- Saade M., Robert S., Lempereur C., Grill M. (2024) Passive seismic tomography for 3D imaging of the subsurface in a tunnel area, Journées Scientifiques AGAP 2024, <https://doi.org/10.1051/e3sconf/202450402001>, EDP Sciences.
- Shapiro N.M., Campillo M. (2004) Emergence of broadband Rayleigh waves from correlations of the ambient seismic noise, *Geophys. Res. Letters* 31, L07614, <https://doi.org/10.1029/2004GL019491>.
- Shapiro N.M., Campillo M., Stehly L., Ritzwoller M. (2005) High Resolution Surface-Wave Tomography from Ambient Seismic Noise, *Science* 307, 1615-1618.
- Souvannavong V., Aziez Y., Allo F., Rathore R., Stopin A., Bordenave A., Issautier B., Beccaletto L. (2024) Deep geothermal reservoir characterization with rock physics guided DNN, 5<sup>th</sup> Global Energy Transition Conference & Exhibition, Rotterdam, Nederland.
- Vermeer G.J.O., Hornman K. (2000) Introduction to a 3D design problem, *First break* 18(5), 184-185.
- Wyllie M.R.J., Gregory A.R., Gardner L.W. (1956) Elastic wave velocities in heterogeneous and porous media, *Geophysics* 21, 41-70.
- Yang S., Wu G., Yang L., Zhang B., Jia Z. (2024) Velocity and temperature full waveform inversion from thermoacoustic equation based on L-S theory, 85<sup>th</sup> EAGE Annual Conference & Exhibition, Oslo, Norway.
- Yilmaz O. (1987) Seismic data processing, SEG, Tulsa.



# Borehole geophysical methods

J.L. Mari

---

Surface geophysical methods are stand-alone methods which enable the construction of a 2D or 3D geophysical model of the subsurface link to one or more physical parameters, such as resistivity for MT or EM methods, seismic wave velocities and density for seismic methods. Geological surveys associated with surface geophysical surveys lead to build a structural geological model to detect heterogeneities or tectonic features such fractures or faults. Such models are used to define the location of boreholes.

Drilling of a borehole gives geophysicists the opportunity to perform borehole geophysical measurements and record additional data.

Borehole geophysical methods give borehole measurements used to validate and calibrate geophysical models, to convert in depth geophysical models obtained in time (as example time migrated seismic sections in depth sections), to transform geophysical models in physical or petrophysical models. As example, seismic models in amplitude are converted into velocity models and then into porosity models. Borehole geophysical methods provide high-resolution, localized information on properties like lithology, porosity, and fluid content.

Borehole geophysical methods can be classified as conventional logging methods, borehole surface imaging methods, hydrogeological logging methods, full

waveform acoustic logging and borehole seismic methods. We present examples of some borehole geophysical methods and applications.

For more and detail information, we recommend reading specific books in well logging (Boyer and Mari, 1997; Serra and Serra, 2000; Chapellier, 2001a,b among others) and borehole seismic (Hardage, 1985, 1992; Mari et Vergnault, 2018 among others), as well as specific magazines, as “*The log analyst*”.

### 3.1 Conventional logging methods

The logging tools currently run are calipers, natural radioactivity tool (natural gamma ray GR), electric resistivity and electric conductivity tools (laterologs and induction) with shallow or large depth investigation, induced radioactivity tools (neutron and density), dipmeters and acoustic tools. The logs have a vertical and horizontal resolution of several tens of cm.

Well logs are recorded to identify the different geological formations crossed by a borehole. Using the response equations of logging tools and after correction for environmental effects, it is possible to obtain the physical parameters of a geological formation such as the resistivity  $R_t$  of the virgin zone, the neutron porosity  $\Phi_N$ , the slowness  $\Delta t$  (inverse of the propagation velocity), the density  $\rho_b$ .

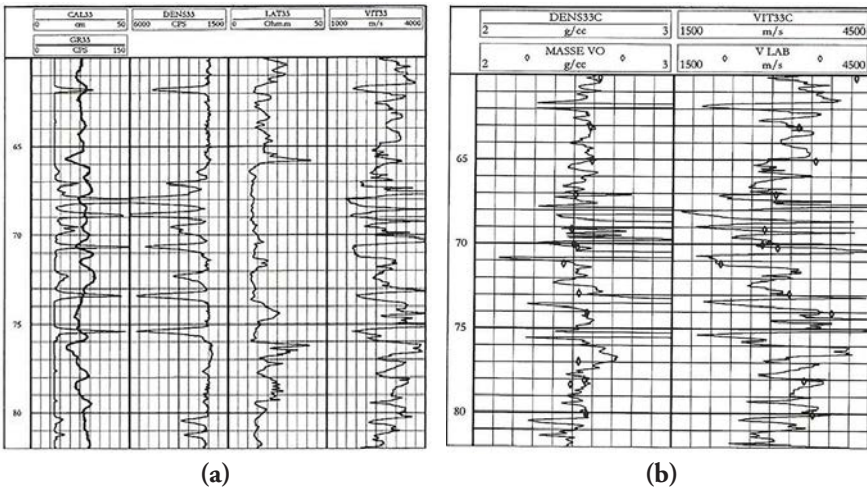


Figure 3.1 Example of logs recorded in an altered formation (after Chapellier, in Mari et al., 1999). (a) Caliper (CAL33), gamma ray (GR33), density (DENS33), Resistivity (laterolog LAT33), slowness  $\Delta t$  converted in velocity VIT33). (b) Comparison between core measurements and density and velocity logs after environmental corrections

Quick look or sophisticated quantitative interpretation methods (Boyer and Mari, 1997) based on relationships between measured physical parameters and petrophysical parameters are used to obtain petrophysical (such as porosity) and mechanical (such as Poisson's ratio) parameters of geological formations.

Figure 3.1 is an example of logs recorded in the molasse of the Swiss Plateau. The geological formation, constituted of argillaceous sandstone, is strongly altered.

The caliper shows numerous caved zones in shaly beds (Figure 3.1a) strongly marked on the density and velocity logs. After correcting the logs according to the caliper, the logs are not perfect, but the values are close to those obtained on cores (Figure 3.1b).

Archie (1942) has shown empirically that for water-saturated permeable formations, the relation between the true formation resistivity,  $R_t$ , and the resistivity,  $R_w$ , of the water impregnating the formation is given by:

$$R_t/R_w = F = \Phi^{-m} \quad (3.1)$$

where  $F$  is the "resistivity formation factor".  $\Phi$  is proportional to the formation porosity and  $m$  is a "cementation factor", that is a formation characteristic. An approximate value equal to 2 is generally adopted for the cementation factor.

Wyllie et al. (1956) has established a linear relationship between the slowness  $\Delta t$  and the porosity  $\Phi$  and shaliness  $V_{sh}$  of a water-saturated permeable formation:

$$\Delta t = (1 - \Phi - V_{sh})\Delta t_{ma} + V_{sh}\Delta t_{sh} + \Phi \cdot \Delta t_f \quad (3.2)$$

where  $ma$ ,  $sh$  and  $f$  represent respectively the matrix, the shales and the fluid.

The same relationships are used for the neutron porosity  $\Phi N$  and the density  $\rho_b$ .

$$\Phi N = (1 - \Phi - V_{sh})\Phi N_{ma} + V_{sh}\Phi N_{sh} + \Phi \cdot \Phi N_f \quad (3.3)$$

$$\rho_b = (1 - \Phi - V_{sh})\rho_{ma} + V_{sh}\rho_{sh} + \Phi \cdot \rho_f \quad (3.4)$$

Logs are also recorded to add constraints in the processing and interpretation of geophysical models.

The University of Poitiers (France) has developed a Hydrogeological Experimental Site (HES) for the sole purpose of providing facilities to perform long-term monitoring and experiments for a better understanding of fluid flow and transfers in fractured rocks (Bourbiaux et al., 2007). 35 boreholes, including two vertical and two inclined cored boreholes, were drilled on the site in two separate campaigns: 2002-2003 and 2004 (Figure 3.2a). All the boreholes are crossing completely the Dogger Aquifer (depth of boreholes = 125 m). A 3D survey has been designed to obtain a 3D interval velocity cube in depth (Mari and Porel, 2007). Figure 3.2b shows the resistivity log recorded in borehole M09 as well as the velocity distribution extracted from the 3D velocity block at the location of borehole M09.

Faust (1953) has established an empirical relationship between seismic velocity  $V$ , depth  $Z$ , and electrical resistivity measurements  $R_t$ . For a formation of a given lithology, the velocity  $V$  can be written as a function of the depth  $Z$  and resistivity  $R_t$  as follows:

$$V = C \cdot (Z \cdot R_t)^{1/b} \quad (3.5)$$

with:

- $V$  the P-wave velocity of the formation in m/s,
- $Z$  the depth in m,
- $R_t$  the electrical resistivity in  $\Omega \cdot m$ ,
- $C$  and  $b$  the coefficients associated with Faust's equation.

At each well where a long normal log has been recorded, an interval velocity log has been extracted from the 3D seismic interval velocity block. The two sets of data (resistivity and seismic velocity) have been combined to calibrate an empirical Faust's law, which has then been used as a local constraining function to transform the 3D pseudo-velocity block into a 3D pseudo-resistivity block. For each well, the two coefficients,  $C$  (constant coefficient) and  $b$  (power law exponent), of that empirical law were determined through a least-square minimization of the difference between the 3D-block-extracted seismic velocities and the velocities predicted from Faust's law using the long normal resistivity log data as input. The previous seismic-derived 3D resistivity block ( $R_t$ -seis) was converted into a 3D pseudo-porosity block, by using the Archie-law-derived formula (equation (3.1) with  $m = 2$ ). The results are shown in Figures 3.2c and 3.2d. Figure 3.2c shows the long normal resistivity log  $R_t$ , the resistivity log  $R_t$ -seis converted from seismic velocity log using Faust's law, the estimated seismic porosity log using Archie's law. Figure 3.2d shows porosity and velocity sections extracted from the 3D blocks, oriented South-East North-West, and passing close to borehole M09. The high porosity layer, observed on the porosity log at 87 m depth (Figure 3.2c) clearly appears on the porosity section in the 45–100 m interval distance (Figure 3.2d).

The example shows how long normal resistivity logs can be used as constraints to transform seismic velocity sections into seismic sections in porosity, using petrophysical equations established by Faust and Archie.

In addition to conventional logging tools, borehole wall imaging tools, such as formation micro scanner, high resolution acoustic or optical televiwers are currently run. The tools provide high resolution (several cm) oriented images of the borehole walls. They are used to detect dips, discontinuities, features such as fractures, to show diameter changes with open fractures and breakouts. They are also used to identify facies and perform stratigraphic interpretations (Gaillard et al., 2024).

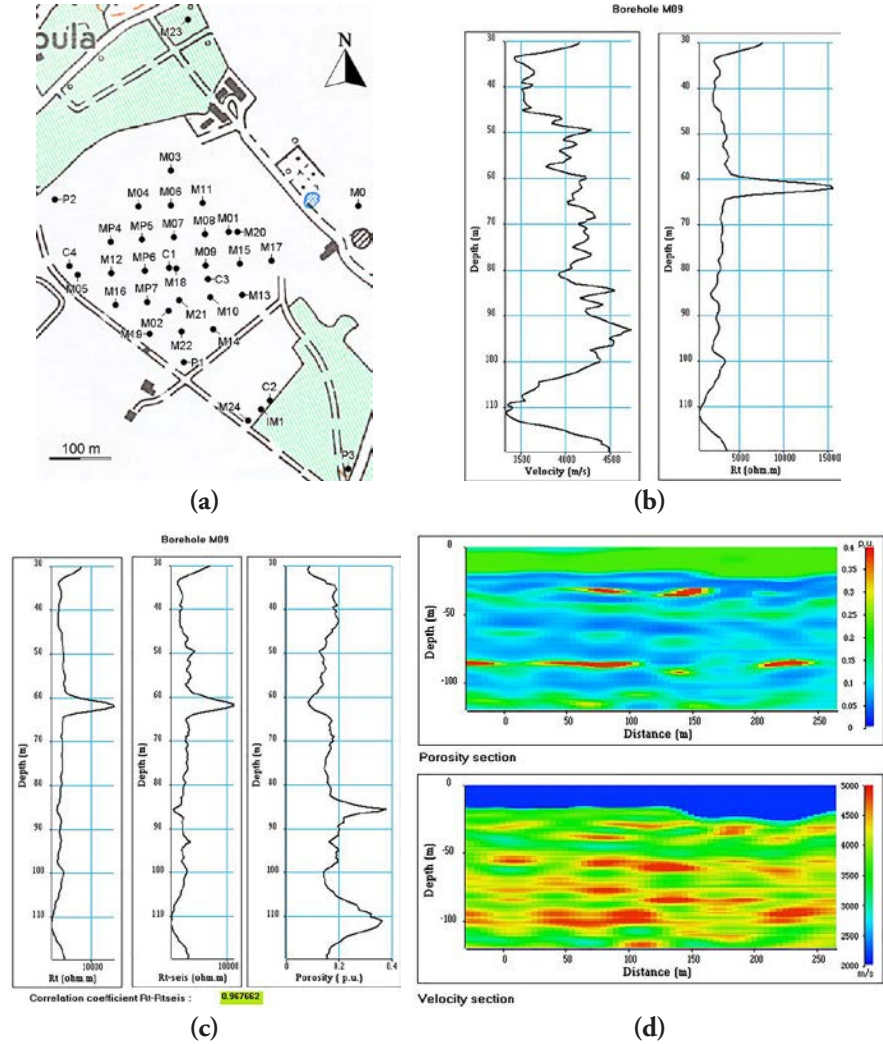


**Figure 3.2** Seismic velocity to porosity transforms using long normal resistivity logs and Faust's law. (a) Borehole location, (b) seismic velocity log and log normal resistivity log at borehole M09, (c) long normal resistivity log  $R_t$ , resistivity log  $R_t$ -seis converted from seismic velocity log using Faust's law, estimated seismic porosity log using Archie's law, (d) porosity and velocity seismic sections.

## 3.2 Hydrogeological methods

Conventionally, hydrogeological investigations concern hydraulic measurements such as flows and temperature. They also concern hydraulic testing such slug test and pumping test (Mari et Porel, 2024).

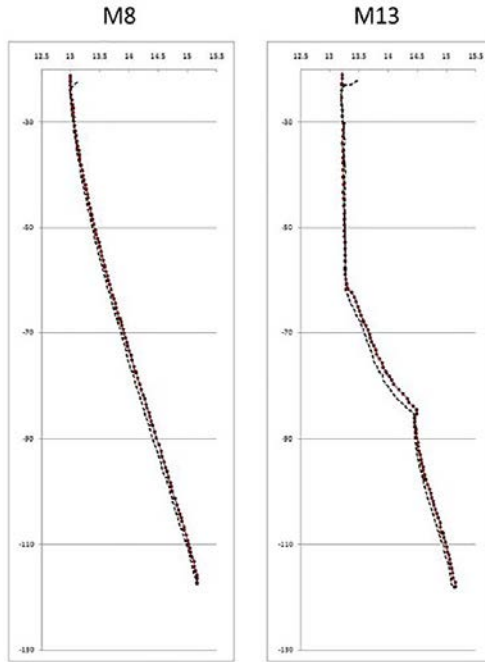
A GFTC logger records logs which show the evolution of the Gamma radiation (G), the water velocity (F), the water temperature (T) and the electrical conductivity of the water (C) as a function of depth.

Temperature logs are carried out in wells to detect any anomalies linked to water intakes in the borehole. Figure 3.3a shows temperature logs recorded in wells M8 and M13 of the HES (Figure 3.2a). For well M8, the temperature increases steadily with the depth. The increase is consistent with the regional geothermal gradient, which is about 2.5 degrees per 100 meters. For well M13, the temperature log shows abrupt variations about 60 and 85 meters deep. These variations are likely related to water intake.

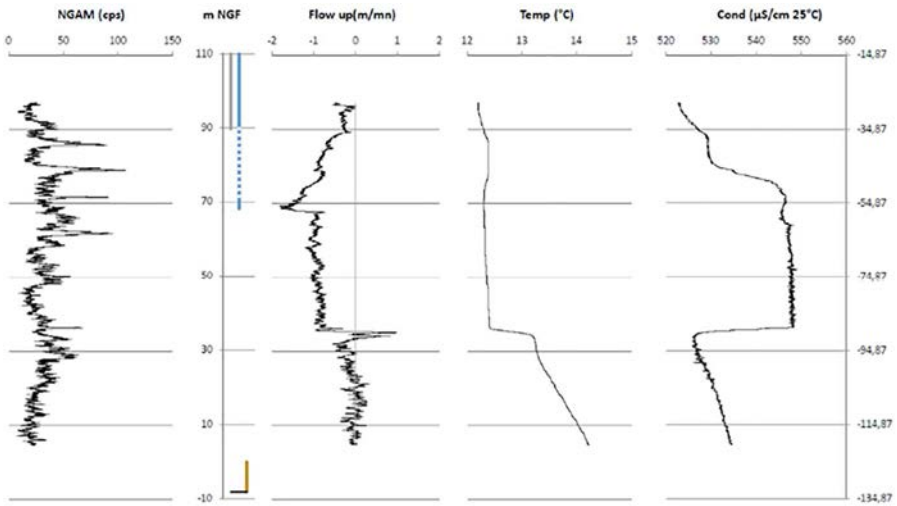
Recording the vertical velocity of the water makes it possible to determine the direction of flow circulation in a borehole (upward or downward flow). The type of experimentation can be carried out under static conditions or in dynamic conditions, either by pumping in the monitored well, or by pumping in a well offsetted from the well being monitored. The experiment makes it possible to know precisely the depths of the producing levels. Figure 3.3b shows an example of flowmeter test performed in M07 well with pumping in M06. The flow log shows a downward flow between 35 and 88 meters, where the flow enters the formation, also visible both on temperature and conductivity logs.

A slug test is a particular type of aquifer test where water is quickly added or removed from a groundwater well, and the change in hydraulic head is monitored through time, to determine the near-well aquifer characteristics. Figure 3.4 is an example of a slug test carried out on the well M19 (Figure 3.2a). The changes in hydraulic head versus time observed on the nearby wells (M16, P1, MP7, M22, MP6, M21) are displayed in Figure 3.4a.

The slug test shows that wells MP7 and P1 are not directly connected to well M19. On the other hand, well MP6 shows oscillations due to the injection of water into M19. MP21 and MP22 seem to be strongly connected to M19. By repeating these operations on various wells of the experimental site, a map of connectivity between wells can be elaborated as shown in Figure 3.4b.

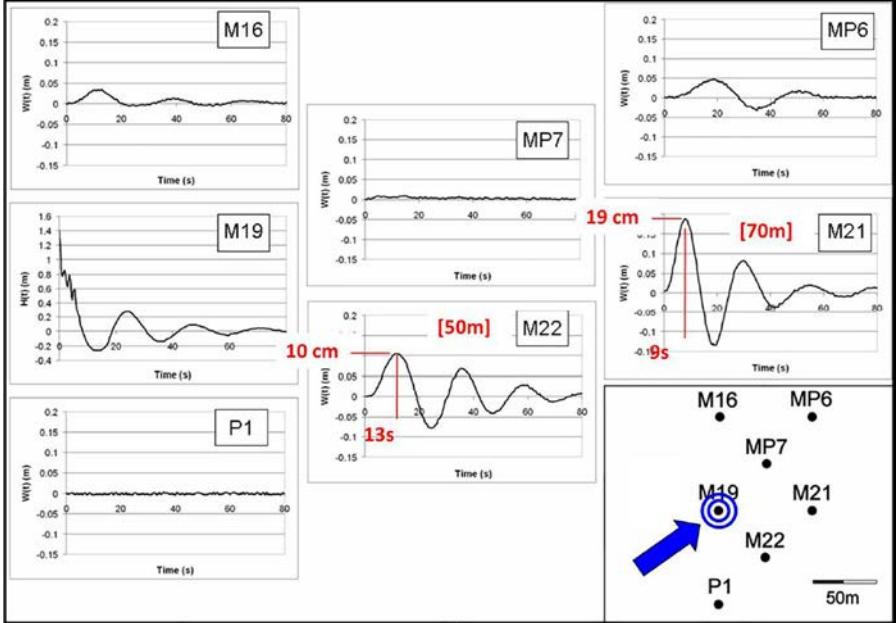


(a)

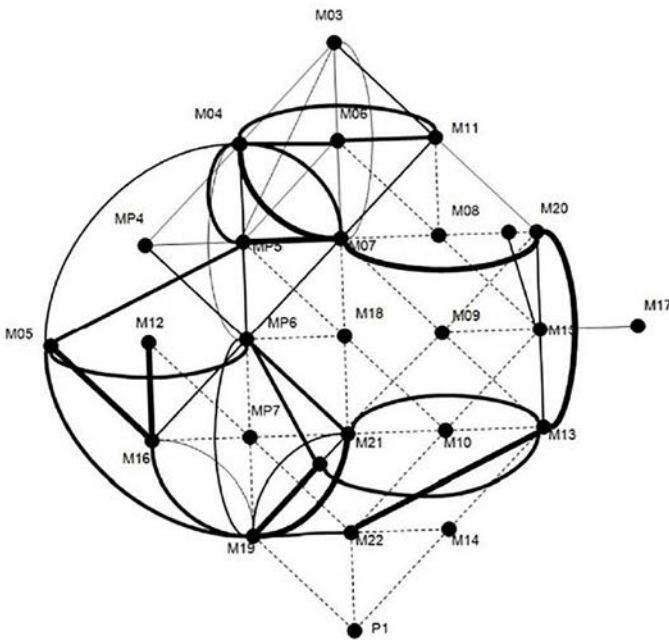


(b)

Figure 3.3 Examples of GFTC logs (after Mari and Porel, 2024). (a) Temperature logs, (b) flow log obtained under dynamic condition in borehole M07 with pumping in M06 well (from left to right: gamma ray, flowmeter, temperature, conductivity observed in M07 well).



(a)



(b)

Figure 3.4 Example of slug test (a) and connectivity map (b) (after Mari and Porel, 2024).

### 3.3 Full waveform acoustic methods

Acoustic tools are currently run to measure velocities (P-wave velocity  $V_P$ , S-wave velocity  $V_S$ ) of geological formations. The tools used are of monopole or dipole type. Monopole-type tools are the most used. For monopole tools, sources and receivers are multidirectional. In the fluid, sources generate a compression wave which creates in the formation a compression wave (P wave) and a shear wave (S wave) at the refraction limit angles. Dipole tools are used to access the shear velocity ( $V_S$ ) of geological formations and are equipped with polarized transmitters and receivers. Such tools generate polarized compression waves perpendicular to the well axis. The compression waves create flexure modes at the well wall which generate in the formation pseudo-shear waves propagating parallel to the well axis.

Acoustic tools are built with one source (multidirectional) and 2 receivers (multidirectional) at least, or several sources (multidirectional and polarized) and several receivers (multidirectional and polarized). Acoustic tools are working in wide frequency bandwidths: 1–40 kHz for monopole tool and 1–3 kHz for dipole tool. Consequently, the sampling rates are of several  $\mu\text{s}$  in time (5 or 10  $\mu\text{s}$  for monopole tool, 20  $\mu\text{s}$  for dipole tool) and of several centimetres in depth (5 to 30 cm). Full waveform acoustic measurements can be represented as constant-offset sections. A constant-offset section is a set of acoustic records represented as a function of depth and obtained with a fixed source-to-receiver distance.

In a vertical well, monopole tools can enable the recording of five propagation modes as: refracted compression waves (P), refracted shear waves (S, only in fast formations  $V_S > V_P$  fluid, P-wave velocity of the borehole fluid), fluid waves (F), and two dispersive guided modes as pseudo-Rayleigh waves (in fast formations), and Stoneley waves (ST). The acoustic logs associated with the different waves are very high-resolution logs and can be compared with core measurements. The acoustic logs currently obtained for each type of wave are velocity or slowness logs, frequency and attenuation logs.

In addition to these modes, constant-offset acoustic sections may show coherent slanted events and resonances (R). The slanted events, conventionally named criss-cross events, are refracted events reflected on the edges of geological discontinuities (acoustic impedance discontinuities), such as fractures. For their part, the resonances are related to poor cementation between the casing and the formation. A high level of resonances can result in unusable acoustic data.

Figures 3.5 to 3.8 show an example of acoustic data recorded in boreholes situated on an experimental site located in the Cher region (France) at the transition from Triassic to Jurassic geological formations, partly overlaid by thin superficial formations. The sedimentary formation is mainly composed of limestone up to 120 m depth and sandstones with some argillite and dolomite intercalations between 120 m and 200 m.

The site was investigated from the surface via hybrid seismic imaging methods and from two boreholes (B1 and B2, Figure 3.5a) via FWAL and VSP (Mari et al., 2021, 2023, 2024). A seismic line was recorded at the site with a seismic spread composed of 48 fixed geophones (2 m lag distance between neighbors,

Figure 3.5a), while the source, as a weight dropper (Figure 3.5a), was moved and fired in the middle of all pairs of adjacent geophones. Hybrid seismic imaging combining refraction (tomography, Figure 3.5a) and reflection seismic results produced an extended depth reflectivity section starting from the surface up to a depth of 240 m (Figure 3.5b). Time to depth conversion was calculated using the time-depth law given by the VSP recorded in borehole B1 (Mari et al., 2021). The site was also investigated by a near surface 3D seismic survey (Mari and Mendes, 2019: see Figures 2.27 to 2.29, chapter 2).

Borehole B1 was drilled to a depth of 80 m and equipped with a cemented steel casing. Borehole B2 was drilled in two drilling phases. In the first phase, B2 was drilled to a depth of 120 m and equipped with cemented steel casing to a depth of 78 m. B2 remains in open hole between 78 and 120 m. In the second phase, B2 was drilled to a depth of 192 m and equipped with a slotted PVC casing in the 78–120 m depth interval. Resonances observed on constant offset acoustic sections reveals that B1 is a poorly cemented case hole (Figure 3.6) and B2 is an uncemented cased hole up to 78 m, B2 being equipped with an uncemented slotted PVC casing from 78 m to 192 m depth.

The acoustic tool used for field experiments is a monopole-type flexible tool with a small diameter of 50 mm. It holds a magnetostrictive transmitter (transmission frequencies: 17–22 kHz) and can be equipped with two pairs of piezoelectric receivers offering an acquisition in near offset configuration (receivers at 1 and 1.25 m beneath the source), and in far offset configuration (receivers 3 and 3.25 m beneath the source).

Figures 3.6 and 3.7 shows a comparison between acoustic data recorded using the tool in the near (or short) offset configuration (receivers at 1 and 1.25 m from the source) and in the far (or large) offset configuration (receivers at 3 and 3.25 m).

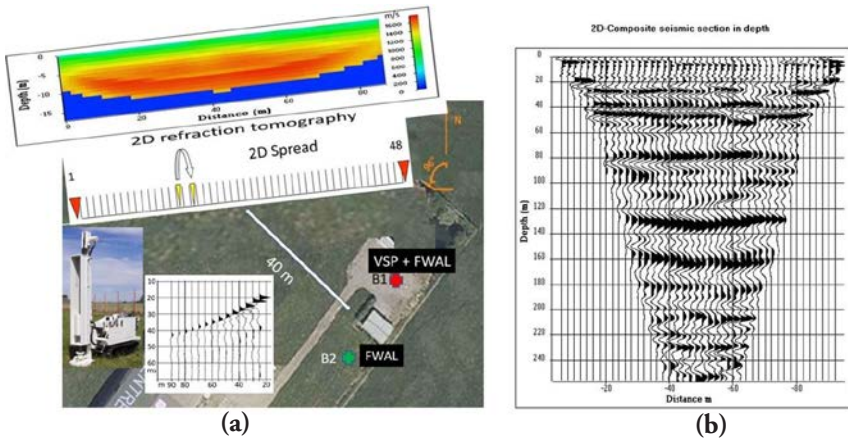
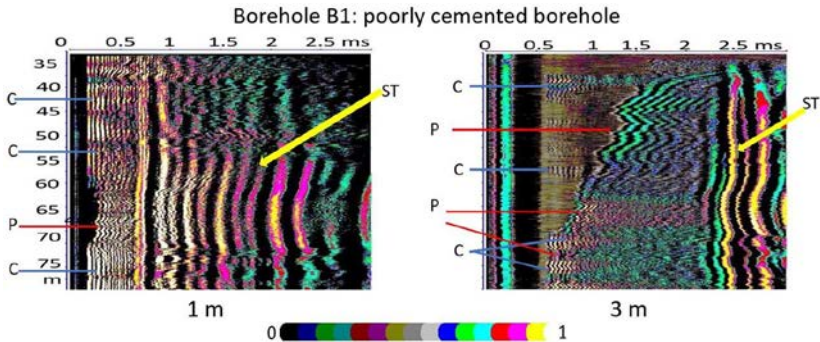
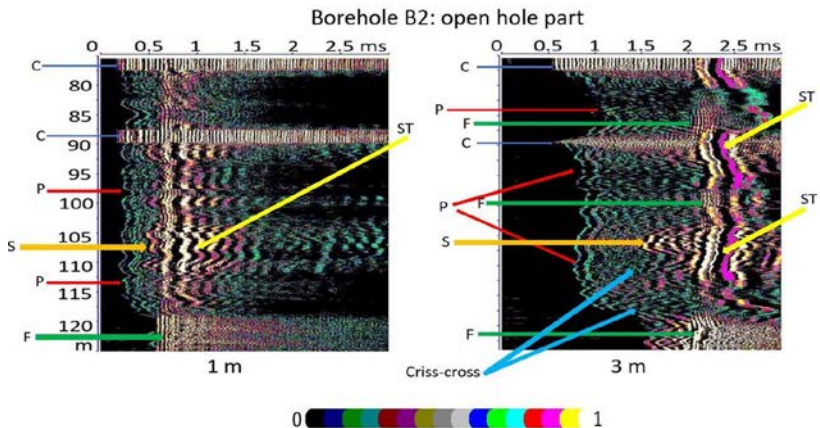


Figure 3.5 Seismic imaging: (a) 2D seismic spread – 2D refraction tomography, borehole locations (B1 and B2), view of the seismic source, VSP recorded in B1, (b) 2D hybrid section over depth (after Mari et al., 2021).

In borehole B1 (Figure 3.6) which is poorly cemented resulting in strong resonances, the short-offset configuration (1 m) only shows refracted P-waves in the 60–70 m depth interval. In contrast, the large offset is less sensitive to resonances, letting clearly appear refracted P-waves along the profile. For both offsets, the differentiation between the refracted P-waves (P) and the Stoneley waves (ST) can be done easily.



**Figure 3.6** Comparison of short offset (1 m) and large offset (3 m) acoustic sections recorded in borehole B1 (poorly cemented borehole). The different wave trains are identified by letters: C casing resonances, P refracted P-wave, ST Stoneley wave. The acoustic sections are normalized and displayed with a color scale ranging from 0 to 1 (after Mari et al., 2023).



**Figure 3.7** Comparison of short offset (1 m) and large offset (3 m) acoustic sections recorded in the open hole part of borehole B2. The different wave trains are identified by letters: C casing resonances, P refracted P-wave, S converted refracted S-wave, F fluid wave, ST Stoneley wave, criss-cross. The acoustic sections are normalized and displayed with a color scale ranging from 0 to 1 (after Mari et al., 2023).

In the open hole part of borehole B2 (Figure 3.7), the presence of a piece of casing generates resonances in the depth interval 88–91 m on the 1 m offset section. The influence of the piece of casing is local on the 3 m offset section, indicating that the length of the piece of casing is a slightly larger than 3 m. On the 1m offset section, it is possible to identify the refracted P-waves, locally the converted refracted S waves, the Stoneley modes and the fluid modes. With a short-offset configuration, the different wave trains can interfere. However, we can notice that a large offset (3 m) better separates the different wave trains over time due to the difference in their propagation velocities. On the 3 m offset section, criss-cross events are visible.

The short-offset configuration must be favored to evaluate the borehole cementation. For measurements of wave parameters such as amplitude, frequency content, propagation velocity, a large offset configuration must be favored.

Full waveform acoustic data, recorded with the large offset configuration (3 and 3.25 m), in borehole B1 (steel cased hole) in the 30–78 m depth interval and in borehole B2 (slotted PVC cased hole) in the 78–192 m depth interval are merged to obtain composite acoustic sections. Figure 3.8 (right side) shows the composite acoustic section with an offset of 3 m. The acoustic data were processed to obtain a very high-resolution velocity log (Figure 3.8) which was converted in pseudo porosity log using the Raymer equation adapted to carbonate formation (Raymer et al., 1980). The porosity log was then used

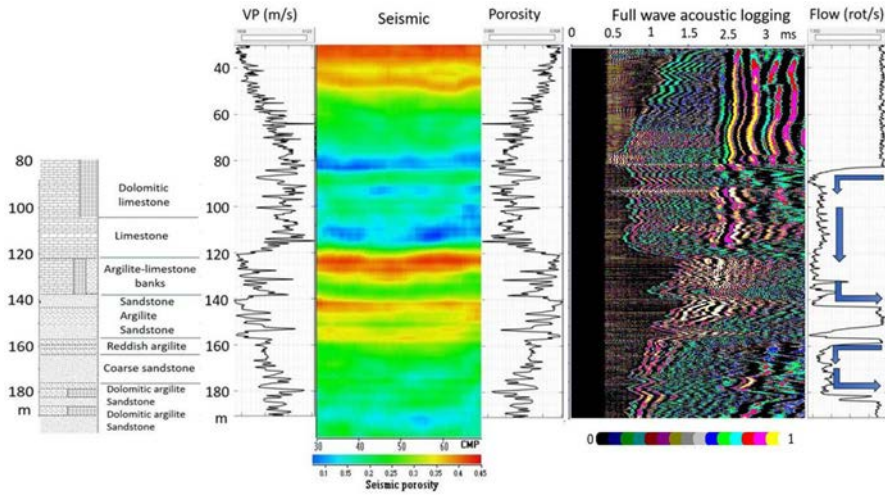


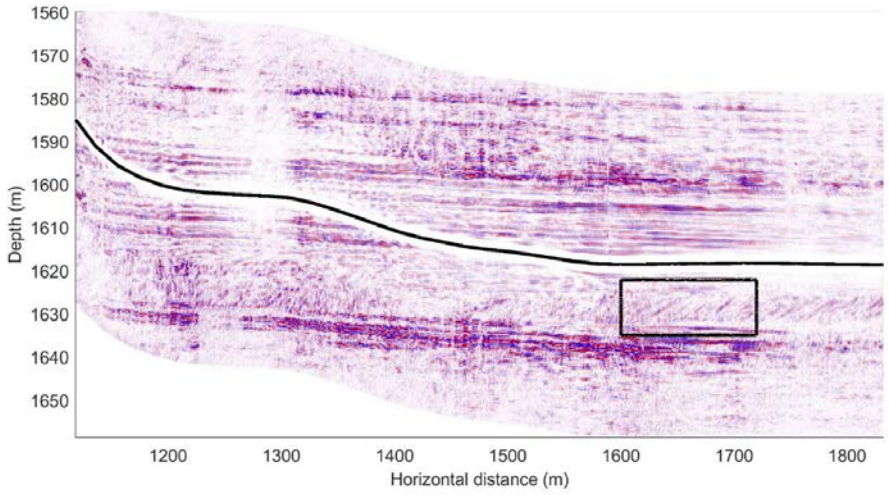
**Figure 3.8** *Seismic imaging and full waveform acoustic logging: from left to right: lithological column, acoustic velocity, seismic section converted in porosity, acoustic porosity, Full wave acoustic composite section (0–80 m: borehole B1, 80–190 m: borehole B2 slotted PVC cased hole) and flowmeter. The acoustic section is normalized and displayed with a color scale ranging from 0 to 1 (after Mari et al., 2021).*

as a constraint to transform the seismic section into pseudo-porosity section. The results are shown within the 30–190 m depth interval in Figure 3.8, with high-porosity layers appearing in red (Mari et al., 2021). The pseudo porosity section, associated with a flowmeter recorded in the slotted PVC part of borehole B2, informs on preferential areas where flows occur. Levels of in-flows or out-flows, indicated by blue arrows on the flowmeter, clearly show two flow loops, completely independent over depth (83–143 m and 159–181 m depth intervals).

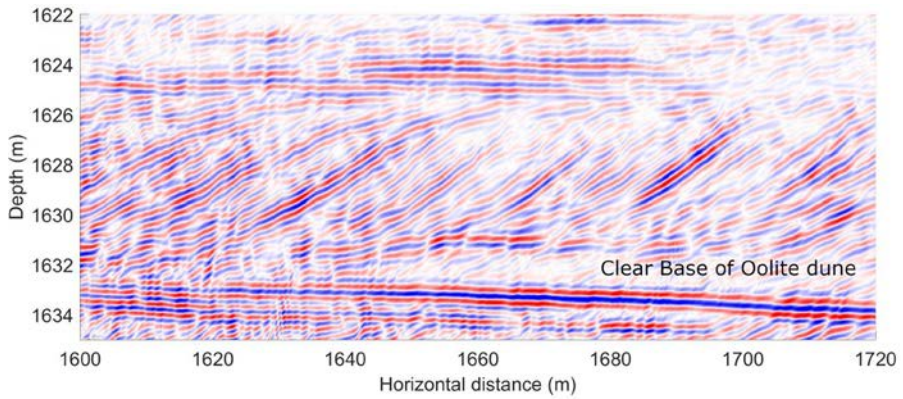
With full waveform data, provided by multi-source and multi-receiver logging tools, recorded in deviated or horizontal boreholes, it is possible to conduct a well micro seismic survey based on the analysis of modes reflected and diffracted on acoustic impedance discontinuities within formations or at formation boundaries. Processing of reflected modes leads to depth migrated acoustic sections with very high resolution (a few tens of centimeters) providing an image with a depth of investigation of several meters from the well trajectory (Hirabayashi et al., 2024).

Hirabayashi et al. (2024) shows an example of depth migrated acoustic section obtained in a highly deviated geothermal well with a sonic tool consisting of 13 receiver stations spaced at 0.1524-m intervals, each with eight azimuthal receivers. The minimum distance between source and receivers is 3.795 m, and a dipole chirp source was used during data acquisition. Figure 3.9a shows depth migration images above and below the actual borehole trajectory indicated by the black curve. Parallel reflectors dipping down to the right by about  $3^\circ$  are consistently observed. Figure 3.9b shows a zoomed image for the black box shown in Figure 3.9a. Stratigraphic structures (of approximately  $10^\circ$  dip) are observed within a potential geothermal reservoir, with the reflector at  $\sim 1634$  m vertical depth corresponding to the base of an oolite dune.

Full waveform acoustic logging has a very good vertical resolution (a few decimeters). Its lateral investigation with respect to the borehole is of a few centimeters for interface dispersive modes, a few tens of centimeters for refracted modes and a few meters for reflected modes (less than 20 meters).



(a)



(b)

**Figure 3.9** Depth migrated acoustic section obtained in a highly deviated geothermal well (after Hirabayashi et al., 2024). Depth migration image and borehole geometry in the vertical depth (a). Enlargement of the 120 m (long)  $\times$  13 m (high) rectangle window shown in a, which shows noiseless, highly defined geological progradations (b).

### 3.4 Borehole seismic method

Vertical Seismic Profile or VSP (Hardage 1985, 1992; Mari et al., 1999; Mari and Coppens, 2003; Mari and Vergniault, 2018) is the most used form of well seismic surveying conducted in vertical wells. VSP is a well seismic method for which the source and the receiver are approximatively on the same vertical. The VSP vertical resolution ranges from meters to tens of meters and its lateral range of investigation can reach a few tens of meters (Fresnel zone). After processing, a VSP provides a seismic trace, that is directly comparable to a surface seismic section recorded in the vicinity of the well.

The lateral range of investigation of a VSP is increased by doing acquisition in deviated wells or can be improved by offsetting the source with respect to the well in case of vertical well. This technique is called Offset Vertical Seismic Profiling (OVSP). The image obtained after processing is thus a single-fold seismic section. A Seismic Walkaway is a series of offset VSPs, with the surface source situated at several locations corresponding to successively increasing offsets with respect to the borehole. The image obtained after processing is a section with a low degree of multiple fold coverage.

For VSP acquisition, the sources are vibrators or weight droppers for on-shore surveys, air guns or sparkers for off-shore surveys. The borehole sensor can be a single-component geophone (vertical geophone) or a three-component geophone (a vertical component and two orthogonal horizontal components). The borehole sensor can also be a hydrophone, or even a four-component sensor: a three-component geophone and a hydrophone. The receiver can also be a string of borehole sensors, allowing the acquisition of data at several depth levels simultaneously (between 4 and 12 levels). Distributed Acoustic Sensing (DAS) is an established technology for recording seismic response using optical fiber cables (Willis, 2022). The DAS technology is being used with increasing success in VSP, especially due to the selective sensitivity of the fiber to axial deformations. Mestayer et al. (2011), Mateeva et al. (2013, 2014), Lesnikov and Allanic (2014) demonstrated that DAS data provides VSP results comparable with conventional VSP acquisition. However, current DAS systems have a much higher noise floor than geophones meaning that small events may be harder to detect (Baird et al., 2024). DAS technology can be deployed in high temperature, highly deviated or horizontal wells. Meantime the current limitations of the DAS VSP are also well known. Directivity pattern, attenuation of the signal with the length of the fiber cable, uncertainty of the depth determination are among the observed problems (Lesnikov and Allanic, 2014). DAS VSP recorded with fiber cable, which can be deployed behind casing (Didraga, 2015) or production tubing, can provide a much denser spatial sampling than a geophone string at a relatively low cost per sensor.

A VSP record is a two-dimensional record, with a vertical axis which represents the recording time and the horizontal axis which represents the depth locations of the borehole sensor. In case of vertical well, the horizontal axis is the vertical depth expressed in m. In case of deviated well, it represents the cable length. The borehole deviation must be measured and considered in the processing sequence. The

frequency content of well seismic data, being generally wider (up to 150–175 Hz) than that of surface seismic data, the time sampling interval does not exceed 2 ms (between 0.5 to 2 ms). The distance between 2 adjacent sensor locations must be chosen to be less than the smallest half-wavelength encountered to avoid spatial aliasing phenomenon (Mari, 2015), usually between 5 and 20 m. For Offset VSP or seismic walkaway acquisition, the offset  $D$  of the source relative to the wellhead depends on the depth  $H$  of the objective. An offset  $D < 3/4 H$  allows to obtain VSP sections, with reflected events for which angles of incidence do not exceed 30 degrees, recommended for amplitude analysis versus angle or offset.

For a VSP recorded in a vertical well, crossing geological layers with small dips, wave field, emitted by a source located at a small offset from the well head, propagates at normal incidence. In these conditions, if the seismic source generates P-waves, VSP records are composed of down-going and up-going P-waves and Stoneley waves. There is no phenomenon of conversion from P-wave to shear wave (S-wave). The P-wave field is composed of primary waves and multiples. Stoneley waves, more commonly known as tube waves, are created when the particles of the sludge column that fills the well are set in motion. Surface waves are the main source of tube waves, which are considered as organized noises that disrupt VSP recordings. However, tube waves, created by conversion of P-wave, are very useful to detect layers of high permeability. In case of wave propagation at normal incidence, VSP can be recorded using a vertical geophone or a hydrophone.

Figure 3.10 is an example of VSP recorded with a vertical geophone and a hydrophone, in a reconnaissance borehole of about 400 m depth drilled to determine the geothermal parameters of the geological formations crossed, as part of a deep

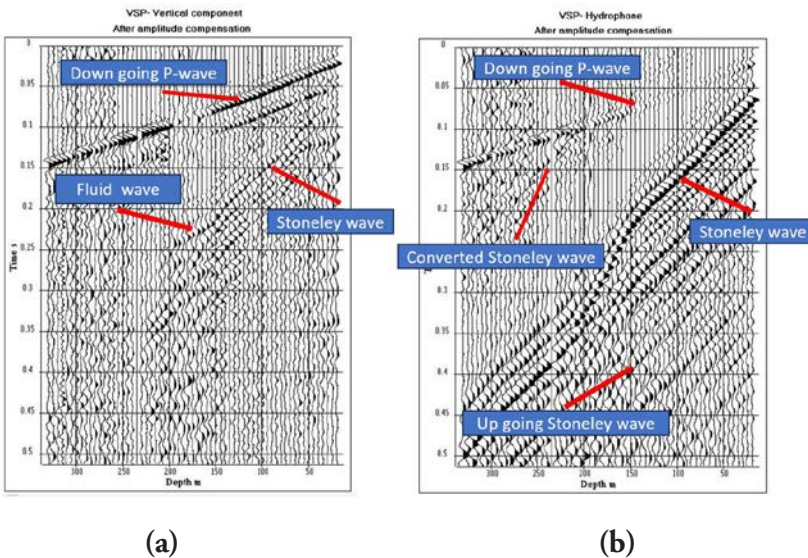


Figure 3.10 VSP sections (a: vertical geophone, b: hydrophone) and wave identification (After Mari et al., 2024).

geothermal project, in southern Luxembourg. The VSP was recorded with a depth sampling interval of 5 m in the 20–330 m depth interval. The source is a vibrating source emitting a sweep in the 20–120 Hz frequency band. The offset of the source from the borehole head is 8 m. The time sampling interval is 0.5 ms. Figure 3.10 shows the VSP sections, after amplitude compensation, observed on the vertical geophone and on the hydrophone. On the vertical geophone section, we observe a downgoing P-wave, strongly attenuated in the 150–200 m depth interval. We note the presence of both a downgoing Stoneley wave attenuated from 150 m and a fluid wave (with a propagation velocity of 1540 m/s) in the 150–200 m depth interval. On the hydrophone section, we observe the downgoing P-wave with a conversion to a Stoneley wave at a depth of about 200 m. We also observe a strong downgoing Stoneley wave with a set of reflected upgoing Stoneley waves, the strongest of which occurs at the depth where the converted downgoing Stoneley wave is created

The processing sequence includes amplitude recovery, picking of the arrival times of downgoing wave fields, wave separation of downgoing and upgoing waves, both for P-wave and Stoneley wave. Figure 3.11a shows the extraction of downgoing and upgoing P-waves. Picking of the arrival times of the downgoing wave fields (P-wave and Stoneley wave) is used to compute time versus depth laws (Figure 3.11b), interval velocity logs, and attenuation logs after flattening of the downgoing wave fields (Figure 3.12).

The reconnaissance borehole crosses, after a few meters of landfill and alluvium, that is unconformably underlain by rather similar mainly marly formations dating from the Upper and Middle Liassic, showing slight facies changes towards more silty and sandy or more calcareous facies (units lo4 to lo1a and lm3 to lm1; Toarcian to Pliensbachian, Lower Jurassic).

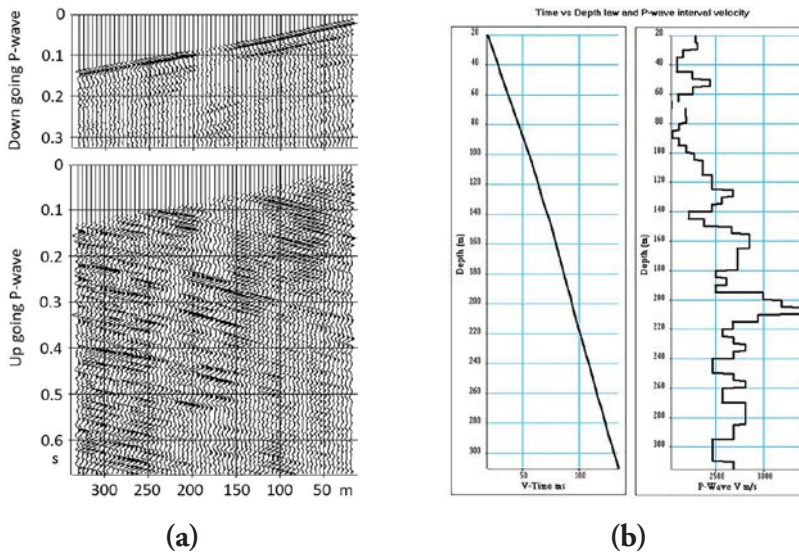


Figure 3.11 VSP vertical geophone processing: Down going and up going P-wave separation (a), Time versus depth law and P-wave interval velocity log (b) (after Mari et al., 2024).

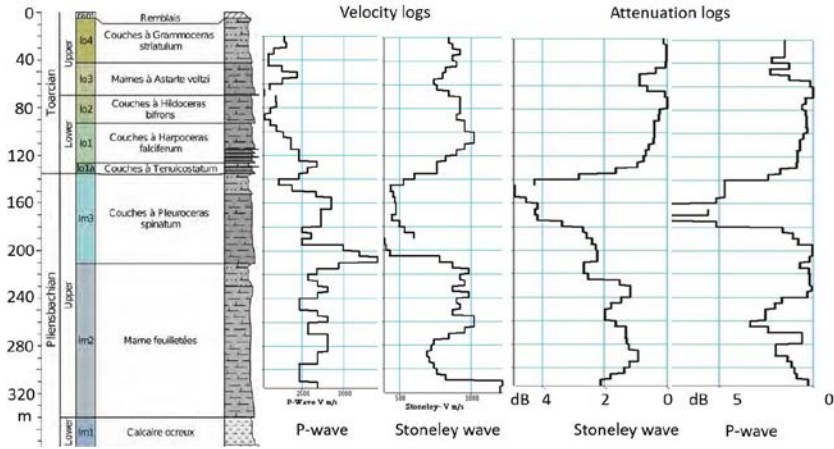


Figure 3.12 Lithology and VSP logs: velocity and attenuation logs (after Mari et al., 2024).

In detail, the lithology record by the Geological Survey shows, after the 2 rather homogeneously marly units lo4 and lo3, a gradually increasing content in organic matter, observed in the lo2 and lo1 units (70–126 m), also showing a thin lamination, culminating in the lo1a unit below (126–139 m), which is more silty, sandy and contains bituminous horizons. Below, the lm3 unit appears to have an even higher sand/silt content but is also richer in limestone nodules and beds (140–210 m). The following lm2 unit, the sand and silt content gradually decreases again until the depth of 230 m and the basis of this unit (at 340 m) is homogeneously marly. We note a significant decrease in shear velocity in the 140–200 m depth interval corresponding to the lo1a and lm3 units, richer in sand/silt and organic matter (lo1a) or limestone (lm3). Figure 3.12 (on the right) shows the attenuation logs computed from the downgoing P and Stoneley waves. The results obtained (decrease of both energy and velocity of the Stoneley wave) are consistent with the results which could be obtained by a Biot-Rosenbaum model (Rosenbaum, 1974) used to access to permeability from the evolution of Stoneley’s phase velocity and attenuation (Mari, 1989). The velocity and attenuation VSP logs show a very good correspondence with respect to the lithological variations observed in the borehole (Figure 3.12).

The well was equipped with a hybrid cable, comprising 2 optical fibers and 2 electrical conductors, suitable for geothermal applications. Fiber optic temperature measurement enables optimal monitoring of temperature distribution and thermal conductivity in the subsurface as a function of depth. Temperature measurements are made before and after heat injection phases, which are carried out by sending an electric current through the electrical conductors of the hybrid cable. Before heat injection, the temperature increases linearly from 12 °C at 20 m to 23 °C at 320 m (Figure 3.13).

Once the heat injection phase has begun, temperature profiles, recorded after different heating time intervals, show the evolution of the subsurface temperature after respectively 1 h (cyan curve), 3 h (yellow curve) and 108 h (red curve) of thermal

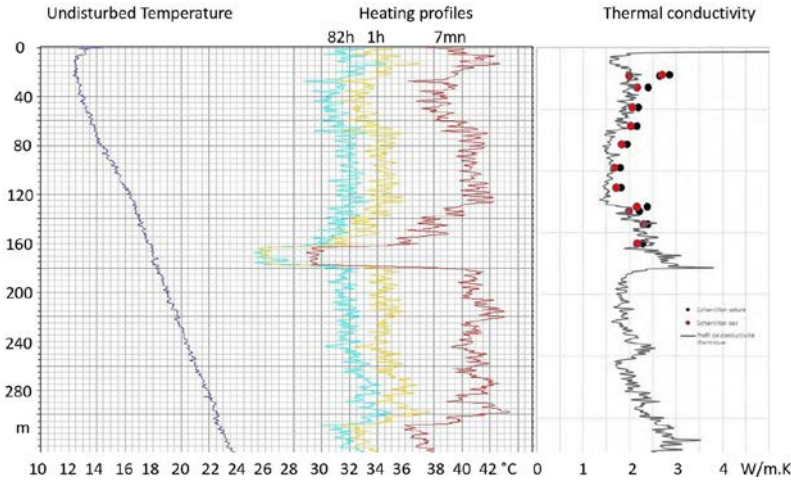


Figure 3.13 Geothermal tests. Service géologique du Luxembourg document.

dissipation (Figure 3.13). Different variations, similar on each of the curves, can be identified during the heat injection phase. The main anomaly, located between 160 and 180 m deep, results in a smaller increase in temperature compared to the surrounding depths. Based on the lithologic description the occurrence of a higher sand/silt, organic matter or limestone content observed in the units lo1a and lm3 can be identified at the depths corresponding to these anomalies with lower temperature increases. These can therefore be interpreted as a due to a higher groundwater flow rate in the facies having a slightly higher permeability, causing a leaching of the thermal plume. The heat supplied is more efficiently dissipated thanks to this flow, resulting in a smaller rise in temperature.

The presence of flows is confirmed by Stoneley wave velocity decrease (Figure 3.12), Stoneley wave and P-wave attenuation increase (Figure 3.14) and the presence of a fluid wave (Figure 3.10) in the 140–180 m depth interval. We also note a good correspondence between the thermal conductivity profile (Figure 3.13) and the attenuation VSP logs (Figure 3.14).

The conventional processing sequence of a VSP includes amplitude recovery, picking of the arrival times of downgoing wave fields, wave separation using both  $f$ - $k$  filters and SVD (singular value decomposition) filters (Mari, 2015), deconvolution of upgoing P-wave fields by the associated downgoing P-wave fields, design of stacking corridor on flattened deconvolved upgoing P-wave section and computation of corridor stacked traces in time. Figures 3.15 and 3.16 illustrate the processing sequence of a near surface VSP recorded in borehole B1 of the experimental site located in the Cher region (Figure 3.5a). The borehole sensor is an anchored vertical geophone. The source is a weight drop (Figure 3.5a).

The VSP is acquired in the 25 to 90 m depth interval, with a depth sampling interval of 5 m (Figure 3.15a). The listening time is 250 ms. The time sampling interval is 0.25 ms.

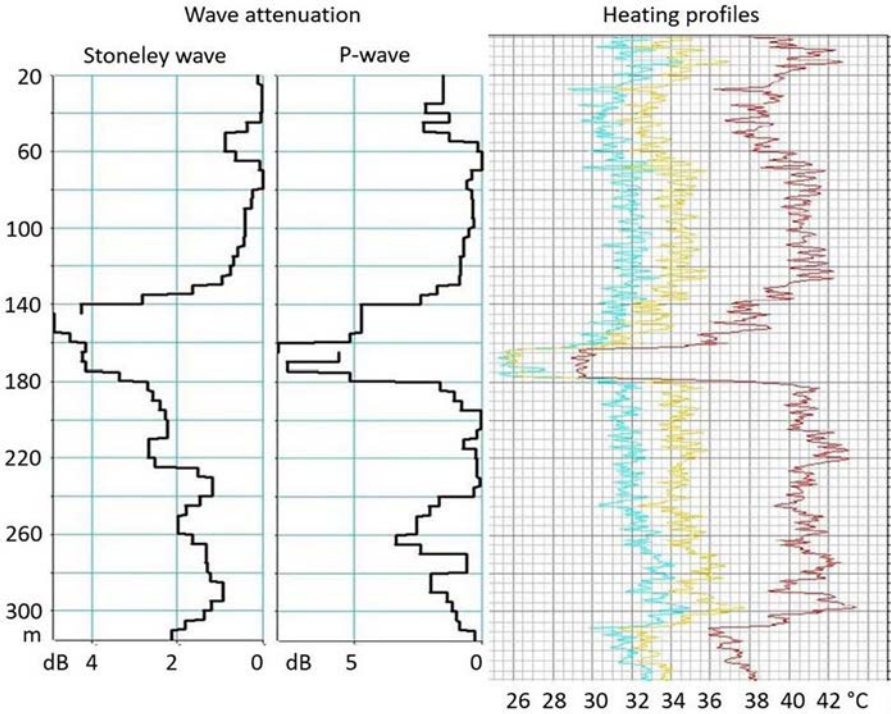


Figure 3.14 Wave attenuation versus heating profiles (after Mari et al., 2024).

The picked times of the first arrivals (downgoing P-waves) are used to compute the time versus depth law and the P-wave interval velocity log (Figure 3.15b). The upgoing and downgoing P-waves are separated by an f-k filter (Figures 3.15c and 3.15d). After deconvolution, the upgoing wave field is flattened (Figure 3.16a), a stacking corridor section is designed and a corridor stacked trace is computed (Figure 3.16b). The VSP trace stacked in a corridor (corridor stacked trace or VSP stacked trace), which represents the reflectivity function filtered in the seismic bandwidth and associated with the geological medium crossed by the borehole, is used to calibrate seismic sections located in the vicinity of borehole B1. The corridor stacked trace is used to identify primary reflections on surface seismic sections. For that purpose, the corridor stacked trace duplicated several times is inserted in a seismic section at the location of borehole B1 (Figures 3.16c and 3.16d). In the example, the seismic section is extracted from the 3D block, obtained by a 3D survey conducted on the site (Mari and Mendes, 2019: see Figures 2.27 to 2.29, chapter 2). Another approach is to use both velocity log obtained by acoustic logging (Figure 3.7, right side) and density log to compute synthetic seismograms (SS). The VSP stacked traces (indicated by a red rectangle) and the synthetic seismograms (indicated by a blue rectangle) are inserted in the 3D seismic section. The results are

shown both in time and depth (Figures 3.16c and 3.16d), after depth conversion using the time versus depth conversion law (Figure 3.15b). The synthetic seismogram enables the identification of reflectors in the depth range where the logs have been recorded. The VSP stacked trace allows the identification in the same depth range, but it also enables the prediction of reflectors under the well, particularly in the 90 to 140 m range.

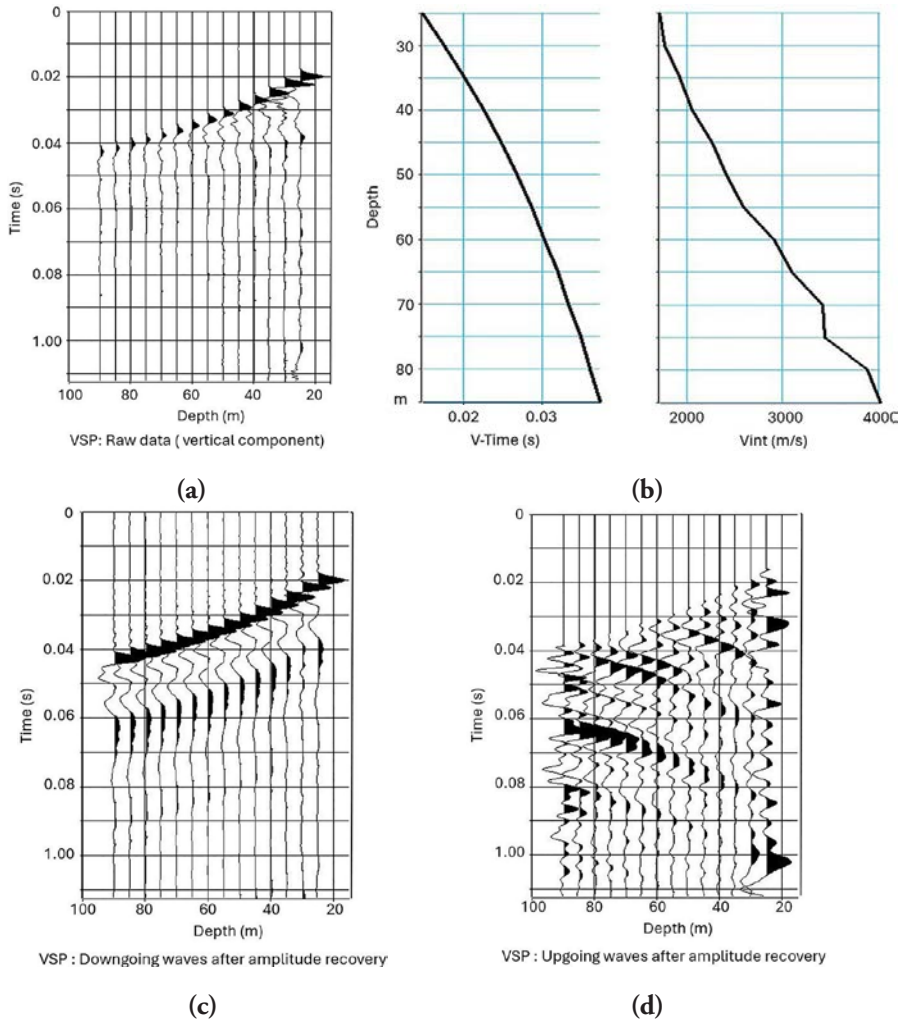


Figure 3.15 Processing of a near surface VSP, after Mari and Vergniault (2018). (a) Raw data, (b) vertical time and interval velocities, (c) downgoing P-waves, (d) P-upgoing waves.

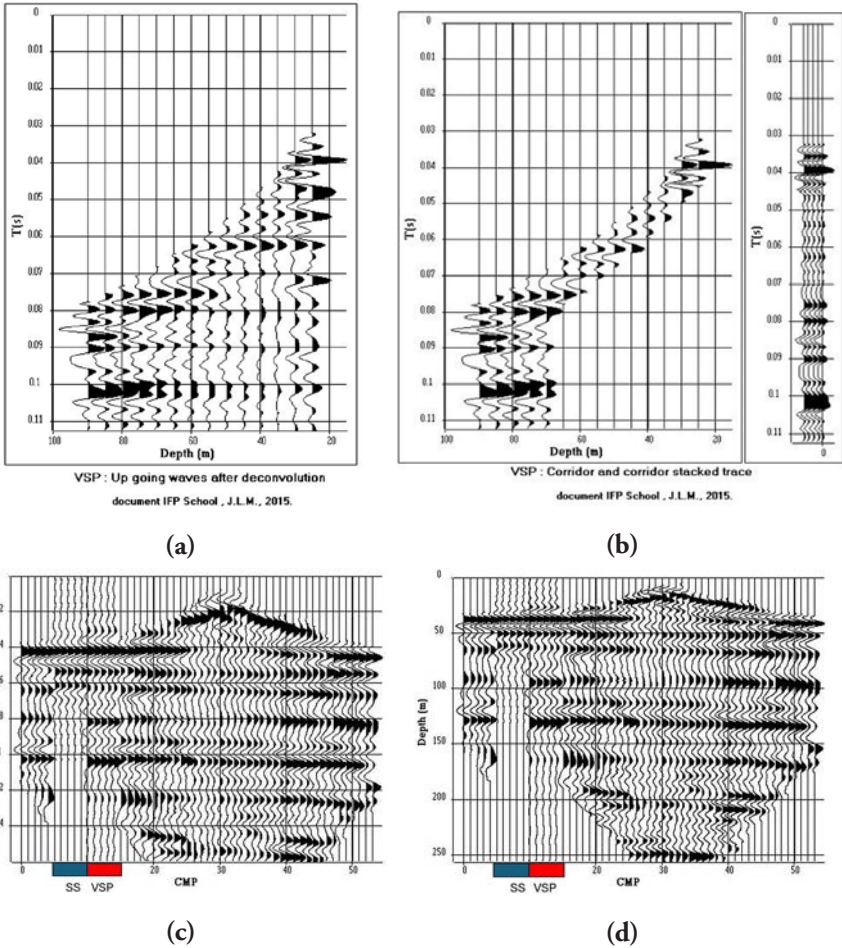


Figure 3.16 Processing of a near surface VSP, after Mari and Vergnault (2018). (a) Deconvolved upgoing P-waves, (b) stacking corridor and stacked trace; (c) and (d) seismic section, VSP stacked trace and synthetic seismogram in time (c) and in depth (d).

In case of acquisition of wave fields that do not propagate at normal incidence, it is recommended the use of 3-component borehole sensors to record the different wave trains, in particular the waves converted from P to S. Wave propagation at not normal incidence occurs in acquisition of:

- VSP in boreholes drilled in complex geological structures (dips and faults),
- VSP in deviated wells,
- Offset VSP and walkaway.

Considering the trajectory of the well and the fact that the borehole sensor can rotate from one depth to another, the 3 components (X, Y, Z) of the sensor must be oriented using either hardware orientation device or algorithms based on the analysis of wave polarizations used to define rotation angles for orientation (Naville, 2024). Figures 3.17 and 3.18 are an example of a 3C VSP orientation in a deviated well (Kazemi, 2009). After rotations, the oriented components are defined as follows: Z-component (ZV) is vertical pointing downward, X-component (HN) is horizontal pointing to North and Y-component (HE) is horizontal pointing the East true geographic direction.

After orientation, the 3C VSP processing sequence (Hardage, 1985; Mari and Coppens, 2003; Serbutoviez et al., 2003) includes wave separation with apparent velocity filter and polarization filters (Mars et al., 1999) to extract P and S-waves and separate downgoing and upgoing waves, deconvolution of the upgoing wave fields (P and S waves) by a single operator extracted from the downgoing wave fields, normal moveout correction of deconvolved upgoing waves and stack in CMP gather, or prestack migration in time or depth. The most used method is the VSP -CDP stack method proposed by Wyatt and Wyatt (1982). The VSP migrated seismic section is directly comparable to a surface reflection seismic section. The VSP migrated section has a lateral range of investigation of a few tens to a few hundreds of meters.

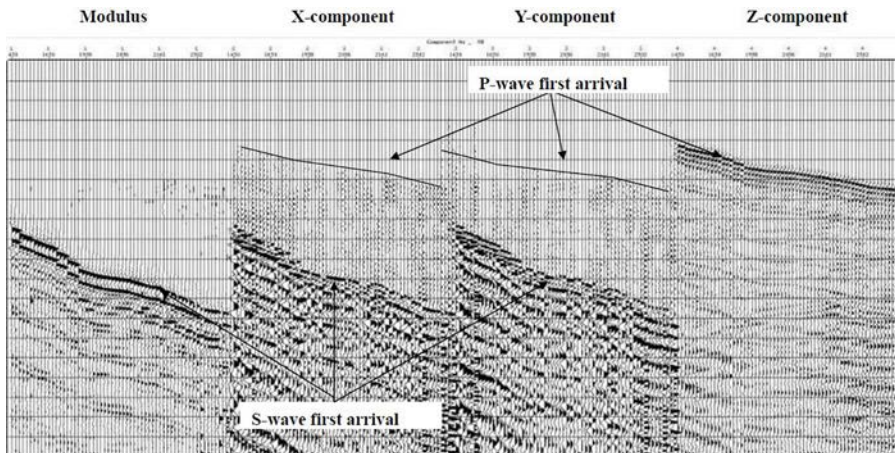


**Figure 3.17** From left to right Modulus, X, Y and Z-components before orientation. First arrival S-waves are clear on horizontal components while on the Z-component P-wave first arrivals are sharp to pick. The first arrival S-waves are not consistent before orientation while modulus ( $X^2 + Y^2$ ) clearly shows the S-wave first arrivals. X, Y and Z components are displayed with the same constant gain while modulus has been normalized (after Kazemi, 2009).

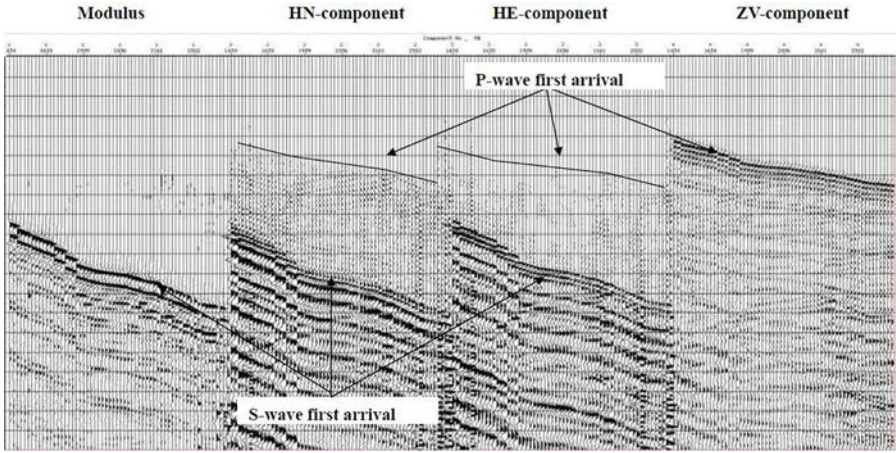


**Figure 3.18** From left to right Modulus, HN, HE and Z-components after orientation. On the Z-component P-wave first arrivals are sharp to pick. First arrival S-waves are coherent after orientation. The filtered modulus is identical before and after orientation. HN, HE and Z components are displayed in constant gain while modulus has been normalized. The modulus first arrivals are identical before and after orientation (after Kazemi, 2009).

Naville et al. (2024a,b) shows an example of a 3C VSP obtained in the deviated section of the high-angle geothermal borehole of Grigny GGR5, targeting intra-Dogger thin, porous beds. Figure 3.19 shows the survey geometry and gives a summary of field parameters. One can notice the wide frequency bandwidth used for the vibrator sweep (5 to 175 Hz). Figure 3.20 shows the PP and PS VSP migrated sections. The reflectors surrounding the top Bathonian are slightly dipping to NE, and affected by several step faults, attenuated by lateral enhancement and migration. On the right side, the PS image converted to P-wave twt scale is restituted with higher definition due to the shorter shear wavelength. Main faults F1 & F2 are drawn on the bottom half of Figure 3.20, underlining lateral interruptions of reflectors. Many additional small faults are present on both PP and PS images (Naville et al., 2024a,b). To assist in a depth prediction of potential low velocity/high porosity target beds beneath the well, an inversion of the VSP PP-up image to acoustic impedance and acoustic velocity was performed. The inverted VSP sections highlight a depth interval of lower relative velocity and impedance at 1600–1612 m, which was revealed porous and productive (Figure 3.21).

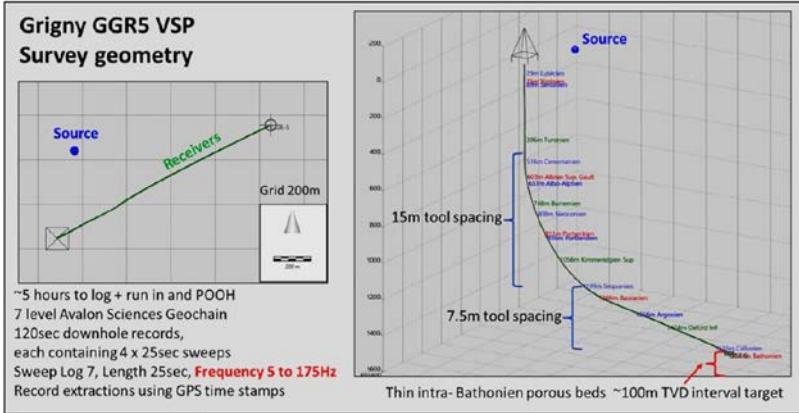


Figure 3.19 GGR5-VSP, survey geometry, and summary of field parameters: plan view (left), 3D view (right) (after Naville et al., 2024a,b).

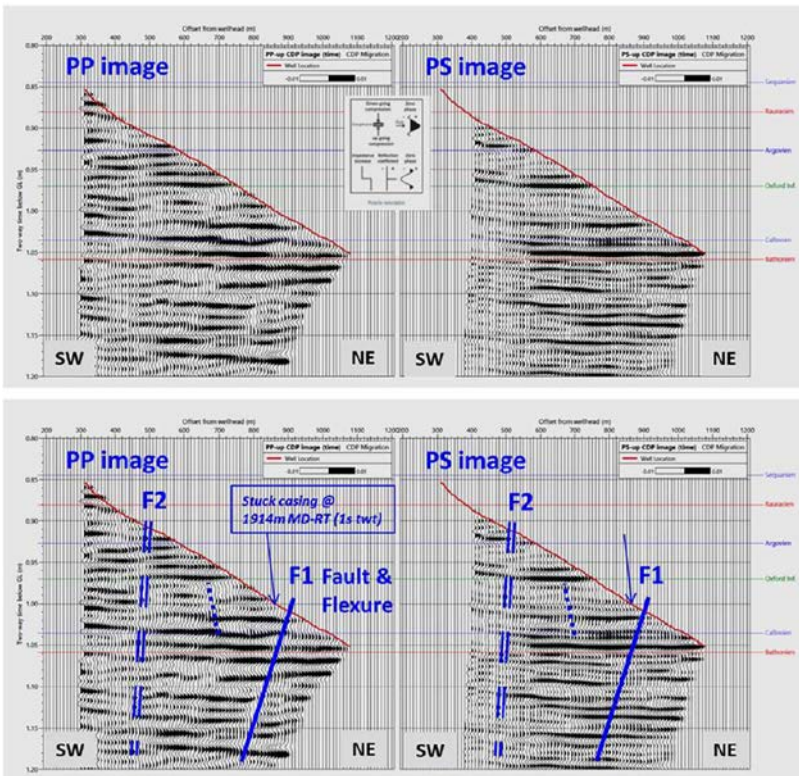


Figure 3.20 PP-up and PS-up reflection images converted to time (tw). Main apparent faults are underlined on the bottom display, on both images (after Naville et al., 2024a,b).

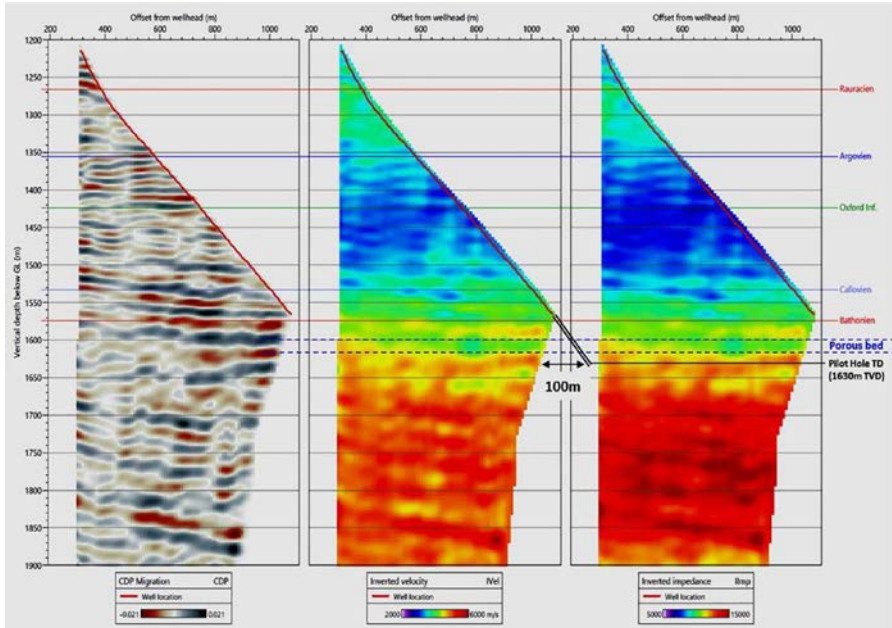


Figure 3.21 *PP-up image inverted, displayed in-depth scale. The VSP inversion predicted a porous zone below/ahead, which was confirmed by the pilot hole drilled after the VSP operation (after Naville et al., 2024a,b).*

## Conclusion

Drilling of a borehole gives geophysicists the opportunity to perform borehole geophysical measurements and record additional data. Borehole geophysical methods can be classified as conventional logging methods, borehole surface imaging methods, hydrogeological logging methods, full waveform acoustic logging and borehole seismic methods such as VSP. Borehole geophysical methods provide high-resolution, localized information on rock properties like lithology, porosity, and fluid content. They also give borehole measurements used to validate and calibrate geophysical models, to convert in depth geophysical models obtained in time, to transform geophysical models into physical or petrophysical models.

With full waveform data, it is possible to conduct a well micro seismic survey based on the analysis of modes reflected and diffracted on acoustic impedance discontinuities within formations or at formation boundaries. Processing of reflected modes leads to depth acoustic sections with very high resolution (a few tens of centimeters) providing an image with a depth of investigation of several meters from the well trajectory. An example of depth acoustic section obtained in a highly deviated

geothermal well shows the benefit of the acoustic method to detect stratigraphic structures observed within a potential geothermal reservoir

Offset 3C VSP data can be processed to obtain PP and PS migrated VSP sections, with a very high resolution. An example of a 3C VSP obtained in the deviated section of a geothermal borehole shows the detection of a low impedance thin layer (10 m thick) which was revealed porous and productive. VSP data, recorded with both a vertical geophone and a hydrophone, allows the detection of fluid waves and flows. As example, in a reconnaissance borehole drilled to determine the geothermal parameters of geological formations, the velocity and attenuation VSP logs show a very good correspondence with respect to the lithological variations observed in the borehole and confirm the presence of flows detected by a fluid wave. Furthermore, a good correspondence between the thermal conductivity profile and the attenuation VSP logs has been noticed.

The field examples show the benefit of using full waveform acoustic data and VSP, in addition to conventional and hydrogeological logs, for the characterisation of potential geothermal reservoirs.

## References

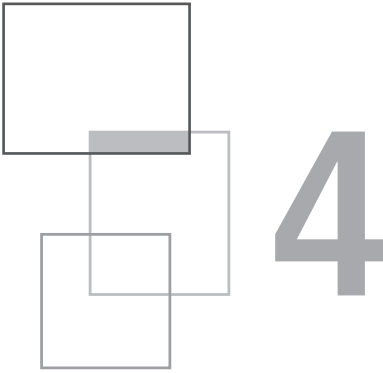
*The writing of the chapter (text and relative figures) is mainly based on the following papers and books.*

- Archie G.E. (1942) The electrical resistivity log as an aid in determining some reservoir characteristics, *Petroleum Technology* 1, 55-67.
- Baird A., Vernier J., Goertz-Allmann B., Langet N., Rebel E., Wienecke S., Oates S. (2024) Improving the detection threshold of borehole DAS for seismic monitoring of CCS fields, paper 1367, 85<sup>th</sup> EAGE annual conference & exhibition, Oslo, Norway.
- Bourbiaux B., Callot J.P., Doligez B., Fleury M., Gaumet F., Guiton M., Lenormand R., Mari J.L., Pourpak H. (2007) Multi-Scale Characterization of a Heterogeneous Aquifer through the Integration of Geological, Geophysical and Flow Data: A Case Study, *Oil and Gas Science and Technology, Rev IFP* 62, 347-373.
- Boyer S., Mari J.L. (1997) *Seismic surveying and well logging*, Editions Technip, Paris.
- Chapellier D. (2001a) Aquifer logging course, from On-line course of geophysics (<http://www-ig.unil.ch/>).
- Chapellier D. (2001b) Petroleum logging course, from On-line course of geophysics (<http://www-ig.unil.ch/>).

- Delay F., Mari J.L., Porel G., Chabaux F., Ackerer P. (2022) Is subsurface geophysics as seismic and acoustic investigations a rescue to groundwater flow inversion?, *Comptes Rendus Geoscience*, Part of Special Issue: Geo-hydrological data & models, <https://doi.org/10.5802/crgeos.157>.
- Didraga C. (2015) DAS VSP recorded simultaneously in cemented and tubing installed fiber optic cables, TU N11814, 77<sup>th</sup> EAGE annual conference & exhibition, IFEMA Madrid, Spain.
- Faust L.Y. (1953) A velocity function including lithologic variation, *Geophysics* 18, 271-288.
- Gaillard T., Moreau M., Mari J.L. (2024) Seismic and stratigraphic characterization of karstogenic horizons in a sequence of carbonate deposits: Example of the Dogger limestones of the Poitou threshold, *Journées Scientifiques AGAP Qualité 2024, E3S Web of Conferences 504, 05005*, <https://doi.org/10.1051/e3sconf/202450405005>
- Hardage B.A. (1985) *Vertical seismic profiling*, Part A: principles, Part B: advanced concepts, Geophysical Press, London.
- Hardage B.A. (1992) *Cross well Seismology and Reverse VSP*, Geophysical Press, London.
- Hirabayashi N., Dahlhaus L., Kumar R., Jocker J., Wielemaker E., Khaitan M.L., Naville C. (2024) Analysis of geologic structures using deep sonic imaging, in *International Meeting for Applied Geoscience & Energy*, <https://doi.org/10.1190/image2024-4091360.1>.
- Kazemi K. (2009) Seismic imaging of thrust fault structures in Zagros Iranian oil fields, from surface and well data, PhD, Université de Cergy-Pontoise, [https://hal.inria.fr/file/index/docid/414628/filename/Thesis\\_kazemi.pdf](https://hal.inria.fr/file/index/docid/414628/filename/Thesis_kazemi.pdf).
- Lesnikov V., Allanic C. (2014) DAS VSP acquisition: perspective and challenges, WS15-D01, 76<sup>th</sup> EAGE annual conference & exhibition, Amsterdam RAI, The Netherlands.
- Mari J.L. (1989) Q-log determination on downgoing wavelets an tube wave analysis in vertical seismic profiles, *Geophysical prospecting* 37(3), 257-277, <https://doi.org/10.1111/j.1365-2478.1989.tb02206.x>.
- Mari J.L. (2015) *Signal processing for geologists & geophysicists*, e-book, <http://books.ifpenergiesnouvelles.fr/ebooks/signal-processing>.
- Mari J.L., Coppens F. (2003) *Well seismic surveying*, Éditions Technip, Paris, ISBN 2-7108-076-9, ISSN 1271-9048.
- Mari J.L., Delay F. (2024) Stoneley wave detection by acoustic interferometry: Estimation of shear velocity of a geological formation, *Journées Scientifiques AGAP Qualité 2024, E3S Web of Conferences 504, 02004*, <https://doi.org/10.1051/e3sconf/202450402004>.

- Mari J.L., Porel G. (2007) 3D seismic imaging of a near – surface heterogeneous aquifer: a case study, *Oil and Gas Science and Technology, Rev IFP* 63, 179-201, <https://doi.org/10.2516/ogst:2007077>.
- Mari J.L., Porel G. (2024) The hydrogeological experimental site of Poitiers: Hydrogeological versus geophysical investigations, Journées Scientifiques AGAP Qualité 2024, E3S Web of Conferences 504, 05003, <https://doi.org/10.1051/e3sconf/202450405003>.
- Mari J.L., Vergniault C. (2018) *Well seismic surveying and acoustic logging*, EDP-Sciences, <https://doi.org/10.1051/978-2-7598-2263-8>.
- Mari J.L., Arens G., Chapellier D., Gaudiani P. (1999) *Geophysics of reservoir and civil engineering*, Editions Technip, Paris, ISBN 2-7108-0757-2.
- Mari J.L., Delay F., Porel G., Gaudiani P. (2021) Characterizing flow in the first hundred-meter depth of a fractured aquifer using hybrid seismic methods, acoustic logging, and flow log measurements, *Oil & Gas Science and Technology, Rev. IFP Energies Nouvelles* 76, 62, <https://doi.org/10.2516/ogst/2021048>.
- Mari J.L., Delay F., Voisin C., Gaudiani P. (2023) Active and passive acoustic logging applied to the detection of preferential flow in a sedimentary aquifer, *Science and Technology for Energy Transition*, <https://doi.org/10.2516/stet/2023018>.
- Mari J.L., Mendes M. (2019) *Seismic imaging: a practical approach*, EDP Sciences, <https://www.edp-open.org/seismic-imaging-a-practical-approach>.
- Mari J.L., Münzberger P., Colbach R., Peignard L., Al Khatib H. (2024) Contribution of 2-component VSP measurements to the characterization of a geothermal site, paper 715, 85<sup>th</sup> EAGE annual conference & exhibition, Oslo, Norway.
- Mari J.L., Porel G., Delay F. (2020) Contribution of Full Wave Acoustic Logging to the Detection and Prediction of Karstic Bodies, *Water* 12(4), 948, <https://doi.org/10.3390/w12040948>.
- Mars J., Glangeaud F., Boelle J.L., Vanpe J.M. (1999) Wave separation by an oblique polarization filter, PSIPP'99, First international symposium on Physics in Signal and Image Processing, 18- 19 January 1999, Paris, France, 94-108.
- Mateeva A., Lopez J., Mestayer J., Wills P., Kiyashchenko D., Yang Z., Berlang W., Detomo R., Grandi S. (2013) Distributed acoustic sensing for reservoir monitoring with VSP, *The Leading Edge* 32, 1278-1283.
- Mateeva A., Lopez J., Potters H., Mestayer J., Cox B., Kiyashchenko D., Wills P., Grandi S., Hornman K., Kuvshinov B., Berlang W., Yang Z., Detomo R. (2014) Distributed Acoustic Sensing for reservoir monitoring with Vertical Seismic Profiling, *Geophysical Prospecting* 62, 679-692.
- Mestayer J., Cox B., Wills P., Kiyashchenko D., Lopez J., Costello M., Bourne S., Ugueto G., Lupton R., Solano G., Hill D., Lewis A. (2011) Field trials

- of distributed acoustic sensing for geophysical monitoring, 81st SEG Annual International Meeting, Expanded Abstracts.
- Naville C. (2024) IFPEN-APS-PPZG: Orientation of 3 component rig source VSPs, in IFPEN Online presentation, <https://www.ifpenergiesnouvelles.fr/breve/ifpen-aps-ppzg-orientation-3-component-rig-source-vsp>.
- Naville C., Bailey J., Humphries M., Vicelli J., Hanot F. (2024a) HF/HR VSP acquisition processing, and interpretation in the deviated section of the high angle geothermal borehole of Grigny GGR5, targeting intra Dogger thin, porous beds, Science and Technology for Energy Transition, <https://doi.org/10.2516/stet/2024051>.
- Naville C., Soulas S., Antics M., Ungemach P. (2024b) Illustration of a land VSP field operation with vibrator source around the drilling site, Grand Paris area, France, in Researchgate, <https://doi.org/10.13140/RG.2.2.10611.09765>.
- Raymer L.L., Hunt E.R., Gardner J.S. (1980) An improved sonic transit time to porosity transform. Trans. SPWLA 21st Annual Logging Symposium, July 8-11, 1980, 1-12.
- Rosenbaum J.H. (1974) Synthetic microseismograms: logging in porous formation, *Geophysics* 39, 14-32.
- Serbutoviez S., Naville C., Throo A., Bruneau J. (2003) 3C VSP Processing and Interpretation, in IFPEN Online presentation, November 2003, revised July 2020, <https://www.ifpenergiesnouvelles.com/sites/ifpen.fr/files/inline-images/NEWSROOM/Actualit%C3%A9s/2020-True%20Amplitude%203C-VSP-method.pdf>.
- Serra O., Serra L. (2000) *Diagraphies, Acquisition et applications*, Editions Serralog, ISBN: 9782951561601.
- Willis M.E. (2022) Distributed Acoustic Sensing for Seismic Measurements – What Geophysicists and Engineers Need to Know, Society of Exploration Geophysicists: Houston, TX, USA, pp. 45–52 <https://doi.org/10.1190/1.9781560803850>.
- Wyatt K.D., Wyatt S.B. (1982) Determination of subsurface structural information using the vertical seismic profile, *Geophysics* 47(7), 1123-1128.
- Wyllie M.R.J., Gregory A.R., Gardner L.W. (1956) Elastic wave velocities in heterogeneous and porous media, *Geophysics* 21, 41-70.



# Towards a revisited geothermal conceptual model in the Upper Rhine Graben

A. Genter, C. Baujard, C. Glaas and V. Maurer

---

New concepts of deep geothermal energy in Western Europe were mainly initiated by a French-German consortium in the Upper Rhine Graben, at Soultz-sous-Forêts, France. A series of deep boreholes were drilled till 5 km deep within a crystalline basement, reputed tight and lying below the former Pechelbronn oil field where the first electric log was achieved for detecting petroleum in sedimentary reservoirs in the 1920s.

The main geothermal concept developed at Soultz-sous-Forêts, was to create from scratch, a down-hole heat exchanger by injecting water via a vertical borehole in a very low matrix porosity crystalline rock and by pumping it out hotter via deviated boreholes. It was derived from geothermal projects developed worldwide (US, Japan, Germany, UK), called Hot Dry Rock (HDR). However, after the achievement of several deep drilling at Soultz, the HDR concept slightly evolved to become Enhanced or Engineered Geothermal Systems (EGS), consisting of pumping hot

water already present in the underground. Based on an extensive deep geoscientific characterization including geophysical exploration and geophysical logging, this chapter explains how a better knowledge of the geothermal resource allows improving the conceptual model of this deep resource and thus how to optimize geothermal targets by derisking drilling depths and well design.

## 4.1 Geothermal development in the Upper Rhine Graben

In Western Europe, deep geothermal energy started in the 90s by a French-German scientific cooperation in the Upper Rhine Graben, at Soultz-sous-Forêts (SsF), France. This research site was the location of many deep geothermal wells reaching 5 km in the Carboniferous crystalline basement, various geophysical logging including borehole imagery logs, well testing and hydraulic circulation. After an extensive phase of purely scientific research on the underground, the site slowly evolved to a pre-industrial site by building a first binary plant producing electricity in 2008. However, due to severe corrosion induced by the high salinity of natural geothermal fluids, after the dismantling of the first plant, a second but more robust binary plant was constructed and operated in 2016 by Electricité de Strasbourg. Since, it has been producing electricity on the French grid with an installed capacity of 1.7 MWe.

From the SsF experiment, many spin-offs have been created or new competitors tried to duplicate the Soultz concept in the Upper Rhine Graben, mainly in France, Germany and Switzerland. Thus, Landau and Insheim geothermal plants were developed in the Rhine-Palatinate in Germany whereas Rittershoffen plant and Illkirch sites were developed in Alsace (Figure 4.1). Rittershoffen, which is a real SsF cousin, is producing 24 MWth of energy since 2016 to a biorefinery with geothermal wells having a reservoir depth divided by two in comparison with SsF reservoir depth. Therefore, after several decades of geothermal research, exploration and development in Northern Alsace, two geothermal plants are commercially operating in France (SsF and Rittershoffen). In the German part of the URG, three plants are also operating (Landau, Insheim, and Bruchsal) (Figure 4.1). The Bruchsal geothermal doublet was drilled in the 80s in a fractured reservoir on the Eastern side of the URG and penetrated Permo-Triassic sandstones considered as a hydrothermal fractured/faulted reservoir (Kolbel et al., 2020). Those sites have penetrated the sedimentary formations of the graben and, for some of them, the deeper crystalline basement (Soultz, Rittershoffen, Insheim, Landau). In Switzerland, at Riehen, a heat plant has been operating from several decades but is located on the Eastern shoulder of the URG (Figure 4.1). This site deliver heat from geothermal hot water pumped in the Middle Triassic reservoir composed of fractured carbonates. In the past, for various reasons, several geothermal projects were stopped in the URG (Trebur, Brühl, Cronenbourg, Basel). For instance, at Cronenbourg in the suburb of Strasbourg, the unique deep geothermal well at 3220 m, drilled in 1980, was not

permeable enough in the Permian sandstones and this site was abandoned without any attempt of flow enhancement. In Basel, the occurrence of an induced seismic event was felt during the shut-in of a post-hydraulic stimulation operation done in a 5 km geothermal well drilled in a granite. A magnitude higher than 3.4 was then felt in 2006 causing the full stop of the Basel geothermal project (Häring et al., 2008).

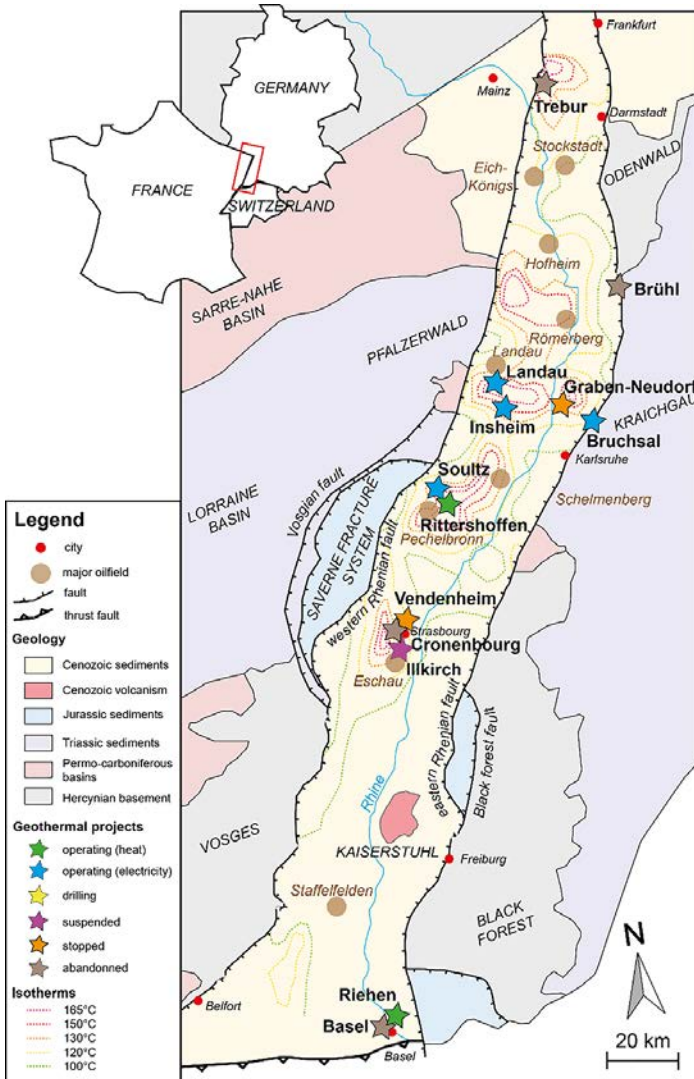


Figure 4.1 Geothermal projects in Northern Alsace, and Southern Rhine Palatinate and Baden Württemberg.

More recently, in the Strasbourg area (Vendenheim), a new competitor came for developing geothermal projects for producing electricity. However, after the drilling of two deep wells at about 6 km measured depth, a series of man-made seismic events were felt on surface during well testing or various operations between 2019 and 2021 with a local maximal magnitude of 3.9 (Schmittbuhl et al., 2021). It turned out that social acceptability became a real issue in this urban area because some structural damages were observed on houses around Strasbourg as well as on the German side around the city of Kehl. About 4000 requests from inhabitants have been made due to the occurrence of cracks observed on the walls of their houses. In parallel, by using the precautionary principle, the Illkirch geothermal project which was under development South of Strasbourg at the same time, was suspended by the French mining authorities in order to anticipate any further issue related to man-made seismicity. Now, the Vendenheim project has a new geothermal owner, but the site is still stopped by the mining authorities. In parallel, the Illkirch project is still suspended even if it did not cause any nuisances. The operator is waiting for the possibility of drilling at least a second geothermal well if the social acceptability is acceptable. Moreover, new geothermal projects are under development in Northern Alsace in the area of SsF with a geothermal well that could be planned for 2025 for exploiting the reservoirs at the fractured interface between the deep sediments and top basement.

In parallel to the geothermal development of the URG, a new era is rising with the booming of geothermal lithium. Several French and German companies aim to extract the geothermal lithium which is dissolved into the geothermal brine with a concentration ranging between 160 and 210 mg/L. After a phase of research for extracting lithium from the brine and then producing lithium carbonate of battery grade quality, several companies are currently obtaining geothermal and lithium leases in order to conduct pre-feasibility and feasibility studies before investment decisions for conducting industrial projects for producing lithium.

## 4.2 Evolution of the geothermal concept during the SsF adventure

The basic concept started on the Hot Dry Rock (HDR) concept considering that many geothermal wells reached interesting temperatures, but their flowrates were too low, even though fully dry, for reaching viable economic balance. Therefore, based on previous geothermal research dealing with the creation of artificial heat exchanger by hydraulic fracturing in US, UK, Japan or Germany (Figure 4.2), a jointed European research site was selected in Alsace, Eastern part of France, based on well-known temperature field measured in the former oil mines and oil wells close to Pechelbronn where the Schlumberger brothers did their first geophysical well logging in 1927 for detecting hydrocarbon reservoirs based on electrical measurements.

Firstly, the French-German SsF project started based on the Hot Dry Rock (HDR) concept. It consists in exploiting the vast energy resource that resides as heat in the low-permeability rocks which underlie most continental regions of the Upper crust at practically drillable depths. Thus, it was planned to drill a vertical well in the area of SsF because the geology was very well-known from several thousand of former petroleum wells mainly drilled in the Cenozoic reservoirs where interesting temperatures could be accessible at low drillable depths (Figure 4.2). Therefore, a first vertical well, called GPK-1, was planned to intersect about 1400 m of Cenozoic and Mesozoic sediments before to penetrate into the Carboniferous top crystalline basement.

In such theoretical HDR concept, at the end of each drilling operation, it was planned to inject fresh water under pressure in order to create artificial fractures that can be used as a heat exchanger. Then, it is needed to drill and then to inject under pressure in a second vertical well for connecting hydraulically the first one by creating newly-formed planar fractures in the deep heat exchanger. Considering the absence of natural permeability, fresh water must be injected from one well (injection well), and by heat transfer taken on the newly created artificial fractures, the cold injected water becomes hotter and could be produced at surface in the second well (production well) for producing steam and thus electricity. The SsF project started with this HDR concept by developing permeability in a crystalline basement lying below the super-hot sedimentary cover.

After the drilling of the GPK-1 well in 1987, the main findings were a very high geothermal gradient in the first km with about 110 °C. However, below those depths, the geothermal gradient declined sharply indicating the occurrence of natural fluid circulations within the natural fractures inside the Triassic formations and the crystalline basement, the uppermost sedimentary cover acting as a thermal insulator. It turned out that 140 °C was measured at 2000 m depth in the granite instead of the 200 °C planned initially. The second main finding is the occurrence of a native brine within the crystalline basement proving that the top basement between 1400 and 2000 m depth was not tight as anticipated by many geoscientists (Vuataz et al., 2000). By taking into account those findings, the capacity to develop post-stimulation permeability was investigated considering two cases. First, the top basement was considered as a medium with a residual permeability due to individual natural fractures partly sealed by hydrothermal deposits. Its stimulation could lead to preferential flow paths and thus a rapid cooling. Therefore, a second option was also considered. Indeed, the deepest depths probably correspond to complex fractured rock where closed natural fractures took place within brittle crystalline rocks (Gerard et Kappelmeyer, 1987). In this deeper case, it would be possible to stimulate a volume of fractured rocks and thus to engineer structural linkages between the future doublet for extracting large amounts of heat by circulation through this created down-hole heat exchanger.

However, before to drill at great depths, it turned out that for better exploring the Soultz basement an old petroleum well was deepened and fully cored in 1990-1991 from the Middle Triassic limestone to the deep granite from 930 till 2230 m depth.

This newly exploration well with a low borehole diameter brought new geological characterization about the natural fracture system. The main finding was the confirmation of highly fractured zones with associated hydrothermal alterations in this shallow basement reservoir. Natural fractures are organized in clusters and intense argillic hydrothermal alteration took place in the granite evidencing the impact of paleo or recent fluid circulations (Genter et al., 2010). It was also shown that the natural fracture density in the granite was more than three times higher than in the Permo-Triassic sandstone (Genter et al., 1997).

Then, in order to achieve hotter temperature conditions, it was planned to deepen the GPK-1 geothermal well from 2000 to 3600 m in 1992 and to drill a second geothermal well, GPK-2, from surface to 3890 m in 1995 which is located about 500 m apart from GPK-1. The temperatures measured at total depth of those two wells GPK-1 and GPK-2, were around 160 °C and thus still far from the 200 °C expected. Many tests were conducted in those wells including hydraulic testing, tracer tests, hydraulic stimulations and circulation tests in this intermediate reservoir (Schill et al., 2017). Induced seismicity was monitored both in surface but also in some former oil wells deepened till the top basement (Cuenot et al., 2008; Dorbath et al., 2009).

Finally, GPK-2 was deepened to 5058 m measured depth for reaching 200 °C at total depth and two additional deep geothermal wells, GPK-3 and GPK-4 were drilled to about 5000 m and reached 200 °C (Genter et al., 2010). As the HDR concept was still in mind, it was planned that GPK-2 and GPK-4 would be two production wells and GPK-3 an injection well. All these new drill pads were drilled from the same platform for optimizing the geothermal operations (stimulation, circulation test and future exploitation). Natural permeability was observed in the granitic sections of all wells mainly related to hydrothermally and fractured sections (Evans et al., 2005). Even if permeability indicators were observed in each well, natural artesian flowrate was too low for a viable economic production. Therefore, each well, which has an open-hole section between 4500 and 5000 m, was hydraulically and chemically stimulated. These stimulations enhanced significantly the hydraulic yield of the three reservoir sections (2000 m, 3500 m, 5000 m), in some instances by about two orders of magnitude (Schill et al. 2017). Kohl et al. (1997) shown that complex hydraulic flow regimes are not restricted to near-well vicinities but rather extend large distances until reaching high capacity far-field faults. The most effective method for enhancing the flow, was the hydraulic stimulation rather than the chemical ones.

In the follow-up geothermal projects such as at Landau and Insheim, the concept of enhancing the naturally most productive reservoir level at the top of the granitic basement was applied, as well as specific hydraulic stimulation techniques (Schindler et al., 2010). Several long-term circulation tests including tracer tests were carried out at SsF for demonstrating that the deep wells are connected after stimulation on a large open geothermal reservoir producing a very saline brine (Sanjuan et al., 2006).

From 2011, the new Rittershoffen geothermal project, located less than 10 km from SsF, was launched for producing heat at high temperatures (170 °C) and high flowrate (>70 L/s) for providing geothermal heat to a biorefinery. The first vertical well

was drilled at 2560 m and targeted a local normal fault steeply dipping in the fractured granite. This first well, GRT-1, was not permeable enough and was thermally, chemically and hydraulically stimulated. Its hydraulic performance was enhanced by a factor 5 and was considered as a successful geothermal well (Baujard et al., 2017). Then, the second well, GRT-2, was drilled to 3200 m and inclined from the same pad and targeted the same permeable normal fault which was better defined thanks to a new 2D seismic survey (representing 16 km length) done in 2013 calibrated with the geological results of the first well. The highly deviated well, GRT-2, crosscut this local fault and its damage zone and was immediately permeable at the end of the drilling operation without any stimulation operations (Baujard et al., 2017). Thus, the first vertical well could be considered as an EGS-like well whereas the second one was fully hydrothermal because several permeable channels bearing by the normal fault were crosscut and contributed to the flowrate. This Rittershoffen EGS project demonstrated that permeable faults took place at great depth, but the main challenge is to adapt the well trajectories with the complex geometry and internal architecture of those local faults. To fill the gap between the lack of deep knowledge of the geothermal resource (lithology, fault geometry, permeable features) and the design of future geothermal wells, innovative geophysical exploration is one of the main tools.

From 2016, GPK-2 is the unique production well at SsF with a mass flowrate of about 30 kg/s. Therefore, both GPK-3 and GPK-4 could be used as reinjection wells. It turns out that it is easier to produce a geothermal fluid with a relevant flowrate, assisted by a production submersible down-hole pump because the wells are artesian, than to reinject in one well only. Thus, it is the reason why GPK-4 became an injection well. Moreover, the fact to use two reinjection wells limits the seismic activity and consequently the occurrence of large felt seismic event. In parallel, from 2016 the geothermal doublet at Rittershoffen is producing a brine at 168 °C in surface with an average flowrate of 80 kg/s.

From 2010 to 2019, a new geothermal project was launched close to Strasbourg at Illkirch (Figure 4.1). It targeted a deep normal fault having a vertical off-set of about 800 m located at the interface between the Lower Triassic sandstone and the top crystalline basement. Thus, a new 2D seismic reflection survey (35 km) was acquired in 2015 as well as other geophysical methods (gravity, aeromagnetic). However, this faulted interface was tight during drilling operation. It could be interpreted as the occurrence of secondary argillic clay halo that plugged this fault due to the past activity of the hydrothermal system (Glaas et al., 2021a). Thus, this first highly deviated well, GIL-1, was deepened to 3800 m depth in the crystalline basement which evidenced some permeability indicators and a high fracture density (Baujard et al., 2022, Glaas et al., 2021b). A stimulation program including hydraulic and chemical operations was developed for enhancing the initial productivity conditions. However, due to felt induced seismicity taking place at Vendenheim (Figure 4.1) and generated by another geothermal operator, the local mining authority suspended unilaterally the Illkirch project, and the second well is still pending to the Alsace prefecture decision.

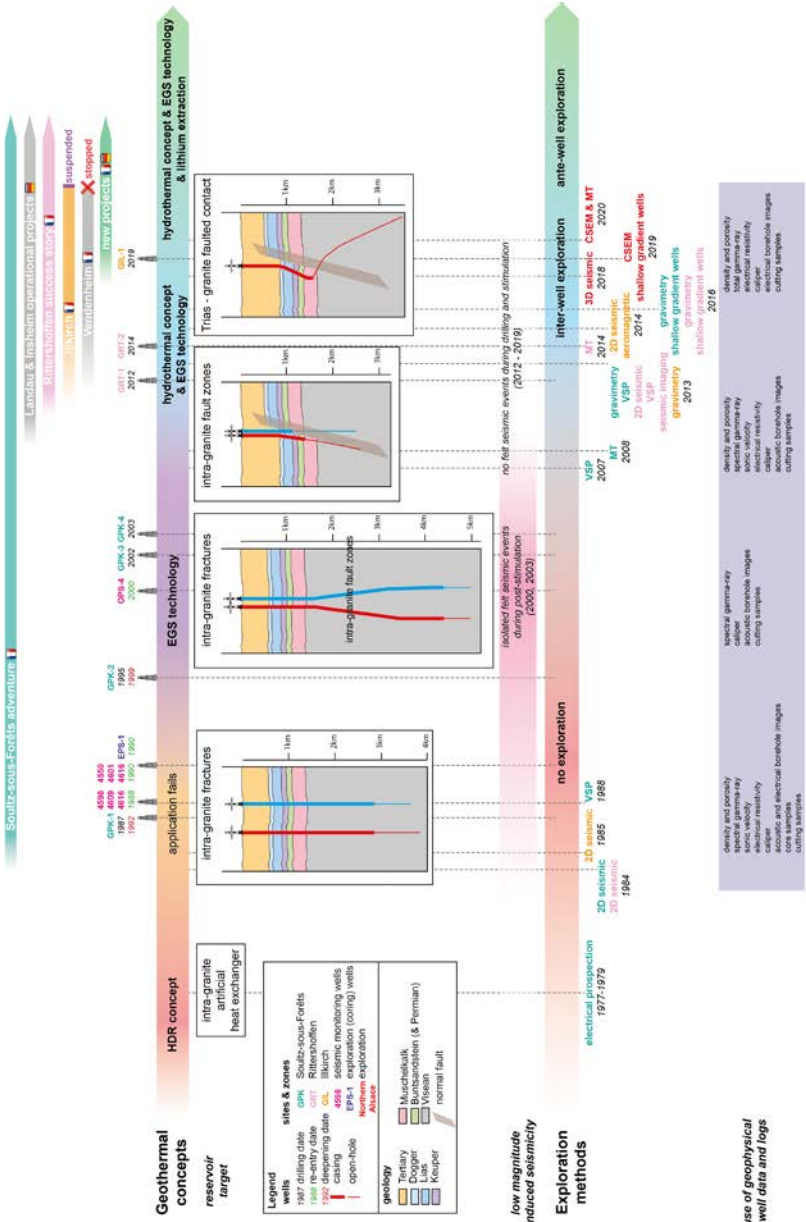


Figure 4.2 Evolution of the geothermal concepts in the Upper Rhine Graben based on the Soultz-sous-Forêts pioneered geothermal project.

Therefore, EGS sites in the URG could be considered as convective-dominated systems characterized by the occurrences of some open natural fractures. The natural fluids circulating within the fracture/fault system could be pumped via suitable borehole trajectories. The shallower Soultz wells were drilled till 2000 m vertically intersecting a steeply dipping fracture system. Therefore, the probability that vertical boreholes intersect subvertical natural fractures was quite low and complex stimulation strategies were needed to connect the open-hole section of the geothermal wells with the partly permeable natural fracture system.

For more recent and future projects in the URG, inclined or deviated wells could be drilled into the nearly vertical fracture system that allowed easier connections to the most convective and permeable fractures (Vidal and Genter, 2018). Then, from the purely HDR concept developed at SsF for creating from scratch a down-hole heat exchanger, the occurrence of natural brines trapped with complex steeply dipping fractures, the initial geothermal concept evolved to Enhanced or Engineered Geothermal Systems (EGS) in order to enhance the hydraulic flowrate. Generally, there is no need to restimulate the geothermal wells during long-term exploitation. There is no decline of the production neither increases of the reinjection pressure, which is below 20 bars both at SsF and Rittershoffen. Then, the stimulated fractured reservoir acts as a hydrothermal reservoir partly reconnected to the far-field due to the impact of the stimulation techniques. Therefore, we can state that there is a kind of physical continuum between EGS, with no or low initial permeability and hydrothermal system, which are prone to be hydraulically improved by post-drilling stimulations.

### 4.3 Pre-exploration phase

The structural and geological context of the SsF area in the URG can be outlined by a thick sedimentary cover of 1400 m made of Mesozoic (Permo-Triassic to Middle Jurassic) and Cenozoic formations lying on the top of a Carboniferous granite horst, limited by local faults striking NNE-SSW to NE-SW dipping 60 to 70° West. There is a huge unconformity between the Mesozoic and the Cenozoic sedimentary successions due to an emersion or an uplift before the Cenozoic. By comparison with the Paris Basin geology, that means that many Mesozoic sedimentary units are lacking like the top Jurassic and all the Cretaceous. As this area was characterized by several tectonic phases during the emplacement of the Rhine Graben, the geophysical methods deployed on surface and sometimes in the wells must consider the specific geological background of this area.

During purely HDR development at SsF, geophysical exploration was rather limited because the basic idea was not to find an aquifer or a specific geological unit but deep-seated brittle rocks showing very low matrix porosity and high temperature conditions. Therefore, there was no real geophysical exploration phase at SsF even if research based on surface electrical methods were done between 1977 and 1979 in order to target deep geothermal resources in the basin (Baudu et al., 1980).

However, for designing properly a vertical deep drilling operation, which is risky and costly, there was a strong need to characterize the overlying sedimentary units. Thus, 2D vintage seismic reflection profiles done for oil exploration in 1984 mainly to image the Mesozoic and the Cenozoic formations were reprocessed and reinterpreted for geothermal targets at the sedimentary-basement interface (Munck et al., 1979). Moreover, a series of former oil wells was used for calibrating the reprocessed 2D seismic profiles and stratigraphy. Therefore, the provisional geological profile of the first well GPK-1 between surface and the top basement was very accurate thanks to the high density of old petroleum wells drilled in this area. At regional scale, older public gravity and magnetic measurements (Rotstein et al., 2006) indicated that the Bouguer anomaly was delineating a large area corresponding to a granite batholith already proved by a core taken in the old petroleum well, 4616, located at SsF that reached the top of the granitic basement at 1380 m depth.

With the drilling of GPK-1 and its stimulation in 1988, three old petroleum wells surrounding the site (4598, 4601, 4616) were reopened in order to instrument down-hole three-directional permanent probes for monitoring induced seismic activity during stimulation operation. Those probes were designed to withstand high temperature (125 °C) and severe corrosion conditions at the bottom of the holes.

In parallel to the coring of the HDR exploration well (EPS-1), three old petroleum wells, 4550, 4601 and 4616 were deepened in 1990 to about 1500 m in order to instrument down-hole seismic sensors. The fact that those sensors would have been installed in the deep Triassic sandstone or the Carboniferous basement, allowed enhancing detection of very low magnitude events and reducing the uncertainty on the location of the induced events. An additional peripheral seismic observation well, OPS-4; was drilled in 2000 and located less than 2 km south of GPK-2. It started from surface to 1540 m in the Lower Triassic formation in order to reduce azimuthal bias during the seismic monitoring. In parallel, a permanent network of surface seismic stations was installed and regularly densified according to stimulation and circulation phases.

The drilling of the first well GPK-1 to 2000 m and its later deepening to 3600 m were also a good opportunity to use innovative image log tools based on acoustic (BHTV, UBI) and electrical methods (FMS, FMI, ARI). In 1987, FMS tool was used probably for the first time in continental Europe for characterizing the fracture depth, the fracture azimuth and their dip in the granite section. Moreover, drilling induced tensile fractures were also characterized for measuring the orientation of the main horizontal stress. Detailed interpretation of standard geophysical logs in the basement of GPK-1 (Traineau et al., 1991) was achieved as well as detailed comparison between borehole image logs and continuous coring done in EPS-1 (Genter et al., 1997). During this early phase of reconnaissance (1987-1991), VSP (Vertical Seismic Profiling) was carried out to better image the fault structures close to the GPK-1 well and for improving the velocity model allowing an accurate location of seismic events to be recorded during stimulation experiments. Moreover, results of VSP were used to reprocess two vintage reflection seismic lines crossing the SsF area. Based on the interpretation of five 2D seismic lines, a 3D geological

model was built in a geomodelling tool (Renard and Courrioux, 1994). After drilling operations, various geophysical logging tools were used in the geothermal wells mainly at SsF. They aimed to characterize both the petrography of the crystalline basement (bulk density, sonic velocity), the hydrothermal alteration due to severe geochemical interactions with natural fluids (spectral gamma ray with U, K and Th, resistivity logs), and temperature and flow logs for identifying discrete permeable fractures. For example, the most striking observation derived from spectral gamma ray, was the significant increase of K related to argillic alteration within fractured zones (Traineau et al., 1991). It corresponds to the precipitation of clay minerals bearing potassium like illite related to fluid circulation.

Acoustic and electrical resistivity image logs were also extensively used for mapping in situ, the orientation of natural fractures as well as orientation of the principal horizontal stress field based on the observations of drilling induced tensile fractures or borehole breakouts (Figure 4.3). Caliper logs were also used systematically during the technical phases for cementing operations. By using various geophysical logs acquired in the Soultz wells, many research attempts have been done by using statistical tools like Principal Component Analysis, Hierarchical Ascending Classification or neuronal network for mapping clay-rich zones in the basement.

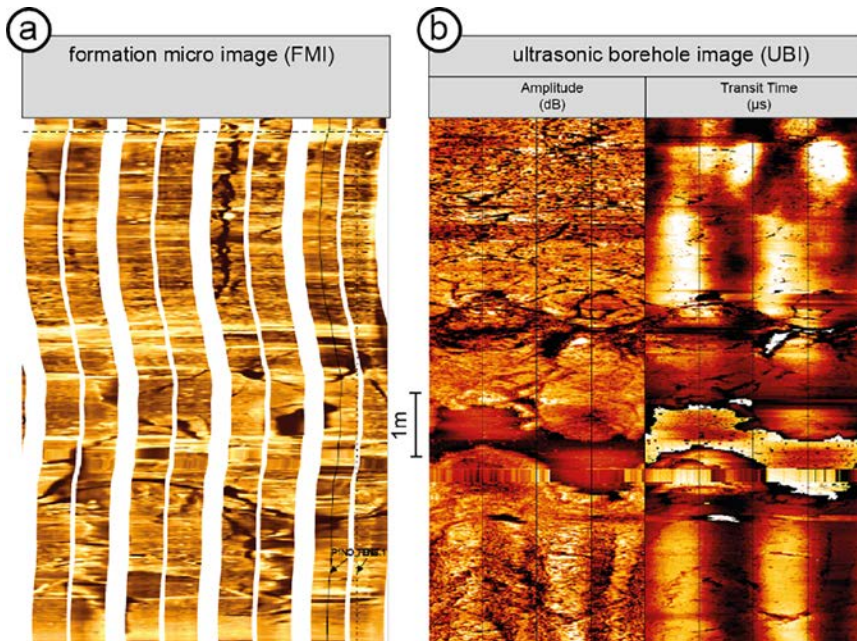


Figure 4.3 Example of borehole imagery logs acquired in the Lower Triassic sandstone (left) or crystalline basement (right) of the geothermal well GRT-2. Natural fractures appear as sinusoidal traces on both electrical and acoustic borehole image logs. Nearly horizontal stratification, and vertical induced drilling fractures are also visible on the electrical image log (left).

During the development of the Rittershoffen project, again vintage 2D seismic lines were used for targeting the first vertical well GRT-1 drilled at 2560 m in the granite. However, those reflection seismic data were mainly acquired for imaging oil embedded in Cenozoic sedimentary reservoirs. Thus, the deepest sediments and the related fault network were not imaged properly. It is the reason why a new reflection seismic campaign was achieved at Rittershoffen as well as a three-component VSP for better targeting the second well, GRT-2, drilled to 3196 m. Then a new 3D geological model was built, and the second deviated well was targeted to the North with the same technical design as the first well (Baujard et al., 2017). This well was drilled parallel to the main local fault and about six permeable fractures crosscut the GRT-2 well in the sandstone and in the granite. This highly deviated well became the production well in which a down-hole line shaft pump was set. Consequently, the first well, GRT-1, became the reinjection well which is mainly crosscut by a branch of the local fault in the granitic section. From 2016, geothermal exploitation is running properly by using this doublet.

After this success story in Rittershoffen, the Illkirch project started in 2010. From the lessons learned at SsF and Rittershoffen, two main sets of geophysical exploration methods were carried out. First, vintage 2D seismic lines were reprocessed and additional new 2D seismic lines were acquired. It aimed to better define the geological and structural properties in this part of the Rhine Graben where the sedimentary layers are rather thick. In this part of the Rhine graben, this sub-basin could reach more than 4000 m thick. In parallel to this new seismic acquisition campaign, two gravity data acquisitions were made in 2013 and 2016 for refining the existing datasets. Moreover, a high-resolution aeromagnetic survey was conducted in 2015 in this area. Both geophysical methods aimed to determine the nature of the deep basement (granite, schist, metamorphic rocks, ...), which was only known from outcrops lying in the Vosges mountains. Therefore, a better image of the local faults and layers was achieved by combining in a geomodeller, both vintage and recent 2D seismic lines. Then, a combined interpretation of gravimetric and magnetic data correlated with a structural interpretation of 2D seismic lines made it possible to highlight nature and the structure of the deep basement (Edel et al., 2018). Moreover, the drilling of the deepest part of the GIL-1 is well confirmed that the deepest basement is characterized by brittle crystalline formation. The drilling of this deviated well perpendicular to a local fault at Illkirch between 2018 and 2019 demonstrated that the faulted interface between the Triassic sandstone and the granite was tight, that the basement was made of granite as predicted by aeromagnetic results and that permeable fractures took place in the crystalline basement. Because of felt induced seismicity triggered by another competitor at Vendenheim in the northern part of Strasbourg during this period, the Illkirch geothermal project was temporarily suspended by local mining authorities in 2021 till now.

In Northern Alsace, a 3D seismic reflection campaign was carried out in 2018 over a surface of about 180 km<sup>2</sup> in superimposition with the geothermal licenses and concessions hold by Électricité de Strasbourg. It was the first 3D seismic survey done in France for deep geothermal energy. The large surface of the 3D seismic acquisition allowed having an underground image at a regional scale rather than at

the level of a single project, which helped in terms of interpretation of the continuity of the structures and of the horizons. The target is to obtain a better geological and structural image of the sedimentary layers and the fault system by focusing on the deep formations in the basin, e.g. the Lower Permo-Triassic sandstone and the top crystalline basement. Therefore, special attention has been paid on the faults intersecting the top basement for evaluating how they rooted into it (Figure 4.4). The main striking parameters of this 3D acquisition correspond to broadband seismic ranging from 2 Hz up to 96 Hz delivered by 62000 lbs vibro-trucks and 27000 vibrated points. Various former old petroleum wells, used for the seismic interpretation, are clustered around the SsF and Rittershoffen geothermal wells (Figure 4.4). The two operational EGS sites of SsF and Rittershoffen were comprised within the 3D acquisition area. It represents a tangible advantage for better calibrate the 3D results from seismic in terms of geology by comparison with the geological layers observed in the boreholes of SsF and Rittershoffen. In order to assess the imaging quality of the deep faulting, the pre-processing flow chart was validated by a 3D migration of the full cube. Iteratively built from picked faults and key horizons on delivered volumes, the 3D structural model was built according to the results of an Advanced Fault Enhanced volume. To refine the fault definition and location, a fault-oriented velocity model was carried out (Toubiana et al., 2020).

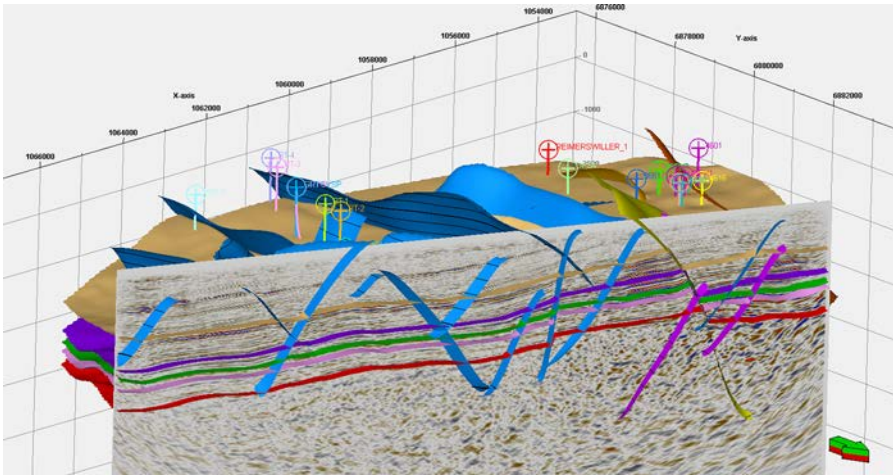


**Figure 4.4** Local 3D model of the geological layers and the main steeply dipping faults in Northern Alsace derived from 3D seismic interpretation. The green arrow indicates the North, and X and Y axes the geographic coordinates. On surface, geothermal and former oil well names from Rittershoffen (left) and SsF (right) geothermal sites are represented. Geological legend for the layers from surface to the deep basement: (brown) Eocene with top of the Dolomitic Zone, (purple) Upper Trias with top of the Keuper, (green) Middle Trias with top of the Muschelkalk, (pink) Lower Trias with top of the Buntsandstein, (red) Carboniferous with top of the crystalline basement.

Based on new gravity data acquired in Northern Alsace and their comparison to the older Bouguer anomaly, a qualitative data analysis reveals several negative Bouguer anomalies suggesting a decrease of the bulk density at the depth that fits with potential geothermal reservoirs like the Lower Trias and the top basement (Abdelfettah et al., 2020). A more quantitative analysis of gravity data combined with 3D geological models outlined areas with low density values that could be explained either by the variation of petrography within the basement and/or the occurrences of highly fractured zones associated with geothermal fluid affecting the bulk density values.

Due to their sensitivity to fluids and particularly brine water in rocks, passive electromagnetic (EM) techniques (e.g. Magnetotellurics or MT) or active (Controlled-Source Electromagnetic or CSEM) have been traditionally used to investigate the subsurface conductivity. Therefore, MT surveys were conducted in Northern Alsace, respectively, close to Soultz in 2007-2008 and Rittershoffen in 2013-2014. MT data collected in the Soultz area were combined with other geophysical data for estimating temperatures at depth below the existing geothermal wells drilled at 5000 m. The main result of this analysis based on MT, was the forecast of a very deep convective cell below GPK-2 at around 6000–8000 m. Results from continuous MT measurements done at Rittershoffen in 2013-2014 suggested transient variations in subsurface conductivity due to the occurrence of fluids at depth. Furthermore, by using MT response versus time, it revealed that fluids could migrate in a NE direction from the injection well GRT1. Therefore, MT is not only a method for geothermal exploration or for assessing temperatures at depth but could be used as a monitoring tool during hydraulic stimulation or geothermal exploitation.

EM methods have shown to be effective to characterize geothermal reservoir geometry in volcanic area, hydrocarbon reservoir geometry in offshore sedimentary area or onshore mineral exploration but not really in EGS. Nevertheless, the ability of EM methods to image targets with high geothermal potential in deep fractured reservoir and in a high man-made noise environment still needs to be demonstrated. Indeed, CSEM sources must compete with high noise levels and a conductive sedimentary cover resulting in low signal to noise ratio. At SsF, a full-scale 3D CSEM campaign done in 2020 demonstrated the ability of the technique to image resistivity variations underneath a thick sedimentary cover (>1400 m).

An assessment of subsurface rock mineral compositions derived from their physical properties measured through geophysical logging, employing a combination of statistical and machine learning techniques has been applied to the Triassic sedimentary reservoirs from the URG (Pwavodi et al., 2024). Based on various geophysical data from the geothermal SsF and Rittershoffen wells, mineral composition was spatially predicted and compared with existing mineral descriptions. This approach based on machine learning helps in deciphering complex mineralogical compositions and geological structures within subsurface geothermal reservoirs from the URG.

A methodology was established by using the thermal logs of the deep geothermal wells of Rittershoffen and SsF and applied to the temperature profiles measured in the gradient wells as an exploration tool. The basic idea is to try to estimate the temperature at the top of the geothermal reservoir. Thus, a series of seven shallow wells (<200 m) were drilled in Northern Alsace and temperatures were measured at equilibrium. Then, by using detailed lithostratigraphy and other relevant geological information, temperatures were extrapolated linearly till the top of the Middle Triassic limestone (Maurer et al., 2018). Above this geological interface, the geothermal gradient is conductive and shows a very high slope. This method is effective in volcanic environments for locating the heat source. It has been adapted to the URG reservoirs for delineating hottest zones related to local faults at the depth corresponding to Middle Triassic layers.

#### **4.4 Optimizing borehole design according to the geological knowledge of the reservoir**

Geophysical exploration was not really used for HDR because there was no need of reconnaissance of a deep heat exchanger nor to identify geothermal permeable reservoirs. However, based on extensive structural characterization by drilling in the URG, faults and fractures are highly dipping ( $>70^\circ$ ) and drilling vertical wells present a high probability to not cross these nearly vertical structures. Some recent wells in the URG (GRT-2 in Rittershoffen, GIL-1 in Illkirch, two wells in Vendenheim) are deviated in order to intersect a maximum of nearly vertical faults and fractures. However, a deviated well is more complicated to drill, to log and to exploit, and consequently more expensive. Insofar the cost of the drilling follows an exponential law correlated to the drilled length. It is the reason why the most recent wells are not drilled into the deep granitic basement only like in SsF but target the fracture network in the overlying Lower Triassic sandstones as well as the first kilometer of crystalline basement just below the interface with the sedimentary cover. It has been demonstrated from extensive structural analysis of the SsF wells that the first km of the top crystalline basement is much more naturally fractured than the overlying Triassic sandstones as well as the deeper basement.

By discovering that the fractures are highly dipping and locally permeable, well design evolved from vertical to deviated or even inclined wells trajectories. Therefore, the first wells were vertical at Soultz (GPK-1, GPK-2) but slightly evolved to a more complex design like GRT-2 in Rittershoffen that was deviated and drilled parallel to the main local faults identified by 2D seismic. The hydraulic performance of this second well was so good, that stimulation operations were not needed (Baujard et al., 2017). The open-hole sections of the geothermal wells are generally aligned with the orientation of the principal horizontal stress (SsF, Rittershoffen). Some wells in Brühl, Insheim or Rittershoffen were not stimulated and presented a sufficient natural permeability for industrial

exploitation (Vidal and Genter, 2018). They are classified as hydrothermal and not strictly EGS wells. Their trajectories were well designed according to the geological and structural context because they crossed out several permeable fractures. The absence of stimulation is a substantial advantage for reducing cost as well as induced seismicity, main nuisance for public acceptance. However, all the geothermal projects in the URG are considered as EGS because they will need to use a reinjection well and to develop induced seismicity related to the geothermal exploitation (Maurer et al., 2020).

## Conclusion and perspectives

In the Upper Rhine Graben, since the earlier development of matrix porosity geothermal projects in sandstones (e.g. Cronenbourg) and HDR projects in deep granitic basement (e.g. SsF) in the 90s, the geothermal concept evolved towards EGS projects by considering the geological properties of the deep geothermal system. The occurrence of fractured reservoirs characterized by natural brine circulations with fractured zones obliged developers to adapt geophysical exploration methods, geophysical well logging strategies as well as technical well design for reaching hydrothermal or EGS geothermal targets.

Therefore, by improving the conceptual model of deep geothermal resources in the URG, well productivity has been improved either by stimulation or by optimizing geothermal targets by derisking drilling depths and well design. The depths of the wells have been divided by factor 2 between SsF and Rittershoffen, the first km of the top basement being highly fractured, hydrothermally altered and permeable. Consequently, the flowrate is higher than 70 kg/s at Rittershoffen compared to the 30 kg/s at SsF only.

In terms of surface geophysical methods, only 2D seismic reflection was used in the past for shallower petroleum targets. By considering the importance of the fractured reservoirs, 2D or even better 3D seismic is now routinely used for deep geothermal resource exploration in the URG for imaging the top basement as well as the fault system at seismic scale. In terms of depth penetration, some progresses were also done from surface to great depths. For instance, some years ago, at Rittershoffen the second well, GRT-2, was targeted based on a specific 2D seismic line. For new geothermal projects based on a doublet, well design and their geothermal targets are defined before any drilling operation based on surface geophysical methods and specific treatments (inversion, machine learning, 3D modelling, ...).

Permeable faults or fractures lying into a deep basement hidden by a thick sedimentary cover are still challenging to image based on surface geophysical methods. Thus, there is a real need for combining various geophysical methods and treatments to propose a multi-physics image of deep fractured geothermal reservoirs in the URG in order to explore with low risks and thus exploit more sustainably the deep geothermal resource.

## Acknowledgments

This contribution has partially received funding from the European Union's Horizon Europe research and innovation programme under grant agreement No 101147171 (FINDHEAT project). This research is also part of the SIMGEO project funded by ADEME (French Agency for Ecological Transition).

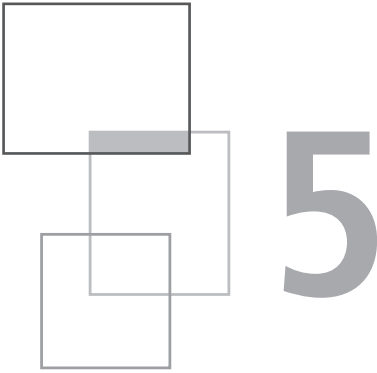
## References

- Abdelfettah Y., Hinderer J., Calvo M., Dalmais E., Maurer V., Genter A. (2020) Using high accurate land gravity and 3D geological modeling to discriminate potential geothermal areas: Application to the Upper Rhine Graben, France, *Geophysics* 85(2), 35-56, <https://doi.org/10.1190/GEO2019-0042.1>.
- Baudu R., Bernard J., Geogel J.M., Griveau P., Rugo R. (1980) Application des méthodes de prospection électriques dipolaires à l'étude géothermique du Fossé rhénan supérieur, BRGM Open file report, 80 SGN 586 GPH, 64 pages.
- Baujard C., Dalmais E., Glaas C., Maurer V., Genter A. (2022) Evaluation du risque géologique, retour d'expérience du projet Illkirch (Strasbourg, France), Journées de la Géothermie 2022, Aix les bains, France, 09 et 10 juin 2022.
- Baujard C., Genter A., Dalmais E., Maurer V., Hehn R., Rosillette R., Vidal J., Schmittbuhl J. (2017) Hydrothermal characterization of wells GRT-1 and GRT-2 in Rittershoffen, France: Implications on the understanding of natural flow systems in the Rhine graben, *Geothermics* 25, 255-268.
- Cuenot N., Dorbath C., Dorbath L. (2008) Analysis of the microseismicity induced by fluid injections at the EGS site of Soultz-sous-Forêts (Alsace, France): Implications for the characterization of the geothermal reservoir properties, *Pure and Applied Geophysics* 165, 797-828.
- Dorbath L., Cuenot N., Genter A., Frogneux M. (2009) Seismic response of the fractured and faulted granite to massive water injection at 5 km depth at Soultz-sous-Forêts (France), *Geophysical Journal International* 177(2), 653-675, <https://doi.org/10.1111/j.1365-246X.2009.04030.x>.
- Edel J.B., Maurer V., Dalmais E., Genter A., Richard A., Letourneau O., Hehn R. (2018) Structure and nature of the Paleozoic basement of the Central Upper Rhine Graben derived from new and old magnetic, gravimetric and seismic investigations. Zoom on the deep geothermal project of Illkirch-Graffenstaden (S. of Strasbourg, France), *Geothermal Energy Journal* 6, 13, <https://doi.org/10.1186/s40517-018-0099-y>.

- Evans K.F., Genter A., Sausse J. (2005) Permeability creation and damage due to massive fluid injections into granite at 3.5 km at Soultz: part 1 - Borehole observations, *Journal of Geophysical Research* 110, B04203.
- Genter A., Castaing C., Dezayes C., Tenzer H., Traineau H., Villemin T. (1997) Comparative analysis of direct (core) and indirect (borehole imaging tools) collection of fracture data in the Hot Dry Rock Soultz reservoir (France), *Journal of Geophysical Research* 102(B7), 15419-15431.
- Genter A., Evans K., Cuenot N., Fritsch D., Sanjuan B. (2010) Contribution of the exploration of deep crystalline fractured reservoir of Soultz to the knowledge of enhanced geothermal systems (EGS), *Comptes Rendus Geoscience* 342, 502-516. <https://doi.org/10.1016/j.crte.2010.01.006>
- Gerard A., Kappelmeyer O. (1987) The Soultz-sous-Forêts project, *Geothermics* 16(4), 393-399.
- Glaas C., Patrier P., Vidal J., Beaufort D., Genter A. (2021a) Clay mineralogy: a signature of granitic geothermal reservoirs of central Upper Rhine Graben, *Minerals* 11, 479, <https://doi.org/10.3390/min11050479>
- Glaas C., Vidal J., Genter A. (2021b) Structural characterization of naturally fractured geothermal reservoirs in the central Upper Rhine Graben, *Journal of Structural Geology* 148, 104370, <https://doi.org/10.1016/j.jsg.2021.104370>.
- Häring M.O., Schanz U., Ladner F., Dyer B.C. (2008) Characterisation of the Basel 1 enhanced geothermal system, *Geothermics* 37, 469-495, <https://doi.org/10.1016/j.geothermics.2008.06.002>.
- Kohl T., Evans K., Hopkirk R., Jung R., Rybach L. (1997) Observation and simulation of non-Darcian flow transients in fractured rock, *Water Resource Research* 33, 407-418.
- Kölbel L., Kölbel T., Wiegand B., Sauter M., Schäfer T., Siefert D. (2020) Identification of fractured zones in geothermal reservoirs in sedimentary basins: a radionuclide-based approach, *Geothermics* 85, 101764.
- Maurer V., Aichholzer C., Richard A., Harlé P., Hehn R., Genter A., Düringer Ph. (2018) Geothermal reservoir temperature estimation derived from gradient wells in a continental rift context (Upper Rhine Graben), Stanford Geothermal Workshop 2018, Stanford, California, USA, 12-14 February 2018.
- Maurer V., Gaucher E., Grunberg M., Koepke R., Pestourie R., Cuenot N. (2020) Seismicity induced during the development of the Rittershoffen geothermal field, France, *Geothermal Energy* 8, 5, <https://doi.org/10.1186/s40517-020-0155-2>.
- Munck F., Walgenwitz F., Maget P., Sauer K., Tietze R. (1979) Synthèse géothermique du Fossé rhénan Supérieur, Commission of the European Communities, BRGM Service Géologique Régional d'Alsace, Geologisches Landesamt Baden-Württemberg.

- Pwavodi J., Marquis G., Maurer V., Glaas C., Montagud A., Formento J.-L., Genter A., Darnet D. (2024) Rock mineral volume inversion using statistical and machine learning algorithms for Enhanced Geothermal Systems in Upper Rhine Graben, eastern France, *J. Geophysical Research: Machine Learning and Computation* 1, e2024JH000154, <https://doi.org/10.1029/2024JH000154>
- Renard P., Courrioux G. (1994) Three-dimensional geometric modelling of faulted domain: The Soultz horst example (Alsace, France), *Computer Geoscience* 20(9), 1379-1390.
- Rotstein Y., Edel J.-B., Gabriel G., Boulanger D., Schaming M., Munsch M. (2006) Insight into the structure of the Upper Rhine Graben and its basement from a new compilation of Bouguer gravity, *Tectonophysics* 425, 55-70, <https://doi.org/10.1016/j.tecto.2006.07.002>
- Sanjuan B., Millot R., Innocent Ch., Dezayes Ch., Scheiber J., Brach M. (2016) Major geochemical characteristics of geothermal brines from the Upper Rhine Graben granitic basement with constraints on temperature and circulation, *Chemical Geology* 428, 27-47, <https://doi.org/10.1016/j.chemgeo.2016.02.021>
- Sanjuan B., Pinault J.-L., Rose P., Gerard A., Brach M., Braibant G., Crouzet C., Foucher J.-C., Gautier A., Touzelet S. (2006) Tracer testing of the geothermal heat exchanger at Soultz-sous-Forêts (France) between 2000 and 2005, *Geothermics* 35, 622-653.
- Schill E., Genter A., Cuenot N., Kohl Th. (2017) History performance history at the Soultz EGS reservoirs from stimulation and long-term circulation tests, *Geothermics* 70, 110-124.
- Schindler M., Baumgartner J., Gandy T., Hauffe P., Hettkamp T., Menzel H., Penzkofer P., Teza D., Tischner T., Wahl G. (2010) Successful hydraulic stimulation techniques for electric power production in the Upper Rhine Graben, Central Europe, in Proceedings of World Geothermal Congress 2010, WGC2010, Bali, Indonesia.
- Schmittbuhl J., Lambotte S., Lengliné O., Grunberg M., Jund H., Vergne J., Cornet F.H., Doubre C., Masson F. (2021) Induced and triggered seismicity below the city of Strasbourg, France from November 2019 to January 2021, *Comptes Rendus Géoscience* 353, 561-584, <https://doi.org/10.5802/crgeos.71>.
- Toubiana H., Salaun N., Mitschler J.B., Carriere X., Gigou G. (2020) Upper Rhine Graben deep Geothermal reservoir imaging, *EAGE Annual*, 82<sup>nd</sup> EAGE Conference & Exhibition 2020, 8-11 June 2020, Amsterdam, The Netherlands.
- Traineau H., Genter A., Cautru J.P., Fabriol H., Chevremont P. (1991) Petrography of the granite massif from drill cutting analysis and well log interpretation in the HDR borehole GPK1 (Soultz, Alsace, France), *Geothermal Science & Technology* 3(1-4), 1-29.

- Vidal J., Genter A. (2018) Overview of naturally permeable fractured reservoirs in the Upper Rhine Graben: Insights from geothermal wells, *Geothermics* 74, 57-73, <https://doi.org/10.1016/j.geothermics.2018.02.003>.
- Vuataz F.-D., Brach M., Criaud A., Fouillac Ch. (1990) Geochemical monitoring of drilling fluids: A powerful tool to forecast and detect formation waters, *SPE Formation Evaluation* 5(2), 177-184.



# DEEP ERT/IP for geothermal exploration and de-risking

A. Rosselli, C. Truffert, F. Barsuglia, F. Fischanger,  
A. Coletti, G. Morelli and S. Del Ghianda

---

## 5.1 Context

In a context of energy transition to limit greenhouse gas emissions, which have a deleterious effect on the climate, geothermal energy is playing an important role on the energy scene. After decades of development, operating technologies are now well mastered. However, one of the main obstacles to the development of this sector remains the investment cost, which can be broken down into several phases, including the discovery of a sufficient and sustainable thermal resource, the installation of the production plant, and its monitoring and maintenance. Locating a suitable and sustainable source of heat in the subsoil involves a high degree of geological risk and uncertainty. Geological risk, i.e. the risk of incorrectly positioning a borehole due to a lack of information about the subsoil and its properties, can be reduced by geophysical surveys that are suitably selected according to the geological context

and the depth of the target. The resource exploration phase and in particular that which leads to the selection of drilling targets, the estimation of the resource volume and its future performance, conditions investors' decision-making. The key challenge is to maximize the probability of a project's success.

This document focuses on the upstream phase, resource exploration and in particular the use of geophysics to limit costs at 1 km depth maximum. This depth is well suited to a few medium-sized enthalpy projects, offering operators a favorable depth/temperature combination for heating or cooling installations, depending on the season. In specific geological contexts, these depths may also be compatible with power-generating geothermal plants.

## **5.2 Why electrical resistivity tomography is useful?**

Electrical Resistivity Tomography (ERT) is a rather low-cost geophysical method, even when it comes to obtaining a three-dimensional image of the subsurface. The method highlights the electrical conductivity of the different parts of the subsoil. Over and above the intrinsic properties of geological formations, it is sensitive to weathering processes, water content and temperature. It has proved its worth not only in tabular geological environments, but also in geological systems with more complex geometries.

## **5.3 Deep electrical resistivity tomography for geothermal exploration – an Italian example**

This article describes an example of a geophysical campaign performed by GEG Experts in Central Italy, in particular a Deep Electrical Resistivity Tomography (DERT) campaign, the aim of which is to gain a better understanding of the subsoil in order to assist operators of the medium-depth geothermal resource, while taking care not to disturb the upper aquifer.

The shallow aquifer, located around 300 m from the surface, is used to capture freshwater for domestic use. The deeper aquifer is potentially saturated in hypothermal water (temperature between 20 and 30 °C) or thermal water (temperature between 30 and 40 °C).

The initial ambition was to have a better knowledge over 1 km<sup>2</sup>, at a maximum depth of 800 m.

The geology of the area under investigation bears witness to two distinct stratigraphic cycles. The first, of early-middle Pliocene age, is characterized by marine facies deposits. The second is marked by a phase of intense alteration, manifested in the form of brackish facies of age early Pleistocene.

An extensive debris layer has also been recognized, deriving from the intense weathering of oldest geological formations. This referred to the Riss-Wurm interglacial about 100 thousand years ago.

### 5.3.1 *Unconventional ERT data acquisition*

The survey is characterized by its significant extension and the required high investigation depth for ERT method. Moreover, the area is characterized by a typical hilly environment, with forests, roads and isolated houses or dispersed hamlets.

Given both these geographical constraints and the high depth of investigation, we considered that a traditional multi-electrode approach, using a conventional resistivity meter connected to multicore cables, would be unrealistic. Investigating at great depth requires an acquisition system that covers a very large area, which is incompatible with the geographical constraints mentioned above.

The acquisition system consists of a set of independent, stand-alone units, which record the variation in electrical potential over time on two measurement channels. The set of recorders is independent of the high-power underground current injection device. The current transmitter is powered by a generator and connected to a current recorder over time. The only cables running through the study area are those connecting the current electrodes to the transmitter. These are two small-section cables, far different from the multiwire cables used for traditional resistivimeter.

In particular, for this project, the configuration described below was used.

**Receiver devices.** The receiver system consists of 34 small and lightweight receiver boxes<sup>2</sup> that were easily deployed on the ground. Each box is independent and autonomous, powered by an internal battery, and allows electrical potential measurements to be performed at two dipoles: P1-P2 and P2-P3 (see Figure 5.1).

Each unit is therefore able to work independently from the others and this allows an “unconventional” 3D acquisition design in such a complex morphologically and logistically context. The receiver is able to continuously measure the electrical potential at the two dipoles with a frequency of 100 measurements per second. Its internal GPS device allows its localization and the timestamp for each measurement. The potential measurements are synchronized a posteriori with the current measurements recorded at the transmitter.

---

2. V-FullWaver from IRIS Instruments.

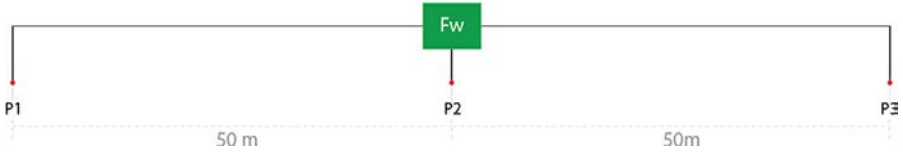


**Figure 5.1** Typical configuration of a recording unit used in this study. Three electrodes (P1, P2 and P3) are arranged for setting up two dipoles (P1-P2 and P2-P3). These dipoles could be either in the same direction (electrodes set up in-line as displayed on this figure) or perpendicular.

**Transmitter device.** A high power current transmitter<sup>3</sup>, specially designed for deep resistivity investigations, was used. It allows of handling a power up to 6 kW and injecting up to 16 A and 3000 V into the ground. The transmitter was powered by a large dedicated three-phase 15 kVA motor generator (see Figure 5.2). The “automatic range” mode allows the optimal injection level to be automatically selected according to the contact resistances at the TX-A and TX-B electrodes. The current is injected into the ground according to a 2 sec IAB+, 2 sec OFF, 2 sec IAB-, 2 sec OFF scheme and is recorded every 10 ms by means of an current recorded box. Thanks to its internal GPS, the current is also timestamped. This allows, as already mentioned, the retrospective synchronization of all potential signals (Vmn) recorded together with the injected electric current (Iab).



**Figure 5.2** On the left, high power transmitter of 6 kW. On the right, the three-phase 15 kVA motor generator which powers the transmitter.

3. TIP6000 from IRIS Instruments.

**Topography** – For an ERT survey, accurate location of the receiving and injection electrodes is essential. The position of each electrode was measured by a DGPS Leica GS18 system with an accuracy of less than 3 cm.

A digital Lidar terrain model with a 2 m×2 m mesh was used to build a detailed 3D finite element mesh for the ultimate phases of data processing.

### 5.3.2 Acquisition methodology

The implementation of a DERT project on the ground can be divided into 4 fundamental phases: survey design, field preparation, data acquisition and equipment recovery.

*The survey design* is a step done at the office that must not be neglected. Backed in part by logistical issues, it contributes to the optimization of human resources, intervention time and data quality. A detailed study of the area based on aerial photos, topographic map and direct inspections allowed to identify the access routes, the ideal position for the receiving units and transmissions electrodes. Using our proprietary ERTdesign<sup>®</sup> software (GEG Experts), we generated an initial theoretical layout of receivers and transmissions over the study area (see Figure 5.3). We then optimized the results by accurately moving each receiver or transmission point based on consideration as access or visibility of satellite constellations to ensure a good GPS connection.

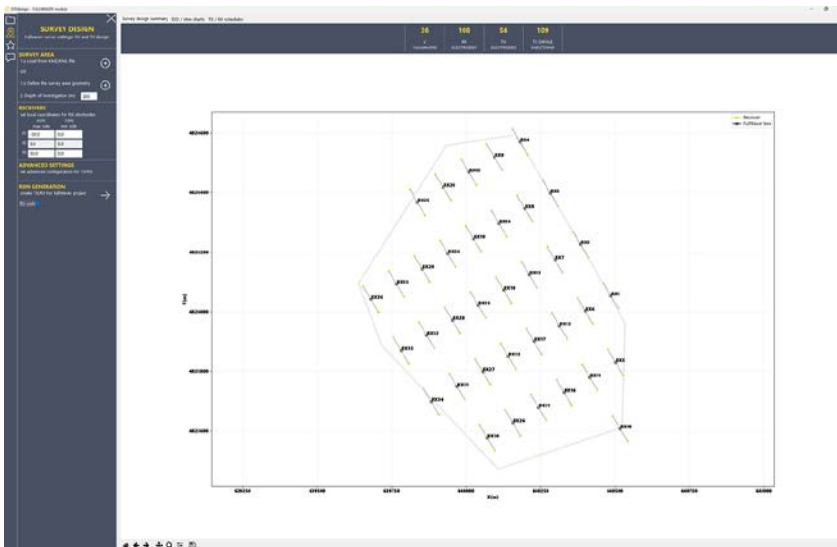


Figure 5.3 Acquisition design performed before the survey with ERTdesign<sup>®</sup>. The software provides the total number of receiver units (displayed on the figure) and transmission points.

The *survey design* phase is followed by the subsequent *field preparation*. It took one day to indicate on the field the future location of injection and receiving electrodes using a wooden sticks. This helps the subsequent deployment of the units and avoid any error (Figure 5.4).



Figure 5.4 Receiver box deployed at the wooden stick location.

The *data acquisition* campaign was completed in 2 days, including *retrieval of equipment*, by a team of 12 people, adequately trained.

### 5.3.3 Acquisition layout

The acquisition was carried out by arranging the receiving (green) and transmitting (red) electrodes according to the design shown in Figure 5.5.

The survey involved the arrangement of a 5.5 km long central transmission axe (from TX1 to TX23, in yellow in Figure 5.5), necessary to be able to achieve a depth of 800-900 meters. Other injection dipoles are positioned in the area of interest. These smaller dipoles (in white), located close to the receiver units (green dots), are designed to improve near-surface resolution.

The field team deployed 34 reception boxes each one connected to three electrodes (in detail in Figure 5.6) according to the design previously described. The size of each receiving dipoles is 50 meters (P1-P2 = 50 m, P2-P3 = 50m). A total of 102 receiving electrodes has been set up.



Figure 5.5 Aerial view of transmissions points (in red) and receivers points (in green). The longest distance on injection dipole along the main axis (in yellow, between TX1 and TX 23) is about 5.5 km. The white lines, more central on the figure, show the cables used for shorter distance transmissions, inside the area of interest.



Figure 5.6 Layout of 102 electrodes and 34 recording units in the area of interest.

### 5.3.4 Current transmissions

The transmissions have been designed according to two approaches, based on the dual need to reach deep layers and, at the same time, to have a fair near surface detail.

A first series of 32 transmissions was carried out with the aim of achieving the maximum sensitivity of the measurements at great depths for the different receivers.

For these currents' injections, a fixed pole "A" in TX1 and a second mobile transmitter "B" with a "forward" acquisition scheme was used: TX1-2, TX1-3, TX1-4, ..., TX1-23 (Figure 5.7). The injection dipole TX1-23 has the maximum aperture of about 5.5 km.



**Figure 5.7** Location of the transmission's electrodes on main central axe. Pole A was in TX1 and pole B was moving on all TX from TX2 to TX23. A backward acquisition was done on the main axe, with pole A fixed at TX23 and pole B moving backward on TX21, TX19, TX17, ..., TX1 (one out of two).

This acquisition sequence was followed by a backward energization scheme with fixed pole "A" in TX23: TX 23-21, TX23-19, TX23-17, ..., TX23-1 (Figure 5.7). The combination of these transmission dipoles schemes allowed to acquire (i) dipole-dipole protocol arrays, when the transmitting dipole is very far from the receiving dipole, (ii) pole-dipole, when the mobile transmitter "B" is close to the receiving dipole, and, (iii) gradient dipole, when both transmitters "A" and "B" are "external" and far from the receiving dipole.

The second group of transmissions (72 dipole combinations) involved electrodes with numbering from TX24 to TX50, each of which has been combined in sequence with three different "remote" transmission poles, fixed respectively at the TX9, TX13 and TX15 electrodes (Figure 5.8). This approach enabled us to achieve high-sensitivity measurements across the area of receivers, effectively covering both shallow and medium investigation depths.

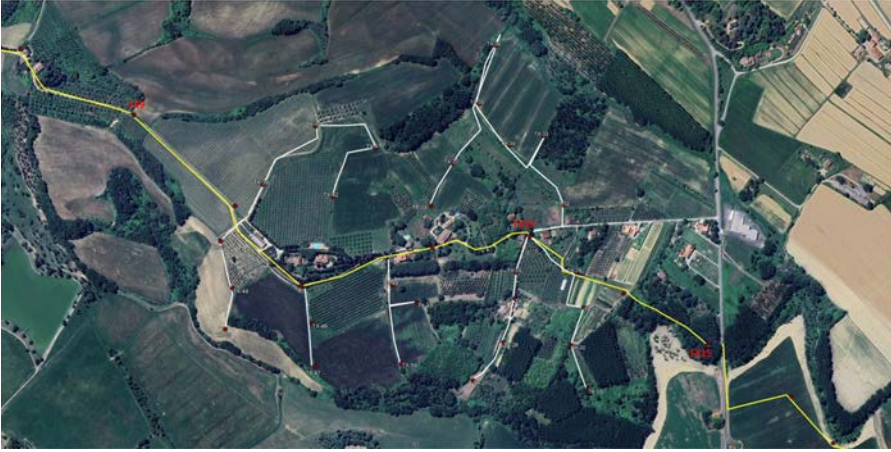


**Figure 5.8** *Close up view of Figure 5.5 showing transmissions performed in the zone of interest. Pole A was alternatively placed at TX9, TX13 and TX15, while pole B was moving on TX24 to TX50.*

### 5.3.5 **Quality control**

With regard to chargeability data (induced polarization), which the receiving system and injection protocol enable to acquire in an auxiliary manner, measurements are of good quality at the first 350 to 400 meters. For deeper measurements, characterized by low-intensity electrical potential signals, the potential discharge curves do not allow this information to be extracted. Figure 5.9 shows the details of the signal recorded at the first channel of the RX3 receiver at the transmission event between the TX1 and TX2 electrodes, the smallest dipole of the main transmission axe. This demonstrates how the receiver effectively detects the subtle signal from the electric field generated by the transmission dipole, even over a significant distance between the injection point and the receiver. The presence of about 40 measuring stacks, recorded during almost 3 minutes of current injection, allows us to identify a very good average signal (graph at the bottom left in Figure 5.9), with an amplitude of the order of 0.04 mV. The chargeability measurements (graph at the bottom right) are of mediocre quality, with potential discharge curves that are difficult to identify.

Figure 5.10 displays the same type of graphs, in the more favorable situation of the TX15-13 transmission dipole recorded by the first channel of receiver no. 16. Note that in this case, by virtue of the higher V signal (about 12 mV), the discharge curve and the consequent derivation of the chargeability measurement is more robust.

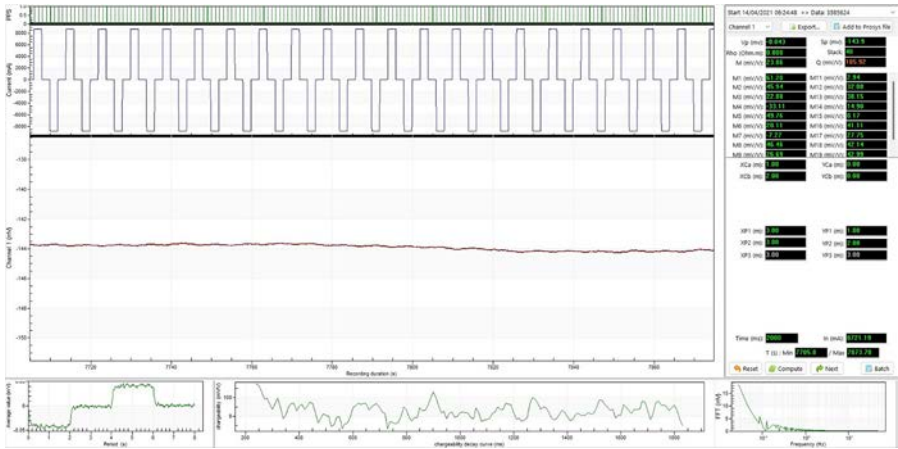


**Figure 5.9** *In blue the graph of the time trend of the current intensity (mA) injected at the TX1-TX2 transmission dipole (about 8720 mA). In red is the graph of the time trend of the corresponding signal V(mV) recorded by the first channel of the receiver box no. 3. At the bottom left the signal averaged on the different measurement stacks. At the bottom right the chargeability discharge curve.*

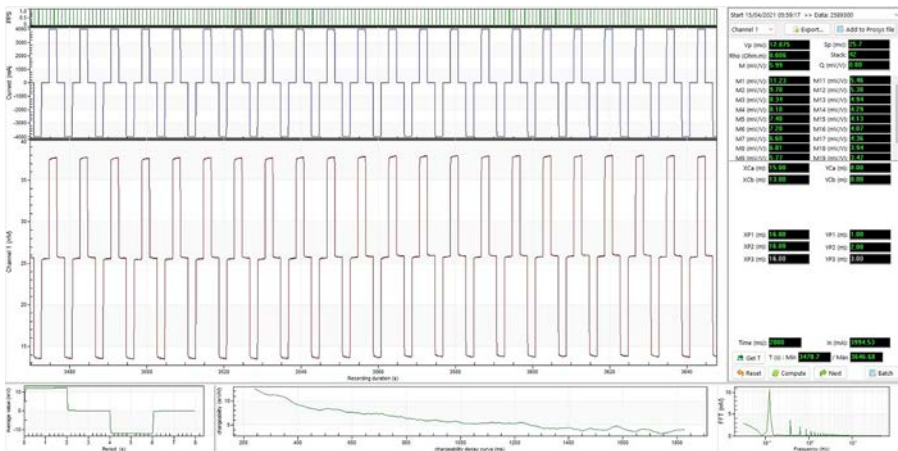


**Figure 5.10** *In blue the graph of the time trend of the current intensity (mA) injected at the TX15-TX13 transmission dipole (about 4000 mA). In red is the graph of the time trend of the corresponding signal V(mV) recorded by the first channel of the receiver box no. 16. At the bottom left the signal averaged on the different measurement stacks. At the bottom right is the chargeability discharge curve.*

In statistical terms, the  $I_{AB}$  currents transmitted during the three days of acquisition are on average of the order of 4.5 A, with minimum values of 3.2 A and peaks of 8.8 A, reached with transmissions in the South-East area on more conductive soils. The average  $V_{mn}$  potentials recorded are of the order of 3 mV, with average apparent resistivities around 20  $\Omega\cdot\text{m}$ , with the lowest values, around 8–10  $\Omega\cdot\text{m}$ , measured at depth (Figure 5.11).

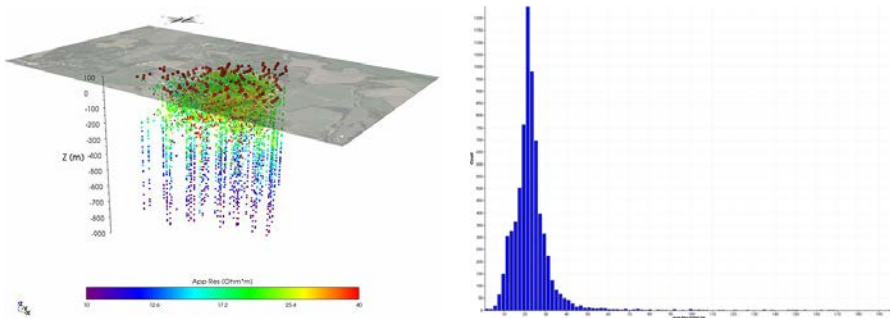


**Figure 5.11** *Pseudo-cloud of measured apparent resistivities (on the left) and histogram of measured apparent resistivities (on the right).*

The cloud of the measured apparent resistivities is displayed on Figure 5.11 (left). The total set of measurements consists of 7072 quadripoles (104 transmissions for 68 receiving dipoles). Before the resistivity measurements were processed from the global set, 147 measurements, equal to about 2%, were removed. Most of them had measured  $V_{mn}$  signal less than 0.01 mV.

For the processing of the chargeability measurements, we opted for an arithmetic sampling of the discharge curve, using a delay time of 240 ms and 20 sampling windows of 80 ms. After resistivity inversion, we filtered the chargeability measurements, excluding data with a standard deviation above 10% and IP values outside the 0.01–30 mV/V range. This filtering removed approximately 2500 inaccurate measurements, representing about one-third of the dataset primarily associated with deeper quadripoles where the larger distance between receiver and transmitter resulted in lower potentials (below 0.5–1 mV). The inverted dataset showed average chargeability values around 5 mV/V.

### 5.3.6 Processing of resistivity and chargeability measurements

The investigation enables us to reconstruct three-dimensional models of the distribution of resistivity and electrical chargeability of the subsoil, which highlight the main lithological characteristics of the site. The geological context is relatively

conductive, with electrical parameters varying within the first 300–350 meters of depth. Low-resistivity formations, such as clays and silts, surround zones of higher resistivity (up to a few tens of  $\Omega\cdot\text{m}$ ), which may correspond to sandier layers and thus indicate potential aquifer formations. Below 300–350 meters, the geological formations exhibit high conductivity with resistivity values around 10  $\Omega\cdot\text{m}$ , continuing uninterrupted down to the survey’s lower limit at 800–850 meters (see Figure 5.12).

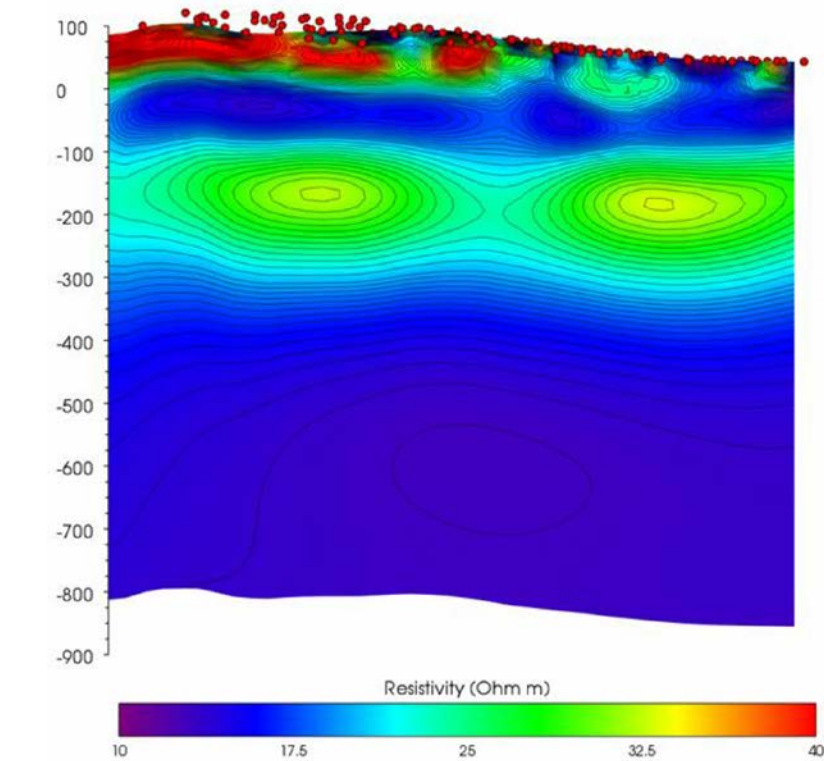


Figure 5.12 Resistivity section.

The ERT measurements were inverted using the ERTLab Studio software, following the removal of inaccurate measurements as outlined in the previous section. The three-dimensional inversion was conducted with the following configuration:

1. implementation of the complete topographic model,
2. mesh size 25 m×25 m×12.5 m in the x, y, and z directions of space,
3. depth of investigation equal to 900 meters from ground level,
4. initial resistivity inversion model set to of 15  $\Omega\cdot\text{m}$ , corresponding to the median of apparent resistivities values,

5. starting model for 5 mV/V chargeability inversion,
6. estimated data noise of 1.5% for resistivity processing and 5% for IP data processing.

The resistivity and chargeability inversions both converged, respectively in 6 and 4 iterations, with an excellent concordance of the modeled measurements with respect to the site acquisitions. This is illustrated on the examples in Figure 5.13, showing the cross-plot of the measured data compared to the modeled data at the end of the inversions.

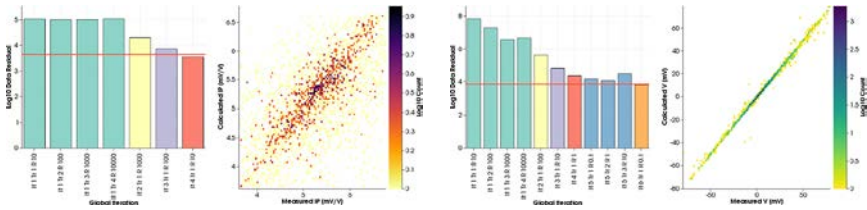


Figure 5.13 *Graphs of resistivity inversion progress. Left: trend of the measure-data misfit modeled as the iterations progress. Right: cross-plot of modeled data vs. measured data at the end of the inversion.*

### 5.3.7 Results

This 3D Deep Electrical Resistivity Tomography approach allowed to highlight potentially aquifer sandy portions within the first 250–300 meters from the ground level. Figure 5.14 shows the geological map of the investigated area as well as a schematic geological section of the same area. These potential sandy portions are characterized by electrical resistivity values around 20–30  $\Omega\cdot\text{m}$  and represented by a red-orange color Figure 5.15. The aquifer is well known from existing boreholes in the same region and is related to a fine sands layer (P3 in Figure 5.16). It is confined at the top by a more conductive layer related to sandy clays (Q1 in Figure 5.16).

With regard to investigations for the deep geothermal aquifer, the 3D model shows the presence of zones with very low electrical resistivity ( $<20 \Omega\cdot\text{m}$ ) starting from 300–350 m below sea level down to the base of the investigated volume. These more conductive zone can be interpreted as related with the blue clays layer (P in Figure 5.16 and 5.14).

We notice that within the conductive layer we can isolate a plume characterized by even lower resistivity values, below 12  $\Omega\cdot\text{m}$  (A, Figure 5.16).

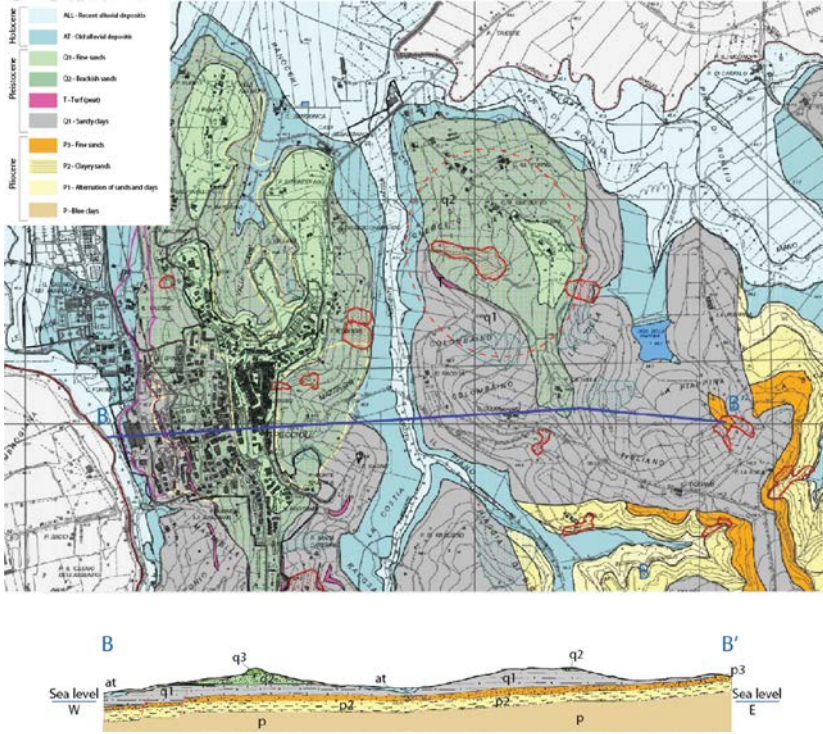


Figure 5.14 Geological map of the investigated area (red circle) and geological section.

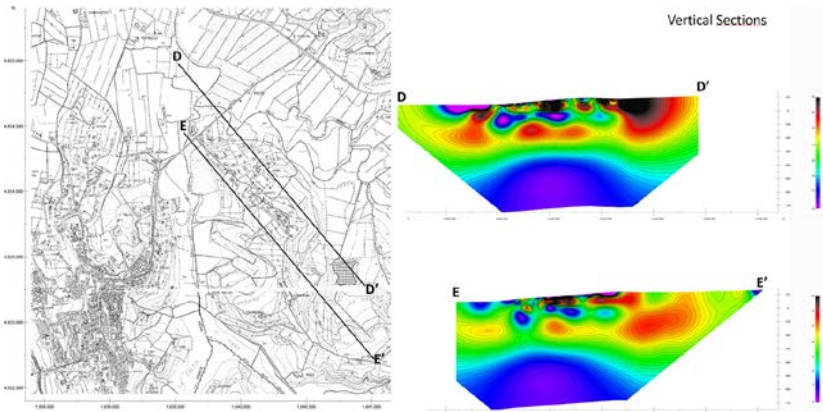


Figure 5.15 The vertical sections issued from the 3D resistivity model show the presence of a possible shallow aquifer (sandy layer) at an altitude of about 150 m below sea level (red-orange color) and a possible thermal reservoir at the altitude of about 350 m below sea level (blue/purple color).

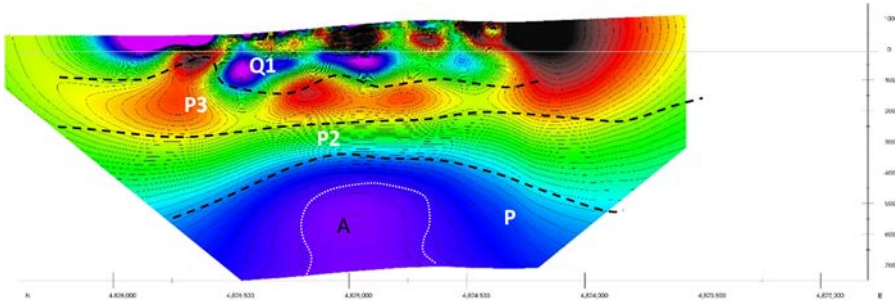


Figure 5.16 Geological interpretation of the 3D ERT model.

The Induced Polarization, despite an extremely heterogeneous chargeability in the first 200 m below the surface that partially hides the deeper signal, shows a very interesting correlation between a deep low chargeability zone (B Figure 5.17) and the conductive plume at about 500 m below sea level.

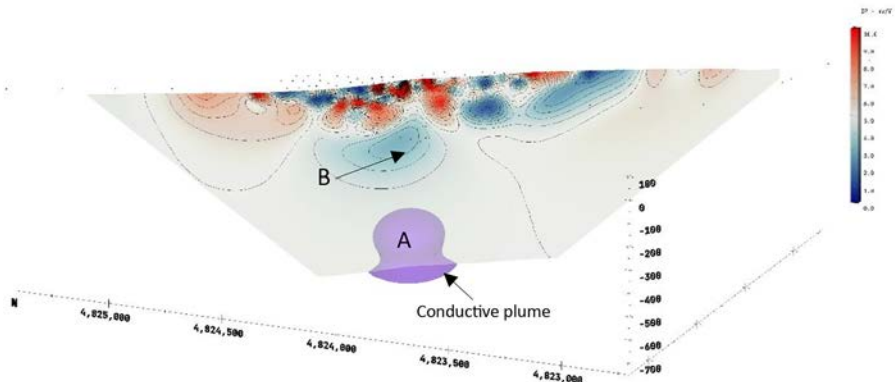


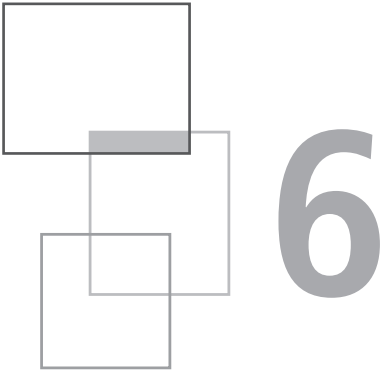
Figure 5.17 IP section with high conductive plume.

The analysis of both resistivity ( $\rho$ ) and chargeability (IP) results suggest that the high conductivity of the deeper layer (A, Figures 5.16 and 5.17) associated with the presence of a low chargeability area (B, Figure 5.17) could be interpreted as being linked to deeper fluids at higher temperatures. This is compatible with the presence of a low-enthalpy geothermal system.

## Conclusion

ERT is one of the geophysical techniques both sensitive to water content and temperature. Traditional ERT equipment, known as resistivitymeters, combining a central instrument that controls current injection and potential measurements, remain highly effective for obtaining high-resolution knowledge of conductivity distribution in the ground. However, the depth of investigation is not compatible with the demands of geothermal energy. The use of recording units separated from high-power transmitters for deep investigation is more appropriate. Unfortunately, this requires the management of long reception cables in the field, which is very laborious and can generate strong coupling effects that are problematic for the final quality of the data.

Thanks to the use of self-contained receivers, deep 3D field surveys are accessible to organized and meticulous field operators. The cost of this type of survey, provided the team is experienced, remains very low when compared with other geophysical techniques or with poorly positioned drilling. ERT alone cannot guarantee geothermal drilling, but when combined with geological knowledge, it can guide the man of the art in his interpretation. These new acquisition systems and protocols pave the way for wider use of ERT in medium-depth geothermal energy.



# The use of passive seismic methods for Geothermal exploration and monitoring

T. Kremer, J. M. Ars, T. Gaubert-Bastide,  
K. Khazraj and C. Voisin

---

## Introduction

Geothermal energy harvesting is gaining momentum as the need for less-carbonated sources of energy arises. Along with this increase of interest comes the need for multiplication of exploration campaigns, dedicated to the localization, the characterization, and the selection of suitable prospective areas for geothermal systems exploitation. In parallel, the perspective of large-scale deployment of Geothermal assets also underlines the need for enhanced surveillance strategies and monitoring tools.

From a geophysical perspective, the characterization and surveillance of geothermal targets usually focuses on the electrical and electromagnetic properties of the subsurface (e.g. Muñoz, 2014). However, as in any geophysical study, multi-physics approaches facilitate interpretation. Thus, both objectives, exploration and surveillance, can benefit from geophysical seismic methods which help to better understand the geological configuration of the subsurface, locating fractured zones and interfaces, identify hydrothermal fluids presence and circulation pathways. Seismic methods are usually a good complementary to electrical and electromagnetic information to understand the distribution and evolution of petro-physical parameters that are key indicators in geothermal contexts.

However, the present state of the geothermal energy market prevents investing as much financial efforts in geophysical exploration strategies as for the hydrocarbons market for instance, hence typically discarding the use of technologies such as 3D active seismic (for exploration) or 4D active seismic (for surveillance). As a consequence, cost-effective strategies must be deployed to accompany this movement.

Passive seismic methods are part of the solution. By opposition to active seismic methods, passive approaches do not require the costly deployment of logistics associated with the use of an active seismic source. Instead, they are based on the analysis of the ambient seismic signal, which can be cost-effectively recorded using seismic sensors in passive mode, and which, if properly processed and interpreted, can provide useful information about the spatial distribution and temporal evolution of the subsurface seismic properties.

### ***Passive seismic methods emergence – The progression of seismic acquisition technologies***

In the 1880s, modern earthquake detection began with the invention of the seismograph, an instrument capable of capturing ground motion produced by seismic waves. British scientist John Milne, often regarded as the founder of modern seismology, created a horizontal-pendulum seismograph sensitive enough to record distant earthquakes. The technical principle was straightforward: as the ground moved, the seismograph's heavy mass remained stationary due to its inertia, allowing the relative motion of the ground and the mass to be traced. These early seismographs gave scientists a new way to measure the strength and duration of seismic waves, leading to the classification of different wave types and laying the foundation for the Richter scale in the 1930s, a scale that quantifies earthquake magnitude based on wave amplitude.

Initially, earthquake recordings were analog, relying on ink pens to trace waveforms onto paper rolls. This method had limitations: recordings had to be reset after each event, and the analog traces could be difficult to interpret, especially for large, overlapping seismic events. In the 1960s, seismology began a significant shift as stations worldwide established standardized networks like the World-Wide Standardized Seismograph Network (WWSSN), which allowed comparison and cross-validation

of seismic data from different locations. Yet, analog technology still limited the extent of what could be captured, often requiring events to “trigger” the recording mechanism. Triggered recordings meant that only seismic events exceeding a certain threshold were captured, resulting in the loss of data from smaller earthquakes and seismic tremors.

The digital revolution in the 1970s transformed earthquake detection. Digital seismometers replaced analog systems, offering higher resolution and accuracy, as well as the capacity to store continuous, high-quality data. The introduction of continuous recording was a breakthrough: it enabled the capture of all seismic activity, from minor tremors to major earthquakes. Continuous digital recording removed the need for triggered mechanisms and allowed real-time monitoring, essential for identifying seismic events before larger quakes. Additionally, with the digital storage of data, seismologists could archive vast amounts of seismic information, facilitating data analysis and pattern recognition across regions and over time.

Through these technological advancements, seismology has evolved from occasional triggered recordings to continuous, high-resolution digital monitoring, culminating in a networked, data-rich approach that enhances our ability to monitor, understand, and respond to earthquakes.

### ***The ambient seismic signal – One person’s trash is another person’s treasure***

Entering the age of continuous seismic recording, the field of seismology has expanded its scope beyond the study of large earthquakes to include the rest of the ambient seismic signal, which was until then often referred to as seismic “noise” and was usually disregarded as irrelevant or undesirable. This negative vision is due to the inherent difficulties of conducting active seismic surveys in such environments where this seismic “noise” shows high amplitude, in which case the picking of body waves arrival time becomes less accurate or impossible.

Rather than filtering out this background motion, scientists now treat seismic noise as a valuable signal, one that can reveal critical details about the Earth’s structure and dynamics. Passive seismic methods designate all the methodologies and tools that have been developed to infer subsurface information from the analysis of those seismic recordings. Figure 6.1 shows a 250 seconds duration recording of the ambient seismic signal, represented in the temporal domain. This signal typically illustrates the dual structure of the ambient seismic signal, which can simplistically be described as two main components, coherent seismic events on one hand, and incoherent seismic signals on the other hand. Different passive seismic approaches exist to extract information from the coherent or incoherent components of the ambient seismic signal.

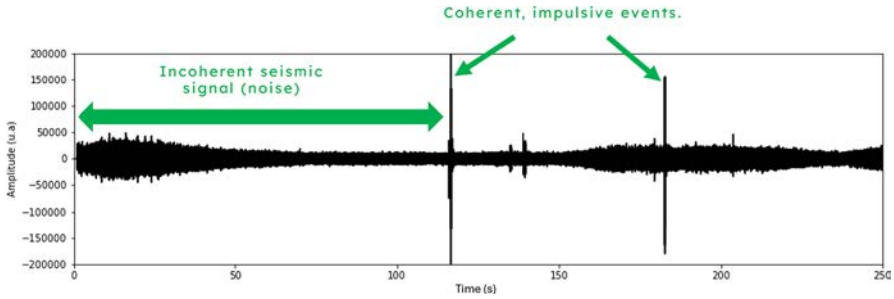


**Figure 6.1** Ambient seismic signal recording of 250 second duration. The seismic sensor used is a 5 Hz geophone.

Coherent seismic events designate impulsive signal such as produced by earthquakes, microseismicity, or other impulsive, high energy seismic sources. The study of how those events propagate within the subsurface (body wave picking, location, focal mechanism, etc.) to infer either seismic properties or characterize their source mechanism is a family of approaches to which we will refer to in the following as **Seismological analysis**.

Incoherent seismic signals designate the large majority of the ambient seismic signal which cannot be directly identified as a single seismic event and isolated to be analyzed as such, but rather the sum of numerous contributions of uncontrolled sources such as ocean waves, atmospheric disturbances, and human activities. Yet even this part of the signal holds valuable information. For instance, Horizontal to Vertical Spectral Ratio (HVSr) analysis is a well-known, robust method to infer the thickness of the sedimentary layer overlying the bedrock, which has seen much use in geotechnical applications. For geothermal characterization and monitoring though, the most relevant family of methods able to take advantage of incoherent seismic signal recordings is the so-called Ambient Noise Seismic Interferometry (ANSI) analysis.

This relatively new approach (Shapiro and Campillo, 2004) has been a major development in the field of passive seismic methods, for seismologists have extended their capacity to retrieve Green's functions, which describe the response of an elastic medium between two points as waves propagate through it. Traditionally, Green's functions were obtained through earthquake-generated waves, providing data only after significant seismic events. However, ANSI achieves similar insights through the cross-correlation of ambient noise recorded at different seismic stations. By continuously recording these incoherent background vibrations and examining the data between paired stations, scientists can derive Green's functions, revealing the Earth's structure without relying on earthquakes. Putting it another way, ANSI tools manage to extract coherent seismic waves components from the incoherent seismic signal, hence making seismic analysis possible. In the rest of the paper, we will refer to this family of methods such as **Ambient Noise Seismic Interferometry (ANSI) analysis**.

Hence, the shift from traditional earthquake seismology to ambient seismic noise seismology relies on the precision of digital technology and the ability to record

data continuously and at high resolution. This approach allows seismologists to capture even faint shifts in wave properties, which would be missed with a triggered or intermittent recording system. These subtle changes in the Earth's wave velocities provide crucial data for understanding not just earthquake-prone areas but also regions experiencing slower processes, like crustal deformation or fluid shifts in fault zones. Through these advances, passive seismic methods now serve as a powerful lens into the Earth's structure and its subtle movements and transformations, further bridging seismology with physics to deepen our understanding of the dynamic planet we inhabit.

## ***A cost-effective, high-value tool in the geothermal geophysical toolbox***

Passive seismic methods present two main interests in the context of geothermal industry development. First, their cost-effectiveness makes it an economically competitive tool for exploring geothermal subsurface context, at different scales, in complementarity to electrical, electromagnetic and other geophysical methods. Second, their input data – the ambient seismic signal – being continuous, free of charge, those methods can also be implemented as a continuous measurement allowing for quasi-real time monitoring of the subsurface.

The problematics surrounding geothermal exploration and the associated geophysical targets are as diverse as the variety of existing geothermal contexts. In this paper we will first present the practical and theoretical basis of the passive seismic approaches that are being used for geothermal exploration and monitoring purposes. Then we will focus on exposing how the diversity of geothermal geological contexts calls for different seismic responses and hence different geophysical objectives and how the global exploration and monitoring strategies can be improved thanks to the integration of passive seismic measurements.

## **6.1 Methods**

### **6.1.1 *Seismological analysis***

The analysis of seismic events and microseismic events can provide significant amount of information about the subsurface, either by better identifying and locating the structural mechanisms that induce the seismicity, or by analyzing the seismic wavefield properties associated with those events, i.e. seismic waves velocity and attenuation properties in the vicinity of the seismic array. The following paragraph proposes a summary of the most used and emerging techniques to achieve both objectives.

## Detection of earthquakes

Earthquake detection has undergone substantial development over the past decades, integrating traditional techniques with advanced computational tools to improve accuracy and reliability. The Short-Time Average/Long-Time Average (STA/LTA) method, introduced in the mid-20th century, remains a widely used and foundational approach for seismic monitoring. This method calculates the ratio of short-term signal energy to long-term background noise to identify sudden energy surges indicative of seismic events. STA/LTA gained prominence in the 1970s with the advent of automated seismic networks, enabling real-time earthquake detection. However, while effective for detecting moderate to large earthquakes, STA/LTA is prone to false positives in environments with high cultural or natural noise, such as urban areas or regions affected by storms.

To address these limitations, template matching emerged in the 1990s and has since become a critical tool for detecting smaller or repeating earthquakes. This technique involves comparing incoming seismic waveforms with a database of previously recorded seismic signals. When a match is identified, it confirms the occurrence of a similar event. Template matching is particularly effective in regions with dense seismic networks, such as California or Japan, where high-quality waveform libraries are available. Its ability to identify microseismic events and repeating patterns, such as slow-slip events or earthquake swarms, has proven invaluable for understanding seismicity in complex tectonic settings.

In the 2010s, machine learning revolutionized earthquake detection by introducing powerful algorithms capable of analyzing vast amounts of seismic data with minimal human intervention. Neural networks are trained on labeled datasets to learn the features that distinguish seismic events from noise. These systems can process continuous seismic streams, detecting small-magnitude earthquakes and events buried within background noise (Mousavi et al., 2020).

Hybrid approaches, combining STA/LTA, template matching, and machine learning, represent the cutting edge of earthquake detection. These integrated systems leverage the strengths of each method, ensuring high sensitivity to small and large earthquakes while reducing false alarms (Yue et al., 2021). Today's detection frameworks reflect decades of innovation, enabling precise monitoring of seismic activity across diverse tectonic environments and laying the groundwork for improved earthquake response and mitigation efforts.

## Localization

Earthquake localization, the process of determining the origin of an earthquake in time and space, has advanced dramatically over the past century. The foundational approach relies on analyzing the arrival times of seismic waves, particularly P-waves (primary waves) and S-waves (secondary waves), which travel at different speeds through the Earth. By measuring the time differences in their arrivals at multiple seismic stations, the distance to the earthquake's epicenter can be estimated. This method, developed in the early 20th century, became a standard tool in global seismology with the

establishment of seismic networks such as the Worldwide Standardized Seismograph Network (WWSSN) in the mid-1900s. However, traditional approaches often struggle with events in regions of sparse station coverage or complex crustal structures, where seismic wave propagation deviates from standard models.

To overcome these challenges, the introduction of seismic tomography and 3D velocity models in the late 20th century represented a major breakthrough. These methods account for variations in the Earth's subsurface, significantly improving the accuracy of earthquake localization, particularly in tectonically complex regions like subduction zones. Template matching has also been instrumental in localization. By comparing real-time waveforms with those of well-located events, the locations of new earthquakes can be inferred with remarkable precision. This method excels at identifying and locating small, repeating earthquakes that may not generate strong signals across broad networks. The rise of machine learning in the 2010s has further transformed earthquake localization by automating seismic waveform analysis and improving accuracy. Neural networks trained on synthetic and real seismic datasets can estimate earthquake hypocenters (the points of origin beneath the Earth's surface) with impressive speed and precision (Zhu et al., 2019). Probabilistic methods, such as Bayesian inference combined with machine learning, allow robust localization even in areas with limited station coverage or high noise levels. These innovations highlight the remarkable progress in earthquake localization, offering critical insights into seismic processes and ensuring effective monitoring of tectonic activity worldwide.

## Magnitude

The estimation of earthquake magnitude has evolved significantly since its inception, transitioning from simple empirical scales to sophisticated, physics-based calculations that leverage global seismic networks and advanced computational tools. The concept of quantifying an earthquake's size was first formalized by Charles F. Richter in 1935 with the introduction of the Richter scale, or the local magnitude (ML) scale. This method measured the amplitude of seismic waves recorded by a specific type of seismograph (the Wood-Anderson torsion seismometer) at a standardized distance of 100 kilometers from the epicenter. The Richter scale was revolutionary because it provided a logarithmic measure of earthquake size, allowing a single number to represent the energy released during an event. While the Richter scale worked well for moderate earthquakes in Southern California, it had limitations for very large earthquakes and those occurring outside the region for which it was calibrated. This led to the development of additional magnitude scales, such as the surface-wave magnitude ( $M_s$ ) suitable for large, shallow events or body-wave magnitude ( $M_b$ ) focusing on compressional body waves useful for deep-focus earthquakes. Despite their broader applicability, these scales also had shortcomings, such as underestimating the size of very large earthquakes (known as saturation).

To address these issues, the moment magnitude scale ( $M_w$ ) was introduced in the late 1970s by Hiroo Kanamori and Thomas Hanks. This scale is based on seismic moment, a physical quantity directly related to the energy released during fault rupture.  $M_w$  considers the area of the fault that slipped, the average slip displacement,

and the rigidity of the rocks involved. Unlike earlier scales,  $M_w$  does not saturate for large earthquakes, making it the preferred standard for global seismology. Modern earthquake magnitude estimation has benefited from advancements in seismic instrumentation and computational methods. Broadband seismometers, capable of capturing a wide range of frequencies, allow for detailed analysis of seismic waveforms across the globe. These instruments provide the data necessary for calculating magnitudes using regional and global network observations.

Machine learning has recently entered the field of magnitude estimation, offering tools to analyze complex seismic datasets and refine magnitude calculations. Algorithms trained on historical seismic data can predict magnitudes with high accuracy, even for events with unconventional waveforms or sparse station coverage. These advancements underscore the ongoing progress in seismology, ensuring that magnitude estimates remain a critical tool for understanding earthquake dynamics and microseismicity.

### Focal Mechanism Determination

The focal mechanism of an earthquake describes the orientation and type of faulting that occurs during the rupture, providing insights into the forces driving tectonic processes (Byerly, 1955). This information is typically represented by a “beachball diagram”, which visually depicts the fault’s geometry and slip direction based on seismic wave patterns. The analysis of focal mechanisms has been integral to seismology since the mid-20th century, offering valuable clues about earthquake dynamics and regional stress fields. Early methods for determining focal mechanisms relied on the first-motion polarity of seismic waves. When an earthquake occurs, compressional P-waves radiate outward, creating zones of compression (upward motion) and dilation (downward motion) recorded at seismic stations. By mapping these first-motion polarities, seismologists can infer the orientation of the fault plane and the direction of slip. While effective, first-motion polarity analysis required a dense distribution of seismic stations for reliable results, limiting its application in remote regions or areas with sparse networks.

The advent of waveform modeling in the 1970s marked a major advance in focal mechanism determination. By analyzing the amplitude and shape of seismic waves, particularly the long-period components, scientists could model the faulting process more precisely. Waveform modeling also enabled the estimation of moment tensors, mathematical representations of the forces involved in an earthquake. Moment tensor inversion, introduced in the 1980s, uses seismic waveforms to solve for the fault plane orientation, slip direction, and seismic moment, providing a comprehensive description of the earthquake source. Modern techniques for determining focal mechanisms combine data from dense regional networks, broadband seismic stations, and advanced computational models.

Automated systems, such as the Global Centroid Moment Tensor (GCMT) catalog, continuously process seismic data to generate focal mechanisms for significant earthquakes worldwide. These systems rely on inversion algorithms that use broadband waveform data to produce accurate and reliable solutions, offering insights into the faulting style and regional stress regime. Machine Learning has recently been applied to focal mechanism analysis, offering tools to process vast amounts

of seismic data efficiently. Neural networks trained on synthetic and real earthquake datasets can rapidly classify faulting styles and estimate moment tensors with high accuracy. The study of focal mechanisms provides critical information for understanding tectonic processes and seismic hazard. For instance, the analysis of focal mechanisms during aftershock sequences can reveal how stress is redistributed on faults after a major event. Additionally, comparisons of focal mechanisms across different earthquakes help map the orientations of active faults and infer the directions of regional tectonic stress. Modern focal mechanism analyses, with their increasing precision and automation, remain a cornerstone of seismology, linking the physics of faulting with broader geodynamic processes.

### 6.1.2 Ambient noise seismic interferometry (ANSI)

At the heart of ANSI is the concept of a “diffuse field”, where energy from seismic waves is dispersed evenly in all directions through a medium like the Earth’s crust. This concept has its roots in statistical physics, where wave energy behaves in random but statistically predictable ways. By understanding how this energy propagates, researchers can use noise as a sort of “natural tomography”, revealing the Earth’s properties, such as wave speed and material composition, down to fine scales.

More practically, the ANSI method designates a signal processing approach that allows to extract coherent seismic waves from the incoherent ambient seismic signal recordings. This reconstruction process is achieved through cross-correlation operations between the diffuse noise signals recorded at two different locations on the earth’s surface (Figure 6.2), yielding empirical Green’s functions (EGFs) that are estimates of the impulse response of the subsurface medium in between the two

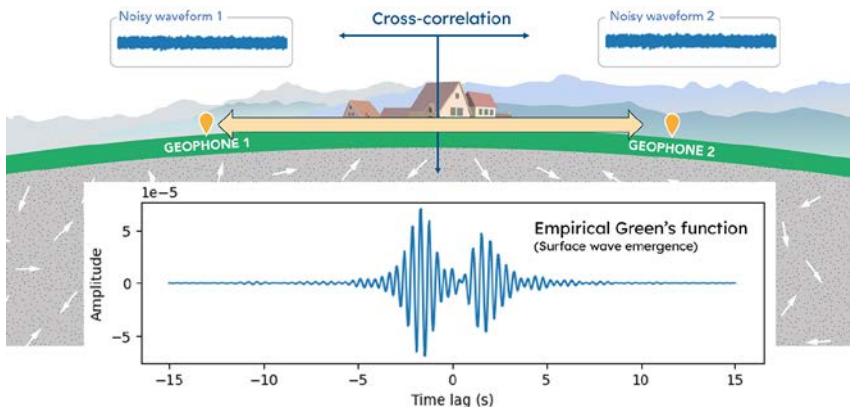


**Figure 6.2** Illustration of the Empirical Green’s function emergence process. Two incoherent noise signals recorded at two different locations are cross-correlated, to extract the EGF of the subsurface in between the two sensors. (White frame) In this example, the reconstructed EGF is highly dominated by surface wave (real data).

sensors. The coherent components of those EGFs, which can then be submitted to a seismic analysis to infer information about the subsurface, depend on the ambient seismic signal composition, that is, its spatial and temporal characteristics. The reconstructed wavefield is usually dominated by interface waves (Rayleigh or Love waves in onshore context, Scholte waves in offshore context, see Mordret et al., 2020), but can also provide coherent body waves if the ambient seismic signal characteristics allows to (Brenquier et al., 2020).

The interferometric process itself is a sequence of signal processing operations (Bensen et al., 2007), which must be carefully parametrized to maximize the signal-to-noise ratio (SNR) of the reconstructed coherent waves. After pre-processing two signals of equal durations recorded at two different locations, cross-correlations operations lead to the final EGF. Finally, the SNR of the reconstructed wavefield can be significantly increased by stacking multiple EGFs that have been reconstructed sequentially in time.

This operation allowing the extraction of coherent seismic waves from the ambient seismic signal then opens the way to two types of seismic analyses, that can be applied to geothermal context studies (or to other geoscience contexts). The first is **Tomography**, where seismic properties (usually shear wave velocity,  $V_s$ ) of the interface waves are analyzed over an array of sensors, to provide as an output 3D models of  $V_s$  spatial distribution within the subsurface. The second is **Monitoring**, where the changes in  $V_s$  value are measured in between EGFs reconstructed at different times. The following paragraphs provide a few elements about how the methods are implemented, what inputs are required and what outputs are expected.

### 6.1.3 Tomography

Ambient noise tomography (ANT) aims to resolve a 3D shear wave velocity ( $V_s$ ) distribution of the investigated area using the dispersion properties of surface wave reconstructed throughout the cross-correlation operation described above. Traditionally, a two-step inversion approach is conducted to map dispersion properties and then define a pseudo-3D  $V_s$  velocity model by stitching local 1D velocity models.

First, group velocity dispersion curves of surface waves (usually the fundamental mode, but higher modes can also be included) are determined using a Frequency-Time Analysis (FTAN) over a frequency ranges (Levshin et al., 1972). This operation is performed by picking the dispersion curve within the FTAN diagram, as illustrated in Figure 6.3.

Recovered dispersion curves are estimated from cross-correlated waveforms, hence averaging the dispersion properties of the medium along the ray between pairs of stations. To resolve spatial seismic velocity variation, inter-station dispersion curves are inverted into group velocity maps (fundamental and higher modes if available) defined over the selected frequency range using a straight ray seismic wave tomography approach (Barmin et al., 2001; Mordret et al., 2013) or Eikonal equation (Lin et al., 2009).

Local dispersion curves sampled from each point of the maps at every available frequency are inverted independently into 1D shear wave velocity models constrained with depth. The final pseudo-3D shear wave velocity model is built by stitching 1D models side by side. Note that recent advances in seismic ambient noise tomography lead to a 1 step full 3D imaging procedure (Zhang et al., 2018) where 3D  $V_s$  model is resolved using a probabilistic inverse approach.

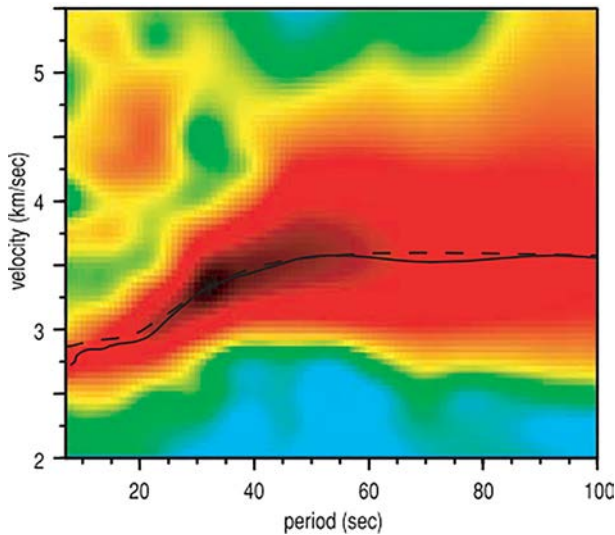


Figure 6.3 Illustration of a raw FTAN diagram, measured group speed curve as the solid line, from Bensen et al. (2007).

Note also that recent advances have started to pave the way for ambient noise tomography of attenuation properties, which can bring valuable insights for geothermal characterization and surveillance (Pérez and Cuellar, 2018), as will be discussed in the following paragraphs. Attenuation analyses through ANSI methods is still in relatively early developments, hence in this paper we do not provide an overview of the technical description of the process or different possible approaches, but we refer the reader to the work of Boschi et al. (2019), Magrini and Boschi (2021) for – non exhaustive – examples of how the seismic attenuation properties of the subsurface can be derived from the ambient seismic signal using ANSI processes.

### 6.1.4 Monitoring

The cross-correlation operation described in the previous section, which leads to an estimate of the EGF and the emergence of coherent seismic waves can be done sequentially, using any temporal resolution (minutes, hours, days, month, year), depending

on observation purpose and on the characteristics of the noise distribution. If the seismic noise sources are globally stable in both time and space, it is possible to extract the waveform evolution over time and perform a velocity variation analysis. Several strategies can be considered, such as studying velocity variation measured on the ballistic part of the waveform, often corresponding to surface waves, or on the so-called coda waves, which correspond to late arrival time and represents the multiple contribution of highly diffracted waves within the medium. The choice between the two strategies can depend on the noise stability characteristics, the coda waves often being favored in case of unstable ballistic wave reconstruction.

Various methods exist for extracting velocity variations (for a review, see Yuan et al., 2021). The doublet method (Poupinet et al., 1984) is preferred for working with the coda, as it is more effective in cases of strong decoherence across seismic signals and small velocity variations ( $\sim 10^{-1}\%$ ) (Olivier et al., 2017). Windowed cross-correlation (Snieder, 2006) and stretching methods (Sens-Schönfelder and Wegler, 2006), on the other hand, can be more easily applied to ballistic waves, as they tend to have a high signal-to-noise ratio and show strong velocity variations (Voisin et al., 2016). An illustration of the stretching method is shown in Figure 6.4. The correlogram is a collection of EGFs reconstructed at different times. A reference waveform is selected or computed (e.g. average waveform) which is then stretched and compressed applying multiple coefficients. A semblance analysis is then performed with each waveform of the correlogram. The stretching coefficient that shows the highest semblance with a given waveform yields the corresponding velocity variation, also often referred to as the  $dv/v$  value.

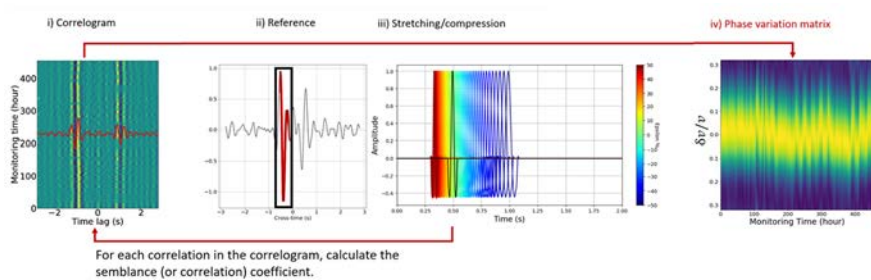


**Figure 6.4** Illustration of the stretching process. (i) Raw correlogram, (ii) chosen stack and time windows to perform the stretching process (red waveform), (iii) sketch of the application of the stretching/compression on a waveform by an epsilon factor (shift to red, compression, shift to blue, stretch), (iv) coherency matrix of the resulting stretching process, where the yellow show the best correlation coefficient between each stretched/compressed seismic trace and each line of the correlogram. The  $dv/v$  value is extracted from this matrix.

The velocity of seismic waves can vary depending on several physical parameters and hence provide capacity for monitoring different phenomenon within the subsurface. As a non-exhaustive summary, Wada et al. (2017) demonstrate that variations in

seismic velocity within the Earth's crust can be influenced by environmental disturbances, such as precipitation (Sens-Schönfelder and Wegler, 2006; Tsai, 2011), atmospheric pressure loading (Olivier and Brenguier, 2016), thermoelastic stresses (Hillers et al., 2015; Meier et al., 2010), ground water change (Voisin et al., 2016; Gaubert-Bastide et al., 2022). Noise-based velocity monitoring has also improved understanding of tectonic and volcanic processes, allowing for the detection of long-term post-seismic relaxation in fault zones (Brenguier et al., 2008; Hobiger et al., 2012), velocity decreases as precursors to volcanic eruptions (Brenguier et al., 2011; Wegler and Sens-Schönfelder, 2007), and interactions between seismic and volcanic systems (Brenguier et al., 2014). Application to geothermal monitoring contexts is addressed in the following paragraphs.

## 6.2 Passive seismic methods for geothermal exploration

Geothermal exploration aims at detecting subsurface areas that hold favorable conditions for geothermal exploitation. Depending on the geological context, and particularly on the type of geothermal field being considered, the targeted geological configuration can vary, as will the associated geophysical signature. Moeck et al. (2014) propose a classification of geothermal contexts in two main categories:

**Convective systems:** which are characterized by the presence of fluid in a reservoir that is set in motion within a convective loop induced by the presence of a heat source. The heat is transported to the surface by the fluid as a function of the permeability of the medium. Convective systems can take place in various geological contexts:

- **Volcanic reservoirs:** where the convection is controlled by the magma chamber. The productive zone of the reservoir is the up-flow zone, which concentrates the hottest fluids and the top of the reservoir is enclosed by conductive clay-caps.
- **Magmatic reservoirs:** where fluids circulate in a network of permeable faults near a recent hot magmatic body acting as the heat source.
- **Non-magmatic reservoirs:** where fluids are circulating in a permeable fault network set up during extensive crustal dynamics. As the crust gets thinner, the upwelling of the Moho increases heat flow, creating local thermal anomalies.

**Conductive systems:** In these geothermal systems, the heat comes from the natural thermal gradient, to which may be added heat flows from granites. As the heat sources are too weak to allow convection, the temperature field is distributed by conduction through the material. Again, one can distinguish different geological contexts leading to conductive geothermal systems:

- **Igneous reservoirs:** which are not reservoirs per se, but thermal anomalies linked to radioactive disintegration. Exploiting the geothermal type of resource implies

fracturing the rock and stimulating fluid circulation within the formation to extract energy.

- Sedimentary reservoirs are typical contexts where geothermal energy extraction is based on the exploitation of the natural thermal gradient, which can be locally accentuated by thermal conductivity contrasts, such as in a deep porous and permeable sedimentary layer.
- “Mountain” reservoir: where the heat from the natural thermal gradient is advected upwards through fluid circulation in deep crustal faults linked to the formation of mountain ranges.

### 6.2.1 *Seismological analysis*

The analysis of seismic events, whether they occur locally or have a more regional origin, can provide a range of information to characterize a geothermal area, understand the global geological configuration and locate the most suitable prospection zones. Several seismic attributes can be derived during those analysis, depending on the data available and the geophysical context. Overall, those methods have been used for the location and characterization of multiple geothermal targets such as heat sources, hydrothermal activity, faulted and permeable zones, of fluid migration pathways and to characterize reservoir properties. Pérez and Cuellar (2018) provide a synthetic summary of the different kinds of analysis that can be performed within a seismological analysis dedicated to geothermal exploration. The following paragraphs transcribe some of this summary, while adding more recent references and analysis.

The most direct approach is to analyze the seismic activity itself. Locating events, evaluating magnitudes, identifying focal mechanisms and statistical distributions are different and complementary ways to relate the temporal and spatial distribution of seismic activity with geothermal key parameters.

Another set of methods aims to understand and map the seismic properties of the subsurface by analyzing how the seismic events propagate within it. The aim is to evaluate seismic velocity models or seismic attenuation models and track the specific signature of geothermal targets.

### *Seismic activity characteristics analysis*

#### *Location and magnitude of events*

The intensity of seismic activity can be associated with tectonic processes but also with fluid dynamics related to geothermal heat sources. Overall, the characteristics of seismic activity provide a direct signature of the energy contained within the magmatic and hydrothermal system, i.e. the geothermal target potential (Pérez and Cuellar, 2018).

Hence, a seismological array can be set-up in the exploration area for a given period to try and record multiple seismic or microseismic events for which specific information such as location, magnitude and focal mechanisms can be inferred and compiled into a catalog. Such an approach will typically provide information about active fault zone geometry, location of fractured zones that facilitate hydrothermal fluid flow (Simiyu, 2009; Faulds and Hinz, 2015).

Figure 6.5 shows an example of microseismic analysis carried out at the Menengai geothermal prospect in Kenya (Simiyu, 2009). The location of microseismic event epicenters underlines the existence of two different trends that could be associated with fault zones, which intersect at the Menengai crater. Such observation suggests that these faults are likely still active, and at their intersection magma and thermal-fluid flow are occurring.

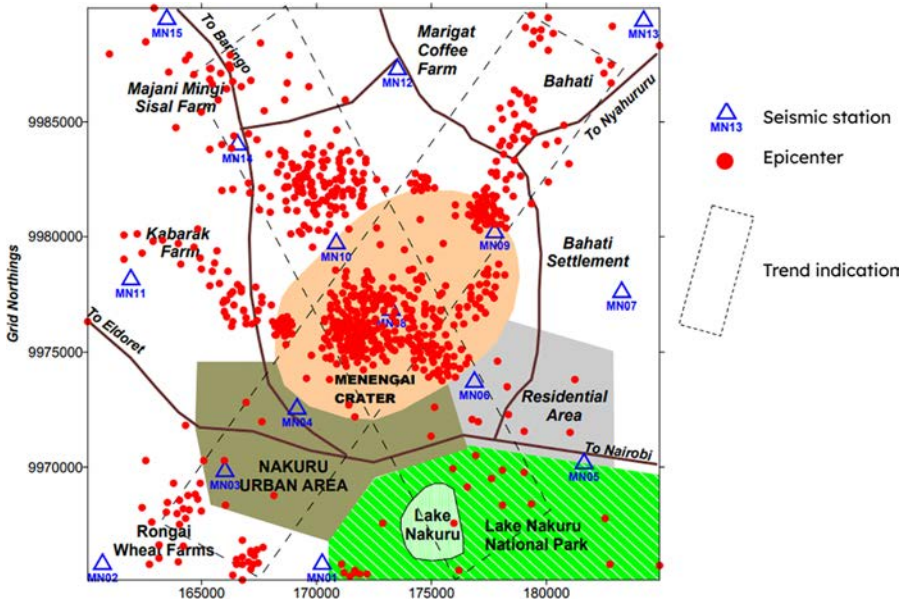
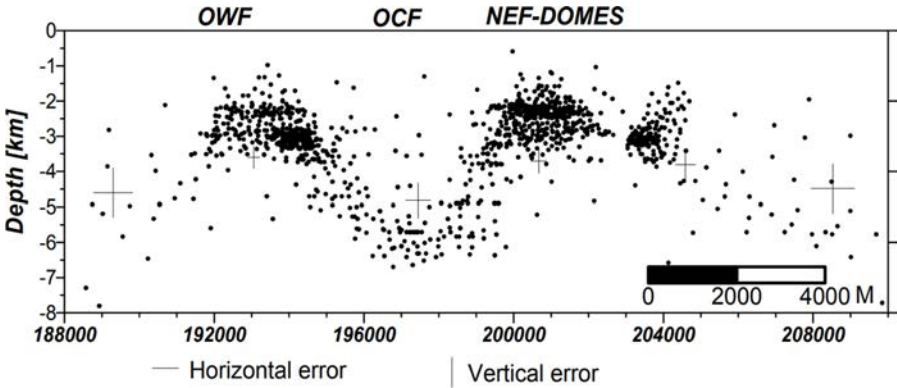


Figure 6.5 Map indicating a passive seismic network (blue triangles) and the location of microseismic events epicenters (red dots) in the area of the Menengai Crater. Modified after Simiyu (2009).

Another potential insight from seismic catalogs relates to the detection and location of zones where the brittle/ductile boundary is characterized by a relatively high elevation. Close to the surface, the rocks of the crust tend to have a brittle behavior which can relate to significant seismic activity. But progressing in depth, the increase of temperature induces a transition from brittle to ductile behavior (e.g. Tanaka, 2004; Suzuki et al., 2014), which leads to a drastic decrease in seismic events activity and occurrence. Figure 6.6 shows an illustration of such an observation

at the Olkaria geothermal field in Kenya. The main production fields (OWF and NEF-DOMES) are associated with a highly elevated brittle/ductile transition, indicating highly elevated heat sources.



**Figure 6.6** Illustration of highly elevated brittle/ductile transition zone which correlate with geothermal production fields (OWF and NEF-DOMES). Modified after Georgsson (2009).

### Focal mechanisms

In addition to locating microseismic events, understanding their focal mechanism provides additional understanding about the tectonic processes that drive the geothermal context of an area. It helps understanding the regional and/or local stress field and provides information about the type of faults in the exploration area and the orientation of the fault planes and/or fractured zones. Analyzing jointly the stress field and the faults and fracture configuration is useful to understand the local thermal fluid flow process (i.e. identifying the most permeable zones and their potential to serve as thermal fluids pathways).

Figure 6.7 illustrates the kind of results that can be obtained through focal mechanisms analysis. Antayhua-Vera (2017) produced this map after a microseismic analysis conducted at the geothermal prospect of Las Tres Virgenes, in Mexico. Their findings demonstrated the correlation of the stress field at that site with the regional tectonic regime of the Gulf of California, and provided local understanding of fault location, orientation and type, and hence of how hydrothermal fluids are expected to flow within the geothermal system.

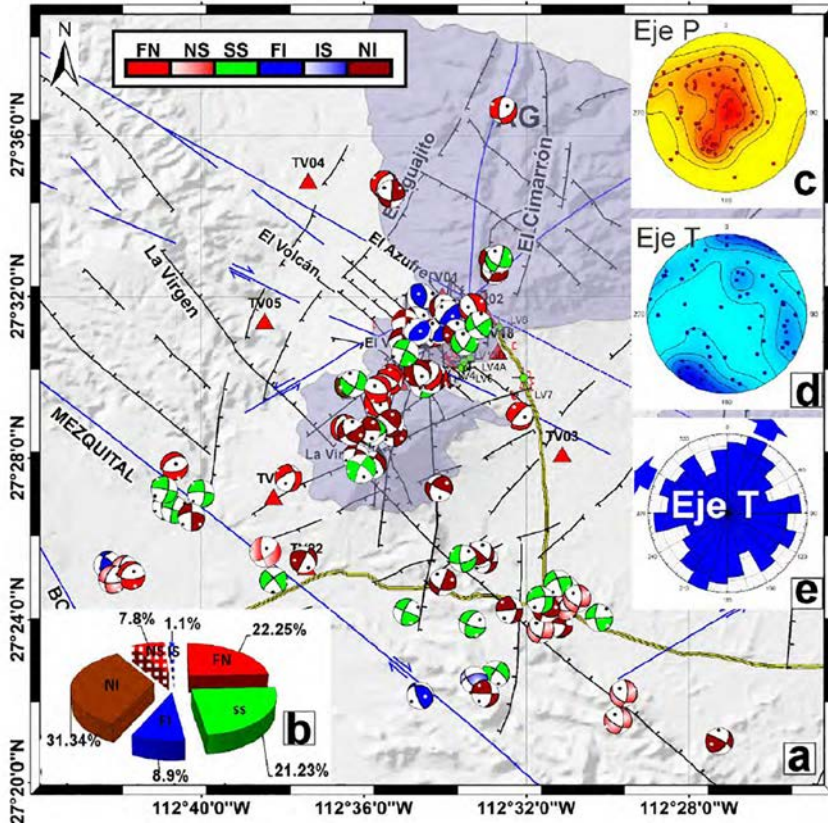


Figure 6.7 Modified after Antayhua-Vera (2017). (a) The map shows focal mechanisms obtained from 91 seismic events. (b) Classification of events. (c) Spherical projection of pressure. (d) Spherical projection of tension axis (e) is the Rose diagram of the tension axis, with arrows indicating the preferential directions of all focal mechanisms.

### Statistical seismology

In this context, statistical seismology refers to a method dedicated to analyzing the statistical relationship that exists between the number of seismic events and the magnitude of the events. Gutenberg and Richter (1944) identified an exponential relationship between the number of earthquakes and their magnitude, and express the frequency of occurrences of seismic events as:

$$\log N = a - bM \tag{6.1}$$

where  $N$  represents the cumulative number of earthquakes whose magnitude exceeds  $M$ , and  $a$  and  $b$  are fitting parameters that describe the relationship at a given location for a given observation period.

Among those two parameters, the so-called  $b$ -value is critical and defines the slope of the straight line that characterize the relationship (Pérez and Cuellar, 2018). The  $b$ -value is considered an indication of the type of process that drives the seismic mechanisms, with values close to 1 associated with tectonic process, considering a homogeneous crust submitted to high stress field, whereas  $b$ -values greater than 1, sometimes close to 2, are representative of geothermal and volcanic environments. Multiple reasons are invoked to explain this difference, such as heterogeneity, low effective stress, fracturing, high thermal gradient, change of fluid composition and distribution, we refer the reader to Pérez and Cuellar (2018) to access multiple references on that topic.

As an illustration of the method, shows the results of a pseudo 3D tomography of  $b$ -values conducted by Benton et al. (2011) at the geothermal field of Tres Virgenes in Mexico. Several high  $b$ -values anomalies are identified that seem correlated to different known faults in the area that exhibit high fracturing degree and intense hydrothermal fluid circulation (Antayhua-Vera et al., 2022).

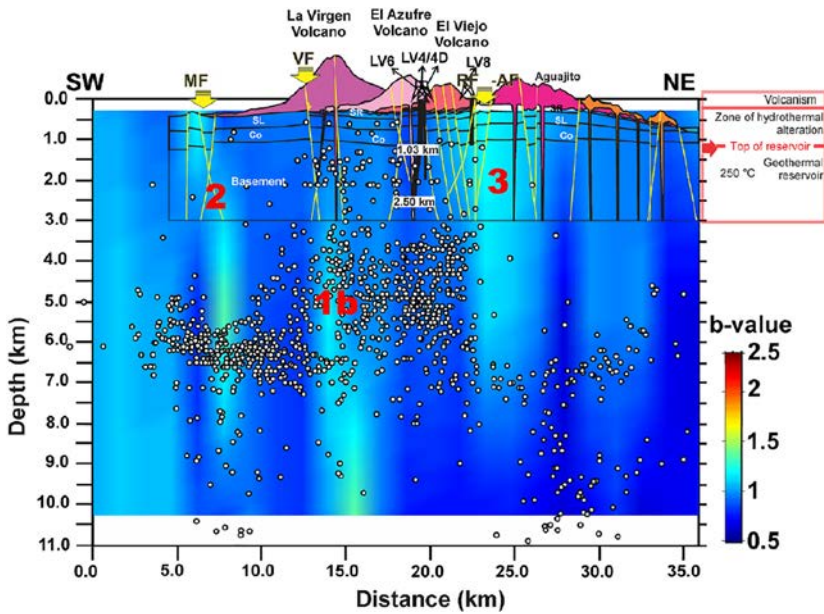


Figure 6.8 Modified after Antayhua-Vera et al. (2022). Results of a pseudo-3D tomography of  $b$ -values conducted at the Tres Virgenes geothermal field.

### Waveform analysis

Following a similar logic as for  $b$ -values analysis, geothermal or volcanic contexts tend to induce seismic events whose waveform might differ from events produced in “pure” tectonic context. Waveform analysis, in the temporal or frequency domain can be a way to distinguish both environments, hence better characterizing

the geothermal sites of interest. Examples of typical seismic signals produced in volcanic environments can be found in the work of Wassermann (2012), Zobin (2011) and Inza-Callupe (2014).

### ***Subsurface seismic properties analysis – The interest of joint velocity/attenuation analysis***

Beyond the study of the intrinsic properties of seismic events such as location, focal mechanism, statistical characteristics or waveform, the recording of the events over an array of seismic sensors also opens the way for characterizing directly an estimate of the subsurface seismic properties' distribution in the area. Using the earthquake as an uncontrolled, yet coherent source of energy, and tracking how the seismic waves propagate within the explored area can help derive 3D models of seismic properties and infer geothermal assets characteristics. The following paragraphs propose some examples of such analysis, distinguishing between attempts to retrieve a **seismic velocity** model of the area from studies focused upon **seismic attenuation** analysis.

In many seismic analysis, seismic velocity is the “favored” studied parameter and velocity-focused work usually treat seismic attenuation as an “undesirable” effect (Vardy and Pinson, 2018), because strong attenuation contexts tend to decrease the accuracy of velocity estimation. However, attenuation properties are also very relevant to be investigated if one seeks to infer complementary types of information. Indeed, the intrinsic seismic attenuation properties characterizing the anelastic behavior of subsurface rocks are sensitive to different parameters of the rock nature, type and composition than seismic velocity, which makes the joint study of those properties relevant in an exploration context.

#### **Velocity models**

If a sufficient number of seismic events are recorded through a seismic sensor array, it is possible to pick body wave time arrivals and process the travel times to infer a 3D seismic velocity model of the subsurface. Such an approach, sometimes called “Earthquake tomography”, requires specific processing methodologies such as joint inversion of the seismic events hypocenters and of the subsurface velocity model, for in that case the location of the seismic source (the earthquake) is also an unknown parameter.

Muksin et al. (2013) performed such an earthquake tomography to characterize the seismic properties of the Tarutung geothermal area, in Indonesia. Their method included simultaneous inversion of micro-earthquake locations and 1D velocity models, followed by a 3D tomographic inversion. The resulting 3D Vp model helped them to accurately delineate the structure of the Tarutung and Sarulla basin, identifying complex zones, and orientation of fault areas, as illustrated in Figure 6.9a). They also derived a Vp/Vs ratio 3D model in which high Vp/Vs values

anomalies are potentially related to a configuration of fluid bearing sediments associated with fracturing, such context suggesting favorable conditions for geothermal exploitation (Figure 6.9b).

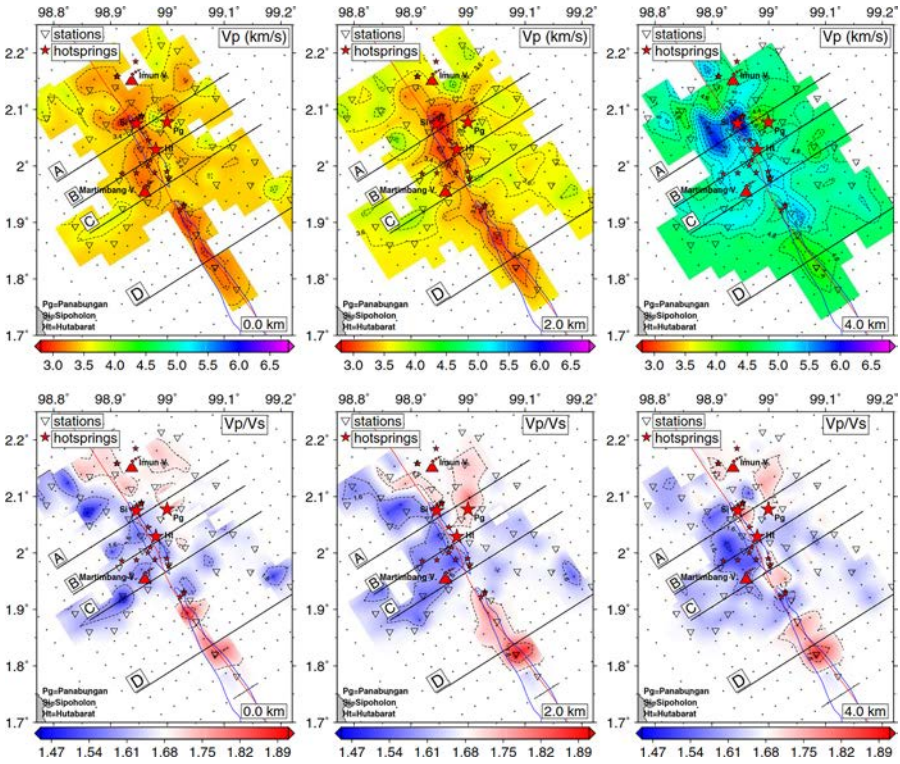


Figure 6.9 Modified after Muksin et al. (2013). Horizontal slices of the Vp and Vp/Vs 3D models at depth of 0, 2, and 6 km for Vp in (a), (b), and (c), and for Vp/Vs in (d), (e), and (f).

Vp/Vs ratio measurements designate the analysis of the velocity ratio of the P (compression) and S (shear) body waves. It allows a qualitative interpretation of the subsurface elastic properties, and has proven a useful approach in seismic geothermal exploration as Vp/Vs anomalic values have been able to identify different geothermal favorable contexts. For instance, as discussed, Muksin et al. (2013) identified fluid-bearing sediments through high Vp/Vs anomalies, whereas Simiyu (2009) identify and delineate the heat source of the Menengai caldeira in Kenya as a low Vp/Vs anomaly (Figure 6.10). In geothermal context, low Vp/Vs values are usually associated with a local decrease of P-wave velocity due to low pore pressure, high heat flow, fracture systems and vapor/gas saturation presence in the surveyed area (Pérez and Cuellar, 2018).

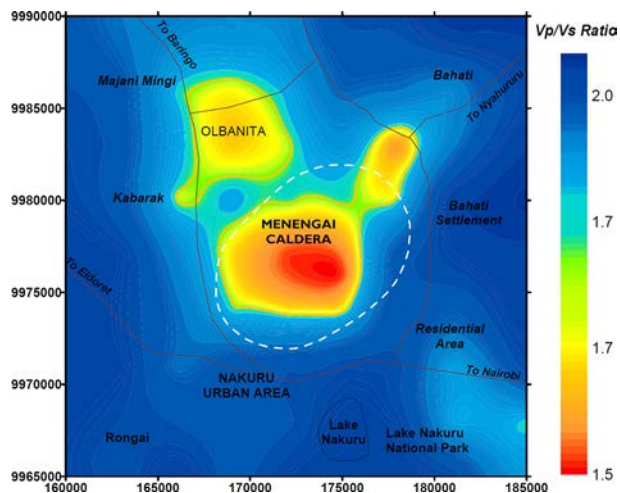


Figure 6.10 Modified after Simiyu (2009).  $V_p/V_s$  ratio map extracted from a 3D tomography at the Menengai geothermal area. The low value anomaly correlated with the expected location of the heat source at this geothermal site.

### Attenuation models

In the context of geothermal exploration, the two key resources to identify are heat and fluid. Attenuation anomalies have been shown to highlight such favorable targets. Sato et al. (1989) and Mavko (1980) propose that an increase of seismic attenuation properties can be related to an increasing temperature. Hough et al. (1999) interpret a pseudo mapping of the thermal distribution by imaging the variability of attenuation structure in Coso geothermal reservoir. This behavior of dependence between attenuation and temperature of geothermal rocks at reservoir conditions as been highlighted by Jaya et al. (2010) and Poletto et al. (2018) with a petrophysical approach using Biot-Gassmann relation.

On the other hand, Haberland et al. (2009) associate attenuation increasing to an augmentation of the fluid content. For Grab et al. (2017) velocity structures reflect lithology while attenuation is a better indicator for reservoir permeability and fluid saturation in magmatic geothermal reservoir. Hudson et al. (2023) use attenuation tomography to map crustal fluid pathways and hydrothermal/geothermal systems in volcanic context. Attenuation imaging method can also provide complementary information to the traditional approaches used in geothermal exploration. In volcanic context, Muskin et al. (2013) demonstrate that regions of high attenuation and high conductivity are related to high fluid content.

Multiple studies have also proven anelastic properties to be a good indicator of the presence of magma or melting materials, which tend to significantly dissipate seismic energy during wave propagation. This correlation has typically been documented in studies investigating mantle properties and characteristics (e.g. Karato, 2004; Nakajima, et al. 2013).

However, as mentioned previously, evaluating intrinsic attenuation properties of the subsurface through seismic events analysis is not an easy task, for it requires to discard or correct for other seismic attenuation mechanisms which are rather related to the propagation path of the seismic waves such as geometrical spreading and multipathing (Ko et al., 2012).

Lin et al. (2024) present a recent study of attenuation structures in the northern T aiwan volcanic zone where they explore the attenuation features of the area and their relation to the local magmatic and tectonic mechanisms.

The authors collected seismic waveforms from 43 earthquakes using a seismic array of 118 stations, for a period of about 1 year, and isolated the P-waves and S-waves arrivals. Their data analysis process begins with a 1D inversion to establish a baseline attenuation model, corrected using a frequency-dependent power law that adjusts for changes in attenuation across frequencies. This model initializes a 3D inversion, where amplitude data is standardized to a reference frequency (5 Hz) to ensure consistency across frequencies and Fr echet kernels were computed by 3D ray tracing through the tomographic velocity model. The inversion estimates differential inverse quality factors ( $Q^{-1}$ ) perturbations, with prior covariances and smoothing ensuring model stability and resolution robustness. Ultimately, the authors manage to estimate 3D models of  $Q_p$  and  $Q_s$  (quality factors) in the area.

The results of this analysis for geothermal exploration are the potential identification of hydrothermal activities and magma reservoirs at varying depth, which are characterized by high attenuation values (low Q factors), as illustrated in Figure 6.11.

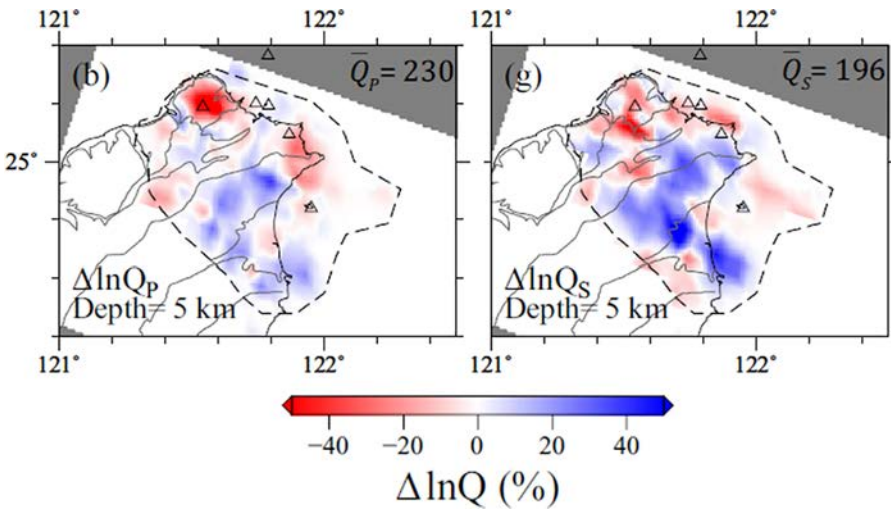


Figure 6.11 Illustration of subsurface attenuation characterization based on seismological analysis (modified after Lin et al., 2024). The maps show lateral variation of attenuation values extracted from the global attenuation 3D model, focusing on a specific depth of 5 km.

Another example of geothermal areas characterization through attenuation assessment can be found in the work by Antayhua-Vera (2017). Quality factors were computed using the coda of a collection of seismic events to derive coda attenuation ( $Q_c$ ) maps, at multiple frequencies (i.e. probing different depth of the medium). In their interpretation, the authors relate high  $Q_c$  values (low attenuation) with area of high permeability (Figure 6.12).

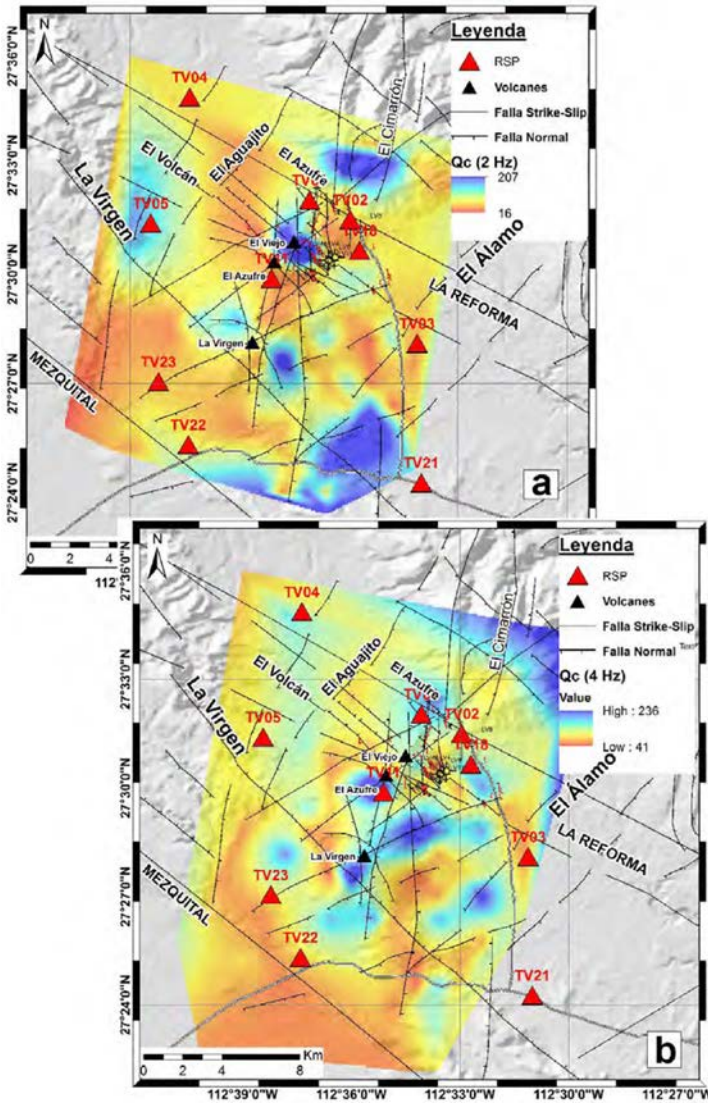


Figure 6.12 Modified after Antayhua-Vera (2017). Iso-maps of coda quality factor ( $Q_c$ ) values at the geothermal field of Tres Virgenes, Mexico.

As for  $V_p/V_s$  analysis, examining the quality factor ratio of P and S waves ( $Q_p/Q_s$  Ratio) can also inform on the specific features of the geothermal field. For instance, low  $Q_p/Q_s$  ratio (P-waves more attenuated than S-waves may indicate a medium partially saturated with fluids (Pérez and Cuellar, 2018). The presence magmatic bodies, on the contrary, would result in almost complete attenuation of the S-wave, hence high  $Q_p/Q_s$  ratio (Georgsson, 2009). Another interesting example is found in the work by Yeh et al. (2021), who used  $Q_p/Q_s$  analysis to investigate the subsurface context of the Taipei area in Taiwan. They observe low  $Q_p/Q_s$  values that they interpret a due to a dominance of scattering attenuation due to a highly fractured medium but denying the existence of a magmatic chamber, as was pointed out by an earlier study based on velocity analysis only (Lin, 2016), hence illustrating the interest of analyzing jointly both velocity and attenuation features to obtain a geological and geothermal assessment as complete as possible.

## 6.2.2 *Ambient noise seismic interferometry (ANSI)*

ANSI methods are another possibility to derive 3D models of the subsurface seismic properties. By opposition to earthquake-based velocity tomography, ANSI tools present the advantage of allowing data acquisition and producing results even in areas where earthquake activity is low, where tomography analysis based solely on detection of seismic events would not be possible. The geophysical value brought by ANSI studies (3D models of seismic properties), their flexibility for implementation in various contexts (passive sensors deployment over a few days or weeks), along with the economic advantage inherent to passive seismic studies has brought ANSI methods and particularly 3D  $V_s$  tomography technology as a nearly common geophysical tool in today's geothermal exploration strategies. Hence a several applications of ANSI-based tomography models are presented in the literature, addressing various geothermal contexts.

Toledo et al. (2022) investigated the potential of the method in the volcanic context. The authors derived a 3D  $V_s$  model at the Theistareykir geothermal field in Iceland, where a clear separation between a high  $V_s$  anomaly and a low  $V_s$  anomaly is observed, which follows a N/NW orientation (Figure 6.13). Such observation agrees with the trend and pattern observed through a Magnetotelluric investigation of the site, hence confirming the interest of ANSI based  $V_s$  models for geothermal characterization. Overall, low velocity anomalies coincide with bodies of low electrical resistivity, which would consistently suggest the presence of rocks saturated with hydrothermal fluids (Toledo et al., 2022)

Also in the volcanic context, Sánchez-Pastor et al. (2021) also observe a consistent correspondence between low electrical resistivity anomalies and low  $V_s$  anomalies at the Hengill geothermal field in Iceland. The authors also pushed their interpretation to identify iso-velocity curves as transition zones within the geothermal system, proposing the 2 km/s iso-velocity curve as being a proxy

to the bottom of the steam cap and the 3 km/s iso-velocity curve as being the base of the stratification composing the Hengill volcanic system. Another illustration of 3D Vs tomography application for geothermal characterization of volcanic contexts can be found in Martins et al. (2020), where the authors identify a low-velocity cavity which is interpreted as an area of up-flowing fluids where temperature and permeability are enhanced.

Cheng et al. (2021) propose an ANSI tomographic application in a crustal fault context where hydrothermal fluids are known to reach the surface. They use relative spatial velocity variations observed in the area to infer the presence of faults (Figure 6.14) where hydrothermal fluids are expected to circulate. Their seismic analysis also shows good correspondence with resistivity models obtained with controlled sources audio-magnetotellurics (CSAMT) measurements, where low velocity anomalies correspond to low resistivity anomalies.

In a sedimentary context, Planès et al. (2020) used a 3D Vs tomography to improve their understanding of the geological context at the Greater Geneva basin. They manage to identify geological and topographical relationship and also interpret iso-velocity curves depth variation as a mean to identify the thickness of the sedimentary cover.

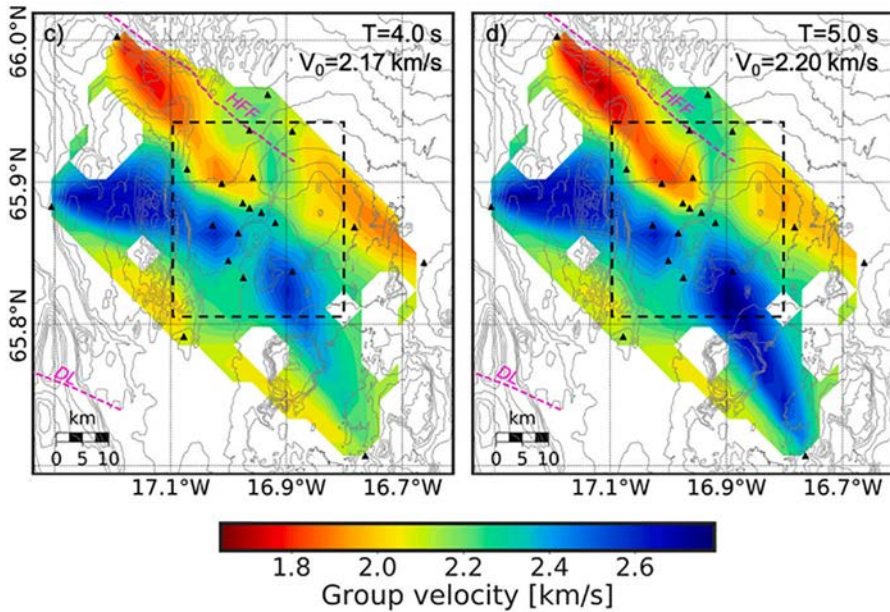


Figure 6.13 Modified after Toledo et al. (2022). Rayleigh wave group velocity maps at two different frequencies.

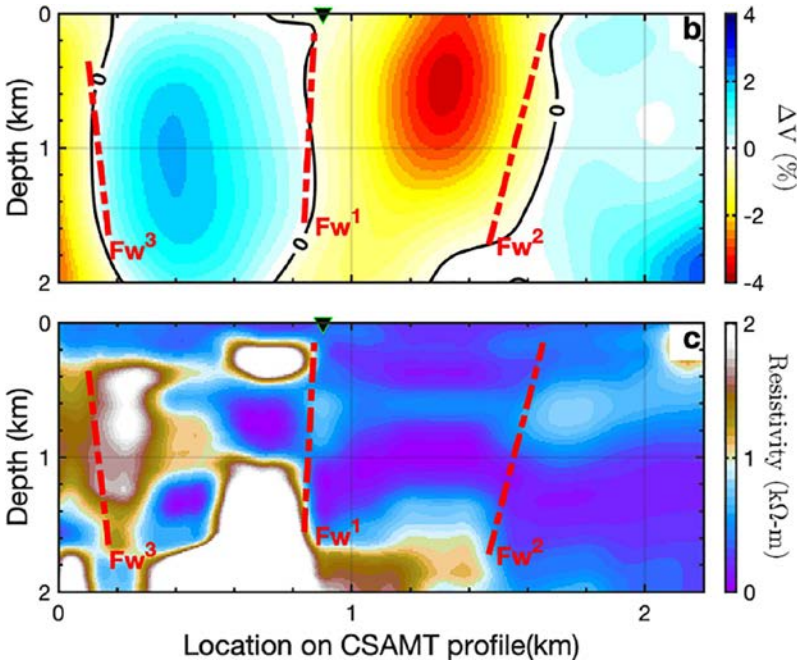


Figure 6.14 Modified after Cheng et al. (2021). (Up) Spatial relative velocity variations section. (Down) Resistivity cross-section derived from CSAMT acquisition.

Many other examples of ANSI based tomography application to geothermal systems characterization can be found in the literature. Overall ANSI-based 3D Vs tomography allows a better understanding of the geological context and features, identifying faults, delineating geological layers limits and highlighting geothermal systems key characteristics. Many authors point out that seismic information provided by ANSI tomography tools is consistent with information obtained through electrical or electromagnetic surveys, hence introducing the complementary role of passive seismic methods within geothermal exploration workflows, as discussed in the following paragraph.

### 6.2.3 Integration into the geothermal exploration workflow

Within geological exploration workflows, the role of geophysical methods is to provide data or models that inform on the subsurface response to the solicitation by a given physical field (e.g. electromagnetic, electrical, seismic, magnetic, gravimetric). Energy is propagated within the medium and the propagation modes and characteristics inform on the physical properties of the rocks associated with those physical fields (e.g. resistivity, velocity, attenuation).

As in many geophysical exploration strategies, it is rarely one method that brings in the open useful information, but rather a multi-physics approach where complementary data and models are compared or even inferred simultaneously, so that different information converge toward the most logical interpretation.

From that perspective, passive seismic methods are a relevant tool within the geothermal exploration toolbox. In general, the most utilized strategies to detect and characterize geothermal targets are based on electromagnetic methods (Muñoz, 2014) as geothermal reservoirs display clear conductive signature. Nevertheless, seismic properties can also highlight similar geological features (Toledo et al., 2022) driven by the presence of water-filled fractures which tend to decrease seismic velocity and increase seismic attenuation. Joint interpretation of passive seismic with other geophysical methods is usually highly valuable. Several approaches can be adopted, we provide below a non-exhaustive list of those methodologies along with a few literature examples:

- Workflow integration: Exploration workflows can benefit from dedicated multi-physics workflow such as “Play and Fairway analysis” (Craig et al., 2021) where ANSI-based Vs tomography brings insight on the elastic structures of the investigated area allowing to characterize complex geothermal context.
- Statistical integration: Models obtained from multiphysics imaging methods are always the resulting complex combination of geophysical responses of the heterogeneous subsurface (e.g. faults, layers, fluids, petrophysics, lithology etc.). Statistical integration approaches aim to highlight and isolate specific geological targets that can affect differently the geophysical responses of various geophysical methods (e.g. Ars et al., 2024; Muñoz et al., 2010; Bauer et al., 2012).
- Constrained inversion: Going beyond the “simple” co-interpretation of Vs velocity models in parallel to other geophysical models, one can also use a constrained inversion approach where ambient noise tomography is proceeded under the constrain of a 3D resolved pre-obtained model describing the distribution of other physical parameters such as resistivity (Ars et al., 2024).
- Joint inversion: In this case, the geophysical inversion process itself is parametrized to find the best fitting models under the constraint of a given relationship coupling the physical model properties. A typical example in geothermal exploration context of such an approach is the joint inversion of ANSI-based surface wave dataset with gravimetric dataset. Both physical fields are sensitive to elastic properties of the underground, and the joint inversion process results in an improved resolution of both geophysical models (e.g. Carillo et al., 2024; Ars et al. 2024).
- Perspectives: So far, ANSI based tomography methods have been focused on deriving Vs models of the subsurface. However, recent developments have highlighted to possibility to also derive 3D seismic attenuation models from the ambient seismic signal (e.g. Soergel et al., 2020; Cabrera-Perez et al., 2024). Such evolution may lead to future co-processing of seismic and resistivity datasets for better imaging of attenuation and conductive structures, since they both exhibit high sensitivity to the presence of fluids.

## 6.3 Geothermal monitoring

Another crucial aspect of Geothermal energy large-scale deployment is the surveillance of the subsurface environment during operations to ensure performance and conformance. 4D active seismic survey cannot fulfill this objective, again due to their prohibitive deployment cost, in addition to complex logistics for repeated onshore deployment. Yet again, passive seismic methods can be deployed to enhance our capacities for monitoring the evolution of Geothermal assets and their seismic properties, continuously and cost-effectively. Just like for exploration purposes, in this paper we distinguish two “families” of passive seismic methods that can be used for enhanced surveillance of geothermal fields. First, all the methods based on the analysis of impulsive seismic events, independently of their magnitude (from large earthquakes to micro-tremors), which we refer to as **Seismological analysis**. Second, the methods and analysis tools based on **Ambient Noise Seismic Interferometry (ANSI)**, where incoherent parts of the ambient seismic signal are analyzed and processed to extract coherent seismic wavefields, which can then be analyzed to infer the seismic properties (velocity, attenuation) of the subsurface.

### 6.3.1 *Seismological analysis monitoring*

Seismological analysis methods have been used to fulfill a variable number of objectives in the geothermal monitoring context. Possibly one of the most known functions of passive seismic monitoring is the detection and analysis of microseismic events to track for potential operation-induced seismicity and ensure that such seismicity remains in the range of expected epicenter locations and events magnitude. This constitutes a typical objective of passive seismic monitoring of Enhanced Geothermal Systems (EGS). This denomination designates geothermal contexts where fluid circulation is artificially stimulated through enhancement of the rock formation permeability by means of hydraulic stimulation technics. Locating and analyzing the microseismic events that are induced by the stimulation operations allows for operators to assess the effectiveness of the process in time, by following the extent of the resulting fracture network, analyze the effect and relationship of the operations with the local stress field, and ultimately avoid the triggering of undesired, large magnitude seismic events.

Statistical seismological analysis tools, such as *b*-value computation, can also be used as a monitoring tool, to fulfill various objectives. The possibility of monitoring water injection processes through *b*-value analysis within the reservoir has been illustrated by multiple authors, many of which can be found in the review from Pérez and Cuellar (2018). As an illustration for this chapter, we refer to the study of Antayhua-Vera et al. (2022) where the authors studied the spatio-temporal distribution of *b*-values at the geothermal field of Tres Virgenes in Mexico (Figure 6.15). Their observations report that increases of *b*-value are generally coincident sudden increases in water injection dynamics.

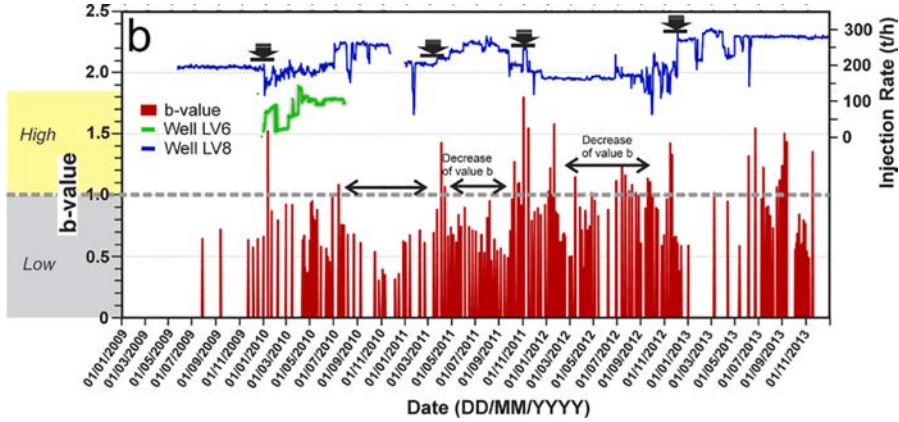


Figure 6.15 Modified after Antayhua-Vera et al. (2022). Water injection rates comparison with  $b$ -values for a period of about 4 years at the Tres Virgenes geothermal field (vertical black arrows indicate sudden water injections).

Another interesting report describing microseismic monitoring applications on geothermal sites can be found in Cruz-Noé et al. (2018). The authors report key observations following the 30 years duration monitoring of microseismicity of three Mexican geothermal fields, namely Los Azufres, Los Humeros and La Tres Virgenes. Multiple analysis are presented which relate to various interpretation and links to the geothermal field production activity itself, including fault reactivation due to modification of the local stress field, but also induced seismicity related to geothermal water injection and geothermal fluid extraction. They also report on the effects of drilling, hydraulic stimulations, and well testing on the micro seismic activity itself.

Beyond the analysis of microseismicity activity characteristics such as statistical distributions or source mechanism, information about geothermal assets evolution in time can also be obtained through the analysis of seismic properties, typically seismic velocity and seismic attenuation. A sound illustration of such analysis can be found in the work by Guo and Thurber (2022). The authors applied a time-lapse tomographic approach based on a double-difference workflow. They analyze a catalog of earthquakes and apply two different tomographic analysis to evaluate both the changes in P-wave velocity (DDV tomography) and P-wave attenuation (DDQ tomography), during a relatively long monitoring period (>5 years). Their work allows them to produce 4D models of velocity and attenuation parameters and to relate the observed variations to injection processes within the geothermal reservoir. An interesting diagram is available in the “Supporting information” document associated with their work (Figure 6.16), which depicts how P-wave attenuation ( $Q_p$ ) and velocity ( $V_p$ ) are expected to vary depending on the on-going process induced by fluid injection within the geothermal system.

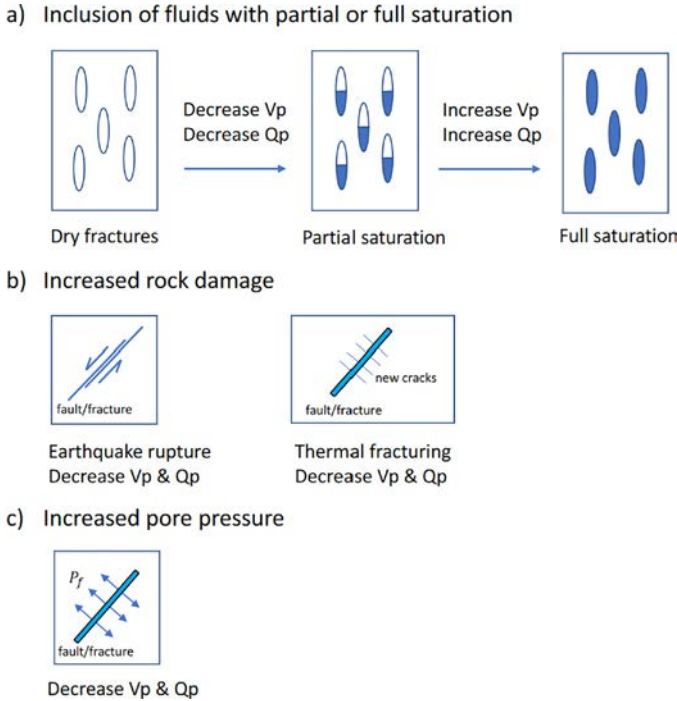


Figure 6.16 Schematic illustration of different injection-induced processes occurring in geothermal reservoir and their associated seismic response in terms of  $P$ -wave seismic velocity and attenuation. Modified after Guo and Thurber (2022) – Supporting information.

### 6.3.2 Ambient noise seismic interferometry monitoring

ANSI-based methods have been gaining momentum during the last two decades as relevant tools for seismic monitoring of the subsurface. ANSI-based monitoring approaches are often referred to as the  $dv/v$  method, since it consists of tracking velocity changes by comparing ANSI-based reconstruction waveforms in time through phase-shifts measurements. Such an approach has the potential to detect very subtle shear wave velocity changes (when dealing with surface wave), possibly on the order of 0.1% and lower depending on the site conditions. Geophysicists have demonstrated the sensitivity of the method to various phenomena such as precipitation, atmospheric pressure loading, thermoelastic stresses, ground water change, stress relaxation and others. Applications to geothermal monitoring have not yet been very numerous, but edifying studies yet exist that highlight the strong potential of ANSI for geothermal operations surveillance.

For instance, Muñoz-Burbano et al. (2024) have been monitoring seismic velocities using ANSI approaches at the Domo de San Pedro Geothermal field, in Mexico, using a seismic array of 20 broadband stations. The authors have been able to reconstruct velocity relative variations maps sequentially in time and to relate significant velocity changes to fluid injection dynamics and to the associated stress distribution.

In addition to this study, Taira et al. (2018) demonstrate that detailed analysis of velocity variations may describe the temporal evolution (5 years) of the Salton Sea geothermal field stress state. Figure 6.17 presents time-lapse measurements of seismic velocity variations in several frequency ranges that were computed as the average of the 9 components of the Green's tensor. The events marked as DBC, EMC and BS represent sudden drops in the seismic velocity and are related to some local earthquakes. Taira et al. (2018) show that the amplitudes of those drops are too great to be linked solely to the earthquakes for the BS event and suggest that the sudden evolution in the velocity variation time series is linked to an aseismic deformation related to fracture opening. In addition, a long-term upward trend (0.25% in the range 0.5–2 Hz) can be observed in all frequency bands. The authors propose that this long-term trends relate to a progressive poro-elastic contraction linked to geothermal production and the associated evolution of the stress field within the reservoir.

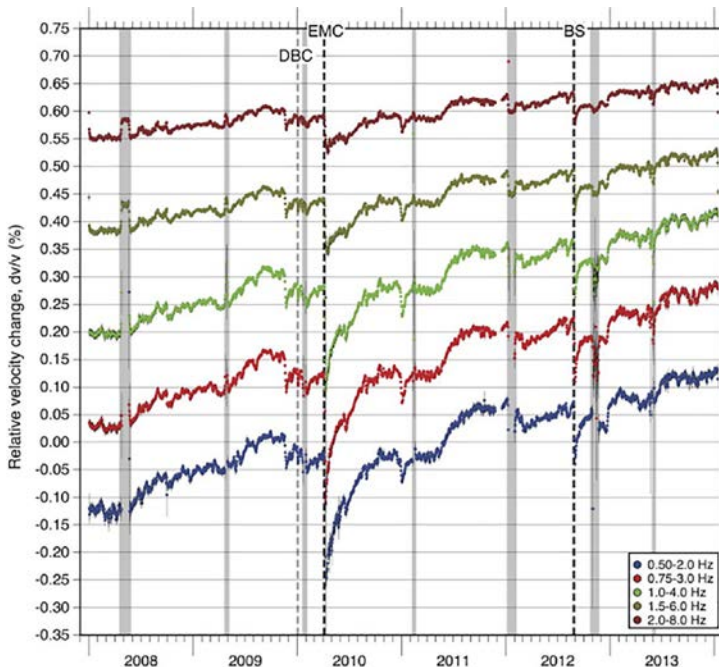


**Figure 6.17** Modified after Taira et al. (2018). Relative velocity variations time-series computed for several frequency ranges. Dashed black lines indicates sudden drops of seismic velocity, partly related to earthquake events and to deformation processes.

Another edifying study is the work by Sanchez-Pastor et al. (2021), who present an ANSI based method to monitor the Hengill geothermal field (Iceland). This site presents a challenge inherent to geothermal systems operations which is to probe the steam fluctuation inside the reservoir. During geothermal exploitation, the estimation of the steam content is key from both operational and economical perspectives. To quantify these quantities, the authors used an array of 50 stations and compute auto-correlation (ACs) on the vertical component. The nuance of the velocity variation measurement on ACs compared to cross-correlation between two sensors is essentially that the reconstructed wavefield in ACs will be much more sensitive to volume waves, and mainly to P waves. This means that the velocity variation measurement will be correlated with the fluid content, and not anti-correlated as is classically observed in studies targeting ground water table using surface wave (for example). The velocity variations measurements obtained on the ACs are compared with some rock physics model including hydrological and gas saturation information.

The results of the various modelling work performed by the authors and the final comparison with the observations is shown in Figure 6.18. The subfigure (a) presents the pressure and temperature variation, the subfigure (b) the estimated steam cap evolution, the subfigure (c) the modeled  $V_p$  and  $V_s$  evolution over the monitoring time. Finally, the subfigure (d) shows the monitored  $dv/v$  versus the subsidence of the geothermal field. The author demonstrates that the seismic velocity values are decreasing over the monitoring time, when the steam ratio continues to rise which is consistent with the expected variation in  $V_p$  as water content decreases. This study highlights the economic possibilities to monitor the steam evolution during long periods with a low-cost method associated with robust modelling.

The examples previously presented demonstrate that the measure of seismic velocities through ANSI-based approaches is feasible and is a useful tool to monitor changes in the state of stress in geothermal reservoirs (Taira et al., 2018; Muñoz-Burbano et al., 2024) or changes of fluid distribution (Sanchez-Pastor et al., 2021).

Nevertheless, as for ANSI-based tomography, ANSI-based monitoring techniques also start evolving toward the study of other seismic attributes than seismic velocity. The work by Obermann et al. (2015) is an example of such evolution. The authors propose to survey the geothermal reservoir using another attribute called the decoherence of the reconstructed waveforms. Initially the decoherence is an indicator of the quality of the reconstructed signal between a reference waveform (e.g. at the beginning of the monitoring period) and each waveform reconstructed at a later time and on first order is affected by site-dependent noise conditions that change too abruptly. In the study by Obermann et al. (2015) though, a strong decoherence is observed that seems associated with a gas kick event which led to the failure of the St Gallen deep geothermal project. Figure 6.19 illustrates the evolution of decoherency time-series for multiple station pairs. For all the seismic stations pairs crossing the reservoir, a strong decoherence is observed between the 10th of July and the 14th of August, which period correlates with the injection

procedure inside the geothermal reservoir that led to the gas kick (Figure 6.19a). Figure 6.19b shows that for the pairs not crossing the reservoir this decoherence drop is not observed.

The authors argue that the decoherence drop can also be the result of changes in the scattering properties of the subsurface (e.g. Larose et al., 2010; Obermann et al., 2013, 2014; Planès et al., 2014), which in the St Gallen case may be associated to geothermal induced processes such as pore pressure changes related to gas release, critical prestressing of a fault, or changes in attenuation properties also due to the presence of gas.

Although the physical interpretation of the decoherence variation is not clear, this study highlights the fact that other seismic attributes possibly more sensitive to some physical phenomena can also be derived from ANSI based monitoring analysis and that a strong potential also exists in the development of such novel approaches. In particular, the focus on attenuation properties monitoring is a promising research lead since attenuation is particularly sensitive to the temperature field and the nature and distribution of fluids within the subsurface, which are both key aspects of geothermal surveillance strategies. In the end, deriving attenuation properties will allow to provide the full seismic response of the geothermal system, in space, and in time.

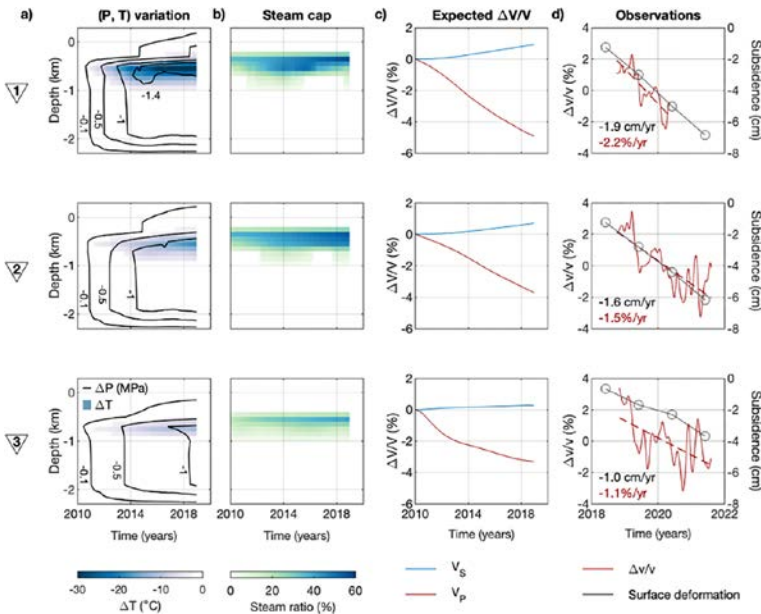
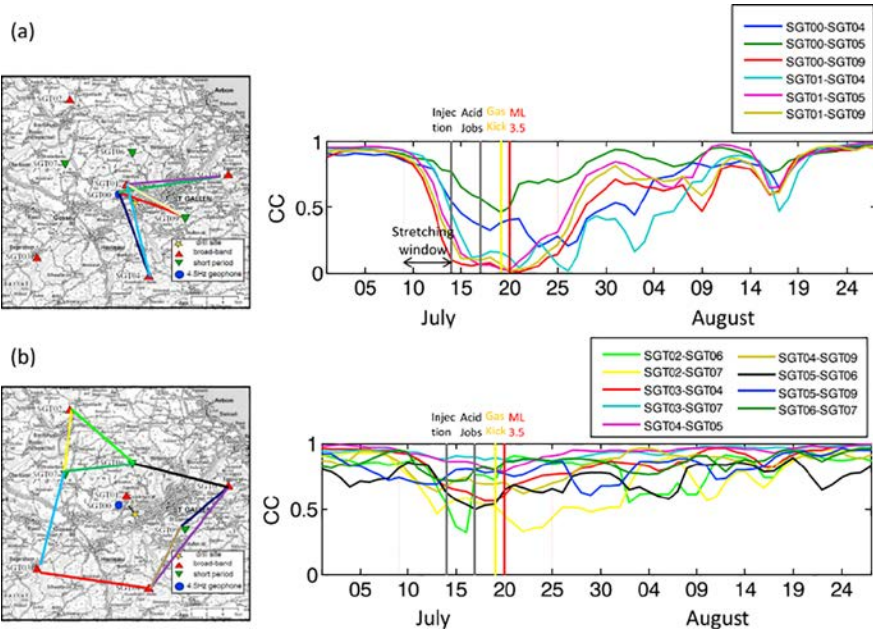


Figure 6.18 Modified after Sanchez-Pastor et al. (2021). Each line highlights a different seismic station. (a) Modelisation of the temperature variation in the medium, (b) Estimated steam evolution (c)  $V_p$  and  $V_s$  computed from rock physics modelisation (d) Monitored  $dv/v$  and monitored subsidence.



**Figure 6.19** Modified after Obermann et al. (2015). Decoherence time series measured for multiple seismic station pairs at the St Gallen geothermal field. (a) Pairs crossing the reservoir. (b) Pairs not crossing the reservoir. Colored vertical lines indicate different phases in the geothermal operations sequence leading to the gas kick.

## Concluding remarks

Passive seismic methods have been able to emerge in the geophysicist toolbox mainly thanks to the evolution of seismic acquisition technologies, which finally allowed for continuous recordings and storage of the ambient seismic signal instead of simple “triggered” recordings. This major change ultimately allowed scientists to investigate and develop a large scope of tools and methods using a passive seismic approach bringing value for many geoscience fields including geothermal characterization and monitoring. Today, enhancing the potential of passive seismic methods still depends on, and will benefit from technological advances in the acquisition process. Typical key characteristics that are being proposed in recently produced seismic sensors or in phase of implementation for future models are:

- **Autonomy**, with longer lasting batteries for autonomous nodes in the context of monitoring.
- **Real-time communication** of the data, to avoid multiple intervention on site to retrieve the data and allow quasi-continuous monitoring.

- **Low frequency sensitivity:** to allow for detection and analysis of low frequency waves, a key parameter for instance to analyze interface waves while requiring a high penetration depth (in ANSI-based approaches for instance).
- **Cost:** to allow for dense networks deployment, hence improving the accuracy of earthquake-based seismological analysis and enhancing the resolution of the seismic models derived either from ANSI methods or earthquake tomography approaches.

All those improvements will participate in further highlighting the very strong potential of passive seismic methods to serve as key methods in geothermal exploration and monitoring geophysical strategies.

Passive seismic methods are the most cost-effective way to provide information about the subsurface seismic properties. In geothermal contexts, geophysicists typically track velocity and attenuation anomalies to infer the presence of faults, heat sources, hydrothermal fluid circulation patterns, and address the general geological and tectonic context. In addition to the intrinsic value of such passive seismic characterization strategies, they can also be used to improve the accuracy of the global geophysical approach by completing other geophysical datasets and enhancing their interpretation. Further developments and applications of joint or constrained inversion schemes will likely be a cornerstone of passive seismic methods integration in geophysical assessments in geothermal contexts, as in many other geo-resource explorations (e.g. natural H<sub>2</sub>, helium).

Monitoring strategies for geothermal operations surveillance have naturally benefited from passive seismic methods thanks to the intrinsic continuity of the data acquisition. The most known application is microseismic monitoring, which aims to track in time and space the seismicity potentially induced by geothermal operations. In addition, methods based on monitoring the subsurface seismic properties – not only the seismic activity – have been gaining momentum in the last few years to better understand the geothermal target behavior in production phase. Methods such as time-lapse earthquake tomography and ambient seismic noise interferometry (ANSI) provide such capacities, yet developments and applications to multiple different contexts are required to improve their sensitivity to operations-induced processes and hence propagate their use as common tools in geophysical geothermal monitoring strategies.

The strength of passive seismic methods relies on the fact that they have been built while searching for the tiniest, hidden bit of information within a seismic signal that is initially not well understood, globally uncontrolled, yet continuously produced by our environment. The dedication of scientists for exploiting and enhancing the information contained in what originally appeared to be a disturbance for active seismic studies is remarkable. As of this day, and as is illustrated within this chapter, geophysicists have now the possibility to extract spatial and temporal seismic information from the whole ambient seismic signal, including both the coherent part of the signals (through earthquake and microseismic analysis) and the incoherent part of the signal (through ANSI approaches in particular). They have turned the ambient seismic signal into a highly valuable source of information from which every

part can be exploited. This chapter illustrates the diversity and complementarity of the passive seismic methods which provide many means of obtaining subsurface information while all relying on the recording of the same input data that is the ambient seismic signal. It is the view of the authors that geothermal exploration and surveillance – as many other geoscience fields – can, and will benefit from full passive seismic implementation, where the multi-purposing of passive seismic networks to integrate multiple approaches is key to a complete seismic assessment of geothermal assets.

## References

- Antayhua-Vera Y.T. (2017) Caracterización sismológica, areomagnética y magnetotélúrica del Campo Volcánico y Geotérmico de las Tres Vírgenes (BCS), México. Universidad Nacional Autónoma de México, Mexico.
- Antayhua-Vera Y.T., Zuñiga F.R., Lermo-Samaniego J., Campos-Enríquez J.O., Quintanar-Robles L. (2022) Spatio-temporal distribution of the b-value in the volcanic complex and geothermal field of Tres Vírgenes; Baja California Sur, Mexico, *Journal of South American Earth Sciences* 116, 103864.
- Ars J.-M., Tarits P., Hautot S., Bellanger M. (2024) Geophysical models integration using principal component analysis: application to unconventional geothermal exploration, *Geophysical Journal International* 239(3), 1789-1798, <https://doi.org/10.1093/gji/ggae357>.
- Barmin M., Ritzwoller M., Levshin A. (2001) A fast and reliable method for surface wave tomography, In *Monitoring the comprehensive nuclear-test-ban treaty: Surface waves*, Springer, pages 1351-1375.
- Bauer K., Muñoz G., Moeck I. (2012) Pattern recognition and lithological interpretation of collocated seismic and magnetotelluric models using self-organizing maps, *Geophysical Journal International* 189(2), 984-998, <https://doi.org/10.1111/j.1365-246X.2012.05402.x>.
- Bensen G.D., Ritzwoller M.H., Barmin M.P., Levshin A.L., Lin F., Moschetti M.P., Yang Y. (2007) Processing seismic ambient noise data to obtain reliable broadband surface wave dispersion measurements, *Geophysical journal international* 169(3), 1239-1260.
- Benton A., García F., Silis J., Cruz S. (2011) Estudio geohidrologico de la cuenca de Las Tres Vírgenes, B.C.S. Report DEX-DGL-TV-16-11, Gerencia de Proyectos Geotermoelectricos. Comision Federal de Electricidad, p. 196.
- Boschi L., Magrini F., Cammarano F., van Der Meijde M. (2019) On seismic ambient noise cross-correlation and surface-wave attenuation, *Geophysical journal international* 219(3), 1568-1589.

- Brenguier F, Campillo M., Hadziioannou C., Shapiro N.M., Nadeau R.M., Larose É. (2008) Postseismic relaxation along the san andreas fault at parkfield from continuous seismological observations, *Science* 321(5895), 1478-1481.
- Brenguier F, Campillo M., Takeda T., Aoki Y., Shapiro N., Briand X., Emoto K., Miyake H. (2014) Mapping pressurized volcanic fluids from induced crustal seismic velocity drops, *Science* 345(6192), 80-82.
- Brenguier F, Clarke D., Aoki Y., Shapiro N.M., Campillo M., Ferrazzini V. (2011) Monitoring volcanoes using seismic noise correlations, *Comptes Rendus Geoscience* 343(8-9), 633-638.
- Brenguier F, Courbis R., Mordret A., Campman X., Boué P., Chmiel M., Hollis D. (2020) Noise-based ballistic wave passive seismic monitoring. Part 1: body waves, *Geophysical Journal International* 221(1), 683-691.
- Byerly P. (1955) Nature of faulting as deduced from seismograms. Crust of the Earth. Geol. Soc. Am. Sp. Paper.
- Cabrera-Pérez I., D'Auria L., Soubestre J., Del Pezzo E., Prudencio J., Ibáñez J.M., Pérez N.M. (2024) 3-D intrinsic attenuation tomography using ambient seismic noise applied to La Palma Island (Canary Islands), *Scientific Reports* 14(1), 27354.
- Carrillo J., Pérez-Flores M.A., Calò M. (2024) Three-dimensional joint inversion of surface wave dispersion and gravity data using a petrophysical approach: an application to Los Humeros Geothermal Field, *Geophysical Journal International* 239(2), 1217-1235.
- Cheng F, Xia J., Ajo-Franklin J.B., Behm M., Zhou C., et al. (2021) High-resolution ambient noise imaging of geothermal reservoir using 3C dense seismic nodal array and ultra-short observation, *Journal of Geophysical Research: Solid Earth* 126(8), e2021JB021827.
- Craig J.W., Faulds J.E., Hinz N., Earney T.E., Schermerhorn W.D., Siler D., Deoreo S. (2021) Discovery and analysis of a blind geothermal system in southeastern Gabbs Valley, western Nevada, USA, *Geothermics* 97, 102-177.
- Cruz-Noé E., Lorenzo-Pulido C., Soto-Peredo J., Pulido-Arreola S. (2018) Micro Seismic Monitoring During Production Utilization And Case Examples For Mexico, Geothermal training programme, 13.
- Faulds J.E., Hinz N.H. (2015) Favorable tectonic and structural settings of geothermal systems in the Great Basin region, western USA: Proxies for discovering blind geothermal systems, In Proceedings of the World Geothermal Congress, Melbourne, Australia (pp. 19-25).
- Gaubert-Bastide T., Garambois S., Bordes C., Voisin C., Oxarango L., Brito D., Roux P. (2022) High-resolution monitoring of controlled water table variations from dense seismic-noise acquisitions, *Water Resources Research* 58(8), e2021WR030680.

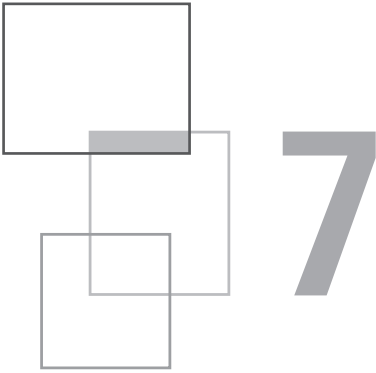
- Georgsson L.S. (2009) Geophysical methods used in geothermal exploration. Short Course on Surface Exploration for Geothermal Resources.
- Grab M., Quintal B., Caspari E., Maurer H., Greenhalgh S. (2017) Numerical modeling of fluid effects on seismic properties of fractured magmatic geothermal reservoirs, *Solid Earth* 8(1), 255-279.
- Gutenberg B., Richter C.F. (1944) Frequency of earthquakes in California, *Bulletin of the Seismological society of America* 34(4), 185-188.
- Guo H., Thurber C. (2022) Temporal Changes in Seismic Velocity and Attenuation at The Geysers Geothermal Field, California, From Double-Difference Tomography, *Journal of Geophysical Research: Solid Earth* 127(5), e2021JB022938.
- Haberland C., Rietbrock A., Lange D., Bataille K., Dahm T. (2009) Structure of the seismogenic zone of the southcentral Chilean margin revealed by local earthquake travelttime tomography, *J. Geophys. Res.: Solid Earth* 114, 1–17.
- Hilliers G., Ben-Zion Y., Campillo M., Zigone D. (2015) Seasonal variations of seismic velocities in the san jacinto fault area observed with ambient seismic noise, *Geophysical Journal International* 202(2), 920-932.
- Hobiger M., Wegler U., Shiomi K., Nakahara H. (2012) Coseismic and postseismic elastic wave velocity variations caused by the 2008 iwate-miyagi nairiku earthquake, Japan, *Journal of Geophysical Research: Solid Earth* 117, B09313.
- Hough S.E., Lees J.M., Monastero F. (1999) Attenuation and source properties at the Coso geothermal area, California, *Bulletin of the Seismological Society of America* 89(6), 1606-1619.
- Hudson T.S., Kendall J.M., Blundy J.D., Pritchard M.E., MacQueen P., Wei S.S., Lapins S. (2023) Hydrothermal fluids and where to find them: Using seismic attenuation and anisotropy to map fluids beneath Uturuncu volcano, Bolivia, *Geophysical Research Letters* 50(5), e2022GL100974.
- Inza-Callupe L.A. (2014) Understanding magmatic processes and seismo-volcano source localization with multicomponent seismic arrays (Doctoral dissertation, Université de Grenoble).
- Jaya M.S., Shapiro S.A., Kristinsdóttir L.H., Bruhn D., Milsch H., Spangenberg E. (2010) Temperature dependence of seismic properties in geothermal rocks at reservoir conditions, *Geothermics* 39(1), 115-123.
- Karato S.-I. (2004) *Mapping Water Content in the Upper Mantle*, Geophysical Monograph Series (edited by J. Eiler), <https://doi.org/10.1029/138GM08>.
- Ko Y.-T., Kuo B.-Y., Hung S.-H. (2012) Robust determination of earthquake source parameters and mantle attenuation, *J. Geophys. Res.* 117, B04304, <https://doi.org/10.1029/2011JB008759>.

- Larose E., Planes T., Rossetto V., Margerin L. (2010) Locating a small change in a multiple scattering environment, *Applied Physics Letters* 96, 204101.
- Levshin A.L., Pisarenko V.F., Pogrebinsky G.A. (1972) On a frequency-time analysis of oscillations, *Annales de geophysique* 28(2), 211-218.
- Lin C.H. (2016) Evidence for a magma reservoir beneath the Taipei metropolis of Taiwan from both S-wave shadows and P-wave delays, *Scientific Reports* 6(1), 39500.
- Lin F.-C., Ritzwoller M.H., Snieder R. (2009) Eikonal tomography: Surface wave tomography by phase front tracking across a regional broad-band seismic array, *Geophysical Journal International* 177(3), 1091-1110.
- Lin Y.P., Ko J.T., Huang B.S., Lin C.H., Shih M.H. (2024) Unveiling attenuation structures in the northern Taiwan volcanic zone, *Scientific Reports* 14(1), 4716.
- Magrini F., Boschi L. (2021) Surface-wave attenuation from seismic ambient noise: Numerical validation and application, *Journal of Geophysical Research: Solid Earth* 126(1), e2020JB019865.
- Martins J.E., Hooper A., Hanssen R.F. (2020) Geothermal Reservoir Characterization and Monitoring through Seismic (Ambient Noise) And Geodetic (InSAR) Imaging applied on Torfajökull Volcano and Reykjanes Peninsula, Iceland. In Proceedings World Geothermal Congress (p. 1).
- Mavko G.M. (1980) Velocity and attenuation in partially molten rocks, *J. Geophys. Res.: Solid Earth* 85, 5173-5189.
- Meier U., Shapiro N.M., Brenguier F. (2010) Detecting seasonal variations in seismic velocities within Los Angeles basin from correlations of ambient seismic noise, *Geophysical Journal International* 181(2), 985-996.
- Moeck I.S. (2014) Catalog of geothermal play types based on geologic controls, *Renewable and sustainable energy reviews* 37, 867-882.
- Mordret A., Courbis R., Brenguier F., Chmiel M., Garambois S., Mao S., Hollis D. (2020) Noise-based ballistic wave passive seismic monitoring—Part 2: surface waves, *Geophysical Journal International* 221(1), 692-705.
- Mordret A., Landès M., Shapiro N., Singh S., Roux P., Barkved O. (2013) Near-surface study at the Valhall oil field from ambient noise surface wave tomography, *Geophysical Journal International* 193(3), 1627-1643.
- Mousavi S.M., Ellsworth W.L., Zhu W., Chuang L.Y., Beroza G.C. (2020) Earthquake transformer – an attentive deep-learning model for simultaneous earthquake detection and phase picking, *Nature Comm.* 11(1), 3952.
- Muksin U., Haberland C., Bauer K., Weber M. (2013) Three-dimensional upper crustal structure of the geothermal system in Tarutung (North Sumatra, Indonesia) revealed by seismic attenuation tomography, *Geophysical journal international* 195(3), 2037-2049.

- Muñoz G. (2014) Exploring for geothermal resources with electromagnetic methods, *Surveys in geophysics* 35, 101-122.
- Muñoz G., Bauer K., Moeck I., Schulze A., Ritter O. (2010) Exploring the GroßSchoNebeck (Germany) geothermal site using a statistical joint interpretation of magnetotelluric and seismic tomography models, *Geothermics* 39(1), 35-45.
- Muñoz-Burbano F., Calò M., Savard G., Reyes-Orozco V., Lupi M. (2024) Using time-lapse seismic velocity changes to monitor the Domo de San, *Geothermics* 120, 103010, <https://doi.org/10.1016/j.geothermics.2024.103010>.
- Nibe T., Matsushima J. (2021) Monitoring of seismic attenuation change associated with vapor-liquid phase transition using time-lapse reflection seismic data in Kakkonda geothermal field, Japan, *Geothermics* 91, 102034.
- Nakajima J., et al. (2013) Seismic attenuation beneath northeastern Japan: Constraints on mantle dynamics and arc magmatism, *J. Geophys. Res. Solid Earth* 118, 5838-5855, <https://doi.org/10.1002/2013JB010388>.
- Obermann A., Kraft T., Larose E., Wiemer S. (2015) Potential of ambient seismic noise techniques to monitor the St. Gallen geothermal site (Switzerland), *Journal of Geophysical Research: Solid Earth* 120(6), 4301-4316.
- Obermann A., Larose E., Margerin L., Rossetto V. (2014) Measuring the scattering mean free path of Rayleigh waves on a volcano from spatial phase decoherence, *Geophys. J. Int.* 197, 435-442.
- Obermann A., Planès T., Larose E., Sens-Schönfelder C., Campillo M. (2013) Depth sensitivity of seismic coda waves to velocity perturbations in an elastic heterogeneous medium, *Geophys. J. Int.* 194, 372-382.
- Olivier G., Brenguier F. (2016) Interpreting seismic velocity changes observed with ambient seismic noise correlations, *Interpretation* 4(3), SJ77-SJ85.
- Olivier G., Brenguier F., Wit T., Lynch R. (2017) Monitoring the stability of tailings dam walls with ambient seismic noise, *The Leading Edge* 36(4), 350a1-350a6, <https://doi.org/10.1190/tle36040350a1.1>.
- Pérez L., Cuellar M. (2018) Passive Seismic Exploration of Geothermal Resources, Generalities, [https://www.researchgate.net/publication/329732977\\_PASSIVE\\_SEISMIC\\_EXPLORATION\\_OF\\_GEOTHERMAL\\_RESOURCES\\_GENERALITIES](https://www.researchgate.net/publication/329732977_PASSIVE_SEISMIC_EXPLORATION_OF_GEOTHERMAL_RESOURCES_GENERALITIES).
- Planès T., Larose E., Margerin L., Rossetto V., Sens-Schönfelder C. (2014) Decorrelation and phase-shift of coda waves induced by local changes: Multiple scattering approach and numerical validation, *Waves Random Complex Medium* 2, 1-27.
- Planès T., Obermann A., Antunes V., Lupi M. (2020) Ambient-noise tomography of the Greater Geneva Basin in a geothermal exploration context, *Geophysical Journal International* 220(1), 370-383.

- Poletto F., Farina B., Carcione J.M. (2018) Sensitivity of seismic properties to temperature variations in a geothermal reservoir, *Geothermics* 76, 149-163.
- Poupinet G., Ellsworth W., Frechet J. (1984) Monitoring velocity variations in the crust using earthquake doublets: an application to the Calaveras Fault, California, *J. Geophys. Res.* 89(B7), 5719-5731.
- Sánchez-Pastor P., Obermann A., Reinsch T., Ágústsdóttir T., Gunnarsson G., Tómasdóttir S., Wiemer S. (2021) Imaging high-temperature geothermal reservoirs with ambient seismic noise tomography, a case study of the Hengill geothermal field, SW Iceland, *Geothermics* 96, 102207.
- Sato H., Sacks I.S., Murase T., Muncill G., Fukuyama H. (1989) Qp melting temperature relation in peridotite at high pressure and temperature: attenuation mechanism and implications for the mechanical properties of the upper mantle, *J. Geophys. Res.: Solid Earth* 94, 10647-10661.
- Sens-Schonfelder C., Wegler U. (2006) Passive image interferometry and " seasonal variations of seismic velocities at Merapi Volcano, Indonesia, *Geophys. Res. Lett.* 33(21), L21302, <https://doi.org/10.1029/2006GL027797>.
- Shapiro N.M., Campillo M. (2004) Emergence of broadband Rayleigh waves from correlations of the ambient seismic noise, *Geophys. Res. Letters* 31, L07614, <https://doi.org/10.1029/2004GL019491>.
- Simiyu S.M. (2009) Application of micro-seismic methods to geothermal exploration: Examples from the Kenya Rift, Proceedings of the Short Course VIII on Exploration for Geothermal Resources, Lake Naivasha, Kenya, 31.
- Snieder R. (2006) The theory of coda wave interferometry, *Pure and Applied geophysics* 163(2), 455-473.
- Soergel D., Pedersen H.A., Stehly L., Margerin L., Paul A., AlpArray Working Group (2020) Coda-Q in the 2.5–20 s period band from seismic noise: application to the greater Alpine area, *Geophysical Journal International* 220(1), 202-217.
- Suzuki Y., Ioka S., Muraoka H. (2014) Determining the maximum depth of hydrothermal circulation using geothermal mapping and seismicity to delineate the depth to brittle-plastic transition in northern Honshu, Japan, *Energies* 7, 3503-3511.
- Taira T., Brenguier F., Manga M. (2018) Monitoring reservoir response to earthquakes and fluid extraction, Salton Sea geothermal field, California, *Science Advances* 4(1), e1701536, <https://doi.org/10.1126/sciadv.1701536>.
- Tanaka A. (2004) Geothermal gradient and heat flow data in and around Japan (II): Crustal thermal structure and its relationship to seismogenic layer, *Earth Planets Space* 56, 1195-1199.
- Toledo T., Obermann A., Verdel A., Martins J.E., Jousset P., Mortensen A.K., Krawczyk C.M. (2022) Ambient seismic noise monitoring and imaging at the

- Theistareykir geothermal field (Iceland), *Journal of Volcanology and Geothermal Research* 429, 107590.
- Tsai V.C. (2011) A model for seasonal changes in gps positions and seismic wave speeds due to thermoelastic and hydrologic variations, *Journal of Geophysical Research: Solid Earth* 116, B04404, <https://doi.org/10.1029/2010JB008156>.
- Vardy M., Pinson L. (2018) Seismic Attenuation-Friend or Foe. In 3rd Applied Shallow Marine Geophysics Conference (Vol. 2018, No. 1, pp. 1-5). European Association of Geoscientists & Engineers.
- Voisin C., Garambois S, Massey C., Brossier R. (2016) Seismic noise monitoring of the water table in a deep-seated, slow-moving landslide, *Interpretation* 4(3), SJ67-SJ76.
- Wada Y., Bierkens M.F., De Roo A., Dirmeyer P.A., et al. (2017) Human–water interface in hydrological modelling: current status and future directions, *Hydrology and Earth System Sciences* 21(8), 4169-4193.
- Wassermann J. (2012) Volcano seismology. In New manual of seismological observatory practice 2 (NMSOP-2) (pp. 1-77). Deutsches GeoForschungsZentrum GFZ.
- Wegler U., Sens-Schönfelder C. (2007) Fault zone monitoring with passive image interferometry, *Geophysical Journal International* 168(3), 1029-1033.
- Yeh Y.L., Wang W.H., Wen S. (2021) Dense seismic arrays deny a massive magma chamber beneath the Taipei metropolis, Taiwan, *Scientific Reports* 11(1), 1083.
- Yuan C., Bryan J., Denolle M. (2021) Numerical comparison of time-, frequency- and wavelet-domain methods for coda wave interferometry, *Geophysical Journal International* 226, 828-846, <https://doi.org/10.1093/gji/ggab140>.
- Yue H., Jianbao S., Min W., Zhengkang S., Mingjia L., Lian X., Weifan L., Yijian Z., Chunmei R., Thorne L. (2021) The 2019 Ridgecrest, California earthquake sequence: Evolution of seismic and aseismic slip on an orthogonal fault system, *Earth and Planetary Science Letters* 570, 117066, <https://doi.org/10.1016/j.epsl.2021.117066>.
- Zhang X., Curtis A., Galetti E., de Ridder S. (2018) 3-D Monte Carlo surface wave tomography, *Geophysical Journal International* 215(3), 1644-1658, <https://doi.org/10.1093/gji/ggy362>.
- Zhu L., Peng Z., McClellan J., Li C., Yao D., Li Z., Fang L. (2019) Deep learning for seismic phase detection and picking in the aftershock zone of 2008 Mw7.9 Wenchuan Earthquake, *Physics of the Earth and Planetary Interiors* 293, 106261, <https://doi.org/10.1016/j.pepi.2019.05.004>.
- Zobin V.M. (2011) *Introduction to volcanic seismology*, Elsevier (Vol. 6).



# Seismic inversion and characterization applied to geothermal energy

R. Baillet, T. Chrest, T. Defremenville and E. Masse

---

## Introduction

Seismic inversion is a method used to obtain models of the subsurface in terms of the elastic properties of rocks, called impedances, using seismic reflection data. Seismic characterization, on the other hand, allows the estimation of the key properties of the reservoir, in 3D, in 2D sections or in map, using, among other possible attributes, seismic inversion outputs. The combination of both disciplines unveils, either in 3D, in 2D sections or as maps, the distribution of key reservoir properties, relative to their matrix, fluid or fracture characteristics, between scarce and irregularly distributed well data. It is therefore crucial either to prospect new areas, in exploration, or to increase the production of an already proven geothermal system.

Unlike the direct model which creates a synthetic signal from impedances, seismic inversion, as an inverse problem, consists in iteratively optimizing an impedance model from observed seismic data (Figure 7.1).

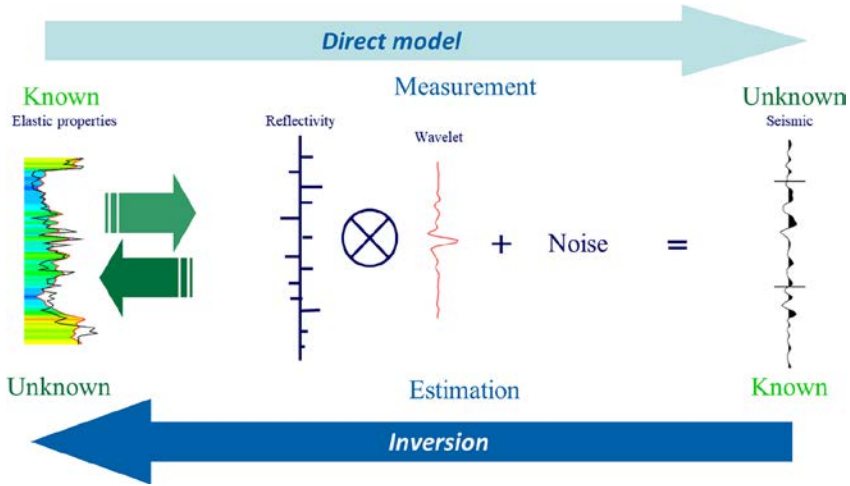


Figure 7.1 Seismic inversion versus direct modelling.

The objectives of a seismic inversion are:

- To optimize impedance values. They depend on the intrinsic properties of the rock, while the seismic signal depends on their contrast. Seismic characterization, sometimes called quantitative interpretation, is a discipline that links elastic properties (or other signal derivatives) with key reservoir properties (lithology, porosity, fluid...) or fractures. Learned directly from raw results (unsupervised) or guided by well data (supervised), the discipline allows the estimation of key properties through the application of machine learning techniques.
- To reduce random noise, depending on the inversion technique used, and therefore improve legacy seismic data and its subsequent seismic attributes, revealing better the faults and fractures, or facilitating seismic interpretation.

After describing key concepts related to these disciplines, we will describe the methodology using InterWell, the software solution from Beicip-Franlab, part of IFPEN group, for seismic inversion, seismic characterization and time-depth conversion. This will be followed by a practical case study.

## 7.1 Technical background

### 7.1.1 Seismic gathers and partial stacking

Following acquisition and a sequence of data processing and migration, *preserving amplitudes*, seismic data are *gathered* such that traces correspond to the same CMP (Common Middle Point) or CDP (Common Depth Point) depending on the

migration technique used. The delay with the offset, called *NMO effect*, is corrected. For the same time (TWT), they image the same subsurface point. Traces are classified with an *offset* key, defined by the distance between the source and the receiver (Figure 7.2).

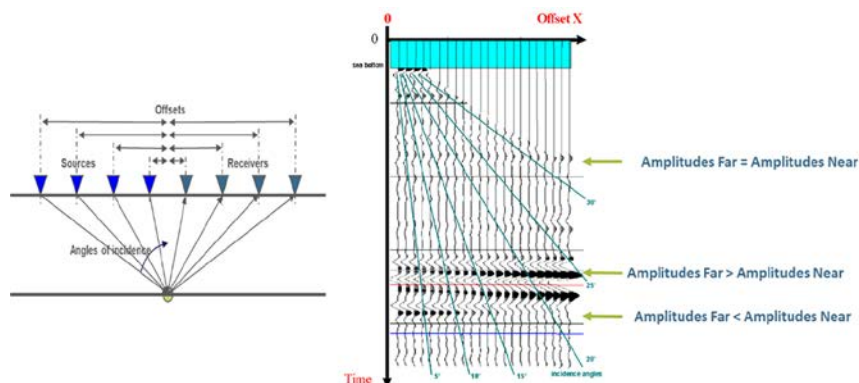


Figure 7.2 Conceptual view of a seismic gather after the process sequence, including NMO.

In practice, gathers are stacked to reduce random noise:

- *Full stack*: Information is summed over a wide angle or offset range, allowing a strong reduction of random noise. This result is the basis of seismic interpretation, but in this process, the variation of amplitude with offset and, if available, with azimuth is lost.
- *Angle-stack*: Offsets are converted with a velocity trace into angles, from which theoretical responses can be modeled by wave equations. They are often denominated Near, Mid, Far and UFar to the reference of their angle ranges.

### 7.1.2 The subsurface as an isotropic elastic medium

In seismic reflection, in a supposed homogeneous isotropic medium, the reflectivity of the PP (incident P, reflected P) wave at an interface between two layers is governed by the Zoeppritz equation. It depends on three elastic properties, P-wave velocity ( $V_P$ ), S-wave velocity ( $V_S$ ), and density, as well as the incidence angle at which the wave arrives at the interface. In addition, P-impedance, product of velocity (P) and density, is the capacity of a compressive wave to cross a medium. S-impedance, linked to S-velocity, is a similar property, but related to the shear waves.

When seismic data are fully stacked, the amplitude variation with incidence angle is lost. The considered hypothesis is therefore of normal incidence: the amplitude of the reflected wave only depends on the gradient of P-impedance. The optimization

of this variable during seismic inversion under this hypothesis is called *acoustic inversion* or *post-stack inversion*.

When working on gathers, or on partial angle-stacked seismic data, the Zoeppritz equation can be applied. In practice, the Aki-Richards equation (Aki and Richards, 1980), a simplification, is preferred during *elastic inversion* or *pre-stack inversion*, whose partial derivatives are linear and offering a valid approximation up to an incidence angle of  $45^\circ$ . These elements allow good behavior during numerical optimization (inverse problem) and good optimization of P-impedances and S-impedances. Density, however, is not well optimized by this process; other techniques allow improving this result. As we will describe later, dealing with not only one but two variables to explain the characteristics of the reservoir allow capturing combined changes (lithology and fluid, or lithology and porosity, for instance).

Figure 7.3 summarizes the two techniques in terms of inputs and outputs, respectively for acoustic inversion (left) and elastic inversion (right).

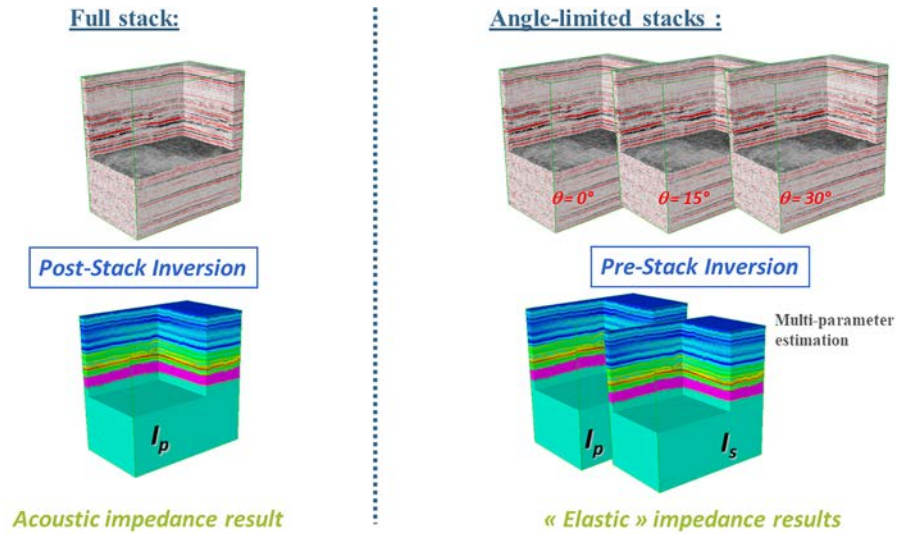


Figure 7.3 Results obtained according to the full-stack (acoustic) or angle-stack (elastic) assumption.

### 7.1.3 Convolution and resolution

Considering the medium as a series of reflection coefficients, the seismic response, in the two-way time domain, results from the convolution of this with an impulse response, called a wavelet. This operator has its own characteristics: (1) shape, (2) frequency spectrum, and (3) phase spectrum. It represents the impulse signal of the

source, which, after its path, can be deformed (phase, energy) and some frequencies can be absorbed.

Limited by its bandwidth, the result of the convolution acts as a frequency filter. If the reflection coefficients are defined more precisely, the convolution models the interferences; thus, in this case, there are series of reflection coefficients for which the synthetic has the same response (Figure 7.4). This is called a resolution problem.

$$(f * g)(n) = \sum_{t=-\infty}^{+\infty} f(n-t).g(t) = \sum_{t=-\infty}^{+\infty} f(t).g(n-t)$$

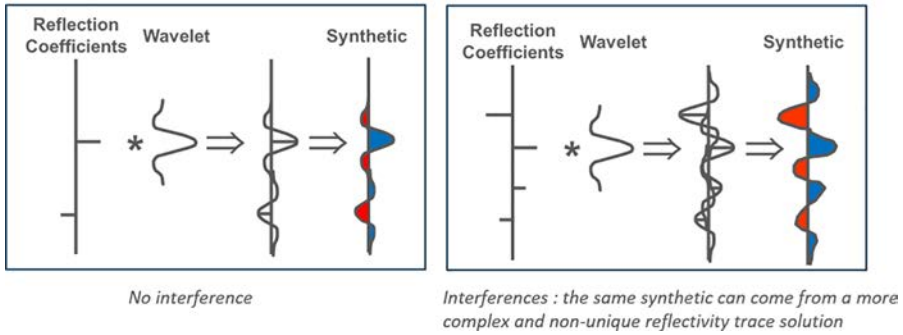


Figure 7.4 Convolution and model of the interferences.

In the industry, several considerations are commonly accepted:

- *Resolution*: A contrast is “resolved” when it represents a change of half a period of the signal. The signal has the “time” to reach the expected amplitude value.
- *Detection*: A contrast is “detected” when it represents a change of one-eighth of a period of the signal. The signal retains the dynamics without reaching the expected amplitude value. The response is sufficient to interpret a contrast, however, it is insufficient to deduce a quantitative property.

$$T_{\text{resolution}}(s) = \frac{1}{2f} \quad T_{\text{detection}}(s) = \frac{1}{8f}$$

$$Z_{\text{resolution}}(m) = \frac{v}{4f} \quad Z_{\text{detection}}(m) = \frac{v}{16f}$$

where  $f$  represents the dominant or maximum frequency of the signal contained in the wavelet (in Hz), and  $v$  the instantaneous velocity of the medium traversed (in m/s).

The convolution theory is, and the definition of the wavelet, is the main reason why seismic inversion must be performed in *two-way time* domain.

## 7.2 Seismic inversion

### 7.2.1 About seismic conditioning

Either to obtain full-stack or angle-stack data, for acoustic or elastic inversion respectively, gather reprocessing can be considered using up-to-date methodologies to enhance the final image, but must be “*amplitude preserved*”, meaning that no equalization or gain should have been applied to the data. As the inversion translates the amplitude into impedance changes, such processes can annihilate the vertical and lateral property changes normally observed through seismic inversion.

This aspect is even more critical while considering several angle-stacks, as the *amplitude preserved* sequence ensures consistency between them. As the variation of the amplitude with the offset is meant to be translated into properties, any independent processing of each stack may ruin the desired estimation.

In addition, while considering several stacks, seismic inversion is a computational process, and as such, all involved seismic data must be aligned. The NMO, often not perfect, must be completed by a *mis-alignment correction* (called *trim statics* on gathers, or Residual NMO in case of angle-stacks). The shift estimation in volumes through energy or correlation optimization is often preferred. The shifts are dynamic, and, therefore, are not constant vertically. The shift estimation can be post-processed, using smoothing or editions using an uncertainty analysis to prevent the generation of artifacts.

### 7.2.2 Wavelet extraction and optimization

To link the modeled or optimized reflectivity with a seismic signal, the key operator, the wavelet, must be designed for each seismic dataset. A well-spread methodology in the industry is using a two-step procedure (Richard and Brac, 1988), with a statistical zero-phase wavelet extraction, followed by its optimization in phase and energy.

For each seismic data involved in the process, the initial wavelet is extracted statistically by cross-correlation trace by trace, in a lateral zone and a given time window, if the signal correlates trace by trace while the noise, assumed to be random, does not correlate.

To set up both the phase and energy for the wavelet, the wells are used and calibrated at the same time; the objective is to ensure the best match between synthetic traces, computed at well, and real traces, optimizing the wavelet parameters. To increase the robustness of such prediction, several traces can be considered, as displayed Figure 7.5. In this case, the best parameters can be displayed as histograms.

After the process, the well-tie is often updated. In case of elastic inversion, the optimal location of the wells should then consider all the angle-stacks simultaneously.

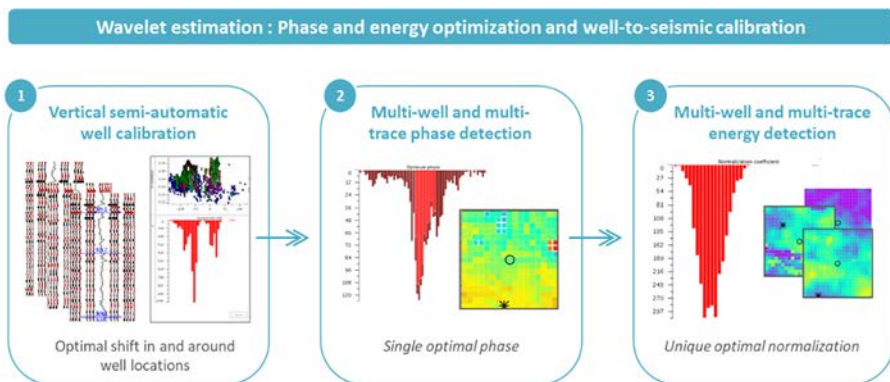


Figure 7.5 Multi-well and multi-traces approach for a unique wavelet estimation

### 7.2.3 Construction of a low-frequency model

Seismic information is limited by its bandwidth, both in low and high frequencies. The high-frequency limit determines the resolution, or the maximum precision of the final inversion results. But there are also low frequencies missing, including compaction trends and other regional changes, that need to be modeled through a *low-frequency model*. In practice, this model is *simple*, so that any complex features retrieved from seismic inversion can only come from seismic data.

Interpreted horizons allow the construction of a structural model, defining different units, and correlation lines. Following the correlation lines the model is obtained by propagating the acoustic impedance values (and S-impedance and density for elastic inversion) from the wells in calibrated positions along the correlation surfaces defined during the creation of the structural grid. The extrapolation method used is inverse distance.

Then, a low-pass filter is applied to eliminate high frequencies coming from the wells, limiting the model at the missing part from seismic data.

The model can be used with several “intensity”, playing a strong role for each following proposal:

1. *low-frequency model*: An elastic model, in the low frequencies missing from the seismic, is used, either before (initial model) or after (by adding the missing frequencies).
2. *initial model*: The starting point of the optimization is an elastic model.
3. *prior model*: During optimization, impedance is compared to a prior model, from which it costs the algorithm to deviate (Tonellot et al., 1999).

For (1), the frequency filter, for its higher limit, must be strict with no overlapping with the dataset. The frequency overlap is possible for (2), and even recommended

for (3) while building a prior model (Figure 7.6). Indeed, the seismic information will be compared with the model during the inversion process, discarding too discrepant information, considered as noise.

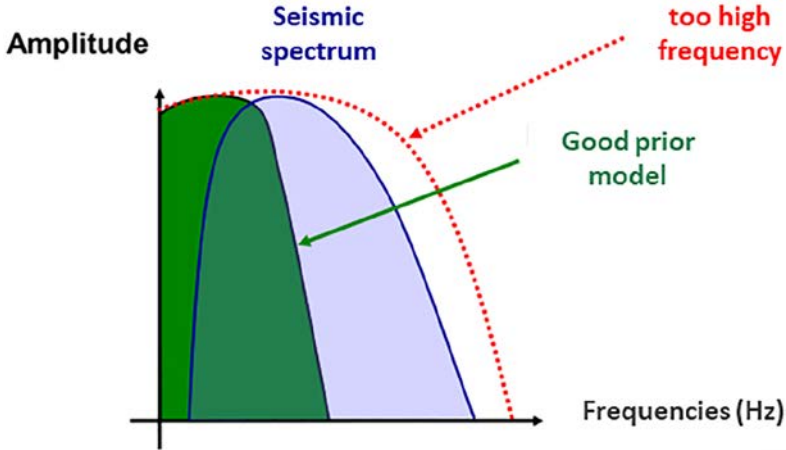


Figure 7.6 Conceptual amplitude spectrum of the prior model compared to the seismic spectrum.

## 7.2.4 Performing a seismic inversion

### Seismic inversion algorithm

Different algorithms for seismic inversion are available and suit different objectives:

- For the *sparse-spike inversion*, each trace is considered independently, introducing the entire trace. Computationally efficient, this technique is ineffective for reducing random noise. This inversion has no parameter but the number of iterations.
- *Model-based inversion* is based on the objective function, or cost function, this inversion type has two parameters weighing the two terms: the *seismic term*, which controls the distance to the seismic, and the *model term*, which controls the distance to the prior model.

For *stratigraphic inversion algorithms*, often preferred in projects for its noise reduction capability (Tonellot et al., 2001), the correlation length, added to the *model term*, controls the lateral continuity of impedance values along the correlation lines. The inversion is thus “multi-channel” when several traces are considered. It is “grid-based” when this comparison is consistent with a priori dip. In recent advances in seismic inversion projects, this dip is directly deduced from seismic independently from seismic interpretation.

All the inversion methods allow us to optimize the elastic properties. The *stratigraphic inversion algorithm* allows the reduction of random noise present in the initial seismic data, and therefore, does not include it into the inversion results.

### Seismic inversion parameters and QCs

In practice, a reduced area is used to optimize the parameters, with the following criteria:

- The *number of iterations* must be adjusted to obtain a maximum decrease in the objective function ending in a plateau (no more improvement by increasing iterations).
- The *residual seismic* must be weak compared to the synthetic, proving that most of the information has been included in the elastic model. If possible, no (laterally) coherent signal must be present in the residuals.

Especially for elastic inversion, additional controls are performed:

- The residual seismic energy must be similar for all angle-stacks or honoring their relative quality.
- The P-impedance and S-impedance, in seismic, must be equally updated and their frequency content comparable, or their difference explainable by a strong frequency difference between the angle-stacks, especially between the Near and the Far stacks.

Extended to the entire seismic, a full-field inversion is performed and generally QC using the following criteria:

- Control in sections (visuals) and control as maps (noise map, frequency map, energy map) to assess the enhancement or *conformity of the synthetic data* compared to the original seismic data. All information in the synthetic is contained in the elastic model.
- *Control of the convergence*, both in terms of plateau and final values (%), expected to be compatible, approximately, with the signal to noise ratio observed in the original seismic.
- *Extraction at well locations* (Figure 7.7), both participating or not (blind wells) in the calibration and modelling process, to assess the predictability of the inversion results. In practice, however, the inversion is often performed with all the wells in a final run, as the well data availability is often rare and valuable.

The correspondence between the inverted properties and the properties computed at wells are often not a surprise for the inversion specialist, as it reflects the quality/difficulties observed during the wavelet estimation. For the professional beginning the seismic characterization, this QC is a good starting point to assess how reliable the inversion results are before propagating valuable reservoir properties.

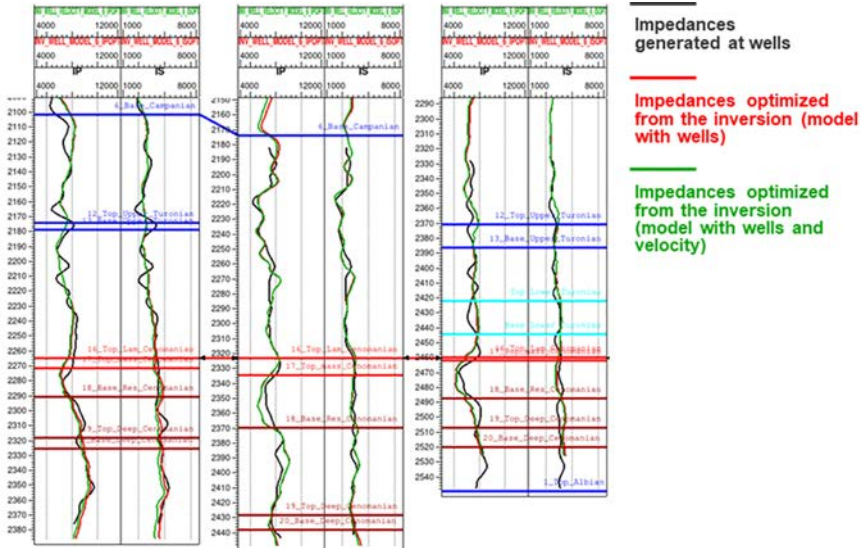


Figure 7.7 Example of inversion QC at well location: the black curve is the “real” property, while the colored curves are retrieved from seismic inversion.

### 7.3 Introduction to seismic characterization

Unlike the seismic inversion workflow, linear, the seismic characterization is composed of diverse techniques to qualitatively or quantitatively link the reservoir properties to the seismic information. In this exploration of methodologies, the seismic inversion results, especially the synthetic seismic data and the impedances, are key inputs, but not the only one, to build a custom-made workflow adapted to each case, considering both its objectives and the data available.

#### 7.3.1 Exploring well response through a petro-elastic model building

The analysis of the well response (in terms of impedances) with the key property changes is called a *petro-elastic model*. Performed before the seismic inversion, it can be proposed as a *feasibility study* to assess its added value in projects. Although these considerations may change by projects, the properties are evaluated in this order, impacting less and less the impedances: lithology, porosity, then fluid.

In practice, P-impedance and S-impedance properties are computed from well logs and compared to the petrophysical properties. In a multi-disciplinary project, geologists may identify dozens of lithologies from core or well logs. The number of lithologies must be limited, as the number of independent attributes is limited to P- and S-impedance only. Some guidelines are as follows:

- The problem can be split into several ones by studying the intervals separately.
- Only the most typical lithologies should be kept, such as clean sand. Porous or tight sands are not lithologies, but sub-groups of the sand lithology that can be detected afterward by identifying the corresponding impedance values in the predicted sand.
- The facies can be grouped (one versus all) or to apply a nested approach.
- An upscaling analysis must be performed to identify lithologies/properties detectable from the seismic data.

Figure 7.8 illustrates the lithology and property changes with the upscaling, removing the information with a frequency content greater than various limits, representing the expected quality of seismic data:

- For a discrete lithology column, a “*most of*” algorithm is used, assigning to the cell the most represented lithology. The size of the cell is computed depending on the resolution formula.
- For a continuous property (like a volume of shale for instance), a *frequency filter (low-pass)* is used, adjusting the frequency limit to the resolution.

In this example, it is interesting to assess the critical frequencies from which each sand layer is no longer detected or merged with another one. It allows the interpreter to predict what to expect from a seismic characterization study.

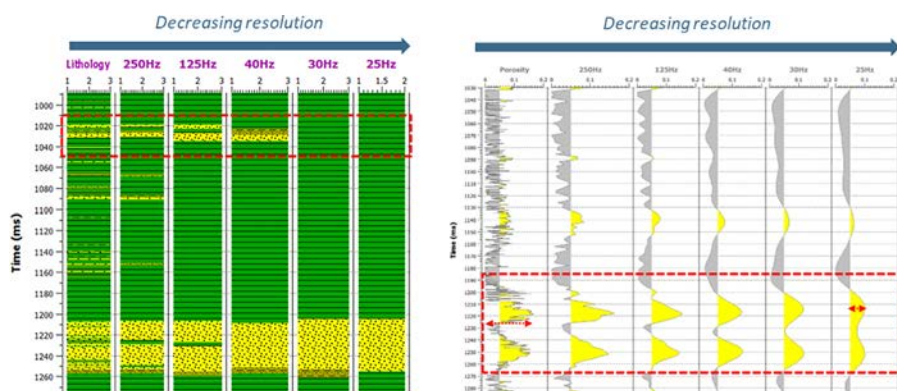


Figure 7.8 Upscaling of lithology (left) or porosity (right) considering different seismic frequencies.

The prediction power of impedances, at fine scale and at seismic scale, represents their ability to isolate well-defined clusters corresponding to lithologies or the ability to derive trends. This is validated using cross-plots, before and after upscaling, to ensure that the cluster organization is conserved. In Figure 7.9, the pale color points in background represent the data at a well scale, while the darker points represented the data at seismic scale, sampled at the seismic rate. In practice, the trends should be valid in both scales to be applied on inversion results.

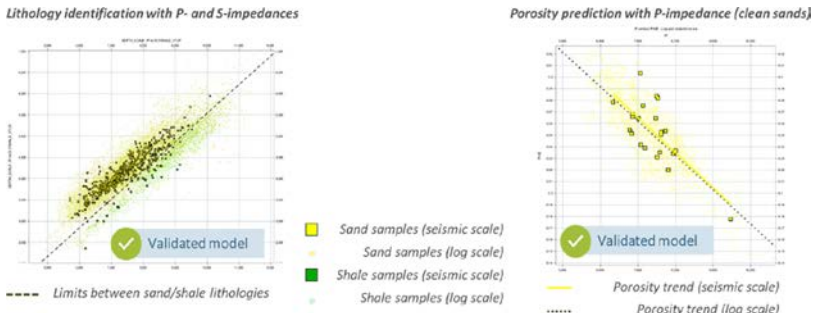


Figure 7.9 Petro-elastic model with and without upscaling, showing the possibility to separate sands from shales (left) and to derive a porosity trend in sands only (right).

In the section concerning Machine Learning techniques, the propagation to 2D or 3D inversion results will be discussed using a classifier (discrete lithology) or a regression (continuous properties) based on this well data, called “training samples”.

### 7.3.2 Seismic attributes related to faults and fractures

Avoiding fastidious work for the geophysicists, the computation of seismic attributes for fracture detection is efficient but presents various challenges:

- To separate geological discontinuities from random noise. Model-based seismic inversion helps reduce the noise content. On synthetic seismic data, parameters for attribute computations can therefore be better tuned to better unveil meaningful fracture response.
- To separate the fault and fracture response from other major structural features, such as highly tilted blocks.
- To sort or separate the regional from the local features.

Several types exist (Chopra and Marfurt, 2007):

- *Geometrical* attributes, such as dip and curvature.
- *Correlation-based* (coherency) attributes, including a steering to tilt the computational window.
- Attributes linked to *energy*, such as envelopes, RMS or spectral decomposition.

These seismic attributes dedicated to discontinuity analysis do not only highlight fractures, but they may also be impacted by other effects depending on the algorithm. For example, correlation-based attributes are highly biased by dips or lithology changes, while dip-based attributes are sensitive to both local and broad-scale dip changes. All the attributes quoted here unveil fractures: the fracture image is then redundant, while the perturbations are inherent to each attribute algorithm.

While analyzing the relevance of an attribute, and before any combination, it can be post-processed using smoothing or threshold, achieving the best compromise between its accuracy and its noise level to capture the fracture intensity.

As a control, fracture patterns can be checked in the seismic, although some of them can be too subtle or too discontinuous to be clearly identified and followed from one seismic section to another. Their orientation and continuity can be validated against the conceptual structural model.

Attribute combination can be performed using two main methods (Kumar et al., 2017):

- Meta-attributes: it consists in a linear combination of the attributes, weighted by their quality. This is an interpretative method.
- Clustering or seismic facies analysis: it consists of an unsupervised machine learning technique, as discussed in the next section. The typical responses such as “faults” or “fractures” are highlighted in the map.

Such results will be illustrated in the case study section.

### 7.3.3 Characterization empowered by machine learning

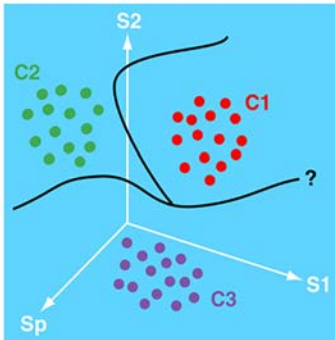
Machine Learning is a powerful tool:

- To infer classifications or trends, either using wells only or even mixing well and attribute data using *supervised approaches*.
- To analyze typical responses in seismic data or inversion results, through *unsupervised approaches*.

#### Supervised approaches

The supervised approaches (Discriminant Analysis, Neural Networks, KNN, ...), consist in building a predictive model to assess a petrophysical property using seismic attributes, commonly, after inversion, P-impedance, S-impedance, and/or their combination (Al-Emadi et al., 2010). This is the *descriptive phase*. A second phase, *predictive phase*, consists in using this model to predict the lithology or facies. These two steps are illustrated by Figure 7.10. In practice, to assess the validity of the model, the prediction is performed on the training sample themselves, before any propagation in 3D. Statistics of good assignments, called *restitution*, are often used. While considering continuous variable prediction, (multi-variable) regression is used, using the same two-step approach. In this case, the *RMS error* (RMSE) is preferred to assess the uncertainty associated with the prediction (De Freslon et al., 2020).

**Step 1: Descriptive phase**



**Step 2: predictive phase**

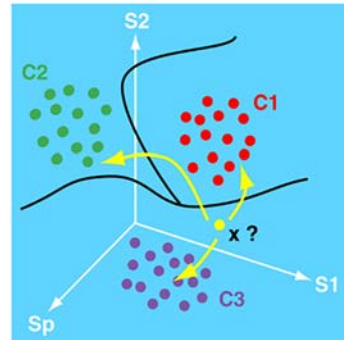


Figure 7.10 Supervised technique as a two-step problem.

In Machine Learning, and in data science in general, it is recommended to prepare the data by splitting the dataset into three, respectively for training, validation and predictability assessment. In practice, in geosciences, well data is expensive, and the reservoir samples are rare and often underrepresented, leading to difficulties while applying these rigorous recommendations.

The data is explored, grouping lithology or facies, considering a property or other, separating by interval using markers and horizons, to propose the best model. The limitation is often the number of input variables, which prevents explaining a too complex system.

Another paradigm, often observed in projects, is the homogeneity between the data on which the training is based (wells) and the seismic resolution. Ideally, the upscaling should be performed to ensure compatibility, but the lack of points, especially in the reservoirs, may also lead to high uncertainty during the prediction.

Finally, considering classification only, the outputs of such approaches are not only labels, but also *scores* or *probabilities*. These latest outputs are key to propose scenarios, considering the uncertainties associated with the predictive model in the seismic characterization (Yareshchenko et al., 2021).

**Unsupervised approaches**

*Clustering* methods (K-means, Self-Organizing Maps, ...) are algorithms, self-trained, and allow to classify the data regarding “typical responses”, labelling the input data as “classes”. These algorithms are applied:

- On maps, for example, in risk analysis or seismic fracture characterization (Kumar et al., 2017).
- On horizon-slice, considering typical shapes of trace from channel or karst identification (Voutay et al., 2002).
- On volume, considering each sample, for reservoir, salt or igneous rock identification (Cardoso et al., 2022).

Easy to put in place, these methods always output results which will, of course, highly depend on the selection of attributes used as inputs. The main challenge of such methods is to properly interpret the obtained features. Coupled with supervised techniques, this is a good methodology to prove that the supervised training is a typical response, well identified in the seismic data. Recent advances in this methodology, suitable for exploration, suggest afterward calibration with well data, or with conceptual section from the proposed by geologists.

## 7.4 Example: identification of lithology, good porosity and fractured areas through a seismic inversion study

In the following example, a seismic inversion and characterization study has been conducted to highlight the most prospective area in carbonates, either in terms of rock properties (lithology, porosity/permeability) and fault/fracture presence over a 3D survey. For this characterization case, the fluid is stored in good matrix properties, while the permeability is ensured by the fractures. In geothermal activities, these parameters are key to ensure the targeted flow rate. The described work can be performed in 2D. This recent case (Baillet et al., 2024) has been scenarized as a geothermal project, and these methodologies have already been applied successfully in this context in Paris basin or in the North of France.

A stratigraphic joint inversion, using angle-stacks, has been performed. Both P- and S- impedance are optimized. The zone is covered by 6 wells, with DT, RHOB and partial DTS completed by empirical laws when needed.

A seismic characterization has been performed to predict lithology (Figure 7.11). A petro-elastic model, built at wells, upscaled at seismic scale, has been used as a training sample for discriminant analysis. Shaly carbonates could have been discriminated against dolomites with a satisfactory rate.

A particularly interesting layer, in terms of porosity/permeability, called unit-C, has been identified, at the limit of the seismic resolution. A connectivity analysis, in 3D, has been undertaken, and proves its connection/extension, invisible in section only. In Figure 7.11, this layer is plotted in orange and has been used to propose an update of the horizon, in red dots.

In each lithology, a law estimating the porosity has been derived from well logs and applied, based on P-impedance. The porosity is very heterogeneous vertically, as observable in another section, Figure 7.12.

If the fluid is present in the most porous matrix lithologies, the provided flow rate might not be enough to sustain a geothermal project. Faults and fractures, identified, can greatly increase the prospectivity of an area. A fracture characterization, processing and mixing key attributes (as dip-steered similarity, spectral decomposition, energy,

shift quality, ...) led to a final attribute, plotted in black Figures 7.11 and 7.12. Connected fractures, crossing unit C, would be an optimal for the flow rate.

The view in map, Figure 7.12, highlights the areas, between two key horizons, where the dolomites are the most present, and where these dolomites have the greatest porosity. Overlay with faults and fractures obtained by the fracture characterization, these final maps led the future development.

Each of these properties, estimated through this work, has a key role in the interpretation:

- The most porous areas contain most of the fluid.
- The dolomite has a better permeability than the shaly carbonate, even with the same low porosity.
- The fracture presence allows a better connection of the layers, and greater porosity (secondary) and overall, a greater permeability.

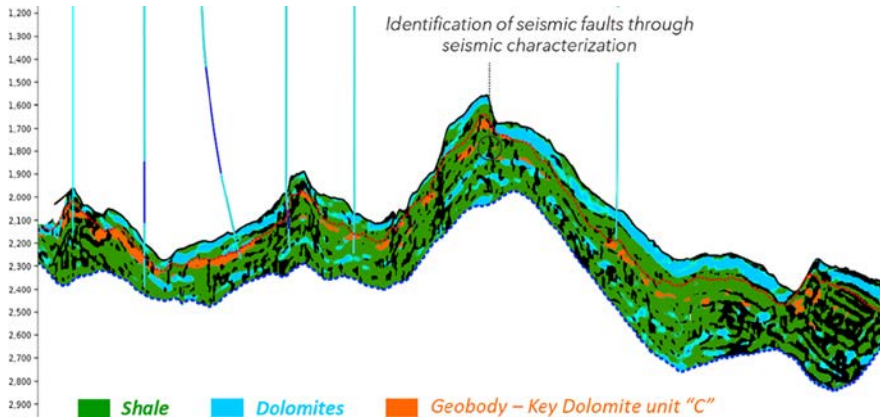


Figure 7.11 Predicted lithology in section.

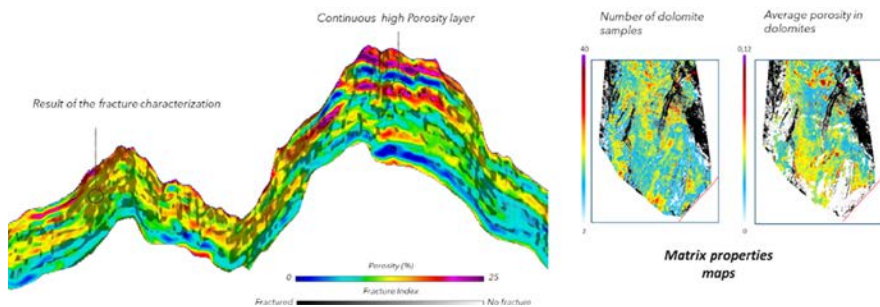


Figure 7.12 Predicted porosity in section and final maps.

## Conclusions and perspectives

The seismic inversion and characterization are disciplines that aim at converting seismic amplitude into key reservoir properties, leading to valuable information between wells to lower the risk while planning exploration or development of geothermal production, either with low or high depth objectives. The state-of-the-art, originally designed for the oil and gas industry, is also perfectly adapted for the geothermal industry, either based on 2D or 3D seismic data.

Either in prospection or development phase for a geothermal project, all available data, including legacy ones, has a lot of value. The proposed case study illustrates how the reservoir presence and quality could have been identified between wells. The fracture characterization plays a crucial role in identifying zones with secondary porosity and enhanced permeability, increasing the prospectivity. This fracture connectivity must be evaluated, not to connect with aquifer of different temperatures. Both matrix and fracture characterization together help build scenarios and derisk the development of the geothermal project.

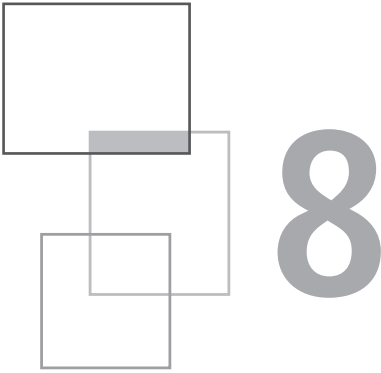
If any seismic data is available in a studied area, this kind of analysis is always a good option, either to identify and confirm the presence, the depth or the thickness of the reservoir, or evaluate the potential flow rate by estimating the porosity (then permeability, by lithology) or the presence of sub-seismic faults and fractures. The petro-elastic model can be analyzed even before acquiring or reprocessing seismic data, to assess what results could be obtained, although some recent advances in unsupervised machine learning techniques may overcome these expectations.

The seismic characterization results are key information to assess the economic viability of geothermal development, completing information from other disciplines such as the thermal gradient assessment, the estimation of the drilling cost to be put against a reasonable time of depreciation of the geothermal project.

## References

- Aki K., Richards P.G. (1980) *Quantitative seismology: Theory and methods*, 1: W. H. Freeman and Co.
- Al-Emadi A., Robinson S., Jedaan N., Desgoutte N., Blum M., Lecante G., Caline B., Fraisse C. (2010) Use of Pre-Stack Seismic Data to Guide the 3D Rock-Type Distribution of Arab-D in Maydan Mahzam High-Resolution Geological Model, <https://doi.org/10.3997/2214-4609-pdb.248.458>.
- Baillet R., de Freslon N., Thomas V., Castellanos R., Denogean E. (2024) Fracture and matrix characterization using wide-azimuth and multi-component seismic data: a case study from offshore Mexico, *Fourth International Meeting for Applied Geoscience & Energy*, 144-148, <https://doi.org/10.1190/image2024-4101418.1>.

- Cardoso G.L., Kolisnyk A., Bronizeski E., de Abreu E., Laudon C. (2022) Applying unsupervised multiattribute machine learning for 3D stratigraphic facies classification in a carbonate field, offshore Brazil, *SEG Technical Program Expanded Abstracts* 2022, 441-445, <https://doi.org/10.1190/image2022-3750985.1>.
- Chopra S., Marfurt K.J. (2007) Seismic attributes for fault/fracture characterization, *SEG Technical Program Expanded Abstracts* 2007, 1520-1524, <https://doi.org/10.1190/1.2792785>.
- De Freslon N., Lucet N., Pain A., Desgoutte N. (2020) Comparison of Two Reservoir Characterization Workflows for Estimating 3D Shale Distribution from Seismic Data, EAGE 2020 Annual Conference & Exhibition Online, Dec 2020, Volume 2020, p. 1-5.
- Kumar R., Al-Kanderi J., Kumar Mishra P., Al-Mutairi T., Baillet R., Stozicky E., Lecante G. (2017) Innovative seismic fracture attributes for fracture characterization workflow: Application in formations affected by interbed multiples, *SEG Technical Program Expanded Abstracts* 2017, 3255-3259, <https://doi.org/10.1190/segam2017-17467633.1>.
- Richard V., Brac J. (1988) Wavelet analysis using well log information, *SEG Technical Program Expanded Abstracts* 1988, 946-949, <https://doi.org/10.1190/1.1892398>.
- Tonellot T., Macé D., Richard V. (2001) Joint stratigraphic inversion of angle-limited stacks, *SEG Technical Program Expanded Abstracts* 2001, 227-230, <https://doi.org/10.1190/1.1816577>.
- Tonellot T., Macé D., Richard V., Cueur M. (1999) Prestack elastic waveform inversion using a priori information, *SEG Technical Program Expanded Abstracts* 1999, 800-803, <https://doi.org/10.1190/1.1821149>.
- Voutay O., Fournier F., Royer J. (2002) Seismic interpretation with new attributes extracted from a prestack multicube analysis, *SEG Technical Program Expanded Abstracts* 2002, 1762-1765, <https://doi.org/10.1190/1.1817022>.
- Yareshchenko S., De Freslon N., Cuilhé L., Rudling C., Lucet N., Desgoutte N., Machault V., Solodkyi Y., Gafych I. (2021) 82nd EAGE Annual Conference & Exhibition, Oct. 2021, Volume 2021, p. 1-5.



# Seismic anisotropy applied to geothermal prospection

R. Baillet, N. Desgoutte, V.Thomas and J. Caudroit

---

## Introduction

Anisotropy estimation allows to go beyond the lateral resolution of the conventional seismic data (Lui and Martinez, 2012); a full-stack full-azimuth seismic inversion and its associated characterization, as described in the previous chapter, assumes a homogeneous and isotropic medium. The proposed azimuthal approach allows us to overcome this limitation by estimating the key properties for each source/receiver direction. Small heterogeneities, such as smaller fractures, can be detected if the impedance varies from one sector to another, generating an azimuthal anomaly. The anisotropy magnitude and orientation can be extracted for further analysis and linked, if possible, to fracture intensity and orientation (Adelinet et al., 2012). This fracture intensity can have a major impact on the expected flow rate or communication between the reservoirs, and, therefore, is often a key element for decision making.

After elaborating briefly the technical background, we will describe the methodology for both VVAZ (Velocity versus Azimuth) and AVAZ (Amplitude versus Azimuth), based on partially stacked seismic according to the azimuth. The software used for the demonstration is InterWell, the software solution from

Beicip-Franlab, part of IFPEN group, able to extract anisotropy either for velocity or amplitude anomalies.

The use of the VVAZ – AVAZ methodology is illustrated by a practical case study in geothermal prospection in Geneva basin, Switzerland (Baillet and Caudroit, 2024).

## 8.1 Technical background

### 8.1.1 The HTI and VTI models for anisotropy models

A VTI media, standing for Vertical Transverse Isotropic, is characterized by horizontal layering, as evidenced in shale overburdens. The stiffening of the rock in the horizontal direction increases the P-wave velocity in this direction compared to vertical propagation. This model is suitable for lithology prediction.

On the other hand, a HTI media, standing for Horizontal Transverse Isotropic, is characterized by vertical layering, such as seen in a fractured reservoir. Here the rock is stiffer along the strike of the fractures giving the fastest P-wave velocity in this direction.

It is important to highlight that both AVAZ and VVAZ approaches are sensitive to both anisotropy models, represented Figure 8.1.

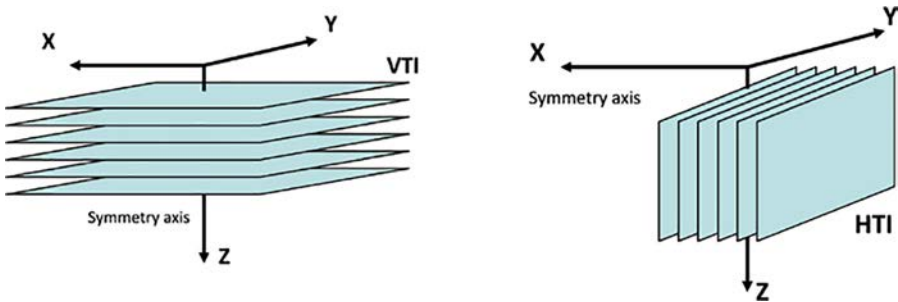


Figure 8.1 VTI (left) and HTI (right) to simplify the anisotropy modeling.

For VTI media, Thomsen introduced three variables (Thomsen, 2002), called *Thomsen parameters*,  $\epsilon$ ,  $\gamma$ , and  $\delta$ . In practice,  $\delta$  and  $\epsilon$  can be derived by adjusting the hyperbola during the NMO, using an additional term in the equation. As such, the VVAZ approach as presented in this chapter is also sensitive to this VTI configuration.

For *HTI media*, rock physics models, such as Mori-Tanaka (Mori and Tanaka, 1973), allow computing the elastic stiffness of an inclusion model, mixing some fracture apertures/orientations. Synthetic seismic data generated in 1D by such models allows us to draw general observations:

- Anisotropy is not detected at short offsets.
- If one fracture set is present, with a given orientation, a large fracture density and large fracture lengths, it leads to a measurable anisotropy in the seismic at large offset (or angle, around 30°).
- Two equivalent perpendicular fracture sets lead to isotropic result and kill the anisotropy effect; while changing the balance between both sets, the anisotropy intensifies at large offset or incidence angle.

In practice, not only faults and fractures can be detected using HTI media approximation. Any brutal and oriented change affecting the wave, such as a lithology or porosity change, can generate similar anisotropy. In addition, the *lateral resolution* is also a key factor: If an element is wide enough to be detected, regardless of the azimuth, no anisotropy will be induced.

### 8.1.2 Azimuthal stacking and required processing

In the previous chapter, the partial stacking was introduced to generate full-stack or angle-stacks from *gather*s. Another stacking method, to detect anisotropy, is possible with *Wide Azimuth (WAZ)* seismic acquisition and associated *gather*s using the *azimuthal key*, representing the direction between the line source/receptor and the north. As for the previous application, the *gather*s must be “*amplitude preserved*”.

The response of the signal is expected to be symmetrical: exchanging the location between the source and the receptor should lead to a similar signal. An azimuthal range of 0-30° is then equivalent to a range of 180–210°. This technique allows more traces to be involved during stacking, and, therefore, to reduce the *noise content* of the azimuthal stacks.

For the *VVAZ* approach, different alignment processes might destroy the expected anomalies, especially:

- All the azimuth dependent velocity picking or RNMO.
- The trim-statics, which is a process that aligns seismic events using dynamic shifts.
- Filters, such as Radon or F-K filters, might not be adapted to preserve the azimuthal information.

As the anisotropy is mostly detectable for the large offsets/angles (Chérel et al., 2010), these must be considered during the stack (even up to very large offsets, further than Aki-Richards classical limitations for elastic inversion workflows). This way, the chance to detect anisotropy would significantly increase.

## 8.2 Velocity versus Azimuth (VVAz): a shift detection methodology

The misalignments between the azimuthal stacks and the full-stack full-azimuth are very informative, as it can be translated as *velocity anomalies* (VVAZ). It is also key to correct them, enhancing the stack's compatibility before comparing their amplitude variations with the azimuth (AVAZ), to get an accurate estimation of such subtle effects.

The shift detection is performed on each *azimuthal stack* (anisotropic) taking a full-stack full-azimuth as reference (isotropic), as described in the previous chapter during the seismic data conditioning for seismic inversion.

The resulting dynamic shifts observed in each sector can be understood as velocity anomalies according to this “isotropic” velocity, associated to the full-stack. Different elements must be considered when choosing this parameter:

- The window for the shift detection must be put at its lowest as it controls the *vertical resolution* of the VVAZ anomaly.
- The induced interval variations must be computed, to QC their values. The parameter set must be refined using trials and errors to remain in realistic ranges.
- In areas where the signal is of low quality, the shift values must tend to zero, which implies no VVAZ effect.

The following sequence is proposed to obtain the interval velocities by azimuthal sector:

1. Compute the average velocity from the interval velocities (isotropic). It corresponds to the average of the interval velocities, in TWT domain.
2. Compute correction coefficients by sector:

$$\text{Coef} = \frac{\text{TWT} - \text{shift}}{V_{\text{avg}}}$$

3. As the depth of events is the same, the multiplication of such coefficients with the average velocities (isotropic) leads to corrected average velocities by azimuthal sector.
4. A Dix formula variation allows to estimate the interval velocities by azimuthal sector from the average velocities.

At the end of the process, as many interval velocity models as azimuthal stacks are obtained, from which anisotropy can be extracted.

### 8.3 Amplitude versus Azimuth (AVAz): an inversion methodology

Amplitudes are related to impedance contrasts rather than impedance itself. Consequently, it is preferred, for Amplitude variation versus Azimuth (AVAZ) methodology, to perform a series of *seismic inversions* (Al-Kandari et al., 2009), to evaluate the anisotropy of a key elastic property of the media, the P-impedance, on each azimuthal stack.

The method is the one described in the previous chapter, applied to *azimuthal stacks*. These stacks must contain information from large offsets to be able to detect anisotropy. In addition, as the amplitude is compared from one azimuthal stack to another, the events should be properly aligned before applying the processes.

To avoid introducing any bias related to the different azimuthal sectors, the key parameters should be defined using the full-stack full-azimuth seismic data:

- Unique optimal wavelet: initial shape, phase rotation, energy.
- Uniform well-to-seismic calibration: the wells are tied the same way to the seismic data. The synthetic at well does not model anisotropy.
- Unique prior model.
- Homogeneous inversion parameter set: the parameters are the same to ensure the same level of convergence of the algorithm.

At the end of the process, as many inverted P-impedance models as azimuthal stacks are obtained, from which the only difference comes from the signal itself.

### 8.4 Ellipse fitting on properties to estimate the anisotropy

Either for the velocity (VVAZ) or the impedance (AVAZ), the ellipse fitting allows to capture the variability of the property according to the azimuth (Adelinet et al., 2013). In polar coordinates, each sector response (for each cell, in 3D) is plotted as a point, for which the radius corresponds to the magnitude of the property, and the angle to the average azimuth angle, as displayed Figure 8.2.

An isotropic response, corresponding to the same magnitude for all angles, will result in a *circle*, while a different response will be approximated by an *ellipse*. This ellipse has two main parameters:

- The *orientation* of the major axis: corresponding to the orientation associated with the major magnitude of the property.
- The *ratio* of the axis: 1 for a circle, greater than 1 for anisotropy detection.

Compared to raw statistics such as variance, the ellipse fitting imposes anisotropy to be organized and oriented. It acts as a powerful denoising, and the orientation of the major axis is a key QC, supposed to be aligned with the fault/fracture orientations. For each source of information, the computation is performed in 3D, then extracted at key levels to evaluate the results, as illustrated in Figure 8.3.

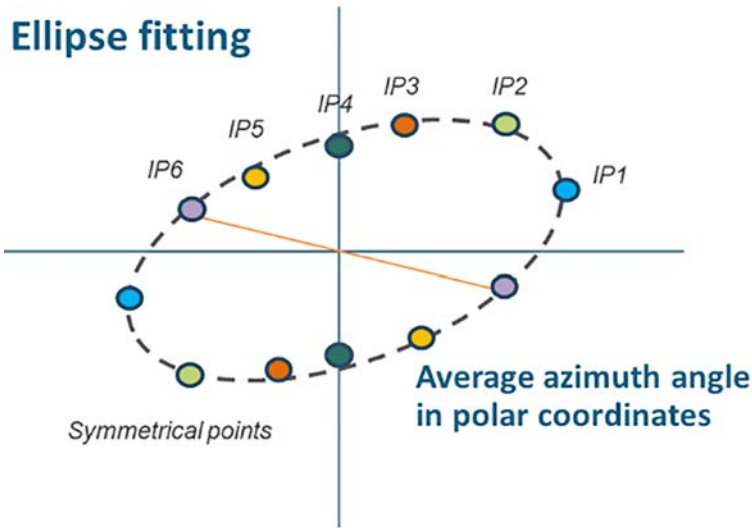


Figure 8.2 *Ellipse fitting to extract the anisotropy intensity and orientation.*

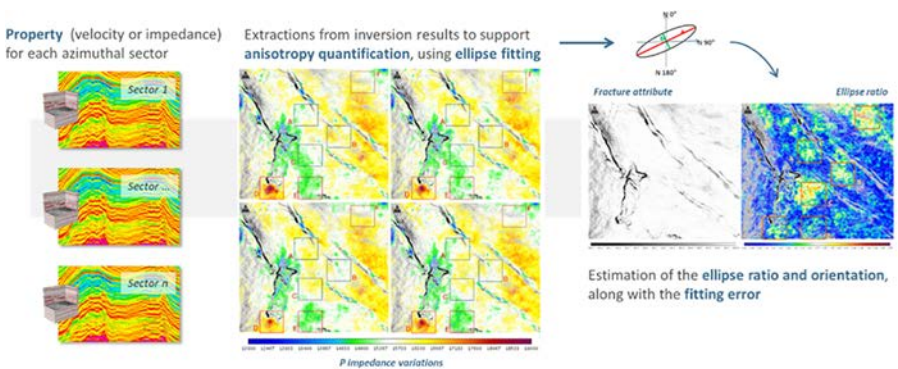


Figure 8.3 *Ellipse fitting, a powerful tool to combine maps into anisotropy estimation.*

## 8.5 From anisotropy to fracture attributes

The relationship between anisotropy and fracture is not direct; a lateral change of any property affecting the impedance (lithology, porosity, fluid, ...) may lead to the same effect. To derisk the anisotropy interpretation, a lateral gradient computed on each of these predicted properties should be calculated (Baillet et al., 2024). This attribute captures their lateral variation rate. Cut-off values can be proposed to mask the anisotropy anomalies where a property is changing too much; in remaining areas, the high anisotropy has been interpreted as fracture density. In the illustration below, Figure 8.4, the remaining high anisotropy, in red in the bottom section, are interpreted as fracture density from the original anisotropy volume, in colors in the top section.

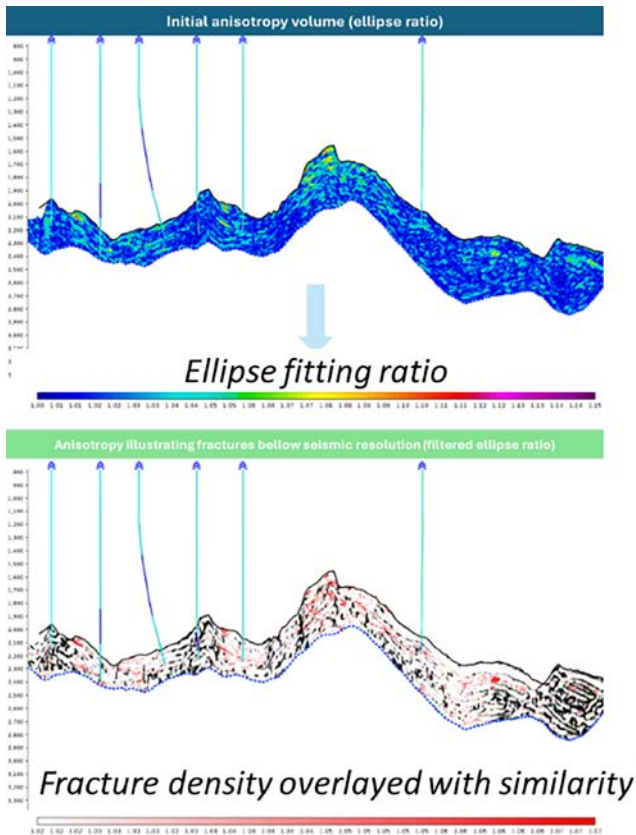


Figure 8.4 Example of derisking anisotropy attribute when other reservoir properties are stable.

## 8.6 Case study: Fracture characterization through azimuthal inversions to prospect the geothermal potential of Geneva basin

To develop the exploitation of geothermal resources in the city of Geneva, a prospection phase has been initiated to better characterize the basin with a newly acquired and processed 3D wide-azimuth land seismic. The Geneva basin location between alpine massifs south side and the Jura north side makes its geology complex and subject to variable constraints which enhanced geothermal energy development. The present project consists of an azimuthal anisotropy intensity analysis at different reservoir levels, to be related to more subtle fracture characterization than using conventional seismic attributes. In this project, both AVAZ and VVAZ approaches as described in this chapter are tested and compared.

### 8.6.1 Processing, conditioning, shift detection

CMP gathers are available at different processing stages, allowing the best choice that suits the needs of the study. The gathers with migration and isotropic NMO (Normal Move Out) have been selected; versions with steps such as trim statics and the Radon filter have been discarded as they might alter both the AVAZ and VVAZ responses.

To eliminate the surface waves, an outer time-variable mute is applied to the original gathers before stacking. As the anisotropy is mostly contained in the far offset traces, all the available data, regardless of the offset, has been considered. The stack generation tests showed the possibility to get 6 azimuthal stacks (Table 8.1), enhancing therefore the possibility to detect anisotropy and the accuracy of its orientation.

Table 8.1 Ranges of the azimuthal stacks.

Name	Full-stack	AZ1	AZ2	AZ3	AZ4	AZ5	AZ6
Range	0–180°	15–45°	45–75°	75–105°	105–135°	135–165°	165–205°

The noise-to-signal ratio is enhanced by considering symmetrical azimuthal ranges; the seismic response varies with the direction source-receptor, regardless of the orientation. Remaining noise content can be managed through the model-based inversions (AVAZ) or the probe size during shift detection (VVAZ).

In addition, full-stack full-azimuth seismic data has been generated as a reference. The following maps (Figure 8.5) illustrate, as QCs, the correlation map (left) and the RMS map (right), highlighting the area of the survey, covering Geneva city. Part of the survey is offshore (in the Lemman Lake), and part of the seismic data is noisier below the city, as visible in both maps.

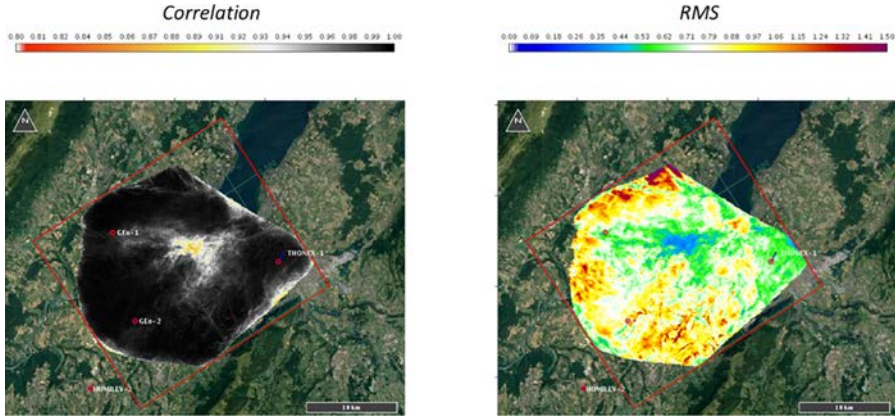


Figure 8.5 Correlation (left) and energy (right) map computed on the full stack

As a base for the VVAZ approach, isotropic interval velocities from RMS velocities have been deduced through Dix formula (Figure 8.6). Trials and errors have been used to set the interval parameter to 40 ms; beyond, the obtained velocities are less accurate, below, the obtained velocities contain gridding artifacts, as observable, attesting of the too high sampling compared to the original RMS picking.

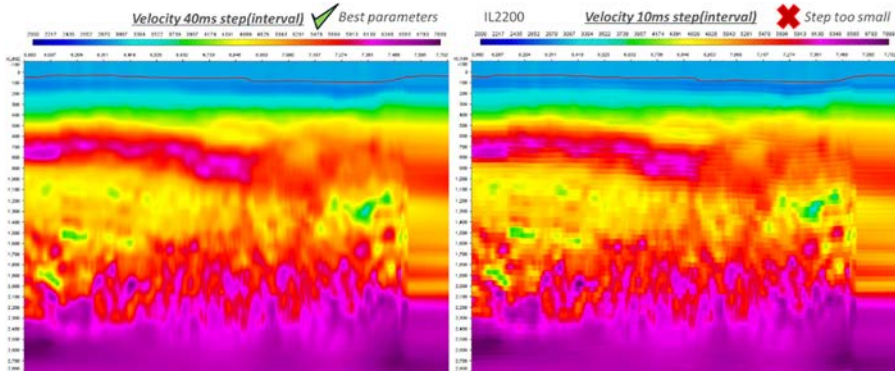
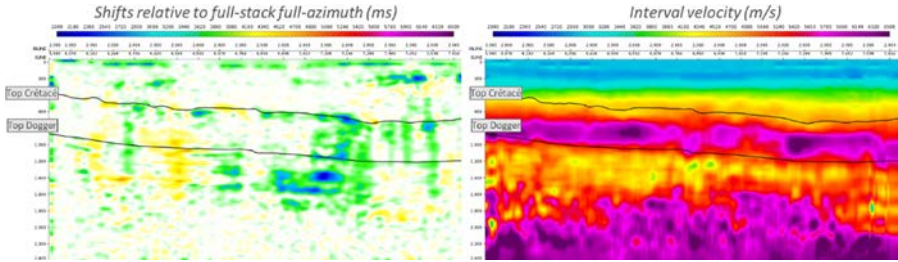


Figure 8.6 interval velocity using Dix formula for 40 ms (left) and for 10 ms (right).

While aligning the stacks, detecting shifts according to the reference, tests (errors and trials) have been undertaken to establish the final parameters. As displayed in Figure 8.7, the shifts obtained are subtle, mainly between  $\pm 5$  ms. They are directly linked to the average velocities, while their vertical gradients are linked to the interval velocities. Therefore, constant shifts (vertically) indicate no anomaly, while abrupt (vertical) changes indicate a presence of VVAZ anomaly.



**Figure 8.7** Shifts detected in milliseconds (left) converted to interval velocity (right) for an azimuthal sector.

Some observations can be made:

- The shifts detected are different from one azimuthal sector to another, already revealing VVAZ effects.
- The shift main shift changes (except the shallow weather zone) are located at the Top Cretaceous level.

In the end, the procedure to derive interval velocities from the shift volume has been applied to the 6 azimuthal stacks, ready to extract the VVAZ anisotropy.

### 8.6.2 Model-based inversions

The azimuthal stacks have been aligned using the detected optimal shifts to optimize their mutual compatibility, for estimating properly the AVAZ effects. Then, to obtain P-impedance model by sector, a series of model-based seismic inversions is performed. To illustrate, an optimized impedance section, for one sector, is proposed Figure 8.8.

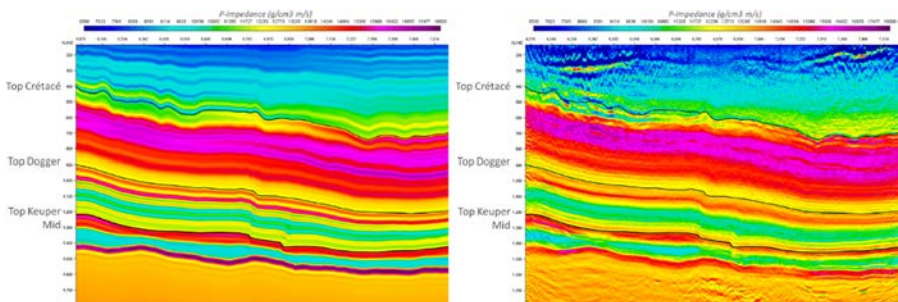


**Figure 8.8** P-impedance section from the prior model (left) and after inversion for stack 1 (right).

Although acoustic inversion technique has been selected, the obtained property can be considered as a “pseudo-P-impedance”, as large offset traces will have more contribution than short offset traces in the amplitude variations, to better capture the anisotropy.

The convergence for the azimuthal stacks varies from 70% to 80%, in accordance with the initial level of noise of each azimuthal stack. The noise, discarded from the synthetic seismic and observable in the residuals, hasn't been included in the 6 optimized impedance models, in order to better estimate the AVAZ effects.

### 8.6.3 Results and way forward

Either for the VVAZ or the AVAZ approach, the focus is based on the variation of the properties with the azimuth rather than their absolute values. In both approaches, the anisotropy has been extracted using ellipse fitting: an isotropic response would result in a circle, while a different response would be approximated by an ellipse, with two main parameters: (1) the orientation of the major axis, corresponding to the tilt associated with the major magnitude of the property (usually parallel to the fractures), (2) the ratio of the axis, greater than 1 for anisotropy detection.

While comparing the results obtained in sections, Figure 8.9, it is observable that:

- The anisotropy from VVAZ is more subtle than AVAZ, so that the scale has been saturated for display purposes.
- The resolution of the anisotropy from AVAZ (right) seems to be better than the VVAZ (left).
- Some anisotropic areas, especially around the Top Cretaceous or the Top Keuper, seem to correlate between both methods, while others don't.
- Where there is no signal, especially around the major fault at the center part of the section, no anisotropy is detected (VVAZ or AVAZ).

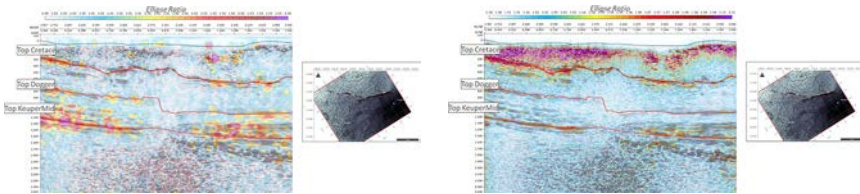


Figure 8.9 Anisotropy in section, VVAZ (left) and AVAZ (right).

At low depth, as illustrated Figure 8.10 in time slice (700 ms), both approaches are compatible with each other, focusing on objects with apparently the same size and resolution.

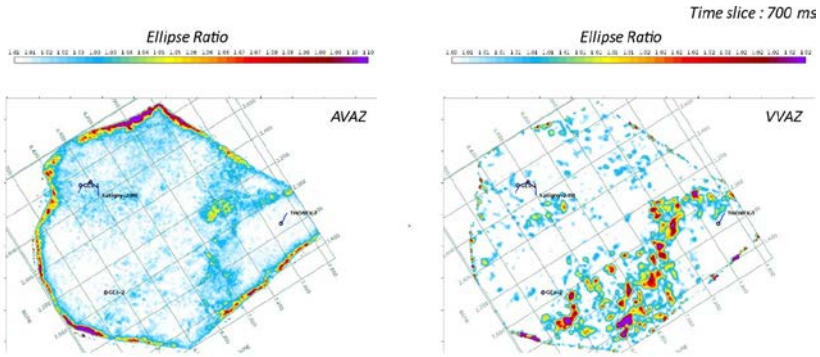


Figure 8.10 AVAZ (left) and VVAZ (right) anisotropy at 700 ms time slice.

The same visual can be performed highlighting the areas with no signal (low energy) and conventional fracture attributes (3D similarity), Figure 8.11. The low energy areas, in pink, indicate no information rather than no anisotropy. The conventional fracture attributes, in black, indicate the presence of faults and fractures at greater scale, completing the understanding of the anisotropy distribution. In these maps, some blocks between major faults can be affected or not by anisotropy, which may indicate the presence or absence of fractures.

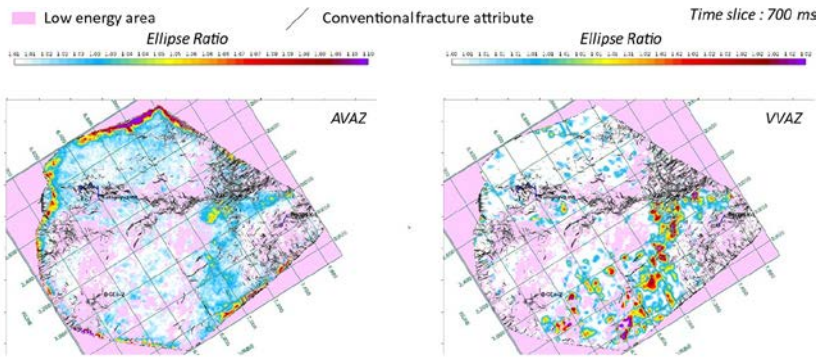


Figure 8.11 AVAZ (left) and VVAZ (right) anisotropy at 700 ms time slice, with weak signal areas in pink.

From Top Cretaceous to Top Dogger, The AVAZ results highlight similar areas (Figure 8.12), while VVAZ results vary at these same levels (Figure 8.13), indicating a poor compatibility between AVAZ and VVAZ.

The strong amplitudes of the Top Cretaceous may affect the deeper events, showing therefore similar anomaly areas. The VVAZ does not depend on this amplitude effect and may be more reliable from below the Top Cretaceous down to the Top Dogger.

The compatibility between the attributes is again observable from the Top Keuper Mid horizon and below (Figure 8.14).

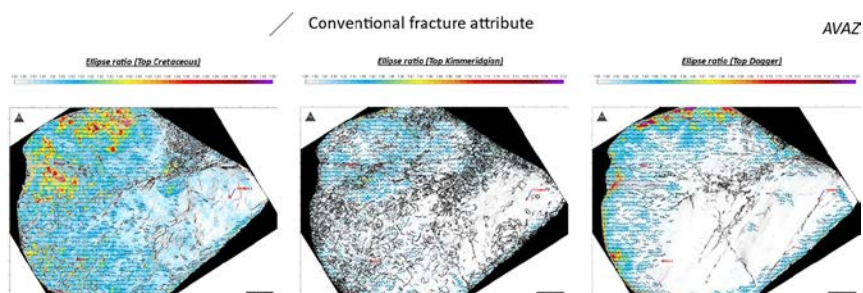


Figure 8.12 AVAZ anisotropy at Top Cretaceous (left), Top Kimmeridgian (middle) and Top Dogger (right).

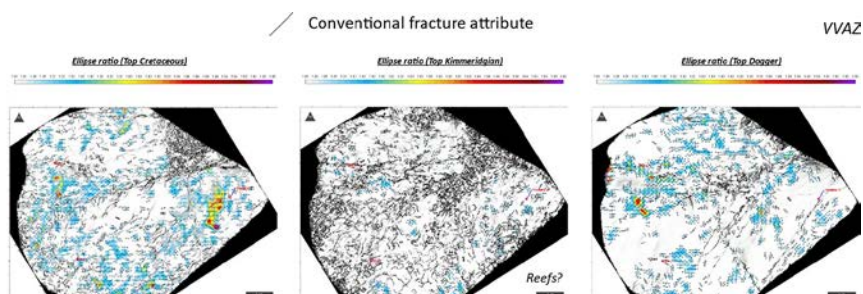


Figure 8.13 VVAZ anisotropy at Top Cretaceous (left), Top Kimmeridgian (middle) and Top Dogger (right).

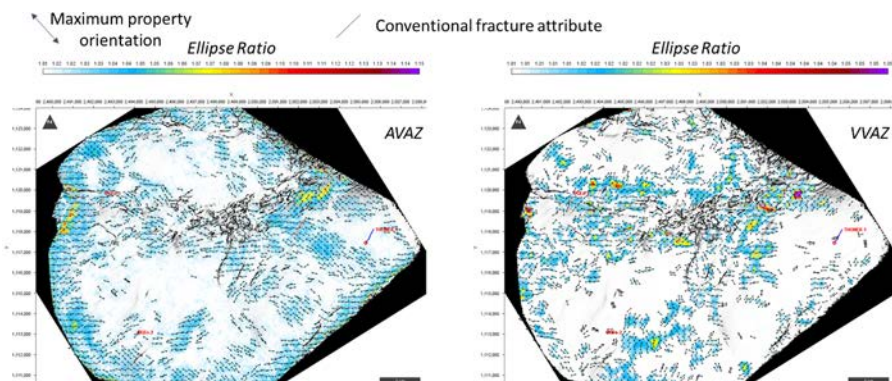


Figure 8.14 AVAZ (left) and VVAZ (right) anisotropy at Top Keuper Mid level.

## Conclusions and perspectives

The work described in this chapter has been applied using newly generated azimuthal stacks, for which the processing sequence has been evaluated very carefully, preventing destructive steps for both AVAZ and VVAZ approaches. When both approaches seem equally acceptable, as along the Top Cretaceous event, labelling depending on the anisotropy range is proposed for AVAZ and VVAZ approaches (Figure 8.15) using cut-offs, and the result would highlight, in red, the most prospective areas outside low-energy areas and outside main seismic faults.

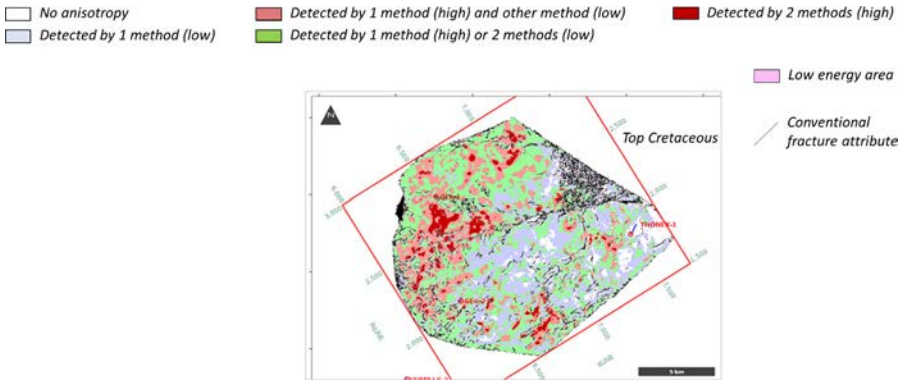


Figure 8.15 *Ellipse fitting, a powerful tool to combine maps into anisotropy estimation.*

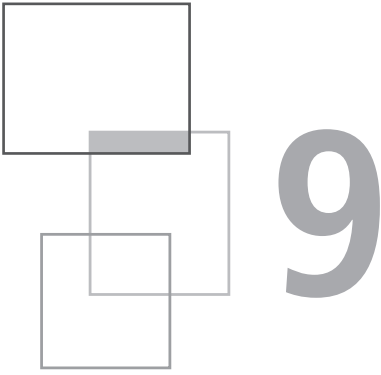
The anisotropy interpretation as a fracture attribute is still a challenge. A brutal and oriented change in properties affecting impedance, such as karsts, can also induce anisotropy. As a way forward, matrix characterization and karst identification will be carried out to further understand the other possible anisotropy sources, using elastic inversion as described in the previous chapter. Still in exploration phase, the new wells to be drilled in the area will reveal key aspects to refine the anisotropy interpretation, using BHI to interpret the fault and fracture clusters to be correlated with the anisotropy results.

## References

Adelinet M., Barnoud A., Clochard V., Ricarte P. (2013) Improved unconventional reservoir characterization using multi-azimuth stratigraphic inversion, case

- study on the Fort Worth Basin, *Journal of Unconventional Oil and Gas Resources* 3-4, 15-26, <https://doi.org/10.1016/j.juogr.2013.10.001>.
- Adelinet M., Clochard V., Barthelemy J.F., Chérel L. (2012) Determination of Crack Orientation in a Fractured Reservoir from Effective Medium Modelling and Multi-azimuth Inversion, 74th EAGE Conference and Exhibition incorporating EUROPEC 2012, cp-293-00564.
- Al-Kandari A., Kumar R., Convert P., Ortet S., Lecante G. (2009) Fracture characterization using seismic data in a West Kuwait field, *SEG Technical Program Expanded Abstracts* 2009, 1775-1779, <https://doi.org/10.1190/1.3255197>.
- Baillet R., Caudroit J. (2024) Seismic fracture characterization using AVAZ and VVAZ anisotropy for geothermal prospection in the Geneva basin, Switzerland, 85th EAGE Annual Conference & Exhibition, Oslo, Norway.
- Baillet R., de Freslon N., Thomas V., Castellanos R., Denogean E. (2024) Fracture and matrix characterization using wide-azimuth and multi-component seismic data: A case study from offshore Mexico, *SEG Technical Program Expanded Abstracts* 2024, 144-148, <https://doi.org/10.1190/image2024-4101418.1>.
- Chérel L., Bruneau J., Dubos-Sallée N., Labat K., Barthelemy J.F., Daniel J.M. (2010) Understanding seismic anisotropy from fractures observed in wells, 72nd EAGE Conference.
- Elapavuluri P., C.J. Bancroft (2002) Estimation of Thomsen's Anisotropy Parameter  $\delta$  and  $\epsilon$  Using EO Gather, *Crewes Research Report* 14, 18.
- Liu E., Martinez A. (2012) Seismic Fracture Characterization: Concepts and Practical Applications, EAGE Publications.
- Mori T., Tanaka K. (1973) Average stress in matrix and average elastic energy of materials with misfitting inclusions, *Acta Metall.* 21, 571-574.
- Thomsen L. (2002) Understanding seismic anisotropy in exploration and exploitation: SEG-EAGE Distinguished Instructor Series No. 5, SEG.





# Defining high enthalpy geothermal drilling target with multi-physics integrated exploration program. Mayotte's Petite-Terre Island case study

A. Stopin, C. Dezayes and T. Farlotti

---

## Introduction

Mayotte is a volcanic island located on the ocean floor of the southern Somali Basin, between Africa and Madagascar, and is part of the Comoros Archipelago (Figure 9.1). The island is mainly composed of volcanic formations and is surrounded by the largest closed lagoon in the Indian Ocean, bordered by a coral reef barrier.

In 2017, Mayotte's electricity mix comprised 5% photovoltaic production distributed across more than 70 installations on the island, with the remaining 95% generated through diesel thermal power plants operated by Électricité de Mayotte. To diversify its electricity supply, the Departmental Collectivity of Mayotte implemented a comprehensive program aimed at leveraging renewable energy sources. As part of this initiative, the potential for geothermal energy production on the island was evaluated.

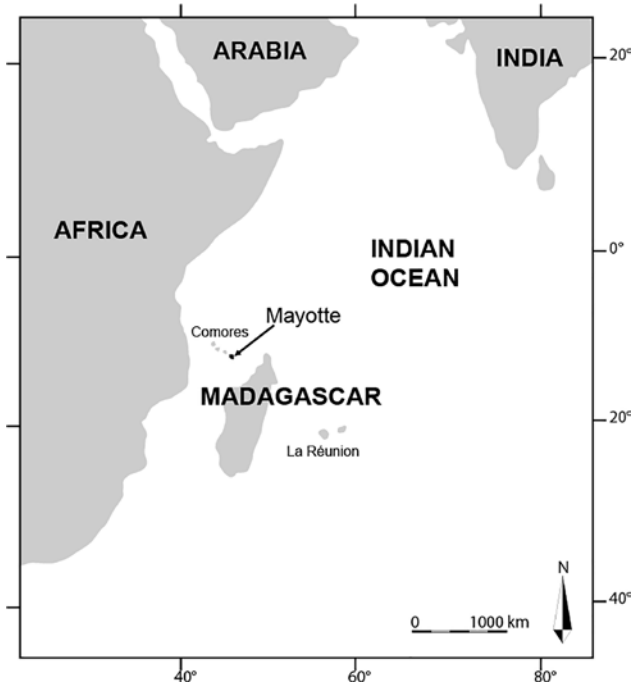


Figure 9.1 Location of Mayotte Island.

The French Geological Survey (BRGM), on behalf of and co-financed by the Departmental Collectivity of Mayotte, conducted a two-phase study titled “Assessment of Mayotte’s Geothermal Potential”. The first phase, conducted between 2005 and 2006, aimed to identify areas on the island with potential geothermal resources for electricity production. Results and main conclusions are detailed in the report by Traineau et al. (2006).

Petite-Terre was identified as a promising area despite the absence of direct evidence of geothermal resources. This selection was based on the island’s recent volcanism (<0.5 Ma), its unusual configuration for geothermal exploration, and the discovery of a significant magmatic CO<sub>2</sub> degassing zone east of the airport (Traineau et al., 2006).

The second phase of the study (2007-2008) focused on Petite-Terre, specifically the CO<sub>2</sub> degassing zone near the airport and the Dziani Dzaha Lake area, previously noted for gaseous emissions. Geophysical surveys (gravity, magnetism, and electrical resistivity) were conducted to detect potential heat sources such as hypovolcanic intrusions or magmatic chambers, as well as the presence of a hydrothermal system. Key results are presented in Pajot et al. (2007).

Based on the findings, including evidence of a dense and magnetic shallow body beneath the CO<sub>2</sub> degassing zone near the airport, a second stage of the study extended the resistivity surveys southward for deeper investigation. This stage also refined geochemical characterizations and natural gas flux measurements. The results, documented by Sanjuan et al. (2008), ruled out the presence of geothermal resources within the first 1000 m of depth and deemed it unlikely up to 1500 m – depths considered economically viable for electricity production.

However, given Petite-Terre's recent volcanism and its geological, geochemical, and geophysical context, the presence of a thermal anomaly or hydrothermal system at greater depths could not be excluded.

To confirm the existence and location of deeper geothermal resources, a comprehensive exploration program, including exploratory drilling, is required. Recognizing the cost and complexity of such an undertaking, Darnet et al. (2019) analyzed previous studies to evaluate the five elements of an active geothermal system (Figure 9.2):

1. heat source presence,
2. a cap rock preventing fluid escape,
3. a sustainable water recharge system,
4. a permeable medium (e.g. fractures),
5. the hydrothermal system's age.

Their analysis indicated a likelihood greater than 50% of finding an active geothermal system, though additional data were necessary. A customized exploration program was therefore defined, incorporating various methods to evaluate parameters such as temperature, volume, porosity, and permeability. Key components included:

- Geological data acquisition to analyze rock permeability and fracturing.
- Geochemical studies, including gas geothermometry, to estimate source temperatures.
- New onshore and offshore magnetotelluric (MT) surveys for 3D imaging of subsurface conductivity.
- Integration of data into GeoModeller™ (Lajaunie et al., 1997; Calcagno et al., 2008) to create a consistent 3D geological model.
- Hydrothermal simulations using the ComPASS (Lopez et al., 2018) platform to locate the optimal exploratory well site.

Dezayes et al. (2023) followed the exploration program described above. This chapter will focus on how the various geophysical methods of the program were used to define the geothermal drilling targets on Petite-Terre.

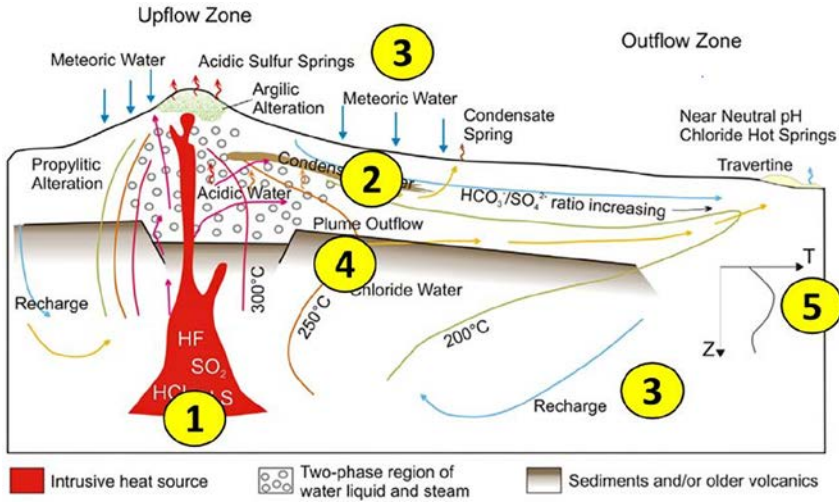


Figure 9.2 Constitutive elements of a volcanic hydrothermal system (Darnet et al., 2019).

## 9.1 Integration of magnetotelluric data

A total of 32 MT stations acquired during different periods (Darnet et al. 2019; Dezayes et al. 2023) are available. This dataset includes land MT stations and, for the first time, marine MT stations around the island, providing a more comprehensive image of the geological structures.

These 32 stations were inverted using the MININ3D code (Hautot et al., 2000, 2007) to create a 3D resistivity model. The results show a conductive structure overlying a resistive body, with a varying depth interface: 600 m below Moya Beach and 1.6 km below the airport (Figure 9.3). The model shares similarities with Pellerin et al. (1992) but reveals a more complex geometry. This interface can be interpreted as the boundary between a geothermal reservoir and its caprock.

In the map view at a depth of 2432 m, the resistive body displays a NW-SE global trend (Figure 9.3). The high quality of the hybrid land and sea MT measurements enabled the construction of a well-constrained 3D image of a potential geothermal target.

The 3D resistivity cube is interpreted based on the cross-sections shown in Figure 9.4. These cross-sections reveal a large, highly resistive volume compared to the surrounding host rock, with values ranging between 30 and 60 Ω·m (Figure 9.5). Based on the reference model, this zone corresponds to the reservoir altered by geothermal fluid circulation. Its boundaries can thus be delineated across all the cross-sections.

Above the reservoir lies the caprock, characterized by lower resistivity values, below 10 Ω·m. On the profiles, this zone is challenging to identify clearly due

to low resolution and likely interference from seawater infiltration at the surface. Nevertheless, a resistivity contrast can be observed between the upper part of the basement and the lower part, where resistivity is slightly higher. This boundary is marked as a dark red line in Figure 9.5.

It thus represents the basal boundary of a portion of the basement that may be partially clay-altered due to hydrothermal alteration, with its deepest levels likely containing the caprock.

Finally, very low resistivity values, again below  $10 \Omega\cdot\text{m}$ , are obtained at the bottom of the grid, towards the east. When placing this in the context of the reference conceptual model, it could correspond to the heat source of the geothermal system, located at around 12 km depth. Its roof is interpreted in the cross-sections (Figure 9.5), although the large depth introduces considerable uncertainty regarding its geometry.

This interpretation work allows for the construction of a 3D model that includes the three main elements of the geothermal system (Figure 9.6).

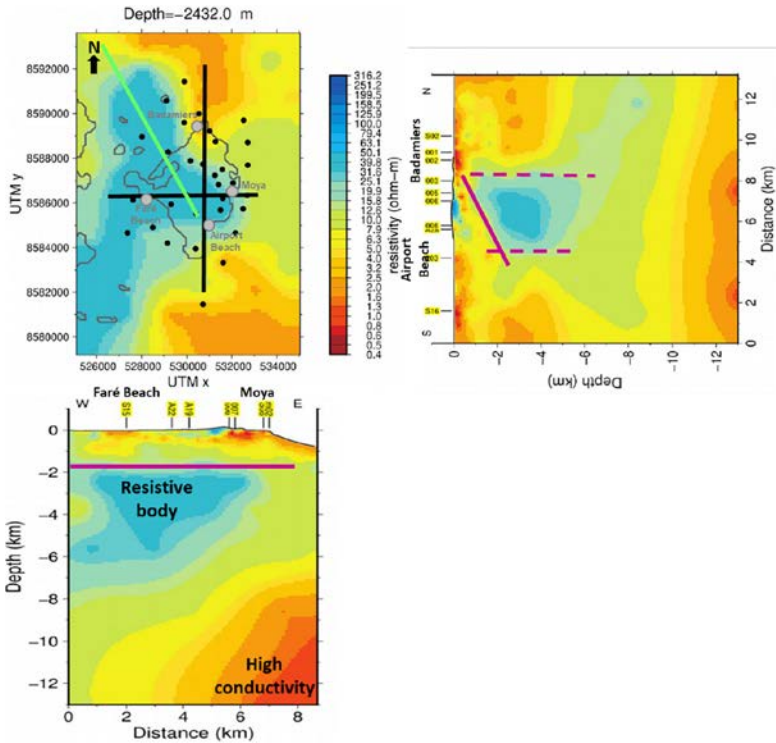


Figure 9.3 Resistivity map and cross-section on Petite Terre Island. On the map, black points: station location, black lines: location of cross-section, green line: SW-SE trend tendency. On cross-section, purple lines: limitation of resistive body.

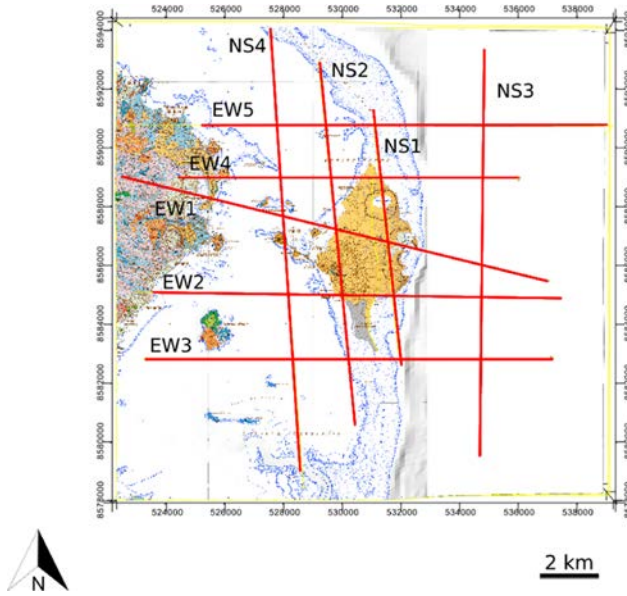


Figure 9.4 Location of the different cross-sections used to trace the boundaries of the formations. EW1 presents an oblique direction to match the conceptual WNW-ESE cross-section from Traineau et al. (2006), which has been integrated into the model.

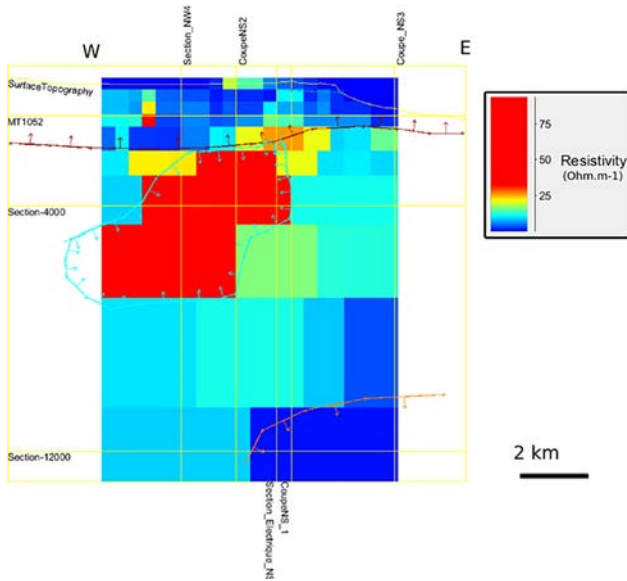


Figure 9.5 Example of interpretation of the EW1 cross-section from the resistivity grid. The drawn lines represent the bases of the formations. Dark red line: substrate, cyan line: reservoir, orange line: heat source.

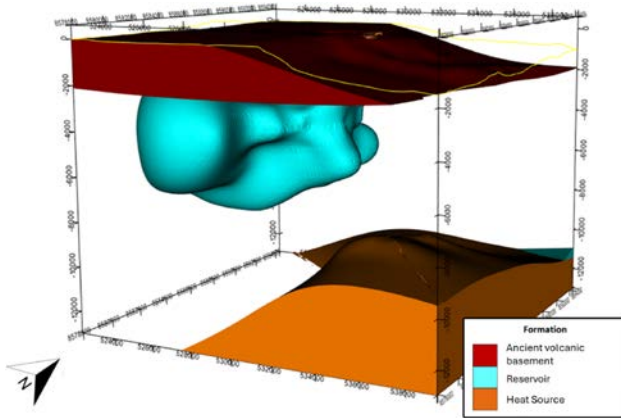


Figure 9.6 First model obtained considering only the results of MT data inversion.

Furthermore, on the field, the following surface manifestations have been observed:

- CO<sub>2</sub> degassing at the airport beach;
- CO<sub>2</sub> upwelling in a well in the center of the island.

These observations indicate the likely existence of a permeable zone passing through these two points, forming a N150°E direction. This is the main direction observed on the island outcrops and also corresponds to the regional geodynamic direction (Famin et al., 2020).

These elements lead to the presence of a possible sub-vertical fault passing through these points, defining a northeast boundary to the reservoir in the subsurface (Figure 9.7).

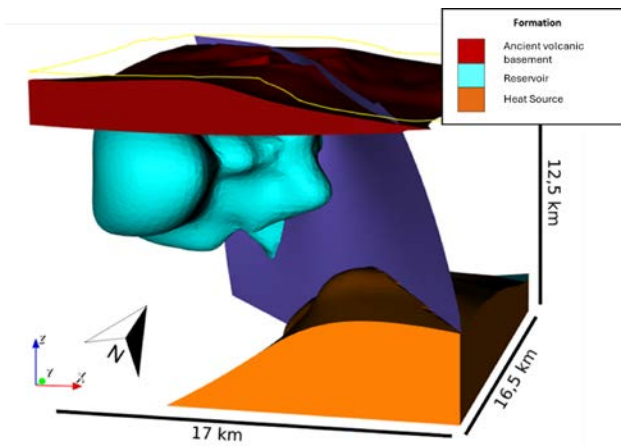


Figure 9.7 First model, with a N150°E fault based on the field observation. The confidence on the existence of this fault is very low at this stage of the model construction.

## 9.2 Electric profile integration

To better define the model at the surface, geophysical data probing shallower depths can be used. The electrical profile crossing the island from one end to the other (Figure 9.8) was carried out during the first geophysical campaign (Pajot et al., 2007) and then supplemented by a second series of acquisitions (Sanjuan et al., 2008).



Figure 9.8 Localisation of the electric profile (Sanjuan et al., 2008).

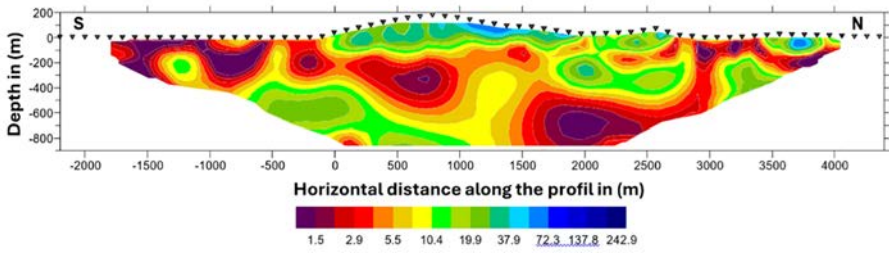


Figure 9.9 Resistivity ( $\Omega/m$ ) profile obtained from the inversion of the electric profile (Pajot et al., 2007).

A first interpretation had already been made of the resistivity profile obtained by inversion (Figure 9.9), but it was not complete enough to be integrated as is into the model. In light of the recent data, a new interpretation (Figure 9.10) is proposed, taking into account the identified formations.

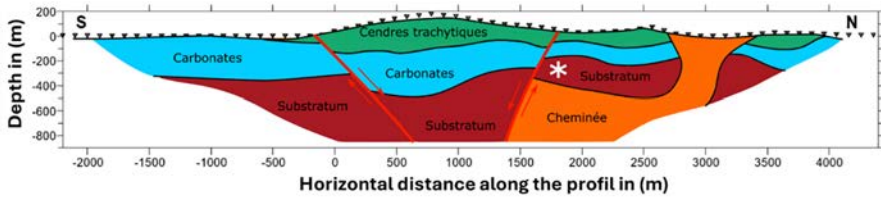
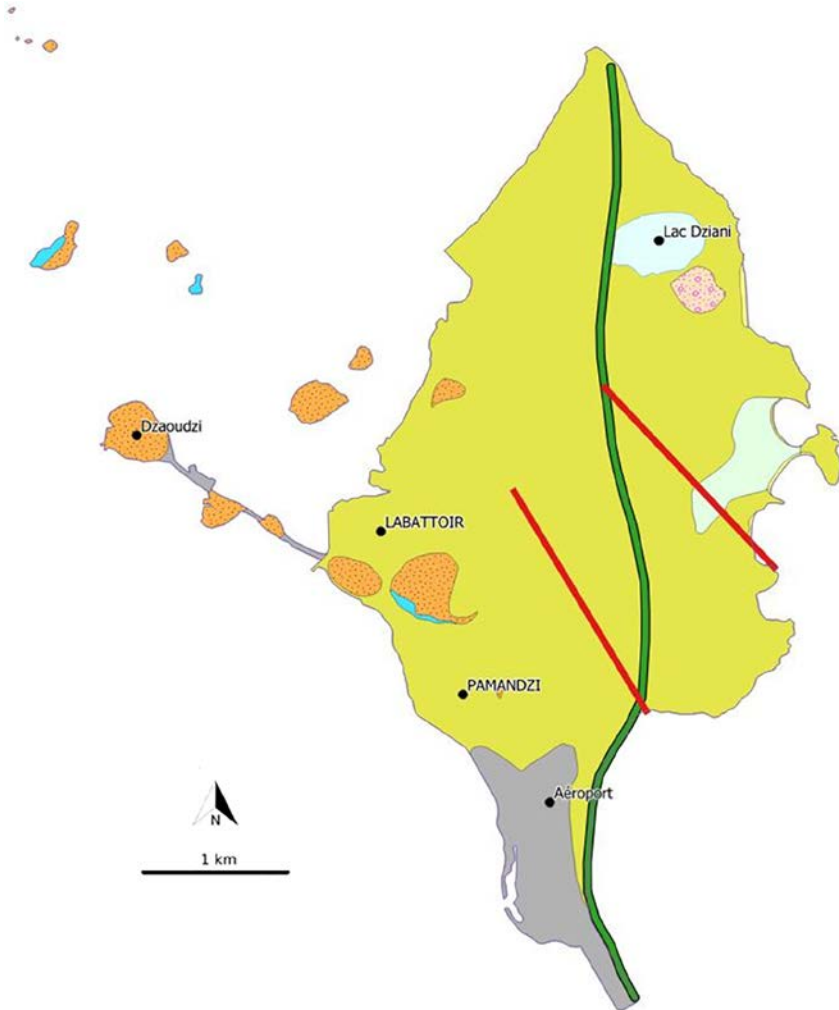


Figure 9.10 New interpretation of the electric profile.

This interpretation aligns with the overall architecture of Petite Terre, where volcanic material cuts through the carbonates, settling on top to form the island. The upper part is therefore composed of resistive trachytic ash and tuff. Below, the carbonated platform is conductive due to the intense water circulation and, in particular, saline intrusions that lower resistivity values. The Dziani lake area shows low resistivity, which extends clearly in depth. However, Dziani Lake is a maar created by phreatomagmatism. Therefore, it is reasonable to think that this low-resistivity zone is a conduit for fluid circulation. A zone of low resistivity, which could be linked to a high permeability zone, could, on the one hand, explain the magma upwelling and, on the other hand, the subsequent water circulation that causes hydrothermalism, leading to the alteration of magmatic rocks and thus low resistivity.

On the profile, two faults can be interpreted. The first to the south aligns with the one previously interpreted from the field data. This provides additional evidence for its presence, which was previously only inferred from gas emissions. The second interpreted fault dips southwest and forms a small graben in the middle of Petite Terre. To trace this fault on the map, however, another anchor point is needed.

During one of the early field campaigns (Traineau et al., 2006), a water seepage point was observed at the tip of one of the coves on Moya beach (Figure 9.11). However, a landslide made the area inaccessible, so the second field campaign in 2021 was unable to confirm and better define this zone. Nevertheless, considering that it is the same fault zone as the one defined on the section (Figure 9.10), its N140° direction appears consistent with the one to the south and with the geodynamic context (Famin et al., 2020; Figure 9.10). Confidence in this structure remains relatively low, however.



**Figure 9.11** Location of vertical permeability indicators used to trace the two faults. The red points indicate the locations of the faults on the electrical profile.

These points provide an orientation for the faults. To model them in GeoModeller, the software requires a dip value. Based on the apparent dips observed in the section (Figure 9.10) and the angle assumed relative to the fault azimuth, obtained from surface observation points (Figure 9.11), it is possible to assign a real dip to the model before creating 3D surfaces (Figure 9.12).

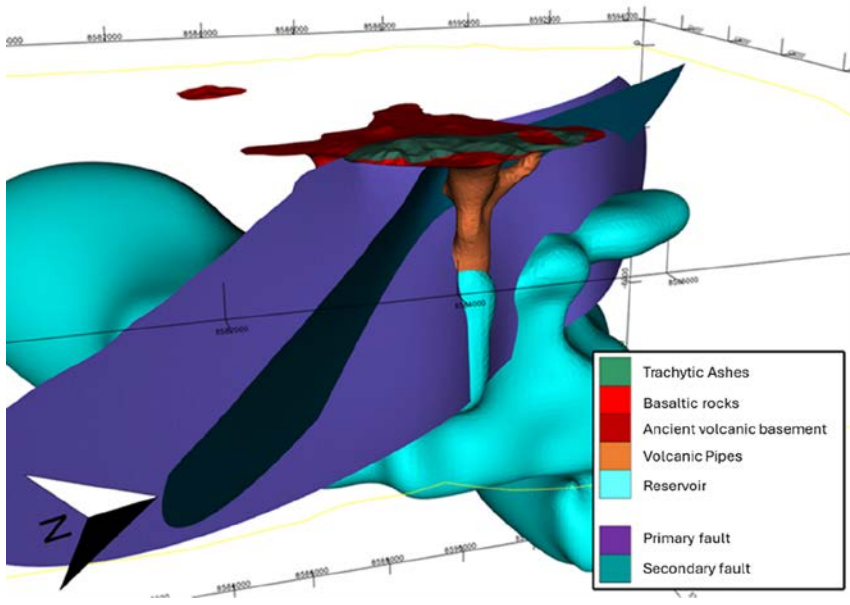


Figure 9.12 *The two normal faults modelled under Petite Terre.*

### 9.3 Gravimetric data integration

A total of 116 gravimetric measurement points acquired during the Pajot et al. (2007) campaign were inverted to obtain a density model. The inversion is performed jointly with the inversion of MT data, using a global correlation of resistivity and density structures as a constraint.

The density structure results (Figure 9.13) show a negative anomaly at the surface between the two interpreted faults forming a small graben. The main direction remains the same as the one observed in the previous paragraph, providing additional evidence supporting the presence of these faults, which were not visible in the resistivity inversion.

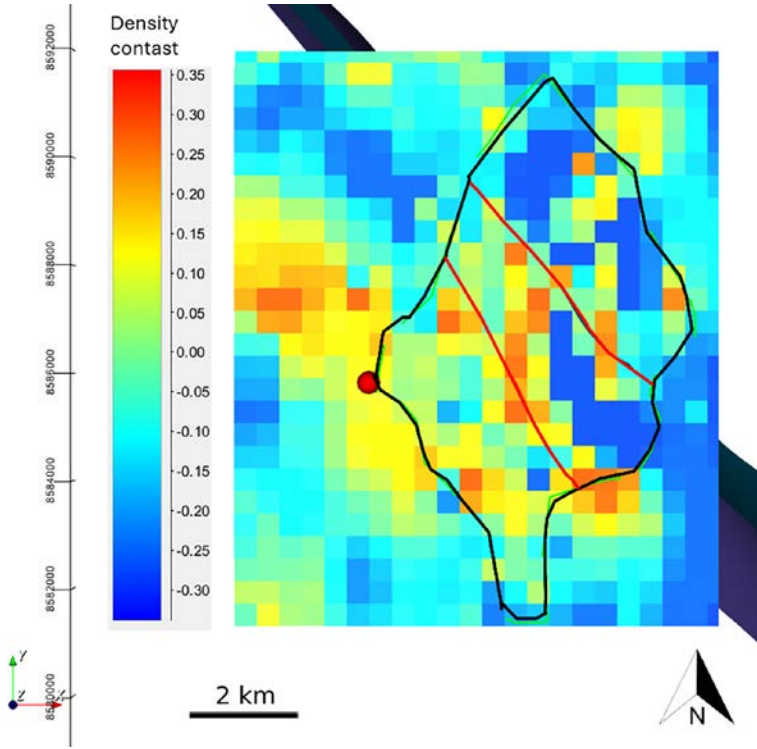


Figure 9.13 Surface density grid, with the outline of Petite Terre in black and the trace of the faults in red. A negative anomaly is observed between the two faults, which may indicate a collapse zone.

## 9.4 Final model

Geophysical data allowed for the placement of a reservoir, a heat source, the base of the volcanic substratum, as well as a number of areas with higher vertical permeability (chimneys) connecting the reservoir to surface material ejection zones. These areas likely correspond to relatively fractured environments, with the two major craters, Lac Dziani and La Vigie, being aligned along the main deformation direction of N150°E. The electrical profile also helped differentiate the volcanic rocks, distinguishing denser basalt-like rocks from the resistive trachytic ashes found around the maars.

The combination of all the data was used to position, with varying degrees of confidence, two N150°E-oriented faults, with the southernmost one being relatively certain, while uncertainties remain regarding the northern one. Following these

interpretation steps, the model underwent a phase of global consistency, during which many modifications were made to better align with reality. Among these, a final chimney was added in the southern part of the island to explain a high value observed in the magnetotelluric data at this location, which also correlates with visible scoria ejections on the surface (Figure 9.14).

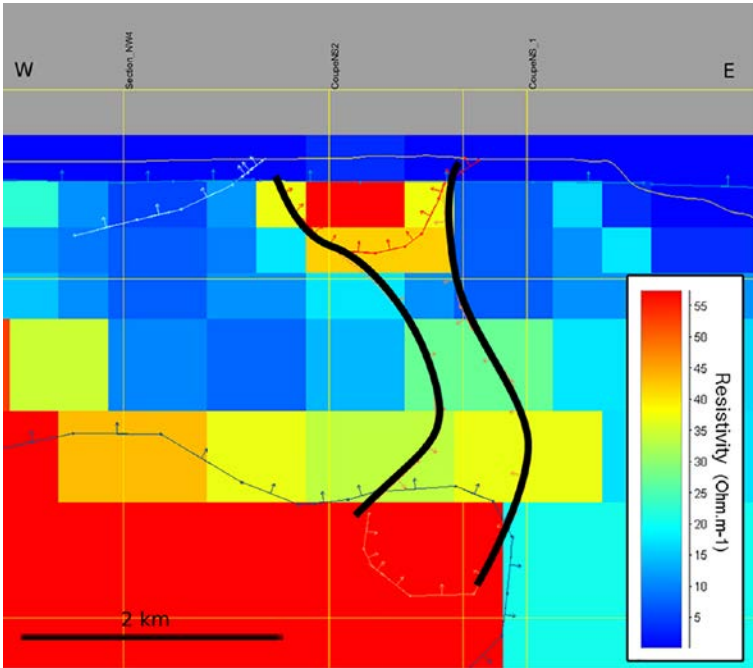


Figure 9.14 EW2 cross-section (see Figure 9.4) highlighting a potential material upwelling zone. The orange lines mark the boundaries of this “chimney”.

The geological model is then ready (Figure 9.15). It is consistent with the surface geological map and respects the general geometries observed. Some simplifications were made, notably the choice to assimilate the entire portion of Grande Terre within the model to volcanic substratum, even though in reality the area is covered by more recent minor lava flows. Since the project focuses primarily on Petite Terre, approximations at the edge of the model are not of major importance. The same applies to the geometry of the reservoir, which is, of course, largely extrapolated where data is absent.

With the finalized 3D geological model, the next step is to create a hydrothermal model. This stage helps determine the heat flow behaviours based on the geometry created, in order to estimate the most favorable region for the location of an initial exploration well.

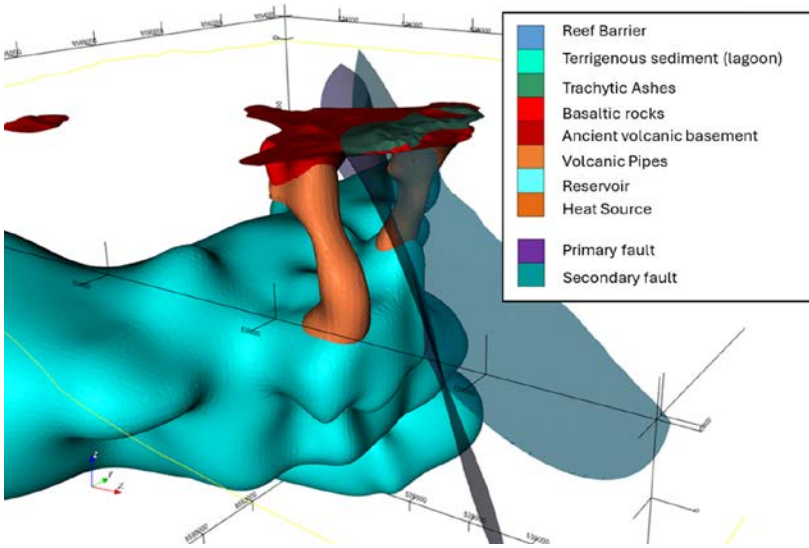
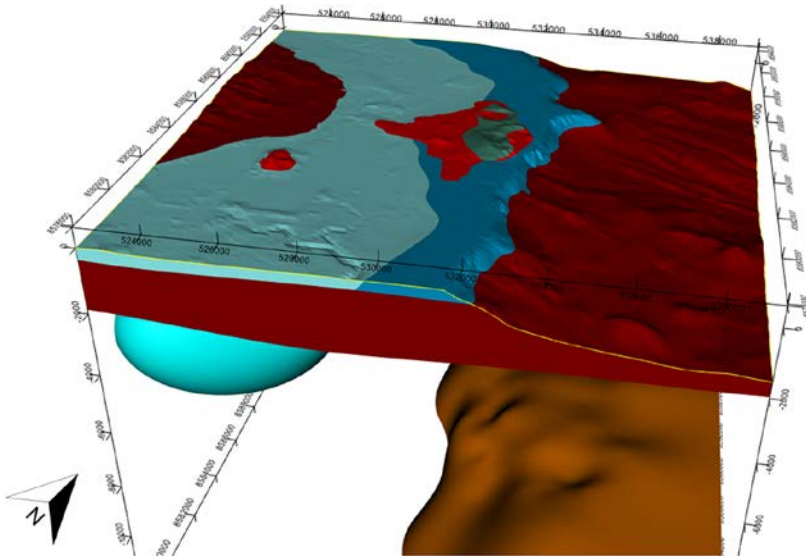
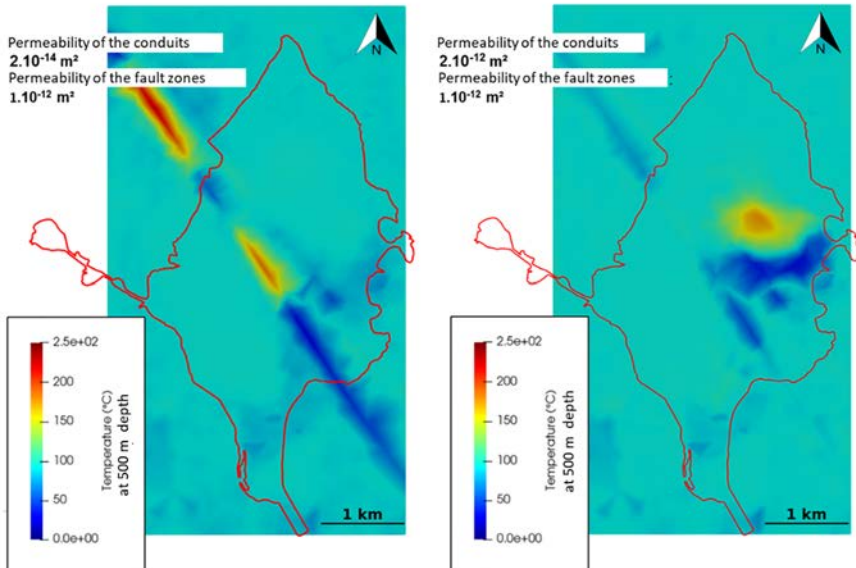


Figure 9.15 Final model. In the second image, the substrate and the more superficial parts have been masked for a better view of the faults and chimneys.

## 9.5 Choice of the drilling target

Based on the created geological model, the conceptual model defines the hydrothermal behavior of the system. The deep high conductivity zone constitutes the heat source. The resistive body forms the geothermal reservoir with a permeability higher than that of the surrounding basaltic rocks, while the upper high conductivity zone represents the impermeable caprock. Faults and conduits could channel deep geothermal fluid near the surface and have also been taken into account with higher permeability. A parametric study was conducted by varying the permeabilities of the different objects (conduits, faults, coral barrier) as well as the heat flow. The results of the various simulations show an upward movement of hot fluid at the center of the island, controlled by the volcanic conduit or the main fault, depending on the scenarios considered (Figure 9.16).



**Figure 9.16** Results of the numerical simulations for two scenarios. On the left, the permeability of the magma conduits is two orders of magnitude lower than the permeability of the fault zones. On the right, the permeability of the conduits and faults is equivalent.

In addition, a data assimilation study highlighted areas favorable to the presence of an underlying reservoir. This study, along with the results of numerical simulations, points to a central area of the island, between the Moya and Dziani maars, which could be a target for deep geothermal exploitation.

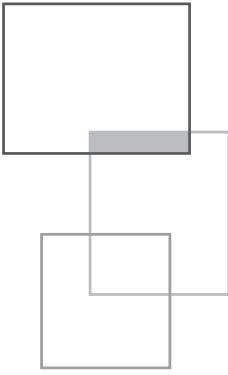
This work has encouraged industry players to submit an Exploration and Research Permit (PER) and to initiate more focused studies and consider an exploration drilling in the near future in the central area of the island. Integration of multi-physics geophysical data was key to obtain these results.

## References

- Calcagno P., Chiles J.P., Courrioux G., Guillen A. (2008) Geological modelling from field data and geological knowledge, *Phys. Earth Planet. Inter.* 171, 147-157, <https://doi.org/10.1016/j.pepi.2008.06.013>.
- Darnet M., Dezayes C., Sanjuan B., Tronel F., Traineau H. (2019) Étude de définition d'un programme d'exploration du potentiel géothermique profond à Petite Terre. Rapport final, BRGM/RP-69398-FR, 72 p., 36 fig., 9 tabl., 1 ann.
- Dezayes C., Stopin A., Wawrzyniak P., Gal F., Farlotti T., Les Landes A., Calcagno P., Traineau H., Hirsinger L., Macedo Serrano E., Chassagne R. (2023) Exploration des potentielles ressources géothermiques profondes de Petite Terre (Mayotte), Rapport final. BRGM/RP-72283-FR, 196 p., 107 fig., 19 tabl., 3 ann.
- Famin V., Michon L., Bourhane A. (2020) The Comoros archipelago: a right-lateral transform boundary between the Somalia and Lwandle plates, *Tectonophysics* 789, 228539, <https://doi.org/10.1016/j.tecto.2020.228539>.
- Hautot S., Single R., Watson J., Harrop N., Jerram D., Tarits P., Whaler K., Dawes D. (2007) 3-D magnetotelluric inversion and model validation with gravity data for the investigation of flood basalts and associated volcanic rifted margins, *Geophys. J. Int.* 170, 1418-1430.
- Hautot S., Tarits P., Whaler K., Le Gall B., Tiercelin J.J., Le Turdu C. (2000) Deep structure of the baringo rift basin (Central Kenya) from three-dimensional magnetotelluric imaging: Implications for rift evolution, *Journal of Geophysical Research: Solid Earth* 105, 23493-23518.
- Lajaunie C., Courrioux G., Manuel L. (1997) Foliation fields and 3D cartography in geology: Principles of a method based on potential interpolation, *Mathematical Geology* 29(4), 571-584.
- Lopez S., et al. (2018) Geothermal Modeling in Complex Geological Systems with the COMPASS Code. Stanford, United States, Stanford Geothermal Workshop 2018 - 43rd Workshop on Geothermal Reservoir Engineering.
- Pajot G., Debeglia N., Miéché J.-M. (2007) Estimation du potentiel géothermique de Mayotte: Phase 2 - Étape 1, Investigations géophysiques par gravimétrie, magnétisme et panneau de résistivité électrique, Rapport intermédiaire, BRGM/RP-56027-FR, 60 p.

- Pellerin L., Johnston J.M., Hohmann G.W. (1992) Evaluation of electromagnetic methods for geothermal exploration, *SEG Technical Program Expanded Abstracts* 1992, 405-408, <https://doi.org/10.1190/1.1822102>.
- Sanjuan B., Baltassat J.-M., Bezelgues S., Brach M., Girard J.-F., Mathieu F., avec la collaboration de Debeglia N., Dupont F., François B., Miehé J.-M., Pajot G., Traineau H. (2008) Estimation du potentiel géothermique de Mayotte: Phase 2 - Étape 2, Investigation géologiques, géochimiques et géophysiques complémentaires, synthèse des résultats, Rapport BRGM/RP-56802-FR, 82 p.
- Traineau H., Sanjuan B., Brach M., Audru J.-C. (2006) État des connaissances du potentiel géothermique de Mayotte, Rapport BRGM/RP-54700-FR, 81 p.





# 10



# Feasibility of monitoring cold fronts of geothermal doublets using 4D active electromagnetic techniques – a field trial in the Dogger play in the Paris Basin

F. Dubois, A. Stopin, F. Bretaudeau and P. Wawrzyniak

---

This project aimed to develop a methodology for imaging the “cold fronts” using the surface-to-borehole Controlled Source Electromagnetic Method (CSEM). To achieve this goal, a CSEM data acquisition campaign was being carried out on an operational geothermal doublet, using a surface-to-borehole measurement configuration. The downhole measurement tool (an induction

magnetic field sensor) developed by the LBNL (Lawrence Berkeley National Laboratory of the University of California), and the detectability of the “cold fronts” had to be validated in situ. The doublet where the measurements were taken is part of Dalkia’s geothermal plant in Evry. In early January 2022, a series of injection points, laid out according to the recommendations from different modellings were prepared in anticipation of the acquisition campaign. On the 1st of March, SDP logging team lowered the probe into the well but was unable to pass through the open-hole section. After some adjustments, the probe successfully detected the surface source signal. Data analysis confirmed that the observed signal was indeed emitted by the surface source, thus validating a key aspect of the technology. Additionally, the models indicated that the secondary field generated by a cold front exceeds the noise level recorded by the downhole probe, demonstrating the detectability of the cold front.

## Introduction

This project is initiated as part of the Géodénergies program. Its goal is to develop a methodology for detecting and monitoring the cold front progress between geothermal doublets of the Dogger formation using Controlled Source Electromagnetic (CSEM) methods. From a theoretical standpoint, the cold-water plume is associated with a variation in electrical resistivity within the reservoir (Revil et al., 1998), which can be detected by geophysical CSEM methods (Wawrzyniak et al., 2016). The project consists of two main parts:

1. At the laboratory scale, a calibration of resistivity variations as a function of temperature and frequency specific to the Dogger formation is conducted to accurately characterize this relationship.
2. Then, at the reservoir scale, a CSEM measurement campaign is carried out on a geothermal doublet using a surface-to-borehole measurement configuration. For this, a magnetic probe developed by LBNL (Lawrence Berkeley National Laboratory at the University of California) is lowered into the production well of the Dogger doublet. This will allow for in situ demonstration of the detectability of the “cold front”. The Evry geothermal doublet operated by Dalkia.

In this study case, we will introduce motivations and a summary of the technology used. We then describe the measurement design, including all preparatory work and the campaign’s execution. Finally, we address the data processing and the interpretation of the results, leading to the validation of the cold fronts detectability.

## 10.1 Context

The risk of thermal breakthrough is a long-term consequence of operating Dogger geothermal doublets with reinjection of cooled brine back into the original aquifer. Currently, measuring the temperature at the wellhead of the production well is the only parameter that enables detection of the arrival of the “cold front”. Thermo-hydrodynamic (TH) predictive modeling allows for extrapolation of its dynamic behavior (Figure 10.1) but cannot precisely predict its arrival in time and space. Consequently, cases of thermal breakthrough may occur unexpectedly, as was the case in L’Hay-les-Roses (1 °C decrease after 30 years of operation) and Alfortville (5 °C decrease after 30 years of operation).

At present, there is no tool available for measuring the aquifer temperature other than direct measurement within a well. The proposed technological development is an important element for monitoring geothermal reservoirs.

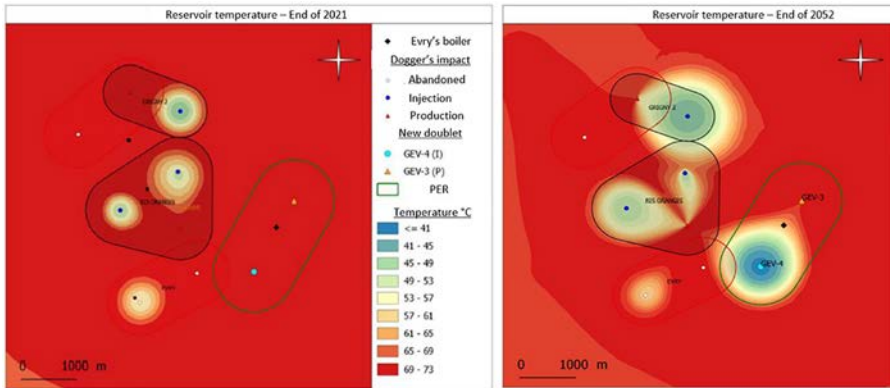


**Figure 10.1** Example of Thermo-Hydrodynamic (TH) modeling used to “predict” the behavior of the cold front over time. Extracted from the activity report submitted by Dalkia for the Evry site.

The CSEM method is sensitive to variations in the subsurface’s electrical resistivity. A source injects electric current into the ground using a square wave signal of predetermined frequency and intensity. One or more receivers simultaneously record electromagnetic fields (electric, magnetic, or both) at the surface or in the borehole. These fields combine the primary field (signal emitted by the source) and a secondary field generated by the distribution of subsurface resistivities. After data processing, the calculated transfer functions can then be “inverted” (a mathematical process) to retrieve the subsurface structure in terms of electrical resistivity.

Wawrzyniak (2019) proposed using CSEM for borehole detection of the cold front within the CO<sub>2</sub> Dissolved project. This work provided guidances and recommendations on the types of sources/receivers and their configurations to use, and it

demonstrated the theoretical detectability of the cold front, particularly identifying the frequencies at which the cold front response would be maximal. We use galvanic sources, injecting current between two electrodes (“poles”) placed in the ground. The placement of these sources is crucial for the success of such measurements. Specifically, it is essential to consider:

1. The distance between the source(s) and receiver(s),
2. The length of the injection dipole(s), or the distance between two electrodes,
3. The orientation of the injection dipole(s),
4. The injected current intensity, related to the grounding resistance (depending on the type of transmitter).

Modeling conducted by Wawrzyniak (2019) and ITES (Strasbourg University) provided guidance on optimal source configurations. For the receivers, preliminary studies showed that a single receiver positioned at the bottom of the well significantly improves the likelihood of capturing the signal. Urban environments have high anthropogenic electromagnetic noise, which can mask the signal. An induction probe is used as the receiver, since measuring the electric field in a cased well must be complex.

## 10.2 Acquisition

The geothermal doublet used for borehole measurements is the Dalkia-operated one in Evry. The injection well GEV4 is targeted, and six zones where injection sites could be established around the well’s shoe have been selected (see Figure 10.2). These sites were surveyed in October 2021. During the survey, factors likely to impact a CSEM survey includes:

1. Presence of power lines, fences, or pipelines.
2. Soil resistivity measurements in areas intended for electrode installation using electrical resistivity tomography (ERT, dipole-dipole) and TDEM with the TEMFAST device (aemr.net). The orientation of the injection dipole(s),
3. Site accessibility.
4. Safety aspects, vehicle traffic, and site activity.

The reconnaissance campaign allowed us to visit each site, resulting in the following observations:

- GEN 1: too small and with high vehicle traffic; low grounding resistance.
- GEN 2: quiet, high electrical resistivity in parts, ample space.
- GEN 3: limited security, low grounding resistance.
- GEN 4: quiet, presence of underground pipes.
- GEN 5: limited security, difficult access, no electrical resistivity measurements.
- GEN 6: inaccessible (fenced), no electrical resistivity measurements.

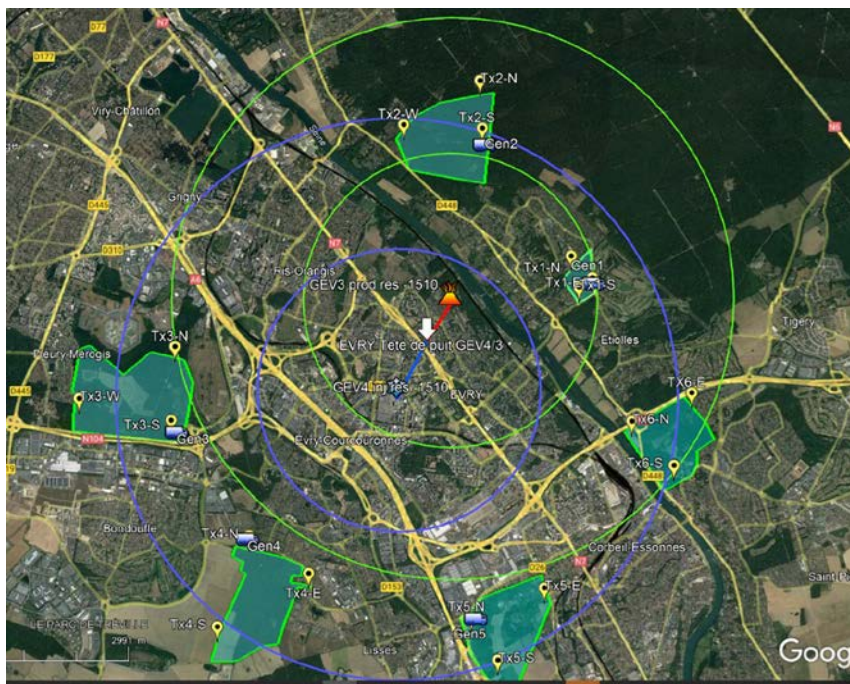


Figure 10.2 Positioning map showing the location of the six identified zones (green polygons) where injection electrodes could be placed. The blue circles are centered on the injection well GEV4, and the green circles on the production well GEV3. The circles have radii of 2 and 4 km.

During a logging control in late October 2021, a foreign object was discovered in the GEV4 injection well. Access to this well was then prohibited due to the increased risk of logging tools becoming stuck. Consequently, the production well GEV3 has been selected by default. Since GEV3 is a production well, access will be more challenging for any future repeat measurements. Furthermore, as the cold front develops in the injection well, it is likely that, even if we gain access to production well in the near future, the cold front signal may be too weak to detect. This will be evaluated during detectability tests, but for this campaign, the decision is to focus on validating the methodology (ability to measure the signal at the bottom of the well and theoretical detectability of the cold front) and to test different source configurations, limiting the campaign to a single injection site. Based on the reconnaissance campaign results, site GEN 2 in the Sénart Forest was selected. Although some surface grounding resistances were high, drilling to a depth of about ten meters should allow for the preparation of electrodes that ensure good current injectivity. Additionally, GEN 2 is the closest site to the well's shoe (2–3 km away) and offers the most suitable conditions in terms of quiet surroundings and adequate space.

In January 2022, a three-day campaign was conducted in the Sénart Forest to drill five holes, each up to 10 meters deep, where copper rods would be placed as injection electrodes. Figure 10.3 shows the location of the drill holes.

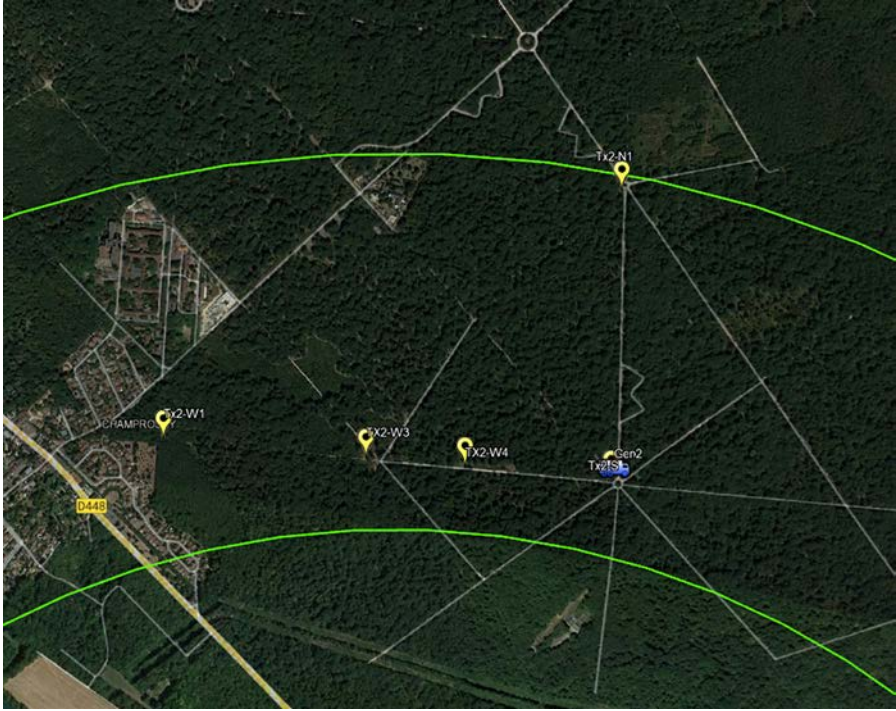


Figure 10.3 Location of the drilled injection electrodes in the Sénart Forest.

We favor the broadside orientation (i.e., perpendicular to the source-to-well shoe axis) of the dipoles, since CSEM modellings indicate this direction to maximize the cold front's response. Then different tests with different dipole lengths in the broadside direction have been conducted as these directly affect the dipole moment of the emitted signal, thus influencing the amplitude of the detectable signal. Finally, a dipole with a radial, in-line orientation is used to validate modeling results showing weaker coupling compared to the broadside orientation.

Between two and five copper rods were inserted into each drilled hole, with bentonite and salt added to enhance coupling between the rods and the ground and lower the grounding resistance. The copper rods were then connected with electrical cable and tape, cut to 10 cm below the surface, and covered with soil, leaves, and stumps to remain inconspicuous and secure. Once the electrodes were prepared, they were connected with electric cables, and grounding resistance was measured to check the dipole's quality and current injection capacity. With

the voltage-regulated transmitter, lower grounding resistance allows for higher injected current. A strong current induces stronger primary and secondary fields, making the signal more detectable. The measured resistances for the four dipoles were as follows:

1. TX2-S – TX2-W1: resistance 50  $\Omega$ ·m, length 1180 m,
2. TX2-S – TX2-W3: resistance 50  $\Omega$ ·m, length 610 m,
3. TX2-S – TX2-W4: resistance 50  $\Omega$ ·m, length 360 m,
4. TX2-S – TX2-N1: resistance 26  $\Omega$ ·m, length 730 m.

These grounding resistances are acceptable and would allow for a minimum current injection of around 10 A (with 550 V voltage). A follow-up inspection in February 2022 confirmed that the electrodes remained intact and well concealed under the branches and leaves placed over them.

### 10.3 Receiver conception

The receiver used to measure the magnetic field at the bottom of the well was developed by LBNL (US) and loaned to BRGM for one year. It is an induction probe (BF4) housed in a fiberglass and epoxy protective casing (see Figure 10.4, left). The BF4 probe is connected to an electronic circuit that provides power and amplifies the measured signal. The probe measures 2.4 meters in length and weighs approximately 20 kg. Its pressure resistance was tested by BRGM at the SDP logging company's logistics base. This test indicated that the probe remained watertight (no internal pressure increase) at a pressure of 220 bars, which is sufficient for the maximum depth of about 1700 meters where it will be deployed in the well. A GO7 head provides the electrical power supply to the probe and transmits the signal back to the surface, while also ensuring the attachment of the probe to the logging cable. With the GO7 head used and due to the design of the probe, it is not possible to connect additional logging instruments to measure other physical properties or to precisely determine the probe's position in the borehole during the measurement campaign. Consequently, when the probe is in the borehole, its location can only be determined by the length of the deployed cable, which is not an exact measurement. Weight bars and centralizers were added below the probe to facilitate its descent and ensure proper positioning at the center of the borehole (see Figure 10.4, right).

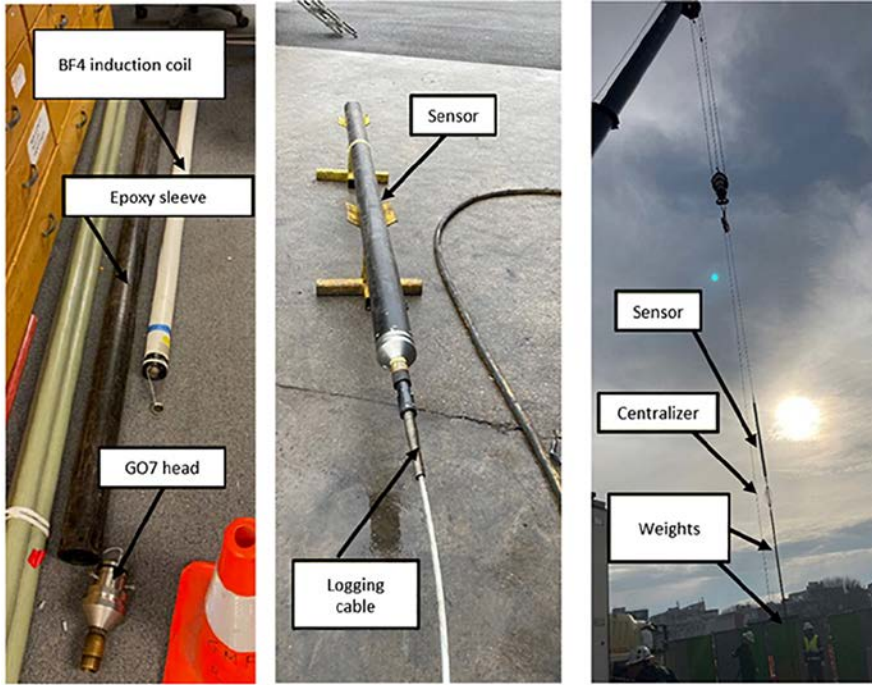


Figure 10.4 Different parts of the LBNL sensors (left) and the probe connected to the logging cable (center), wireline instrument ready to go down into the well (right).

## 10.4 Survey

The survey took place at two sites: the boiler plant site, where the GEV3 borehole (cross-section shown in Figure 10.5) is located and where the logging truck operated the probe (Figure 10.4, right), and the Sénart Forest, where the source (CSEM transmitter) was located. The measurements were carried out on March 1st, 2022, preceded the previous day by the setup of the source equipment and current injection tests to validate proper coupling of the poles. These tests showed improved contact resistance (after pole installation), allowing approximately 15 A of current to be injected. The measurement campaign initially planned to lower the probe into the uncased section of the borehole and perform measurements while raising it, sampling at a minimum of four different depths (Table 10.1). For a given depth, the source emitted the frequency sequence shown in Table 10.2 for a given dipole. This sequence was repeated successively for the four possible dipoles. Once all four dipoles were activated, the probe was raised to the next level, and the operation was repeated.

The schedule planned to start measurements late in the morning (allowing time to install and lower the probe to the bottom of the borehole) and complete measurements for four levels and all dipoles by early evening. The measurements were to be repeated at night to evaluate the signal-to-noise (S/N) ratio, expected to be better at night due to lower anthropogenic noise. However, the transition between cased and uncased sections was complicated to cross. In order to avoid any loss in the well we had to limit our acquisition inside the casing where induced currents may appeared and disturbed the response coming from the reservoir.

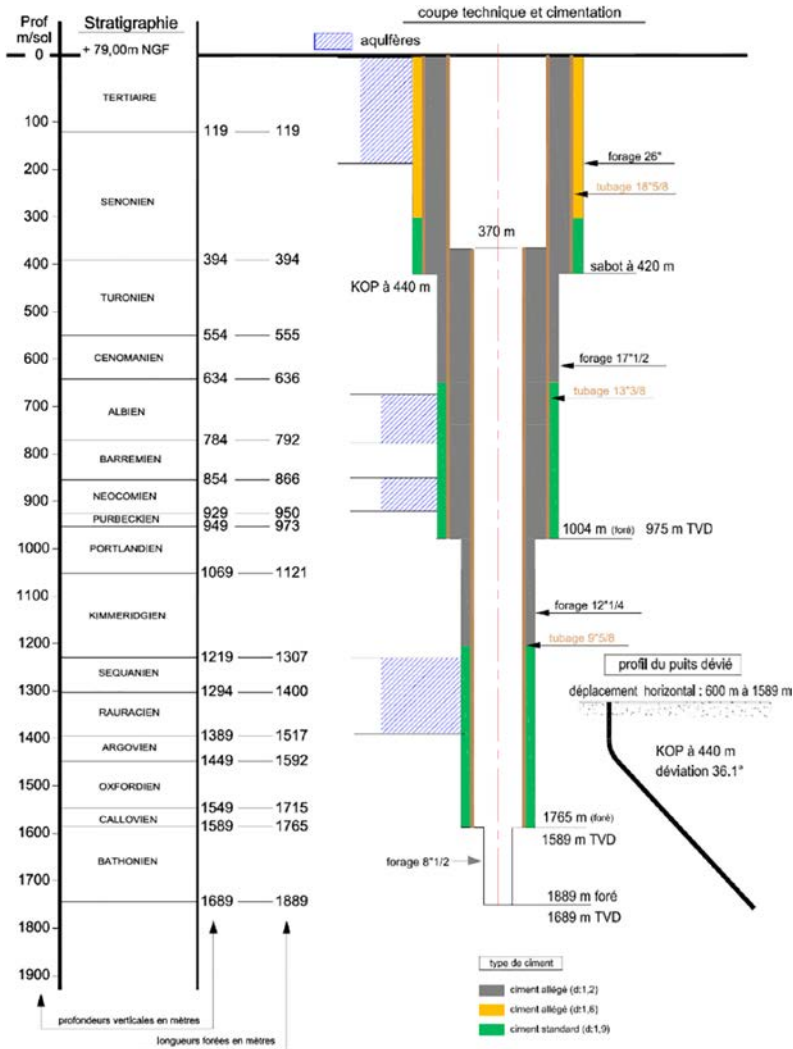


Figure 10.5 Cross-section of the GEV3 production well where the measurements took place (credits: CFG).

## 10.5 Data processing

The data processing is based on the PROCATS processing software developed at BRGM (Bourgeois and Girard, 2010). Transfer functions between the magnetic signal at the borehole bottom, at the surface, and the source are calculated for the different emission frequencies. These transfer functions consist of a real part and an imaginary part, corresponding to the in-phase and quadrature components of the subsurface response resulting from the current injection.

The processing involves extracting, for each station, each transmitter polarization, and each injection frequency, the spectral content of the signals recorded at the stations and normalizing them by the dipole moment emitted at the source (the product of the dipole length and the injected current intensity). The result is a measured magnetic induction field in nT/(A·m). This processing allows the magnetic field measured along the borehole axis (or in three spatial directions for the surface station) to be obtained, along with an estimate of the noise for each component. To provide a reference and compare the surface signal with the borehole signal, a magnetic field measurement station was also installed at the wellhead on the boiler plant site. Figure 10.6 shows the respective positions of the source and the receivers

**Table 10.1** *Sampling depths for the magnetic field recording.*

Measurement point	Depth below the end of casing in m
1	105
2	85
3	65
4	55
5	45
6	20
7	-10 (test inside the casing)

**Table 10.2** *Injection sequences.*

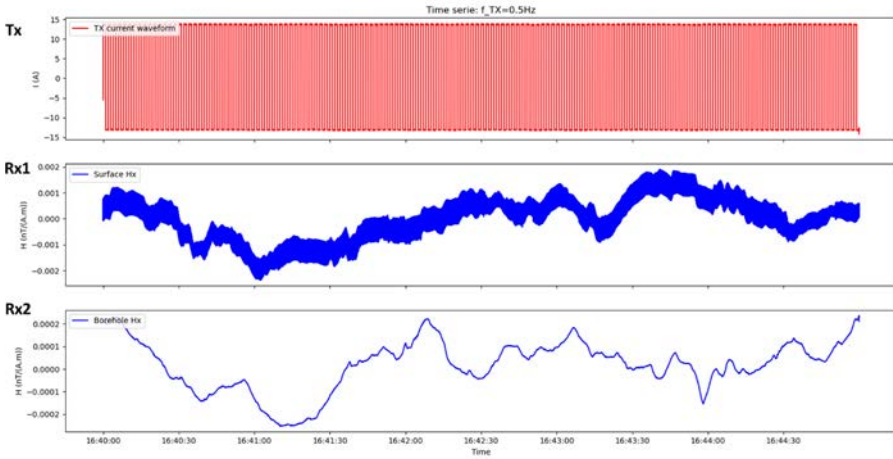
Emitted frequency (Hz)	Duration
0.5	5 min
2	2 min
8	30 s
16	30 s
24	30 s
32	30 s
64	30 s
128	30 s

Figure 10.7 displays the calibrated time series of the signal emitted by the transmitter (TX), the signal received by the surface sensor (RX1), and the signal received by the borehole sensor (RX2). It is clear that the signal emitted by the transmitter is a square wave. A very similar low-frequency behavior is observed between RX1 and RX2. However, the borehole sensor (RX2) shows a significant reduction in high-frequency noise caused by anthropogenic activities. This effect is widely expected as the ground acts as a low-pass filter, removing the high-frequency content from the electromagnetic signal.



Figure 10.6 Positioning map of the source dipole in Sénart Forest (TX2 or TX), the borehole probe at the bottom (RX2), and the surface MT station (RX1).

Figure 10.8 shows the amplitude spectrum of the three time series presented in Figure 10.7. In this example, the signal emitted by the transmitter is a square wave at 0.5 Hz, which appears clearly in the amplitude spectrum's magnitude along with its odd harmonics (1.5, 2.5, 3.5, ...) Hz. Thanks to the noise reduction induced by the ground, the emission peaks from the TX are visible in the borehole magnetometer data (RX2), whereas they are not visible in the surface magnetometer data (RX1). The first clearly visible peak is at 1.5 Hz, which is very distinct on RX2 but completely absent on RX1. These observations clearly show that the signal recorded by the probe corresponds to the signal emitted by the source. The advantage of recording at the borehole bottom to eliminate anthropogenic noise is well validated here. The remaining task is to confirm the order of magnitude of the measured magnetic field value by comparing it with numerical modeling.



**Figure 10.7** Time series of the current emitted by the source (TX), the signal recorded by the surface sensor (RX1), and the signal recorded at the borehole bottom (RX2).

To validate the measurement taken at the borehole bottom, we use a 1D subsurface model, with depth-dependent resistivity variations described in Figure 10.9. We employ the EM3DS software developed by the University of Utah (Wannamaker et al., 1984) to simulate the signal recorded by the probe at the borehole bottom. This software uses a volume integral equation formulation (solved using the method of moments) to compute secondary currents in 3D bounded heterogeneities localized within a 1D stratified structure (infinite horizontal, homogeneous, and isotropic layers). The effect of the casing present in the borehole is not modeled in our case. The signal frequency used for modeling is 0.5 Hz.

The spatial discretization is limited to 3D bodies, while the response of the horizontal stratification is calculated semi-analytically using Hankel transforms. Thanks to this approach, the number of cells in the models remains moderate, generally fewer than 1000 (compared to the typical values of around 100000 in finite-difference or finite-element methods, where the entire 3D space must be meshed), enabling relatively fast computation. The results of this modeling provide a theoretical response at 0.5 Hz of  $7.4 \times 10^{-3}$  nT/(A.m), compared to the recorded signal of  $1.3 \times 10^{-3}$  nT/(A.m). The orders of magnitude are similar, further validating the recorded signal. The observed differences between the modeling and the recorded signal are attributed to the imperfections of the 1D model and the fact that the probe is within the casing.

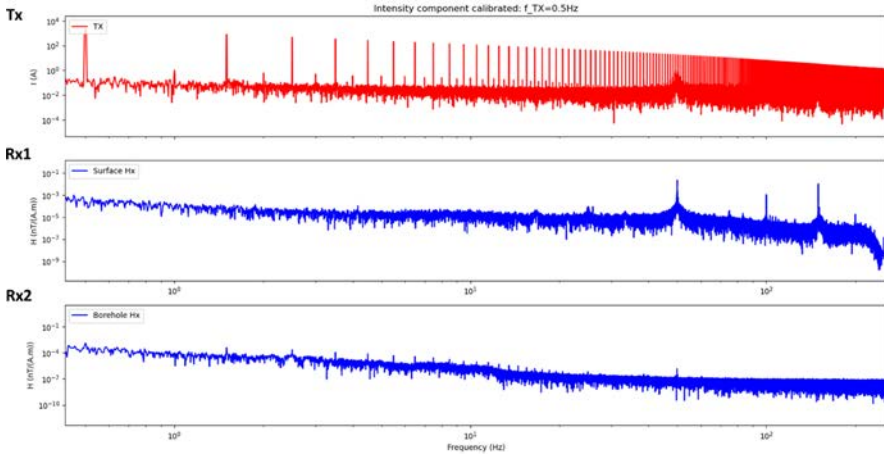


Figure 10.8 Amplitude spectrum of the signal emitted by the source (TX), the signal recorded by the surface receiver (RX1), and the signal recorded at the borehole bottom (RX2).

<b>Top of the layer (m)</b>	0	600	700	1 300	1 400	1 600	1 700	2 000	2 800	3 500
<b>Resistivity (Ω.m)</b>	40	10	40	10	100	1	40	5	20	20

Figure 10.9 Simplified geological model for measurement validation.

## 10.6 Detectability of the cold front

To determine if the cold front is detectable, a new modeling is performed. A parallelepiped with dimensions 100×100×100 m (representing a volume of 10<sup>6</sup> m<sup>3</sup>) simulating water at 40 °C is inserted at the reservoir level. The resistivity of the cold front is chosen to be 41% higher than that of the reservoir layer (based on the experimental tests), which is at 70 °C. Three measurement configurations are modeled (see Figure 10.10) to evaluate the detectability of the cold front. These configurations represent different scenarios we might encounter.

The modeling results are summarized in Figure 10.11. In configuration 1, the magnitude of the secondary field produced by the anomaly (10<sup>-6</sup> nT) is two orders of magnitude higher than the ambient noise level (10<sup>-8</sup> nT). This signal-to-noise ratio

confirms that the cold front could be detected in this configuration, which is a major result of this study. In the other two configurations, 2 and 3, the recorded signal is too weak to allow detection. In configuration 2, the receiver is too far from the source ( $>5$  km), and the response is of the same order of magnitude ( $10^{-8}$  nT) as the noise. In configuration 3, the cold front is too far from the receiver, and the secondary field generated and measured at the receiver is too weak ( $10^{-12}$  nT), well below the noise level, making it undetectable. The main result of this analysis is that in the configuration where the receiver is closest to the anomaly and the source-receiver distance is approximately 3 to 4 km, the anomaly caused by the cold front is detectable.

## Conclusions

The objective of this project was to establish an initial geo-electric state of a geothermal doublet and determine whether a cold front could be detected under ambient noise conditions and using the CSEM sources employed. These objectives were partially achieved. Indeed, the detectability of the cold front was established thanks to the short signal recorded inside the casing. Using the experimental calibrations, which calibrated the variation of resistivity as a function of temperature, the medium's response with and without the cold front was calculated and compared to the noise level extracted from the downhole recordings made by the probe. The modeling shows that the bubble can be detected in specific RX-TX configurations. It was confirmed that the receiver must be as close as possible to the cold front, and the source (transmitter) must be within 4 km of both the bubble and the receiver. These results validate the project's central idea: that a cold front can be detected using the CSEM method (surface-to-well).

During the project's execution, we observed the complexity of installing current sources in a highly urbanized environment. We were fortunate to have the proximity of the Sénart forest to set up the sources and test the method. For this project, we used only one injection site, which would not suffice for imaging purposes. In such cases, several sites at different azimuths would be necessary to accurately locate the cold front in space. During the campaign preparation, six injection sites were identified; however, only three were deemed viable. The others were too close to power lines, pipelines, or in areas where the safety of personnel and equipment could not be ensured. Injection poles require large spaces and the absence of conductive structures (high-voltage lines, pipes, etc.). Therefore, the applicability of the method seems limited to areas with sufficient nearby space to install sources/transmitters unless research efforts can reduce the footprint of these sources.

The receiver may be another project's weak point. It is clear that to further develop this method, work on the probe will be necessary, either internally or through a partnership with specialized manufacturers. For example, integrating three components instead of one could improve result quality. If the above issues are addressed, the most critical challenge remains: access to the well. Obtaining permission to lower

the probe into the GEV3 well was very complicated. The risk of the probe getting stuck is omnipresent, making insurance and risk assessment crucial. Ideally, the measurement should be conducted in the uncased section of the well. There are two main challenges to overcome for this:

1. Obtain authorization to access this zone of the well, where logging tools face a higher risk of getting stuck.
2. Have the physical ability to enter this zone. During this survey, we could not exceed the cased section during the first attempt. Despite repeated efforts by the operator, the probe could not pass through and became temporarily stuck. As a result, measurements were conducted in the cased section of the well. In this case, we currently lack the capability to properly process the data to extract information about the cold front beyond its detectability.

Instrumental and algorithmic developments will thus be necessary to further this concept. Given the undeniable need to monitor the “cold front” and its associated economic implications, it is important to continue exploring solutions to overcome the barriers identified during this project.

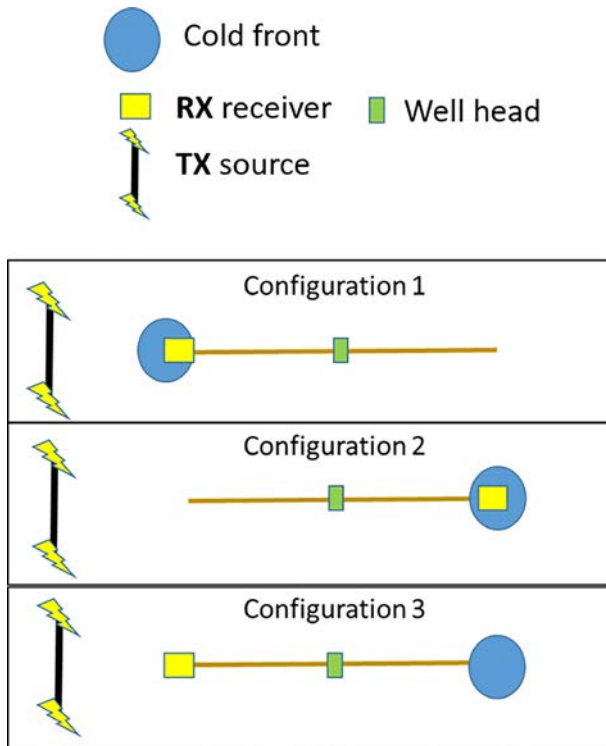


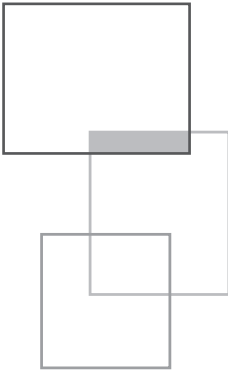
Figure 10.10 Scheme showing the three different geometries between TX-RX modelled to assess the detectability of the cold front.

	configuration 1	configuration 2	configuration 3
<b>Tx</b>	tgt	tgt	tgt
<b>fTx</b>	0,5Hz	0,5Hz	0,5Hz
<b>Rx</b>	puit 1	puit 2	puit 1
<b>Cold front</b>	puit 1	puit 2	puit 2
<b>dRx-Tx</b>	3,5km	5,7 km	3,5km
<b>fRx</b>	<b>0,5Hz</b>	<b>0,5Hz</b>	<b>0,5Hz</b>
<b>Measured signal w/o front nT/A.m</b>	1,3*10 <sup>-3</sup>	??	1,3*10 <sup>-3</sup>
<b>Predicted signal w/o front nT/A.m</b>	7,4*10 <sup>-3</sup>	2,1*10 <sup>-3</sup>	7,4*10 <sup>-3</sup>
<b>fRx</b>	<b>64Hz</b>	<b>64Hz</b>	<b>64Hz</b>
<b>Predicted signal front nT</b>	10 <sup>-6</sup> nT	1,3*10 <sup>-8</sup> nT	10*10 <sup>-12</sup> nT
<b>Noise level (bottom casing nT)</b>	<b>4,7*10<sup>-8</sup>nT</b>	<b>4,7*10<sup>-8</sup>nT</b>	<b>4,7*10<sup>-8</sup>nT</b>
<b>Front detectable?</b>	<b>YES</b>	<b>NO</b>	<b>NO</b>

Figure 10.11 Table summarizing the modeling results and indicating the configurations in which the cold front would be detectable

## References

- Bourgeois B., Girard J.F. (2010) First modelling results of the EM response of a CO2 storage in the Paris Basin, *Oil Gas Sci. Technol.* 65(4), 597-614.
- Revil A., Cathles L.M., Losh S., Nunn J.A. (1998) Electrical conductivity in shaly sands with geophysical applications, *J. Geophys. Res. Solid Earth* 103(10), 23925-23936.
- Wannamaker P.E., SaHohmann G.W., SanFilipo W.A. (1984) Electromagnetic modeling of three-dimensional bodies in layered earths using integral equations, *Geophysics* 149(1), 60-74.
- Wawrzyniak P. (2019) Pilote CO2-Dissolved: Lot 8.1 Monitoring géophysique de la percée thermique par méthode d'Électromagnétisme à Source Contrôlée (CSEM), Rapp. Final BRGM/RP-69370-FR.
- Wawrzyniak P., Coppo N., Bretaudeau F., Vong Chan Q. (2016) CO2-Dissolved: Task 3.2 Geophysical Monitoring, BRGM/RP-66242-FR.



# Synthesis

G. Paixach and J.L. Mari

---

## A range of geothermal systems

The first deliberate attempt to generate power from geothermal energy was made in 1904 in Larderello, Italy, where the French engineer François Jacques de Larderel used steam from a geothermal well to generate electricity. Since then, geothermal technology has evolved significantly, with modern techniques now allowing us to drill deep into the Earth and access high-temperature geothermal reservoirs.

However, it's essential to recognize that geothermal energy is not a one-size-fits-all resource. We can classify geothermal systems based on the intended usage, the fluid or geological context involved, and even the energy production design.

### Classifying by usage:

- **Direct Use of Hot Water:** This is one of the oldest and most straightforward uses of geothermal energy, in which naturally heated water (30–80 °C) from geothermal springs or wells is used for heating buildings, agricultural greenhouses, aquaculture ponds, and industrial processes.
- **Electricity Generation:** Higher temperatures, typically above 150°C, are required to produce electricity. In these systems, steam from geothermal reservoirs drives turbines connected to generators. These are commonly used in areas with high geothermal activity, like volcanic regions.

- Geothermal Heat Pumps (GHPs): GHPs leverage stable ground temperatures (10–16 °C) found a few meters below the surface to provide efficient heating and cooling for buildings. This technology is widely applicable and doesn't require high temperatures.

**Classifying by geological settings:**

- Shallow Geothermal Systems: This involves tapping into the moderate temperatures found at shallow depths, typically up to a few hundred meters, to power geothermal heat pumps.
- Sedimentary Basin Systems: In regions with porous/fractured/karstified sedimentary layers, geothermal reservoirs of hot water can be found at moderate depths, often used for direct heating or low-temperature electricity production.
- Volcanic Systems: High-temperature geothermal reservoirs in volcanic regions are ideal for electricity generation. Countries like Indonesia and New Zealand are renowned for tapping volcanic geothermal resources for power.
- Rift and Fault Zones: In areas where tectonic plates pull apart or fracture, crust is thinner, and heat flow is higher than usual promoting geothermal reservoir development in conjunction with volcanic activity.
- Fractured Granite and Crystalline Rock: Some geothermal resources are found in fractured hard rock, where engineered geothermal systems (EGS) create or enhance pathways for water to circulate and absorb heat.

**Conventional and non-conventional geothermal resources:**

- Conventional Hydrothermal Systems: These systems involve naturally occurring hot water or steam reservoirs. They are typically used in volcanic or high-geothermal-gradient areas and are well-suited for electricity generation.
- Non-Conventional Systems (Enhanced Geothermal Systems and Closed Loop). In regions lacking natural hydrothermal reservoirs, EGS can artificially create or enhance pathways in hot dry rock/low permeability rocks for water to circulate, picking up heat for use at the surface. Closed-loop systems involve circulating a working fluid through pipes underground without any interaction with natural groundwater, making them potentially viable and after a complete economic assessment in a broad range of geological environments.

These advancements allow us to make use of geothermal energy far beyond natural manifestations, making it a sustainable and reliable source of heat and power. The need to characterize subsurface is critical and require the use of geophysical techniques.

## A range of geophysical techniques

Historically, geophysical methods have played a pivotal role in the exploration of oil, gas, and minerals, serving as the backbone of resource discovery for decades. There are various geophysical methods, each based on distinct theoretical principles, that

provide valuable data about subsurface materials. By acquiring and analyzing this data through specific geophysical surveys, we can better understand the subsurface properties and characteristics, offering important insights for exploring and managing subsurface resources and developing geotechnical engineering.

Geophysical methods encompass various techniques, each designed to characterize specific properties.

- Gravity and gravity-gradiometry are sensitive to density variations.
- Magnetic methods respond to rock magnetization properties, including magnetic susceptibility and remanence.
- Electrical and electromagnetic (EM) methods capture resistivity variations.
- Seismic methods are influenced by both velocity and density variations.

By measuring variations in the subsurface's physical properties, geophysical surveys can provide valuable insights into geological features, helping to identify critical characteristics of geothermal systems before the costly process of drilling.

Generally, no single geophysical method can characterize all the elements of a geothermal play. Each technique has unique strengths and limitations, responding to specific subsurface properties and functioning at different scales, depths, and spatial resolutions. Instead, multi-physics approaches combine several geophysical techniques, allowing experts to construct a more reliable picture of the subsurface.

## Geophysics for geothermal systems

This book further illustrates the techniques and strategies that can be employed to investigate geothermal systems via geophysical methods.

Surface geophysical methods enable the construction of a 2D or 3D geophysical model of the subsurface link to one or more physical parameters. Borehole methods help to investigate the nearby well and calibrate the models derived from the surface geophysical methods. As in any geophysical study, multi-physics approaches facilitate interpretation.

By providing insights into the subsurface's physical properties, geophysical methods help better understand, assess, and monitor geothermal resources. The goal is to enable engineers to optimize production, mitigate risks, and ensure the sustainability of the reservoir. Here is a selected list of the key information that geophysicists can contribute.

- Identifying subsurface structures.
- Mapping temperature distribution.
- Characterizing rock types and reservoir properties.
- Differentiating geothermal fluids.
- Assessing fault activity.
- Real-Time well steering during drilling.

Geophysical methods contribute to the understanding of geothermal systems.

Electrical and electromagnetic methods are one of the geophysical techniques potentially sensitive to water content and temperature. Surface-to-borehole Controlled Source Electromagnetic Method (CSEM) can be used to establish an initial geo-electric state of a geothermal doublet and determine whether a cold front could be detected. Active and passive seismic methods help to better understand the geological structure of the subsurface, locating fractured zones and geological formation interfaces and potentially identify hydrothermal fluids presence and circulation pathways. Passive methods, being less invasive and cost-effective, are valuable tools. When combined, passive seismic, MT, and gradiometry can yield a shear velocity model, resistivity distribution with depth, and insights into bedrock location and fault structures. Seismic inversion and characterization are disciplines that aim at converting seismic amplitude into key reservoir properties, leading to valuable information between wells to lower the risk while planning exploration or development of geothermal production, either with low or high depth objectives. Furthermore, anisotropy magnitude and orientation, extracted by both VVAZ (Velocity versus Azimuth) and AVAZ (Amplitude versus Azimuth) analysis, can be linked to fracture intensity and orientation. The fracture characterization plays a crucial role in identifying zones with secondary porosity and enhanced permeability, increasing the prospectivity. The fracture connectivity must be evaluated to derisk the development of a geothermal project.

As an example for a geothermal volcanic system, various geophysical methods were used to confirm the existence and location of deeper geothermal resources in Mayotte's Petite-Terre volcanic Island and to define the geothermal drilling targets. Geophysical data allowed for the placement of a reservoir, a heat source, the base of the volcanic substratum, as well as several areas with higher vertical permeability (chimneys) connecting the reservoir to surface material ejection zones. MT measurements enabled the construction of a well-constrained 3D image of a potential geothermal target, Electrical profiles crossing the island detected the presence of faults, Gravity measurements were inverted to obtain a density model and confirm the presence of faults. The inversion is performed jointly with the inversion of MT data, using a global correlation of resistivity and density structures as a constraint.

As an example of a geothermal rift and fault zones system, a multi-physics image of deep fractured geothermal reservoirs is essential to reduce the risks of deep geothermal resource, as shown by the establishment of the geothermal model In the Upper Rhine Graben. The example shows how the occurrence of fractured reservoirs characterized by natural brine circulations with fractured zones obliged developers to adapt geophysical exploration methods, geophysical well logging strategies as well as technical well design for reaching geothermal targets.

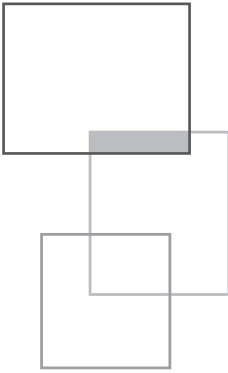
The objective is always to select and combine the most appropriate geophysical methods to build the most comprehensive geological models for the specific geothermal system.

## From resource exploration to drilling project de-risking and asset monitoring

Whatever the geothermal systems, it is important to make an inventory of existing geophysical data at the basin (exploration) or project scale (drilling de-risking). For instance, micro seismic recordings are useful to assess the seismicity of the site. For geothermal projects in sedimentary basins, it is important to make an inventory of the seismic lines that have been recorded for oil and gas exploration. The objective is to reprocess these legacy seismic lines using customized processing sequences that make it possible to obtain both an accurate high resolution structural model with distribution of faults and fractures, and a reservoir model with distribution of physical (acoustic impedance) and petrophysical parameters (porosity, permeability). Conventional processing sequences can be adapted to evaluate the potential of geothermal reservoirs, but innovative sequences are being developed. Among these innovative techniques we can mention the use of full-waveform inversion to directly infer temperature, the use of ambient seismic noise for fluid detection or the use of fiber optic for permanent monitoring.

Overall, the integration of multiple geophysical methods enhances subsurface imaging and offers more reliable insights, enabling more informed decision-making in resource exploration and drilling project de-risking of geothermal sites. Ultimately, geophysical surveys aim to optimize the success of exploration and minimize risks when planning a new well at the project scale. However, more like others, the subsurface industries now face challenges related to the energy transition, which extend beyond merely identifying sustainable energy sources like geothermal energy. It also involves adapting surveillance technologies for new purposes, such as asset and resource monitoring during production, while addressing economic constraints, and environmental concerns.





# Conclusion

**J.L. Mari and G. Paixach**

---

This book provides an overview of geophysical methods and serves as a practical guide, using field examples, to illustrate the contributions of these methods to geothermal exploration. It is written for students and researchers in geoscience, as well as for professionals involved in geothermal energy.

We hope it will encourage readers to evaluate the featured methods themselves, including high-resolution seismic methods, electrical methods (ERT and deep ERT), and electromagnetic methods (MT and CSEM). Examples of integrated approaches combining these techniques are presented using near-surface and sub-surface datasets.

Each chapter includes theoretical concepts, practical guidelines, and, most importantly, real-world application examples. For this reason, the book can serve as a textbook for course lectures or as a resource for continuing education seminars.

The book aims to promote the exchange of information among geologists, geophysicists, and engineers involved in geothermal exploration and production.

**PROfile**

# Geophysics in geothermal exploration: a review

**Jean-Luc Mari and Geoffroy Paixach**

In subsurface characterization studies, surface seismic and electrical-electromagnetic methods are among the most widely used methods for creating 2D and 3D subsurface models. These methods play a growing role in soil investigations for hydrogeological studies, site characterization for wind farms, and the oil and gas industry, particularly in Carbon Capture and Storage (CCS).

The goal of this book is to provide a practical guide on how to apply geophysical methods in geothermal exploration, illustrated with real-world field examples. These methods support resource exploration, the de-risking of drilling projects, and the ongoing monitoring of geothermal assets.

The book begins with an introduction to geothermal energy systems. It then delves into geophysical methods, presenting the current state of knowledge and illustrating how electrical-electromagnetic and active-passive seismic methods can be combined into a Multiphysics approach for geothermal exploration.

Each method has unique strengths and limitations, responding to specific subsurface properties and operating at different scales, depths, and spatial resolutions. Therefore, selecting the most cost-effective and appropriate methods for a given geothermal prospect requires an integrated approach to optimize exploration success while minimizing risks.

In addition to these examples, the authors provide readers with guidelines to carry out these operations, in terms of acquisition, as well as processing and interpretation.

Each chapter includes brief theoretical concepts, mainly practical guidelines and, most importantly, real-world application examples. For this reason, the book can be used as a companion text for course lectures and continuing education seminars.

This book aims to promote the exchange of information among geologists, geophysicists, and engineers involved in the field of geothermal energy.

978-2-7598-3752-6



**edpsciences**  
www.edpsciences.org

Books of the PROfile collection are intended for the transmission of professional knowledge in different disciplines. They are written by recognized experts in their fields and contribute to the training and information of professionals.